Study on Bifurcation Phenomena in Three-Phase Circuit

Takashi Hisakado

May 1997

Study on Bifurcation Phenomena in Three-Phase Circuit

Takashi Hisakado

May 1997

Contents

1 Introduction **1**
- 1.1 General Background . . . 1
- 1.2 Background in Power System . . . 2
- 1.3 Description of Contents . . . 3

2 Fundamental Equation and Its Solution **4**
- 2.1 Introduction . . . 4
- 2.2 Circuit Equation . . . 4
- 2.3 Symmetry of Three-phase Circuit . . . 6
- 2.4 Two-point Boundary Value Problem and Shooting Method . . . 10
- 2.5 Homotopy Method . . . 11
- 2.6 Definition of Bifurcation Points . . . 15
- 2.7 Search of Bifurcation Points . . . 21
- 2.8 Equations of Bifurcation Points . . . 22
- 2.9 Calculation of Bifurcation Sets . . . 26

3 Experimental Circuit **27**
- 3.1 Introduction . . . 27
- 3.2 Experimental Circuit . . . 27
- 3.3 Phase Controller . . . 29
- 3.4 Magnetizing Characteristics . . . 36
- 3.5 Experimental Method . . . 37

4 Single-phase 1/3-Subharmonic Oscillation **42**
- 4.1 Introduction . . . 42
- 4.2 Periodic Solution Curve in Three-phase Circuit . . . 42
- 4.3 Periodic Solution Curve in Singe-phase-like Circuit . . . 47
- 4.4 Mode of Oscillation . . . 49
- 4.5 Coupled Single-phase Circuit . . . 51
- 4.6 Bifurcation Set . . . 55
- 4.7 Experimental Results . . . 57
- 4.8 Concluding Remarks . . . 62

5 Two-phase 1/3-Subharmonic Oscillation **63**
5.1 Introduction 63
5.2 Periodic Solution Curve in Three-phase Circuit 63
5.3 Bifurcation Set in Three-phase Circuit 67
5.4 Comparison with Single-phase 1/3-Subharmonic Oscillation 69
5.5 Bifurcations in Coupled Single-phase Circuit 73
5.6 Experimental Results 74
5.7 Concluding Remarks 79

6 Symmetric 1/3-Subharmonic Oscillation **81**
6.1 Introduction 81
6.2 Pure 1/3-Subharmonic Oscillation 81
6.3 1/3-Subharmonic Oscillation with Beat 84
6.4 Lyapnov Exponent 87
6.5 Experimental Results 87
6.6 Concluding Remarks 91

7 Harmonic Oscillation **92**
7.1 Introduction 92
7.2 Three Modes in Three-phase Circuit 92
7.3 Analytical Results of Symmetric Oscillation 93
7.4 Analytical Results of Single-phase Oscillation 99
7.5 Analytical Results of Unsymmetric Oscillation 102
7.6 Experimental Results 103
7.7 Phase Control 107
7.8 Concluding Remarks 117

8 1/2-Subharmonic Oscillation **118**
8.1 Introduction 118
8.2 Three Modes in Three-Phase Circuit 118
8.3 Single-phase Oscillation 121
8.4 Symmetric Oscillation 127
8.5 Concluding Remarks 132

9 Conclusions **133**

A Generation of Pitchfork Bifurcation **142**

B Chaotic Harmonic Oscillation **145**

Chapter 1

Introduction

1.1 General Background

Symmetries often occur in engineering and physical systems. If a system is linear, a symmetric system leads to a unique symmetric phenomenon. However, if a system is nonlinear, unsymmetric phenomena may be generated. The generation of unsymmetric phenomena formulate patterns. That is, patterns in nature appear by break of symmetries. Then it is important to reveal the relation between symmetric and unsymmetric phenomena in a symmetric system.

As for nonlinear circuits, lower dimensional systems with single nonlinear element have been studied very intensively and large amount of knowledge is gained. In regard to single-phase circuit nonlinear oscillations are investigated in [1] and the notion of chaos is emerged in [2]. In recent years, the advance of computers, that is, the appearance of high-speed CPU and large memories, makes it possible to analyze higher dimensional systems with many nonlinear elements. Then, the analyses of nonlinear circuit systems which have several nonlinear elements receive attention. In nonlinear circuit systems, because of the coupling of single nonlinear circuits, several phenomena such as unsymmetric phenomena and synchronizing phenomena which cannot be confirmed in a single nonlinear circuit are generated.

On the other hand, when there is a qualitative changes in the behavior of a system such as the transition from symmetric to unsymmetric phenomenon and synchronizing to unsynchronizing phenomenon, we call it bifurcation phenomenon. In other words, in a nonlinear system, distinctive features appear through bifurcations. Hence, global behaviors

in nonlinear circuit systems can be revealed by paying attention to the bifurcations.

In this thesis, nonlinear three-phase circuit with symmetry is investigated. The circuit consists of delta-connected nonlinear inductors, capacitors, resistors and balanced voltage sources. This circuit can be represented by a five dimensional system with the nonlinear coupling of inductors and with a structural symmetry. Hence, several phenomena which can't be confirmed in lower dimensional systems with a single nonlinear element are generated. This thesis make manifest distinctive features in the three-phase circuit in the viewpoint of bifurcation phenomena.

1.2 Background in Power System

Symmetrical three-phase circuit is quite fundamental and practical in a power system. In the three-phase transmission line with capacitors in series with voltage sources when the transformer becomes lightly loaded or no-loaded, the exciting impedance can not be neglected. As a result, the nonlinearity of the exciting impedance can not be neglected. There are, however, very few studies concerning oscillations in non-linear three-phase circuits.

In Japan an abnormal oscillation occurred in the Inawashiro transmission line in 1927. Since then the harmonic and higher harmonic oscillations in three-phase circuits have been investigated from both experimental and theoretical points of view [3]. The reference reveals that the undamped oscillation has infinite components of frequency and occur by the nonlinearity of transformers and the capacity of transmission lines. Researches on subharmonic oscillations, although observed in the transmission line compensated with series capacitors has rarely been carried out [4].

In recent years, a permanent non-periodic oscillation is observed on a 400kV power system in France [5]. Further, the researches in the viewpoint of nonlinear dynamics are reported in [6, 7, 8]. The researches, however, investigate the single-phase models of the three-phase power systems.

In the three-phase circuit, higher harmonic and subharmonic oscillations as well as almost periodic and chaotic oscillations are generated. Further, as for the symmetry of the circuit, the breaking of symmetry is confirmed. The subharmonic oscillations of order 1/3 and 1/2 have been analyzed by means of the extension of the asymptotic method originally developed by Krylov, Bogoliubov and Mitropolsky, and are experimentally confirmed [9, 10, 11, 12, 13, 14, 15].

In this thesis, the bifurcation phenomena of the 1/3-subharmonic, 1/2-subharmonic and fundamental harmonic oscillations in the three-phase circuit are investigated from both theoretical and experimental points. As for the theoretical analysis, the steady state is formulated as a two-point boundary value problem and analyzed in detail by the homotopy method combined with a shooting method. Additionally, a real three-phase circuit is made up and by close experiments comparison with the results with homotopy method is made. In these analyses, paying particular attention to the symmetry of the circuit, the effects of nonlinear coupling are revealed and the relevancy of bifurcations in between three-phase and single-phase circuits becomes manifest.

1.3 Description of Contents

This thesis consists of 9 chapters and the outlines are shown as follows.

In Chapter 2, the three-phase circuit is formulated as a two-point boundary value problem and the homotopy method combined with a shooting method is shown. Further, the analytical methods of bifurcation phenomena are described.

In Chapter 3, the configuration of the experimental circuit and the measuring device are illustrated. Further, the configuration of the switching phase controller is described.

In Chapter 4, the bifurcation phenomena of single-phase 1/3-subharmonic oscillations are investigated. For the comparison with the three-phase circuit, a single-phase-like circuit and a coupled single-phase circuit are defined and analyzed.

In Chapter 5, the bifurcation phenomena of two-phase 1/3-subharmonic oscillations are investigated. Additionally, the relation between the single-phase and two-phase oscillations are represented.

In Chapter 6, the bifurcation phenomena of symmetrical 1/3-subharmonic oscillations are investigated. The relations between symmetry and frequency of oscillations are also represented.

In Chapter 7, the bifurcation phenomena of fundamental harmonic oscillations are investigated. Additionally, the relations between the switching phase angle and the generated modes are presented.

In Chapter 8, the bifurcation phenomena of 1/2-subharmonic oscillations are investigated.

Chapter 9 is the concluding chapter summarizing the major results in this thesis.

Chapter 2

Fundamental Equation and Its Solution

2.1 Introduction

In this chapter, the circuit equation of the nonlinear three-phase circuit with symmetry is derived. Then we formulate equations to obtain the periodic solution of the circuit equation, which is a two-point boundary value problem, by using shooting method. Next, the Newton and general homotopy methods and the method of tracing path are shown. Further, co-dimension one bifurcations are defined and the method of searching the bifurcations is shown. Furthermore, the determining equations of bifurcation points are derived and the method of calculating bifurcation sets is shown.

2.2 Circuit Equation

We have the following circuit equations of the three-phase circuit illustrated in Fig.2.1.

$$\left.\begin{aligned} \frac{d\boldsymbol{\phi}}{dt} &= \mathbf{A}\boldsymbol{e}(t) - \mathbf{A}\boldsymbol{v} - (\mathbf{A}\boldsymbol{R}\mathbf{A}' + \boldsymbol{r})\boldsymbol{i}(\boldsymbol{\phi}) \\ \boldsymbol{C}\frac{d\boldsymbol{v}}{dt} &= \mathbf{A}'\boldsymbol{i}(\boldsymbol{\phi}) \end{aligned}\right\} \tag{2.1}$$

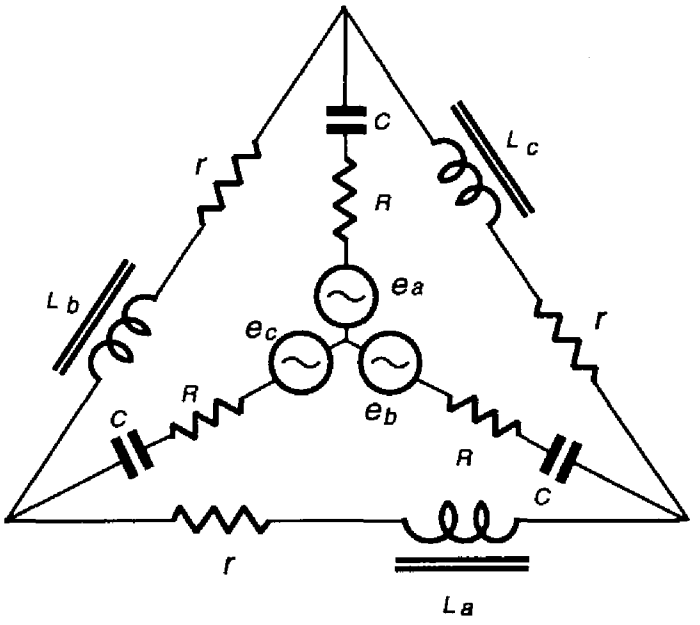

Fig. 2.1: Three-phase circuit.

$\boldsymbol{\phi} = (\phi_a, \phi_b, \phi_c)'$: flux-interlinkage vector of inductor

$\boldsymbol{i}(\boldsymbol{\phi}) = (i_a, i_b, i_c)'$: inductor current vector

$\boldsymbol{e}(t) = (e_a(t), e_b(t), e_c(t))'$: three-phase voltage source vector

$\boldsymbol{v} = (v_a, v_b, v_c)'$: capacitor voltage vector

$\boldsymbol{R} = diag(R, R, R)$: diagonal matrix for series resistor

$\boldsymbol{r} = diag(r, r, r)$: diagonal matrix for delta-connected resistor

$\boldsymbol{C} = diag(C, C, C)$: diagonal matrix for series capacitor

$$\mathbf{A} = \begin{pmatrix} 0 & 1 & -1 \\ -1 & 0 & 1 \\ 1 & -1 & 0 \end{pmatrix}$$

where a prime means transpose, diag() represents diagonal matrix. The vector valued function $\boldsymbol{i}(\boldsymbol{\phi})$ represents the magnetizing characteristics of nonlinear inductors defined by

$$\boldsymbol{i}(\boldsymbol{\phi}) = (i(\phi_a), i(\phi_b), i(\phi_c))' \tag{2.2}$$

where the function $i(\cdot)$ is an odd monotonically increasing function. The three-phase

symmetrical voltage source is defined by

$$e(t) = \left(e_m \cos(\omega t + \varphi),\ e_m cos(\omega t - \frac{2}{3}\pi + \varphi),\ e_m \cos(\omega t + \frac{2}{3}\pi + \varphi)\right)' \tag{2.3}$$

ω : angular frequency of voltage source

φ : initial phase angle.

Introducing scale factors $\alpha_\phi, \alpha_i, \alpha_v$, we transpose variables in Eq.(2.1).

$$\left.\begin{aligned} \tau &= \omega t + \varphi \\ \boldsymbol{\Psi} &= \alpha_\phi \boldsymbol{\phi} \quad : \text{ scaled flux-interlinkage vector of inductor} \\ \boldsymbol{I} &= \alpha_i \boldsymbol{i} \quad : \text{ scaled inductor current vector} \\ \boldsymbol{U} &= \alpha_v \boldsymbol{v} \quad : \text{ scaled capacitor voltage vector} \\ \boldsymbol{E} &= \alpha_v \mathbf{A} \boldsymbol{e} \quad : \text{ scaled three-phase voltage source vector} \\ &= \left(E_m \sin(\tau),\ E_m \sin(\tau - \frac{2}{3}\pi),\ E_m \sin(\tau + \frac{2}{3}\pi)\right)' \end{aligned}\right\} \tag{2.4}$$

where, $E_m = \sqrt{3}\alpha_v e_m$, and we set $\alpha_v = \dfrac{\alpha_\phi}{\omega}$.

Now, we obtain the following scaled circuit equation:

$$\frac{d}{d\tau}\begin{bmatrix} \boldsymbol{\Psi} \\ \boldsymbol{U} \end{bmatrix} = \boldsymbol{f}(\boldsymbol{\Psi}, \boldsymbol{U}, \tau) \tag{2.5}$$

$$\triangleq \begin{bmatrix} \boldsymbol{E}(\tau) - \mathbf{A}\boldsymbol{U} - \xi\widehat{\mathbf{A}}\boldsymbol{I}(\boldsymbol{\Psi}) - \zeta\boldsymbol{I}(\boldsymbol{\Psi}) \\ \eta\mathbf{A}'\boldsymbol{I}(\boldsymbol{\Psi}) \end{bmatrix} \tag{2.6}$$

where

$$\xi = R\frac{\alpha_v}{\alpha_i}, \qquad \zeta = \tau\frac{\alpha_v}{\alpha_i}, \qquad \eta = \frac{1}{\omega C}\frac{\alpha_v}{\alpha_i},$$

$$\boldsymbol{I}(\boldsymbol{\Psi}) = \alpha_i \boldsymbol{i}\left(\frac{\boldsymbol{\Psi}}{\alpha_\psi}\right), \qquad \widehat{\mathbf{A}} = \mathbf{A}\mathbf{A}'.$$

2.3 Symmetry of Three-phase Circuit

2.3.1 Structural Symmetry

The three-phase circuit has symmetries. In this section, the characteristics of the three-phase circuit are shown as to the symmetry.

First, we define the following matrix:

$$\hat{\mathrm{C}}_3 \triangleq \begin{pmatrix} 0 & 1 & 0 \\ 0 & 0 & 1 \\ 1 & 0 & 0 \end{pmatrix}. \tag{2.7}$$

The matrix satisfies the relations

$$\hat{\mathrm{C}}_3^3 = \mathrm{1} \qquad \mathrm{1}: \text{unit matrix} \tag{2.8}$$

$$\mathrm{A}\hat{\mathrm{C}}_3 = \hat{\mathrm{C}}_3\mathrm{A}. \tag{2.9}$$

Considering the relation (2.9), the right-hand side of the circuit equation (2.6) satisfies the following equation [16, 17, 18, 19]:

$$\boldsymbol{f}(\hat{\mathrm{C}}_3\boldsymbol{\Psi}, \hat{\mathrm{C}}_3\boldsymbol{U}, \tau) = \mathrm{C}_3\boldsymbol{f}(\boldsymbol{\Psi}, \boldsymbol{U}, \tau + \frac{2}{3}\pi) \tag{2.10}$$

where

$$\mathrm{C}_3 \triangleq \begin{bmatrix} \hat{\mathrm{C}}_3 & \mathrm{o} \\ \mathrm{o} & \hat{\mathrm{C}}_3 \end{bmatrix}, \qquad \mathrm{C}_3^3 = \mathrm{1}. \tag{2.11}$$

Eq.(2.10) mathematically presents the structural symmetry of the three-phase circuit.

Assume that $[\boldsymbol{\Psi}(\tau), \boldsymbol{U}(\tau)]'$ is a solution of Eq.(2.6), then

$$\begin{aligned} &\frac{d}{d\tau}\mathrm{C}_3 \begin{bmatrix} \boldsymbol{\Psi}(\tau + \frac{2}{3}\pi) \\ \boldsymbol{U}(\tau + \frac{2}{3}\pi) \end{bmatrix} - \boldsymbol{f}\left(\hat{\mathrm{C}}_3\boldsymbol{\Psi}(\tau + \frac{2}{3}\pi), \hat{\mathrm{C}}_3\boldsymbol{U}(\tau + \frac{2}{3}\pi), \tau\right) \\ &= \mathrm{C}_3\frac{d}{d\tau} \begin{bmatrix} \boldsymbol{\Psi}(\tau + \frac{2}{3}\pi) \\ \boldsymbol{U}(\tau + \frac{2}{3}\pi) \end{bmatrix} - \mathrm{C}_3\boldsymbol{f}\left(\boldsymbol{\Psi}(\tau + \frac{2}{3}\pi), \boldsymbol{U}(\tau + \frac{2}{3}\pi), \tau + \frac{2}{3}\pi\right) \\ &= \mathrm{o}. \end{aligned} \tag{2.12}$$

Thus, $\mathrm{C}_3[\boldsymbol{\Psi}(\tau + 2/3\pi), \boldsymbol{U}(\tau + 2/3\pi)]'$ is also a solution of Eq.(2.6). In the same way,

$$\mathrm{C}_3^n \begin{bmatrix} \boldsymbol{\Psi}(\tau + \frac{2n}{3}\pi) \\ \boldsymbol{U}(\tau + \frac{2n}{3}\pi) \end{bmatrix} \qquad (n = 1, 2, \ldots) \tag{2.13}$$

are also solutions of Eq.(2.6). As for oscillations whose period is n times that of the voltage sources (such oscillations will be called period-n oscillation), the following relation is satisfied:

$$\begin{bmatrix} \boldsymbol{\Psi}(\tau) \\ \boldsymbol{U}(\tau) \end{bmatrix} = \begin{bmatrix} \boldsymbol{\Psi}(\tau + 2n\pi) \\ \boldsymbol{U}(\tau + 2n\pi) \end{bmatrix}. \tag{2.14}$$

Therefore, as for the symmetry of $\mathbf{C}_3$ there are $3n$ initial vector values at $\tau = 0$ of the period-n oscillations which are represented by

$$\mathbf{C}_3^k \begin{bmatrix} \boldsymbol{\Psi}(\frac{2k}{3}\pi) \\ \boldsymbol{U}(\frac{2k}{3}\pi) \end{bmatrix}, \qquad (k = 0, 1, \ldots, 3n-1) \tag{2.15}$$

in general. If the relation

$$\begin{bmatrix} \boldsymbol{\Psi}(0) \\ \boldsymbol{U}(0) \end{bmatrix} = \mathbf{C}_3^n \begin{bmatrix} \boldsymbol{\Psi}(\frac{2n}{3}\pi) \\ \boldsymbol{U}(\frac{2n}{3}\pi) \end{bmatrix} \quad or \quad \begin{bmatrix} \boldsymbol{\Psi}(0) \\ \boldsymbol{U}(0) \end{bmatrix} = \mathbf{C}_3^{2n} \begin{bmatrix} \boldsymbol{\Psi}(\frac{4n}{3}\pi) \\ \boldsymbol{U}(\frac{4n}{3}\pi) \end{bmatrix} \tag{2.16}$$

is satisfied, we shall say the solution has a symmetry with respect to $\mathbf{C}_3$.

2.3.2 Symmetry Based on Magnetizing Characteristics

Next, we define the following matrix

$$\widehat{\mathbf{C}}_2 \triangleq \begin{pmatrix} -1 & 0 & 0 \\ 0 & -1 & 0 \\ 0 & 0 & -1 \end{pmatrix} \tag{2.17}$$

The matrix satisfies the relations

$$\widehat{\mathbf{C}}_2^2 = \mathbf{1} \tag{2.18}$$

$$\mathbf{A}\widehat{\mathbf{C}}_2 = \widehat{\mathbf{C}}_2\mathbf{A}. \tag{2.19}$$

Considering the relation (2.19), the right-hand side of the circuit equation (2.6) satisfies the equation

$$\boldsymbol{f}(\widehat{\mathbf{C}}_2\boldsymbol{\Psi}, \widehat{\mathbf{C}}_2\boldsymbol{U}, \tau) = \mathbf{C}_2\boldsymbol{f}(\boldsymbol{\Psi}, \boldsymbol{U}, \tau + \pi) \tag{2.20}$$

where

$$\mathbf{C}_2 \triangleq \begin{bmatrix} \widehat{\mathbf{C}}_2 & \mathbf{o} \\ \mathbf{o} & \widehat{\mathbf{C}}_2 \end{bmatrix}, \qquad \mathbf{C}_2^2 = \mathbf{1}. \tag{2.21}$$

Eq.(2.20) is based on the odd function $\boldsymbol{I}(\boldsymbol{\Psi})$ of magnetizing characteristics of nonlinear inductors.

Assume that $[\boldsymbol{\Psi}(\tau), \boldsymbol{U}(\tau)]'$ is a solution of Eq.(2.6), then

$$\begin{aligned}
&\frac{d}{d\tau}\mathbf{C}_2 \begin{bmatrix} \boldsymbol{\Psi}(\tau+\pi) \\ \boldsymbol{U}(\tau+\pi) \end{bmatrix} - \boldsymbol{f}\left(\hat{\mathbf{C}}_2\boldsymbol{\Psi}(\tau+\pi), \hat{\mathbf{C}}_2\boldsymbol{U}(\tau+\pi), \tau\right) \\
&\quad = \mathbf{C}_2\frac{d}{d\tau}\begin{bmatrix} \boldsymbol{\Psi}(\tau+\pi) \\ \boldsymbol{U}(\tau+\pi) \end{bmatrix} - \mathbf{C}_2\boldsymbol{f}\left(\boldsymbol{\Psi}(\tau+\pi), \boldsymbol{U}(\tau+\pi), \tau+\pi\right) \\
&\quad = \mathbf{o}.
\end{aligned} \tag{2.22}$$

Thus, $\mathbf{C}_2[\boldsymbol{\Psi}(\tau+\pi), \boldsymbol{U}(\tau+\pi)]'$ is also a solution of Eq.(2.6). In the same way,

$$\mathbf{C}_2^n \begin{bmatrix} \boldsymbol{\Psi}(\tau+n\pi) \\ \boldsymbol{U}(\tau+n\pi) \end{bmatrix} \qquad (n = 1, 2, \ldots) \tag{2.23}$$

is also solutions of Eq.(2.6). Therefore, as for the symmetry of $\mathbf{C}_2$ there are $2n$ initial vector values at $\tau = 0$ of the period-n oscillations which are represented by

$$\mathbf{C}_2^k \begin{bmatrix} \boldsymbol{\Psi}(k\pi) \\ \boldsymbol{U}(k\pi) \end{bmatrix}, \qquad (k = 0, 1, \ldots, 2n-1) \tag{2.24}$$

in general. If a relation

$$\begin{bmatrix} \boldsymbol{\Psi}(0) \\ \boldsymbol{U}(0) \end{bmatrix} = \mathbf{C}_2^n \begin{bmatrix} \boldsymbol{\Psi}(n\pi) \\ \boldsymbol{U}(n\pi) \end{bmatrix} \tag{2.25}$$

is satisfied, we shall say the solution has symmetry with respect to $\mathbf{C}_2$.

2.3.3 Relation between $\mathbf{C}_3$ and $\mathbf{C}_2$

The initial values of period-n solutions(2.15) and (2.24) have the following relations

$$\mathbf{C}_3^{3k} \begin{bmatrix} \boldsymbol{\Psi}(2k\pi) \\ \boldsymbol{U}(2k\pi) \end{bmatrix} = \mathbf{C}_2^{2k} \begin{bmatrix} \boldsymbol{\Psi}(2k\pi) \\ \boldsymbol{U}(2k\pi) \end{bmatrix} = \begin{bmatrix} \boldsymbol{\Psi}(2k\pi) \\ \boldsymbol{U}(2k\pi) \end{bmatrix} \quad (k = 0, 1, \ldots, n), \tag{2.26}$$

$$\mathbf{C}_3^k\mathbf{C}_2^l \begin{bmatrix} \boldsymbol{\Psi}(\frac{m}{3}\pi) \\ \boldsymbol{U}(\frac{m}{3}\pi) \end{bmatrix} = \mathbf{C}_2^l\mathbf{C}_3^k \begin{bmatrix} \boldsymbol{\Psi}(\frac{m}{3}\pi) \\ \boldsymbol{U}(\frac{m}{3}\pi) \end{bmatrix} \quad \begin{pmatrix} k = 0, 1, \ldots, 3n-1 \\ l = 0, 1, \ldots, 2n-1 \\ m = 2k + 3l \bmod 6n \end{pmatrix} \tag{2.27}$$

where mod $6n$ is based on the period $2n\pi(= 6n\pi/3)$ of the period-n solution. Considering the relations, there exist $6n$ initial vector values at $\tau = 0$ of the period-n oscillations which

are represented by

$$\mathrm{C}_3^k \begin{bmatrix} \boldsymbol{\Psi}(\frac{2k}{3}\pi) \\ \boldsymbol{U}(\frac{2k}{3}\pi) \end{bmatrix}, \qquad \mathrm{C}_2\mathrm{C}_3^k \begin{bmatrix} \boldsymbol{\Psi}(\frac{l}{3}\pi) \\ \boldsymbol{U}(\frac{l}{3}\pi) \end{bmatrix} \qquad \begin{pmatrix} k = 0, 1, \ldots, 3n-1 \\ l = 3 + 2k \mod 6n \end{pmatrix} \tag{2.28}$$

in general. Assume that the solution has symmetry with respect to C_3, then there exist $2n$ initial vector values at $\tau = 0$ because of the relation (2.16). Assume that the solution has symmetry with respect to C_2, there are $3n$ initial vector values because of the relation (2.25). Further, if the solution has symmetry with respect to C_3 and C_2, then there exist n initial vector values.

2.4 Two-point Boundary Value Problem and Shooting Method

We consider a periodic solution of Eq.(2.6). First, the integration of Eq.(2.6) from an initial state $[\boldsymbol{\Psi}(0), \boldsymbol{U}(0)]' = [\boldsymbol{\Psi}_0, \boldsymbol{U}_0]'$ gives

$$\begin{bmatrix} \boldsymbol{\Psi}(\tau) \\ \boldsymbol{U}(\tau) \end{bmatrix} = \begin{bmatrix} \boldsymbol{\Psi}_0 \\ \boldsymbol{U}_0 \end{bmatrix} + \int_0^\tau \boldsymbol{f}(\boldsymbol{\Psi}, \boldsymbol{U}, s) ds. \tag{2.29}$$

Here, the singularity of matrix $\mathbf{A}$ leads us to the constraint of the capacitor voltages

$$U_a(\tau) + U_b(\tau) + U_c(\tau) = U_a(0) + U_b(0) + U_c(0) = c \tag{2.30}$$

where c is constant. This restriction is due to the capacitor cutset in the three-phase circuit. Substituting Eq.(2.30) into Eq.(2.29), we obtain the solution

$$\boldsymbol{x}(\tau) = \boldsymbol{x}_0 + \int_0^\tau \hat{\boldsymbol{f}}(\boldsymbol{x}, s) ds \tag{2.31}$$

where

$$\begin{aligned} \boldsymbol{x}(\tau) &\triangleq (\Psi_a(\tau), \Psi_b(\tau), \Psi_c(\tau), U_a(\tau), U_b(\tau))' && \in \boldsymbol{R}^5 \\ \boldsymbol{x}_0 &\triangleq \boldsymbol{x}(0) && \in \boldsymbol{R}^5 \end{aligned}$$

and $\hat{\boldsymbol{f}}(\boldsymbol{x}, s) : \boldsymbol{R}^5 \times \boldsymbol{R} \to \boldsymbol{R}^5$ is a vector-valued function obtained by substituting Eq.(2.30) into the function $\boldsymbol{f}(\boldsymbol{\Psi}, \boldsymbol{U}, \tau)$ in Eq.(2.29).

Considering a periodic solution of period T of Eq.(2.31) is a two-point boundary value problem in which the solution to Eq.(2.31) in the interval $[0, T]$ must satisfy the boundary condition [20].

$$\boldsymbol{x}(0) = \boldsymbol{x}(T) \tag{2.32}$$

Using the mapping $\mathbf{T}$:$\boldsymbol{R}^5 \rightarrow \boldsymbol{R}^5$, we can express the above problem

$$\boldsymbol{x}_0 = \mathbf{T}(\boldsymbol{x}_0) \tag{2.33}$$

where

$$\begin{aligned} \boldsymbol{x}_0 &= \boldsymbol{x}(0) \\ \mathbf{T}(\boldsymbol{x}_0) &= \int_0^T \hat{\boldsymbol{f}}(\boldsymbol{x}, s)ds + \boldsymbol{x}(0). \end{aligned}$$

To solve the two-point boundary value problem with a shooting method, we define a nonlinear equation

$$\mathbf{F}(\boldsymbol{x}_0) \triangleq \boldsymbol{x}_0 - \mathbf{T}(\boldsymbol{x}_0) = \mathbf{o}. \tag{2.34}$$

The solution of Eq.(2.34), that is, the fixed point of the mapping $\mathbf{T}$ determines a periodic solution of Eq.(2.6).

2.5 Homotopy Method

2.5.1 Newton Homotopy

To solve Eq.(2.34), we use the Newton homotopy method combined with a shooting method.

First, we define the Newton homotopy function $\mathbf{G}$:$\boldsymbol{R}^6 \rightarrow \boldsymbol{R}^5$ for Eq.(2.34) represented by

$$\mathbf{G}(\boldsymbol{x}_0, \alpha) \triangleq \alpha\mathbf{F}(\boldsymbol{x}_0) + (1-\alpha)[\mathbf{F}(\boldsymbol{x}_0) - \mathbf{F}(\boldsymbol{a})] \tag{2.35}$$

where $\alpha \in \boldsymbol{R}$ is a homotopy parameter and $\boldsymbol{a} \in \boldsymbol{R}^5$ is a given vector. This function satisfies equations

$$\mathbf{G}(\boldsymbol{a}, 0) = \mathbf{o}, \qquad \mathbf{G}(\boldsymbol{x}_0, 1) = \mathbf{F}(\boldsymbol{x}_0). \tag{2.36}$$

Now, we define the Newton homotopy equation

$$\mathbf{G}(\boldsymbol{x}_0, \alpha) = \mathbf{o}, \tag{2.37}$$

and we define a homotopy curve

$$\mathbf{G}^{-1}(\mathbf{o}) = \{(\boldsymbol{x}_o, \alpha) \mid \mathbf{G}(\boldsymbol{x}_0, \alpha) = \mathbf{o}\}. \tag{2.38}$$

We follow the homotopy curve from the initial point $(\boldsymbol{a}, 0)'$ and when we arrive at $\alpha = 1$, we have a solution $\boldsymbol{x}_0$ of Eq.(2.34).

2.5.2 Trace of Homotopy Curve

We define a vector $\boldsymbol{y} \in \boldsymbol{R}^6$ as

$$\boldsymbol{y} \triangleq \begin{bmatrix} \boldsymbol{x} \\ \alpha \end{bmatrix}. \tag{2.39}$$

Assuming that the homotopy curve is represented by $\boldsymbol{y}(\theta)$, where θ represents the arclength of the homotopy curve, we try to trace the curve from

$$\boldsymbol{y}_0 = \boldsymbol{y}(\theta_0) = \begin{bmatrix} \boldsymbol{x}_0 \\ 0 \end{bmatrix}, \tag{2.40}$$

calculating further solutions on the branch $\boldsymbol{y}_k = \boldsymbol{y}(\theta_k)$ $(k = 1, 2, \ldots)$ by a predictor-corrector method.

First, we consider to obtain a tangent vector on the homotopy curve [21]. Assume that the full-rank condition

$$rank \left(\left. \frac{\partial \mathbf{G}}{\partial \boldsymbol{y}} \right|_{\theta=\theta_k} \right) = 6, \tag{2.41}$$

then there exists a tangent vector on the homotopy curve, and we define a vector as

$$\dot{\boldsymbol{y}}_k \triangleq \left. \frac{d\boldsymbol{y}}{d\theta} \right|_{\theta=\theta_k}. \tag{2.42}$$

From Eq.(2.37) we can determine the tangent vector $\dot{\boldsymbol{y}}_k$ which satisfies the following equations

$$\left. \frac{\partial \mathbf{G}}{\partial \boldsymbol{y}} \right|_{\theta=\theta_k} \dot{\boldsymbol{y}}_k = \mathbf{o}, \qquad ||\dot{\boldsymbol{y}}_k|| = 1, \qquad \dot{\boldsymbol{y}}'_{k-1} \cdot \dot{\boldsymbol{y}}_k > 0, \tag{2.43}$$

where $||\cdot||$ represents usual 2-norm of a vector. Hence, we determine a vector $\boldsymbol{l} \in \boldsymbol{R}^6$ which satisfies the following equation

$$\begin{bmatrix} \left. \frac{\partial \mathbf{G}}{\partial \boldsymbol{y}} \right|_{\theta=\theta_k} \\ \dot{\boldsymbol{y}}_{k-1} \end{bmatrix} \boldsymbol{l} = \begin{bmatrix} \mathbf{o} \\ 1 \end{bmatrix}, \qquad \dot{\boldsymbol{y}}_0 = \begin{bmatrix} \mathbf{o} \\ 1 \end{bmatrix}, \tag{2.44}$$

then obtain the vector $\dot{\boldsymbol{y}}_k$ by

$$\dot{\boldsymbol{y}}_k = \frac{\boldsymbol{l}}{||\boldsymbol{l}||}. \tag{2.45}$$

Secondly, we construct a predictor vector. A simple predictor is a tangent predictor, that is, the predictor point for $\boldsymbol{y}_{k+1}$ is

$$\boldsymbol{y}_k + \delta_k \dot{\boldsymbol{y}}_k. \tag{2.46}$$

Here, δ_k is an appropriate step length. This tangent predictor (2.46) is of first order. As another improved method, we adopt the second order predictor $\boldsymbol{y}^*_{k+1}$which use the second order derivative of $\boldsymbol{y}$. That is,

$$\boldsymbol{y}^*_{k+1} \triangleq \boldsymbol{y}_k + \delta_k \dot{\boldsymbol{y}}_k + \frac{1}{2}\delta_k^2 \ddot{\boldsymbol{y}}_k \tag{2.47}$$

where

$$\ddot{\boldsymbol{y}} \triangleq \frac{\dot{\boldsymbol{y}}_k - \dot{\boldsymbol{y}}_{k-1}}{\delta_{k-1}}. \tag{2.48}$$

To determine the step length δ_k, we use the difference between the first order predictor and the second order predictor. That is,

$$\left\| \frac{1}{2}\delta_k^2 \ddot{\boldsymbol{y}}_k \right\| = \epsilon_{max} \tag{2.49}$$

where ϵ_{max} is a given positive constant. Then we obtain

$$\delta_k = \sqrt{\frac{2\epsilon_{max}}{\|\ddot{\boldsymbol{y}}_k\|}}. \tag{2.50}$$

Next, we modify the predictor $\boldsymbol{y}^*_{k+1}$ with the corrector which is based on Newton iteration. That is, we start from the initial point $\boldsymbol{y}^0_{k+1} = \boldsymbol{y}^*_{k+1}$ and iterate the following step

$$\begin{bmatrix} \left.\dfrac{\partial \mathbf{G}}{\partial \boldsymbol{y}}\right|_{\boldsymbol{y}^i_{k+1}} \\ \dot{\boldsymbol{y}}_k + \dfrac{1}{2}\delta_k \ddot{\boldsymbol{y}}_k \end{bmatrix} \boldsymbol{\Delta y}^i_{k+1} = \begin{bmatrix} -\mathbf{G}(\boldsymbol{y}^i_{k+1}) \\ 0 \end{bmatrix} \tag{2.51}$$

$$\boldsymbol{y}^{i+1}_{k+1} = \boldsymbol{y}^i_{k+1} + \boldsymbol{\Delta y}^i_{k+1}. \tag{2.52}$$

Here, the step is iterated until the following condition is satisfied

$$\left\|\boldsymbol{\Delta y}^i_{k+1}\right\| < \epsilon_{\Delta y}, \qquad or \qquad \left\|\mathbf{G}(\boldsymbol{y}^i_{k+1})\right\| < \epsilon_G \tag{2.53}$$

where $\epsilon_{\Delta y}, \epsilon_G$ are given small constants. If the relations

$$\left\|\Delta \boldsymbol{y}_{k+1}^{i}\right\| > \left\|\Delta \boldsymbol{y}_{k+1}^{i+1}\right\| \tag{2.54}$$

$$\left\|\mathbf{G}(\boldsymbol{y}_{kL1}^{i})\right\| > \left\|\mathbf{G}(\boldsymbol{y}_{k+1}^{i+1})\right\| \tag{2.55}$$

are not satisfied, we halve the step length δ_k and calculate the predictor $\boldsymbol{y}_{k+1}^{*}$ once more.

2.5.3 Calculation of Jacobian Matrix

When we trace the homotopy curve, we use the Jacobian matrix given below:

$$\frac{\partial \mathbf{G}}{\partial \boldsymbol{y}} = \left[\frac{\partial \mathbf{G}}{\partial \boldsymbol{x}_0}, \frac{\partial \mathbf{G}}{\partial \alpha}\right] \tag{2.56}$$

$$= \left[\frac{\partial \mathbf{F}}{\partial \boldsymbol{x}_0}, \boldsymbol{F}(\boldsymbol{a})\right] \tag{2.57}$$

$$= \left[\mathbf{1} - \frac{\partial \mathbf{T}}{\partial \boldsymbol{x}_0}, \boldsymbol{F}(\boldsymbol{a})\right] \tag{2.58}$$

where the vector $\mathbf{1}$ represents a unit matrix. In the Eq.(2.58), we obtain $\dfrac{\partial \mathbf{T}}{\partial \boldsymbol{x}_0}$ by integrating the first variational equation

$$\frac{d}{d\tau}\left[\frac{\partial \boldsymbol{x}(\tau)}{\partial \boldsymbol{x}_0}\right] = \frac{\partial \hat{\boldsymbol{f}}(\boldsymbol{x},\tau)}{\partial \boldsymbol{x}} \cdot \frac{\partial \boldsymbol{x}(\tau)}{\partial \boldsymbol{x}_0} \tag{2.59}$$

over the interval $[0, T]$, where

$$\frac{\partial \boldsymbol{x}(0)}{\partial \boldsymbol{x}_0} = \mathbf{1}. \tag{2.60}$$

2.5.4 General Homotopy

In Eq.(2.34), we consider the circuit parameter $\mu \in \{\xi, \eta, \zeta, E_m\}$ and rewrite as the following:

$$\mathbf{F}(\boldsymbol{x}_0 \mid \mu) \triangleq \boldsymbol{x}_0 - \mathbf{T}(\boldsymbol{x}_0) = \mathbf{o} \tag{2.61}$$

When the circuit parameter is increased or decreased, the solution curve is followed by the general homotopy defined by the function $\mathbf{H} : \boldsymbol{R}^6 \rightarrow \boldsymbol{R}^5$

$$\mathbf{H}(\boldsymbol{x}_0, \mu) \triangleq \mathbf{F}(\boldsymbol{x}_0 \mid \mu). \tag{2.62}$$

Now, we define the general homotopy equation

$$\mathbf{H}(\boldsymbol{x}_0, \mu) = \mathbf{o}, \tag{2.63}$$

and we define a solution curve

$$\mathbf{H}^{-1}(\mathbf{o}) = \{(\boldsymbol{x}_0, \mu) \mid \mathbf{H}(\boldsymbol{x}_0, \mu) = \mathbf{o}\}. \tag{2.64}$$

Starting from the parameter $\mu = \mu_0$ for the solution $\boldsymbol{x}_0$, we can follow the solution curve $\mathbf{H}^{-1}(\mathbf{o})$ to the specified value of parameter μ^*.

In this case, the Jacobian matrix for the trace of solution curve is

$$\left[\frac{\partial \mathbf{H}}{\partial \boldsymbol{x}_0}, \frac{\partial \mathbf{H}}{\partial \mu}\right] = \left[\frac{\partial \mathbf{F}}{\partial \boldsymbol{x}_0}, \frac{\partial \mathbf{F}}{\partial \mu}\right] \tag{2.65}$$

$$= \left[\mathbf{1} - \frac{\partial \mathbf{T}}{\partial \boldsymbol{x}_0}, -\frac{\partial \mathbf{T}}{\partial \mu}\right]. \tag{2.66}$$

In Eq.(2.66), we obtain $\dfrac{\partial \mathbf{T}}{\partial \mu}$ by integrating the first variational equation

$$\frac{d}{d\tau}\left[\frac{\partial \boldsymbol{x}(\tau)}{\partial \mu}\right] = \frac{\partial \hat{\boldsymbol{f}}(\boldsymbol{x}, \tau \mid \mu)}{\partial \boldsymbol{x}} \cdot \frac{\partial \boldsymbol{x}(\tau)}{\partial \mu} + \frac{\partial \hat{\boldsymbol{f}}(\boldsymbol{x}, \tau \mid \mu)}{\partial \mu} \tag{2.67}$$

over the interval $[0, T]$, where

$$\frac{\partial \boldsymbol{x}(0)}{\partial \mu} = \mathbf{o}. \tag{2.68}$$

2.6 Definition of Bifurcation Points

2.6.1 Stability of Periodic Solution

We can determine the stability of periodic solutions by the first variational equation. That is, for a value of μ, let $\boldsymbol{x}(\tau)$ be a periodic solution to the equation (2.31) with a period T. The monodromy matrix based on the first variational equation (2.59) is defined by

$$\mathbf{M}(\boldsymbol{x}_0, \mu) \triangleq \frac{\partial \boldsymbol{x}(T)}{\partial \boldsymbol{x}_0} = \frac{\partial \mathbf{T}}{\partial \boldsymbol{x}_0} \tag{2.69}$$

The matrix $\mathbf{M}(\boldsymbol{x}_0, \mu)$ has 5 eigenvalues $\Lambda(\boldsymbol{x}_0, \mu) = \{\lambda_i \mid i = 1, 2, \ldots, 5\}$. If the eigenvalues satisfy

$$|\lambda_i| < 1 \qquad \textit{for all } \lambda_i \in \Lambda(\boldsymbol{x}_0, \mu) \tag{2.70}$$

then the periodic solution $\boldsymbol{x}(\tau)$ is stable. Additionally, we define the degree of unstability σ by the number of $\lambda_i \in \Lambda(\boldsymbol{x}_0, \mu)$ which doesn't satisfy the condition (2.70). If the solution is stable, the degree σ is equal to 0.

When the parameter μ is varied, we can distinguish three ways of the eigenvalue $\lambda_i \in \Lambda(\boldsymbol{x}_0, \mu)$ crossing the unit circle. That is,

(1) $\lambda_i = 1$

(2) $\lambda_i = -1$

(3) $Im(\lambda_i) \neq 0$

where, $Im(\cdot)$ represents imaginary part. Now, we consider co-dimension one bifurcations [22] in the system of Eq.(2.34), that is, saddle-node, pitchfork, period doubling and Neimark-Sacker bifurcations. Then, we assume that only one eigenvalue is on the unit circle in the case (1) and (2), and assume that only two eigenvalues are on the unit circle in the case (3). Here, we can consider that λ_1 is on the unit circle in the case (1) and (2) without loss of generality and that λ_1, λ_2 are complex conjugate on the unit-circle in the case (3) without loss of generality.

2.6.2 Saddle-node and Pitchfork Bifurcation

In the case of the eigenvalue $\lambda_1 = 1$, there exists a vector $\boldsymbol{u}_1 \in \boldsymbol{R}^5$ which satisfies

$$\left.\frac{\partial \mathbf{H}(\boldsymbol{x}_0, \mu)}{\partial \boldsymbol{x}_0}\right|_{\substack{\boldsymbol{x}_0 = \boldsymbol{x}_0^* \\ \mu = \mu^*}} \boldsymbol{u}_1 = \mathbf{o}. \tag{2.71}$$

That is, $(\boldsymbol{x}_0^*, \mu^*)$ is a singular point. The singularity of the Jacobian $\dfrac{\partial \mathbf{H}(\boldsymbol{x}_0, \mu)}{\partial \boldsymbol{x}_0}$ leads to the assumptions

$$kernel\left(\frac{\partial \mathbf{H}}{\partial \boldsymbol{x}_0}\right) \quad \text{is spanned by } \boldsymbol{u}_1 \tag{2.72}$$

$$range\left(\frac{\partial \mathbf{H}}{\partial \boldsymbol{x}_0}\right) \quad = kernel\,(\boldsymbol{v}_1) \text{ with } \langle \boldsymbol{v}_1, \boldsymbol{u}_1 \rangle = 1. \tag{2.73}$$

Here $kernel(\boldsymbol{v}_1) = \{\boldsymbol{z} \mid \langle \boldsymbol{v}_1, \boldsymbol{z} \rangle = 0\}$ and $\boldsymbol{v}_1$ satisfies

$$\boldsymbol{v}_1' \frac{\partial \mathbf{H}}{\partial \boldsymbol{x}_0} = \mathbf{o}.$$

Assume that the operator $\dfrac{\partial \mathbf{H}}{\partial \boldsymbol{x}_0}$ is restricted $kernel(\boldsymbol{v}_1) \mapsto kernel(\boldsymbol{v}_1)$, then we can define the inverse operator

$$\frac{\partial \mathbf{H}}{\partial \boldsymbol{x}_0}^{-1} : kernel(\boldsymbol{v}_1) \mapsto kernel(\boldsymbol{v}_1). \tag{2.74}$$

Now, we classify the singular point by Lyapnov-Schmidt decomposition [23]. First, we give $\mathbf{H}^{-1}(\mathbf{o})$ in the neighborhood of the singular point $(\boldsymbol{x}_0^*, \mu^*)$ as follows:

$$\boldsymbol{x}_0 = \boldsymbol{x}_0^* + x\boldsymbol{u}_1 + \boldsymbol{m}(x,\nu) \tag{2.75}$$

$$\mu = \mu^* + \nu \tag{2.76}$$

where $\langle \boldsymbol{v}_1', \boldsymbol{m}(x,\nu)\rangle = 0$. We define projection $\mathcal{P}, \mathcal{Q}$

$$\mathcal{P}\boldsymbol{x} \triangleq \langle \boldsymbol{v}_1, \boldsymbol{x}\rangle \boldsymbol{u}_1 \tag{2.77}$$

$$\mathcal{Q}\boldsymbol{x} \triangleq \boldsymbol{x} - \mathcal{P}\boldsymbol{x}. \tag{2.78}$$

where $\boldsymbol{x} \in \boldsymbol{R}^5$. Then the general homotopy equation (2.63) is given as

$$\mathcal{P}\mathbf{H}(\boldsymbol{x}_0^* + x\boldsymbol{u}_1 + \boldsymbol{m}(x,\nu), \mu^* + \nu) = \mathbf{o} \tag{2.79}$$

$$\mathcal{Q}\mathbf{H}(\boldsymbol{x}_0^* + x\boldsymbol{u}_1 + \boldsymbol{m}(x,\nu), \mu^* + \nu) = \mathbf{o} \tag{2.80}$$

Next, we expand Eq.(2.80) as

$$\mathcal{Q}\frac{\partial \mathbf{H}}{\partial \boldsymbol{x}_0}\boldsymbol{m} + \nu\mathcal{Q}\frac{\partial \mathbf{H}}{\partial \mu} + \frac{x^2}{2}\mathcal{Q}\frac{\partial^2 \mathbf{H}}{\partial \boldsymbol{x}_0^2}(\boldsymbol{u}_1, \boldsymbol{u}_1) + x\mathcal{Q}\frac{\partial^2 \mathbf{H}}{\partial \boldsymbol{x}_0^2}(\boldsymbol{u}_1, \boldsymbol{m}) + \frac{1}{2}\mathcal{Q}\frac{\partial^2 \mathbf{H}}{\partial \boldsymbol{x}_0^2}(\boldsymbol{m}, \boldsymbol{m})$$
$$+x\nu\mathcal{Q}\frac{\partial^2 \mathbf{H}}{\partial \boldsymbol{x}_0 \partial \mu}\boldsymbol{u}_1 + \nu\mathcal{Q}\frac{\partial^2 \mathbf{H}}{\partial \boldsymbol{x}_0 \partial \mu}\boldsymbol{m} + \frac{\nu^2}{2}\mathcal{Q}\frac{\partial^2 \mathbf{H}}{\partial \mu^2} + \cdots = \mathbf{o}. \tag{2.81}$$

From Eq.(2.81) we obtain

$$\boldsymbol{m}(x,\nu) = \nu\boldsymbol{g} - \frac{\partial \mathbf{H}}{\partial \boldsymbol{x}_0}^{-1}\mathcal{Q}\left\{\frac{1}{2}x^2\frac{\partial^2 \mathbf{H}}{\partial \boldsymbol{x}_0^2}(\boldsymbol{u}_1, \boldsymbol{u}_1) + \nu x\left(\frac{\partial^2 \mathbf{H}}{\partial \boldsymbol{x}_0 \partial \mu}\boldsymbol{u}_1 + \frac{\partial^2 \mathbf{H}}{\partial \boldsymbol{x}_0^2}(\boldsymbol{u}_1, \boldsymbol{g})\right)\right.$$
$$\left.+\nu^2\left(\frac{1}{2}\frac{\partial^2 \mathbf{H}}{\partial \mu^2} + \frac{\partial^2 \mathbf{H}}{\partial \boldsymbol{x}_0 \partial \mu}\boldsymbol{g} + \frac{1}{2}\frac{\partial^2 \mathbf{H}}{\partial \boldsymbol{x}_0^2}(\boldsymbol{g}, \boldsymbol{g})\right)\right\} + \cdots \tag{2.82}$$

where

$$\boldsymbol{g} = -\frac{\partial \mathbf{H}}{\partial \boldsymbol{x}_0}^{-1}\mathcal{Q}\frac{\partial \mathbf{H}}{\partial \mu}. \tag{2.83}$$

From Eq.(2.79), we can define the following bifurcation equation $\tilde{H}(x,\nu)$:

$$\tilde{H}(x,\nu) = \langle \boldsymbol{v}_1, \mathbf{H}(\boldsymbol{x}_0^* + x\boldsymbol{u}_1 + \boldsymbol{m}(x,\nu), \mu^* + \nu)\rangle \tag{2.84}$$

$$= \tilde{H}_{01}\nu + \frac{1}{2}\tilde{H}_{20}x^2 + \tilde{H}_{11}x\nu + \frac{1}{2}\tilde{H}_{02}\nu^2 + \frac{1}{3!}\tilde{H}_{30}x^3 + \cdots = 0. \tag{2.85}$$

where

$$\tilde{H}_{01} = \left\langle \boldsymbol{v}_1, \frac{\partial \mathbf{H}}{\partial \mu} \right\rangle \tag{2.86}$$

$$\tilde{H}_{20} = \left\langle \boldsymbol{v}_1, \frac{\partial^2 \mathbf{H}}{\partial \boldsymbol{x}_0^2}(\boldsymbol{u}_1, \boldsymbol{u}_1) \right\rangle \tag{2.87}$$

$$\tilde{H}_{11} = \left\langle \boldsymbol{v}_1, \frac{\partial^2 \mathbf{H}}{\partial \boldsymbol{x}_0^2}(\boldsymbol{g}, \boldsymbol{u}_1) + \frac{\partial^2 \mathbf{H}}{\partial \boldsymbol{x}_0 \partial \mu}\boldsymbol{u}_1 \right\rangle \tag{2.88}$$

$$\tilde{H}_{02} = \left\langle \boldsymbol{v}_1, \frac{\partial^2 \mathbf{H}}{\partial \boldsymbol{x}_0^2}(\boldsymbol{g}, \boldsymbol{g}) + 2\frac{\partial^2 \mathbf{H}}{\partial \boldsymbol{x}_0 \partial \mu}\boldsymbol{g} + \frac{\partial^2 \mathbf{H}}{\partial \mu^2} \right\rangle \tag{2.89}$$

$$\tilde{H}_{30} = \left\langle \boldsymbol{v}_1, \frac{\partial^3 \mathbf{H}}{\partial \boldsymbol{x}_0^3}(\boldsymbol{u}_1, \boldsymbol{u}_1, \boldsymbol{u}_1) - 3\frac{\partial^2 \mathbf{H}}{\partial \boldsymbol{x}_0^2}\left(\boldsymbol{u}_1, \frac{\partial \mathbf{H}}{\partial \boldsymbol{x}_0}^{-1} Q \frac{\partial^2 \mathbf{H}}{\partial \boldsymbol{x}_0^2}(\boldsymbol{u}_1, \boldsymbol{u}_1)\right) \right\rangle. \tag{2.90}$$

Here, assume that $\tilde{H}_{01} \neq 0$, then we can show by the implicit function theorem [24] that the solution curve doesn't have an emanating branch (saddle-node bifurcation). When $\tilde{H}_{01}$ is equal to 0, the solution curve has emanating branches and the coefficients $\tilde{H}_{20}, \tilde{H}_{11}, \tilde{H}_{02}$ determine the direction of them [25]. That is, let the Hessian matrix of $\tilde{H}(x,\nu)$ be

$$Hes(\tilde{H}) \triangleq \begin{bmatrix} \tilde{H}_{20} & \tilde{H}_{11} \\ \tilde{H}_{11} & \tilde{H}_{02} \end{bmatrix}, \tag{2.91}$$

and we consider the equation

$$\tilde{H}_{20}x^2 + 2\tilde{H}_{11}x\nu + \tilde{H}_{02}\nu^2 = 0. \tag{2.92}$$

If $det(Hes(\tilde{H})) > 0$, then the singular point is an isola center. If $det(Hes(\tilde{H})) < 0$ then, the singular point is a transversal intersection of two branches. Furthermore, if $\tilde{H}_{20} = 0$, then Eq.(2.92) has a solution $\nu = 0$ and the solution curve $\mathbf{H}^{-1}(\mathbf{o})$ has a branch which emanates in the direction of $\boldsymbol{u}_1$ (pitchfork bifurcation).

The saddle-node bifurcation is co-dimension one in general [26]. Additionally, because of the symmetry with respect to $\mathbf{C}_2$, the pitchfork bifurcation can be generated as a co-dimension one bifurcation in the three-phase circuit (appendix A). Now, we define the

saddle-node bifurcation and pitchfork bifurcation.

Definition: $(\boldsymbol{x}_0^*, \mu^*)$ is a *saddle-node bifurcation*, if the following conditions hold:

$$\mathbf{H}(\boldsymbol{x}_0^*, \mu^*) = \mathbf{o} \tag{2.93a}$$

$$rank\left(\frac{\partial \mathbf{H}}{\partial \boldsymbol{x}_0}\right) = 4 \tag{2.93b}$$

$$\tilde{H}_{01} \neq 0 \tag{2.93c}$$

$$\tilde{H}_{20} \neq 0 \tag{2.93d}$$

Hypotheses (2.93a) and (2.93b) guarantee the condition of periodic solutions and $1 \in \Lambda(\boldsymbol{x}_0^*, \mu^*)$, respectively. Hypotheses (2.93c) guarantees that $(\boldsymbol{x}_0^*, \mu^*)$ is not a branching point. Additionally, hypotheses (2.93d) guarantees a non-degeneracy condition.

Definition: $(\boldsymbol{x}_0^*, \mu^*)$ is a *pitchfork bifurcation*, if the following conditions hold:

$$\mathbf{H}(\boldsymbol{x}_0^*, \mu^*) = \mathbf{o} \tag{2.94a}$$

$$rank\left(\frac{\partial \mathbf{H}}{\partial \boldsymbol{x}_0}\right) = 4 \tag{2.94b}$$

$$\tilde{H}_{01} = 0 \tag{2.94c}$$

$$\tilde{H}_{20} = 0 \tag{2.94d}$$

$$\tilde{H}_{11} \neq 0 \tag{2.94e}$$

$$\tilde{H}_{30} \neq 0 \tag{2.94f}$$

Hypotheses (2.94a) and (2.94b) guarantee the condition of periodic solutions and $1 \in \Lambda(\boldsymbol{x}_0^*, \mu^*)$, respectively. Hypotheses (2.94c) and (2.94d) guarantee that the point $(\boldsymbol{x}_0^*, \mu^*)$ is a transversal intersection of two branches and has an emanating branch in the direction of the vector $\boldsymbol{u}_1$, respectively. Additionally, the hypotheses (2.94e) and (2.94f) guarantee non-degeneracy conditions.

2.6.3 Period Doubling Bifurcation

In the case of the eigenvalue $\lambda_1 = -1$ on $(\boldsymbol{x}^*, \mu^*)$, the Jacobian $\dfrac{\partial \mathbf{H}}{\partial \boldsymbol{x}_0}$, which has an eigenvalue 2, is nonsingular. Then a smooth branch $\mathbf{H}^{-1}(\mathbf{o})$ passes through the point $(\boldsymbol{x}_0^*, \mu^*)$ without branching. However, the monodromy matrix of the interval $[0, 2T]$

$$\mathbf{M}_{2T}(\boldsymbol{x}_0, \mu) \triangleq \frac{\partial \boldsymbol{x}(2T)}{\partial \boldsymbol{x}_0} = \frac{\partial \mathbf{T}(\mathbf{T}(\boldsymbol{x}_0))}{\partial \boldsymbol{x}_0} = \mathbf{M}^2 \tag{2.95}$$

has an eigenvalue 1. In other words, as for the general homotopy function for $2T$, pitchfork bifurcation occurs. Then there is an emanating branches of period $2T$ solution in the direction of the eigenvector belonging to the eigenvalue $\lambda_1 = -1$ from $(\boldsymbol{x}_0^*, \mu^*)$.

Now, we define the period doubling bifurcation.

Definition: $(\boldsymbol{x}_0^*, \mu^*)$ is a *period doubling bifurcation*, if the following conditions hold:

$$\mathbf{H}(\boldsymbol{x}_0^*, \mu^*) = \mathbf{o} \tag{2.96a}$$

$$-1 \in \Lambda(\boldsymbol{x}_0^*, \mu^*) \tag{2.96b}$$

Hypotheses (2.96a) is the condition of periodic solutions and (2.96b) guarantees that the stability changes on the point where one of the eigenvalues of $\dfrac{\partial \mathbf{T}}{\partial \boldsymbol{x}_0}$ is equal to -1.

2.6.4 Neimark-Sacker Bifurcation

If the eigenvalues λ_1, λ_2 which is complex conjugate crosses the unit circle, that is,

$$\lambda_1 = e^{i\theta}, \qquad \lambda_2 = e^{-i\theta} \quad for \quad \theta \neq 0,\ \theta \neq \pi \qquad i: \text{ imaginary unit}, \tag{2.97}$$

then the Jacobian $\dfrac{\partial \mathbf{H}}{\partial \boldsymbol{x}_0}$, which has an eigenvalue $1 - e^{\pm i\theta}$, is nonsingular and a smooth branch $\mathbf{H}^{-1}(\mathbf{o})$ passes through the point $(\boldsymbol{x}_0^*, \mu^*)$ without branching. Assume that the angle θ is an irrational multiple of 2π, then the map $\mathbf{T}(\boldsymbol{x}_0)$ has an invariant curve, that is, there exists an almost periodic solution.

Now we define the Neimark-Sacker bifurcation.

Definition:$(\boldsymbol{x}_0^*, \mu^*)$ is a *Neimark-Sacker bifurcation*, if the following conditions hold:

$$\mathbf{H}(\boldsymbol{x}_0^*, \mu^*) = \mathbf{o} \tag{2.98a}$$

$$e^{\pm i\theta} \in \Lambda(\boldsymbol{x}_0^*, \mu^*) \tag{2.98b}$$

$$\theta \neq \frac{2\pi}{n} \qquad n = 1, 2, 3, 4 \tag{2.98c}$$

Hypotheses (2.98a) is the condition of periodic solutions and (2.98b) guarantees that the stability changes on the point where two of the eigenvalues of $\dfrac{\partial \mathbf{T}}{\partial \boldsymbol{x}_0}$ are equal to $e^{\pm i\theta}$. Hypotheses (2.98c) is the condition of weak resonances [27]. When $n = 1, 2, 3, 4$, the bifurcation is called strong resonance, which is co-dimension two bifurcation [26].

2.7 Search of Bifurcation Points

We consider to search the bifurcation points of co-dimension one [28], that is, saddle-node, pitchfork, period doubling and Neimark-Sacker bifurcations, by the general homotopy. We can discriminate the bifurcations by

$$\text{the eigenvalues } \Lambda(\boldsymbol{x}_0, \mu) \tag{2.99a}$$

$$\text{the sign of } \frac{\partial \mu}{\partial \theta} \qquad \theta : \text{arclength parameter of solution curve} \tag{2.99b}$$

on the solution curve $\mathbf{H}^{-1}(\mathbf{o})$.

Next, we show the method of discrimination.

1. Suppose that $\exists \lambda \in \Lambda(\boldsymbol{x}_0, \mu)$ crosses the unit circle

   (a) on $\lambda = 1$.

      i. if the sign of $\dfrac{\partial \mu}{\partial \theta}$ changes, then the point is a saddle-node bifurcation.

      ii. if the sign of $\dfrac{\partial \mu}{\partial \theta}$ doesn't change, then the point is a pitchfork bifurcation.

   (b) on $\lambda = -1$. Then the point is a period doubling bifurcation.

   (c) on $Im(\lambda) \neq 0$. Then the point is a Neimark-Sacker bifurcation.

2. Suppose that $\forall \lambda \in \Lambda(\boldsymbol{x}_0, \mu)$ don't crosses the unit circle.

   (a) if the sign of $\dfrac{\partial \mu}{\partial \theta}$ changes, then the point is a pitchfork bifurcation.

   (b) if the sign of $\dfrac{\partial \mu}{\partial \theta}$ doesn't change, the point is not a bifurcation point.

By the above discrimination, we can obtain the approximate values of bifurcation parameters.

2.8 Equations of Bifurcation Points

After searching the approximate values of bifurcation parameter, we obtain the exact bifurcation points by solving the following equations of bifurcations which are defined for each bifurcations.

Saddle-node bifurcation

The conditions of a saddle-node bifurcation (2.93a) and (2.93b) are formulated with eigenvector $\boldsymbol{u}_1$ as the following [29]:

$$\mathbf{F}_S(\boldsymbol{y}) \triangleq \begin{bmatrix} \mathbf{H}(\boldsymbol{x}_0, \mu) \\ \dfrac{\partial \mathbf{H}}{\partial \boldsymbol{x}_0}\boldsymbol{u}_1 \\ ||\boldsymbol{u}_1||^2 - 1 \end{bmatrix} = \mathbf{o}, \quad \boldsymbol{y} = \begin{bmatrix} \boldsymbol{x}_0 \\ \mu \\ \boldsymbol{u}_1 \end{bmatrix} \in \boldsymbol{R}^{11}. \tag{2.100}$$

By solving Eq.(2.100), we can obtain the vector $\boldsymbol{x}_0$ which is the solution on the bifurcation point, bifurcation parameter μ, and right unit eigenvector $\boldsymbol{u}_1$ belonging to the eigenvalue 0 of Jacobian $\dfrac{\partial \mathbf{H}}{\partial \boldsymbol{x}_0}$.

The Jacobian of $\dfrac{\partial \mathbf{F}_S}{\partial \boldsymbol{y}}$ is given below:

$$\frac{\partial \mathbf{F}_S}{\partial \boldsymbol{y}} = \begin{bmatrix} \dfrac{\partial \mathbf{H}}{\partial \boldsymbol{x}_0} & \dfrac{\partial \mathbf{H}}{\partial \mu} & \mathbf{o} \\ \dfrac{\partial}{\partial \boldsymbol{x}_0}\left[\dfrac{\partial \mathbf{H}}{\partial \boldsymbol{x}_0}\boldsymbol{u}_1\right] & \dfrac{\partial}{\partial \mu}\left[\dfrac{\partial \mathbf{H}}{\partial \boldsymbol{x}_0}\boldsymbol{u}_1\right] & \dfrac{\partial \mathbf{H}}{\partial \boldsymbol{x}_0} \\ \mathbf{o} & 0 & 2\boldsymbol{u}_1' \end{bmatrix}. \tag{2.101}$$

where the elements

$$\begin{aligned} \frac{\partial}{\partial \boldsymbol{x}_0}\left[\frac{\partial \mathbf{H}}{\partial \boldsymbol{x}_0}\boldsymbol{u}_1\right] &= -\frac{\partial}{\partial \boldsymbol{x}_0}\left[\frac{\partial \mathbf{T}}{\partial \boldsymbol{x}_0}\boldsymbol{u}_1\right] \\ \frac{\partial}{\partial \mu}\left[\frac{\partial \mathbf{H}}{\partial \boldsymbol{x}_0}\boldsymbol{u}_1\right] &= -\frac{\partial}{\partial \mu}\left[\frac{\partial \mathbf{T}}{\partial \boldsymbol{x}_0}\boldsymbol{u}_1\right] \end{aligned}$$

are calculated by the following method. First, we define

$$\boldsymbol{w}(\tau) \triangleq \frac{\partial \boldsymbol{x}(\tau)}{\partial \boldsymbol{x}_0}\boldsymbol{u}_1. \tag{2.102}$$

From Eq.(2.102),

$$\frac{d}{d\tau}\boldsymbol{w}(\tau) = \frac{\partial \hat{\boldsymbol{f}}}{\partial \boldsymbol{x}}\boldsymbol{w}(\tau) \tag{2.103}$$

where $\boldsymbol{w}(0) = \boldsymbol{u}_1$. Differentiating Eq.(2.103), we get

$$\frac{d}{d\tau}\frac{\partial \boldsymbol{w}(\tau)}{\partial \boldsymbol{x}_0} = \frac{\partial \hat{\boldsymbol{f}}}{\partial \boldsymbol{x}}\frac{\partial \boldsymbol{w}(\tau)}{\partial \boldsymbol{x}_0} + \frac{\partial^2 \hat{\boldsymbol{f}}}{\partial \boldsymbol{x}^2}\left\langle \boldsymbol{w}(\tau), \frac{\partial \boldsymbol{x}(\tau)}{\partial \boldsymbol{x}_0}\right\rangle \tag{2.104}$$

$$\frac{d}{d\tau}\frac{\partial \boldsymbol{w}(\tau)}{\partial \mu} = \frac{\partial \hat{\boldsymbol{f}}}{\partial \boldsymbol{x}}\frac{\partial \boldsymbol{w}(\tau)}{\partial \mu} + \frac{\partial^2 \hat{\boldsymbol{f}}}{\partial \boldsymbol{x}^2}\left\langle \boldsymbol{w}(\tau), \frac{\partial \boldsymbol{x}(\tau)}{\partial \mu}\right\rangle + \frac{\partial^2 \hat{\boldsymbol{f}}}{\partial \boldsymbol{x}\partial \mu}\boldsymbol{w}(\tau) \tag{2.105}$$

where

$$\frac{\partial \boldsymbol{w}(0)}{\partial \boldsymbol{x}_0} = \mathbf{o}, \qquad \frac{\partial \boldsymbol{w}(0)}{\partial \mu} = \mathbf{o}.$$

By integrating Eq.(2.105), we can obtain

$$\frac{\partial}{\partial \boldsymbol{x}_0}\left[\frac{\partial \mathbf{T}}{\partial \boldsymbol{x}_0}\boldsymbol{u}_1\right] = \frac{\partial}{\partial \boldsymbol{x}_0}\left[\frac{\partial \boldsymbol{w}(T)}{\partial \boldsymbol{x}_0}\boldsymbol{u}_1\right]$$

$$\frac{\partial}{\partial \mu}\left[\frac{\partial \mathbf{T}}{\partial \boldsymbol{x}_0}\boldsymbol{u}_1\right] = \frac{\partial}{\partial \mu}\left[\frac{\partial \boldsymbol{w}(T)}{\partial \boldsymbol{x}_0}\boldsymbol{u}_1\right].$$

We can confirm the hypotheses (2.93c) by the non-generacy of the matrix (2.101).

Pitchfork bifurcation

The conditions of a pitchfork bifurcation (2.94a), (2.94b) and (2.94c) are formulated with eigenvector $\boldsymbol{v}_1$ as the following [30]:

$$\mathbf{F}_P(\boldsymbol{y}) \triangleq \begin{bmatrix} \mathbf{H}(\boldsymbol{x}_0, \mu) + a\boldsymbol{v}_1 \\ \left(\frac{\partial \mathbf{H}}{\partial \boldsymbol{x}_0}\right)' \boldsymbol{v}_1 \\ \left(\frac{\partial \mathbf{H}}{\partial \mu}\right)' \boldsymbol{v}_1 \\ ||\boldsymbol{v}_1||^2 - 1 \end{bmatrix} = \mathbf{o}, \quad \boldsymbol{y} = \begin{bmatrix} \boldsymbol{x}_0 \\ \mu \\ \boldsymbol{v}_1 \\ a \end{bmatrix} \in \boldsymbol{R}^{12}. \tag{2.106}$$

By solving Eq.(2.106), we can obtain the vector $\boldsymbol{x}_0$ which is the solution on the bifurcation point, bifurcation parameter μ, and left unit eigenvector $\boldsymbol{v}_1$ belonging to the eigenvalue

0 of Jacobian $\dfrac{\partial \mathbf{H}}{\partial \boldsymbol{x_0}}$. If the parameter $a \neq 0$, then the bifurcation is called "imperfect bifurcation".

The Jacobian of $\dfrac{\partial \mathbf{F}_P}{\partial \boldsymbol{y}}$ is given below:

$$\frac{\partial \mathbf{F}_P}{\partial \boldsymbol{y}} = \begin{bmatrix} \dfrac{\partial \mathbf{H}}{\partial \boldsymbol{x_0}} & \dfrac{\partial \mathbf{H}}{\partial \mu} & a\mathbf{1} & \boldsymbol{v}_1 \\ \dfrac{\partial}{\partial \boldsymbol{x}_0}\left[\left(\dfrac{\partial \mathbf{H}}{\partial \boldsymbol{x_0}}\right)' \boldsymbol{v}_1\right] & \dfrac{\partial}{\partial \mu}\left[\left(\dfrac{\partial \mathbf{H}}{\partial \boldsymbol{x_0}}\right)' \boldsymbol{v}_1\right] & \left(\dfrac{\partial \mathbf{H}}{\partial \boldsymbol{x_0}}\right)' & \mathbf{o} \\ \dfrac{\partial}{\partial \boldsymbol{x}_0}\left[\left(\dfrac{\partial \mathbf{H}}{\partial \mu}\right)' \boldsymbol{v}_1\right] & \dfrac{\partial}{\partial \mu}\left[\left(\dfrac{\partial \mathbf{H}}{\partial \mu}\right)' \boldsymbol{v}_1\right] & \left(\dfrac{\partial \mathbf{H}}{\partial \mu}\right)' & 0 \\ \mathbf{o} & 0 & 2\boldsymbol{v}_1' & 0 \end{bmatrix} \tag{2.107}$$

The elements of Eq.(2.107) can be calculated in the same manner of Eq.(2.101). We can confirm the pitchfork bifurcation by $a = 0$ and Eq.(2.94d).

Period doubling bifurcation

The conditions of a period doubling bifurcation (2.96a) and (2.96b) are formulated with eigenvector $\boldsymbol{u}$ as the following [31]:

$$\mathbf{F}_D(\boldsymbol{y}) \triangleq \begin{bmatrix} \mathbf{H}(\boldsymbol{x}_0, \mu) \\ \dfrac{\partial \mathbf{T}}{\partial \boldsymbol{x}_0}\boldsymbol{u} + 1\boldsymbol{u} \\ ||\boldsymbol{u}||^2 - 1 \end{bmatrix} = \mathbf{o}, \quad \boldsymbol{y} = \begin{bmatrix} \boldsymbol{x}_0 \\ \mu \\ \boldsymbol{u} \end{bmatrix} \in \boldsymbol{R}^{11} \tag{2.108}$$

By solving Eq.(2.108), we can obtain the vector $\boldsymbol{x}_0$ which is the solution on the bifurcation point, bifurcation parameter μ, and right unit eigenvector $\boldsymbol{u}$ belonging to the eigenvalue -1 of the Jacobian $\dfrac{\partial \mathbf{T}}{\partial \boldsymbol{x_0}}$.

The Jacobian of $\dfrac{\partial \mathbf{F}_D}{\partial \boldsymbol{y}}$ is given below:

$$\frac{\partial \mathbf{F}_D}{\partial \boldsymbol{y}} = \begin{bmatrix} \dfrac{\partial \mathbf{T}}{\partial \boldsymbol{x_0}} & \dfrac{\partial \mathbf{T}}{\partial \mu} & \mathbf{o} \\ \dfrac{\partial}{\partial \boldsymbol{x}_0}\left[\dfrac{\partial \mathbf{T}}{\partial \boldsymbol{x_0}}\boldsymbol{u}\right] & \dfrac{\partial}{\partial \mu}\left[\dfrac{\partial \mathbf{T}}{\partial \boldsymbol{x_0}}\boldsymbol{u}\right] & \dfrac{\partial \mathbf{T}}{\partial \boldsymbol{x_0}} + \mathbf{1} \\ \mathbf{o} & 0 & 2\boldsymbol{u}' \end{bmatrix}. \tag{2.109}$$

The elements of Eq.(2.109) can be calculated in the same manner of Eq.(2.101).

Neimark-Sacker bifurcation

The conditions of a Neimark-Sacker bifurcation (2.98a) and (2.98b) are formulated with eigenvector $\boldsymbol{u}_R + i\boldsymbol{u}_I$ as the following [32]:

$$\mathbf{F}_N(\boldsymbol{y}) \triangleq \begin{bmatrix} \mathbf{H}(\boldsymbol{x}_0, \mu) \\ \dfrac{\partial \mathbf{T}}{\partial \boldsymbol{x}_0}\boldsymbol{u}_R - \lambda_R \boldsymbol{u}_R + \lambda_I \boldsymbol{u}_I \\ \dfrac{\partial \mathbf{T}}{\partial \boldsymbol{x}_0}\boldsymbol{u}_I - \lambda_R \boldsymbol{u}_I - \lambda_I \boldsymbol{u}_R \\ ||\boldsymbol{u}_R||^2 + ||\boldsymbol{u}_I||^2 - 1 \\ \boldsymbol{u}_R' \boldsymbol{u}_I \\ \lambda_R^2 + \lambda_I^2 - 1 \end{bmatrix} = \mathbf{o}, \qquad \boldsymbol{y} = \begin{bmatrix} \boldsymbol{x}_0 \\ \mu \\ \boldsymbol{u}_R \\ \boldsymbol{u}_I \\ \lambda_R \\ \lambda_I \end{bmatrix} \in \boldsymbol{R}^{18} \tag{2.110}$$

where

$$\frac{\partial \mathbf{T}}{\partial \boldsymbol{x_0}}(\boldsymbol{u}_R + \boldsymbol{u}_I) = (\lambda_R + i\lambda_I)(\boldsymbol{u}_R + i\boldsymbol{u}_I). \tag{2.111}$$

By solving Eq.(2.110), we can obtain the vector $\boldsymbol{x}_0$ which is the solution on the bifurcation point, bifurcation parameter μ, and right unit eigenvector $\boldsymbol{u}_R + \boldsymbol{u}_I$ belonging to the eigenvalue $\lambda_R + i\lambda_I$ of the Jacobian $\dfrac{\partial \mathbf{T}}{\partial \boldsymbol{x_0}}$.

The Jacobian of $\dfrac{\partial \mathbf{F}_N}{\partial \boldsymbol{y}}$ is given below:

$$\frac{\partial \mathbf{F}_N}{\partial \boldsymbol{y}} = \begin{bmatrix} \dfrac{\partial \mathbf{T}}{\partial \boldsymbol{x_0}} & \dfrac{\partial \mathbf{T}}{\partial \mu} & \mathbf{o} & \mathbf{o} & 0 & 0 \\ \dfrac{\partial}{\partial \boldsymbol{x}_0}\left[\dfrac{\partial \mathbf{T}}{\partial \boldsymbol{x_0}}\boldsymbol{u}_R\right] & \dfrac{\partial}{\partial \mu}\left[\dfrac{\partial \mathbf{T}}{\partial \boldsymbol{x_0}}\boldsymbol{u}_R\right] & \dfrac{\partial \mathbf{T}}{\partial \boldsymbol{x_0}} - \lambda_R \mathbf{1} & \lambda_I \mathbf{1} & -\boldsymbol{u}_R & \boldsymbol{u}_I \\ \dfrac{\partial}{\partial \boldsymbol{x}_0}\left[\dfrac{\partial \mathbf{T}}{\partial \boldsymbol{x_0}}\boldsymbol{u}_I\right] & \dfrac{\partial}{\partial \mu}\left[\dfrac{\partial \mathbf{T}}{\partial \boldsymbol{x_0}}\boldsymbol{u}_I\right] & -\lambda_I \mathbf{1} & \dfrac{\partial \mathbf{T}}{\partial \boldsymbol{x_0}} - \lambda_R \mathbf{1} & -\boldsymbol{u}_I & -\boldsymbol{u}_R \\ \mathbf{o} & 0 & 2\boldsymbol{u}_R' & 2\boldsymbol{u}_I' & 0 & 0 \\ \mathbf{o} & 0 & \boldsymbol{u}_1' & \boldsymbol{u}_R' & 0 & 0 \\ \mathbf{o} & 0 & \mathbf{o} & \mathbf{o} & 2\lambda_R & 2\lambda_I \end{bmatrix}. \tag{2.112}$$

The elements of Eq.(2.112) can be calculated in the same manner of Eq.(2.101).

2.9 Calculation of Bifurcation Sets

We consider to calculate the bifurcation sets of co-dimension one bifurcations. For each bifurcations of co-dimension one, we define another general homotopy function

$$\mathbf{H}_*(\boldsymbol{y}, \tilde{\mu}) \triangleq \mathbf{F}_*(\boldsymbol{y} \mid \tilde{\mu}), \qquad * \in \{S, P, D, N\}\,. \tag{2.113}$$

where the circuit parameter $\tilde{\mu} \in \{\xi, \eta, \zeta, E_m\}$. Then we can obtain bifurcation sets of co-dimension one by following the curve

$$\mathbf{H}_*^{-1}(\mathbf{o}) = \{(\boldsymbol{y}, \tilde{\mu}) \mid \mathbf{H}_*(\boldsymbol{y}, \tilde{\mu}) = \mathbf{o}\}\,. \tag{2.114}$$

We can obtain co-dimension two bifurcations [33, 26] by searching the intersection of bifurcation sets of co-dimension one.

Chapter 3

Experimental Circuit

3.1 Introduction

In this chapter the experimental circuit is shown. With respect to the initial condition, i.e. the phase angle at which the oscillation starts, an ordinary switch is not adequate to create the accurate timing because it has a time lag which may not be constant for every operation. Then, the semiconductor switches made up by connecting with SCR and power diodes in parallel are adopted. For the purpose of the reappearance of experiment, the voltages must always be applied to the three-phase circuit at a predetermined phase angle of the voltage wave. Then, the switching phase controller which control the phase angle of triggers for the semiconductor switches is devised.

Additionally, the magnetizing characteristics are shown. Further, the methods of experiment are shown and the region of 1/3-subharmonic oscillations are investigated.

3.2 Experimental Circuit

An experimental circuit is shown in Fig.3.1. The circuit consists of Y-connected balanced sources, switches which are managed by phase control circuit, series resistors and capacitors, and delta-connected nonlinear inductors and resistors.

Next, the details of the circuit elements are shown.

Three-phase symmetrical voltage sources: We use Y-connected single-phase autotransformers whose neutral point is not earthed. The rating of autotransformers are given below;

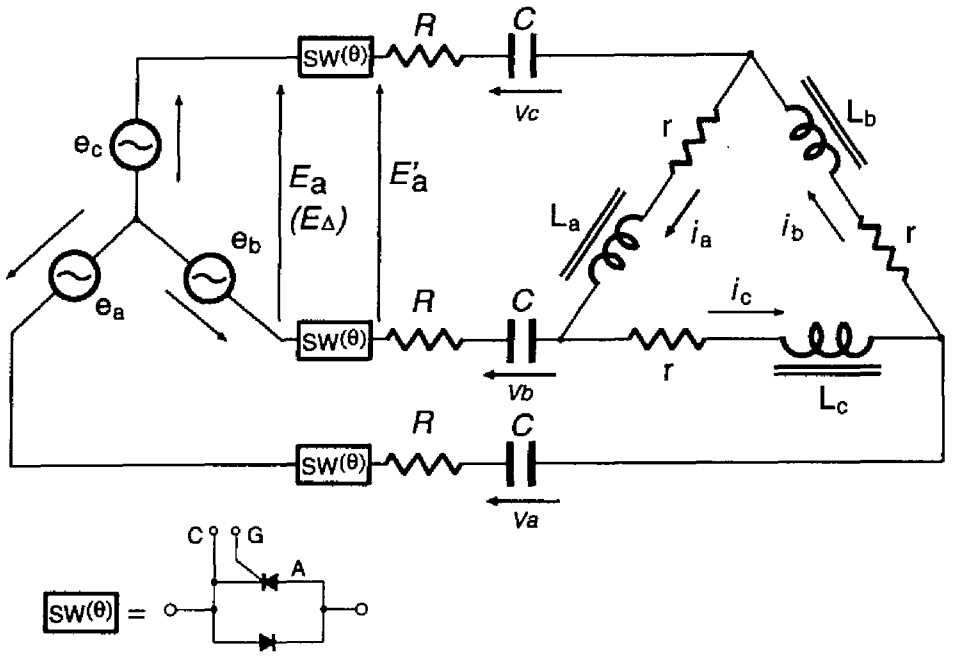

Fig. 3.1: Experimental circuit

Voltage slider.:	20kVA.	**Sec. max. current:**	100A.
Pri. voltage:	200V.	**Sec. voltage:**	$0 \sim 240$V.
Source frequency:	60Hz.		

Series resistor: We use two sorts of wire wound resistors which are connected in series. The ratings of resistors are given below;

Rough adjustment(0.75kW)	$\cdots$	**Max. resistance:**	30Ω
		Max. current:	5A
Fine adjustment(1.0kW)	$\cdots$	**Max. resistance:**	10Ω
		Max. current:	10A

Switch: "SW(θ)" shown in Fig.3.1 is the semiconductor switch made up by connecting with SCR and power diodes in parallel. By applying voltage between cathode and

gate, we can connect the three sources and loads of the experimental circuit at the same time. The phase angle θ indicates that the voltages are applied to the three-phase circuit at phase angle θ of the line-voltage wave E'_a in the figure.

Capacitor: Each capacitors are composed of 21 metalized polyethylene film condensers. We can vary from 7.5μF to 472.5μF by 7.5μF. We can charge the capacitors of each phases(a,b,c) independently with direct-current source. The rating of the capacitors is given below;

Withstand voltage: 500V. **Capacitance:** 30μF.

Nonlinear inductor: We use the three inductors of cut core which are wound by a copper wire with a diameter of 1.1mm. The magnetizing characteristics are shown in section 3.4. The direct-current resistance of inductors are 1.1Ω. The three nonlinear inductors have almost the same characteristics.

Delta-connected resistor: We use wire wound resistors. We can detect the currents of the nonlinear inductors by their terminal voltages.

Phase controller: The phase control circuit can drive pulses for the SCR switch on any phases of the sources. The details of the circuit are described in the next section.

3.3 Phase Controller

3.3.1 Configuration of Circuit

In this section, we show the construction of the phase control circuit. The configuration of the phase control circuit is shown in Fig.3.2. Next, the functions of the circuit elements are shown.

Synchronizing signal generator: By using comparator, we make synchronizing pulse with source(60Hz). The output is pulses of 0 and +5V.

Frequency divider: The frequency of synchronizing pulses are divided to $1/2^n$ (n=1,2,...,8) with counters.

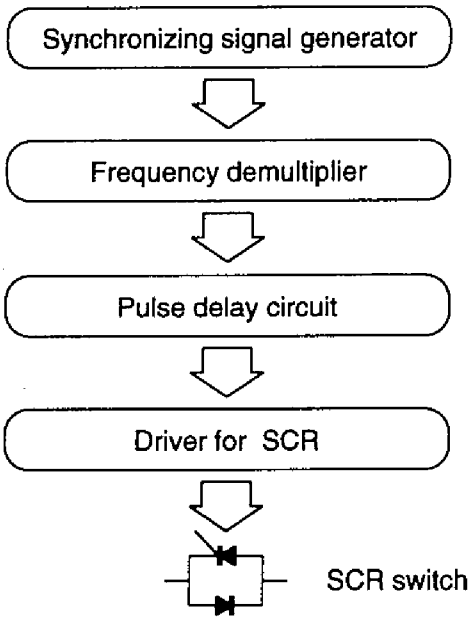

Fig. 3.2: Block diagram of phase control circuit.

Pulse delay circuit: This circuit make the phase of pulses shift and make the width of pulse reduce by a monostable multivibrator.

Driver for SCR: We amplify the output of the pulse delay circuit and drive pulse transformers. Then, the pulses trigger the first SCRs and supply the triggers from DC sources, for the SCR switches in the experimental circuit.

In the following sections, the details of each blocks are shown.

3.3.2 Synchronizing Signal Generator

The circuit diagram of synchronizing signal generator is shown in Fig.3.3. The principle part of the circuit is a relaxation oscillator of comparator. The oscillator is synchronized with the source that synchronizes with the experimental three-phase voltage sources.

Suppose that the diode 1S1585 is opened and $R_2 = R_3$, then the relation between the oscillation frequency f and resistances is represented below;

$$2\left(1+\frac{R_1}{R_2}\right)e^{-\frac{1}{CR_5 f}} = 1. \tag{3.1}$$

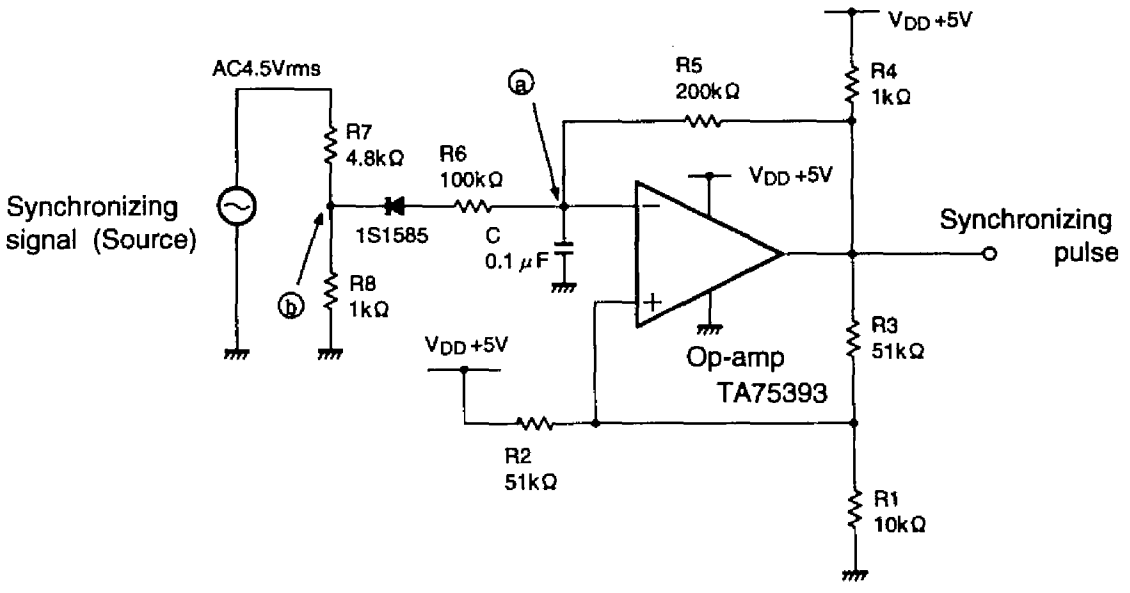

Fig. 3.3: Circuit diagram of synchronizing signal generator.

In this case, because the source frequency is 60Hz we set $f \simeq 60$Hz. If the electric potential on ⓐ becomes larger than that on ⓑ, the diode decrease the time constant of discharge of the capacitor. Hence, by setting the electric potential on ⓑ with resistors R_7 and R_8, we can synchronize the oscillator with the source.

The synchronizing method has the advantage of preventing the noise. That is, suppose that the source is connected directly to the comparator, the noise in the source generate extra pulses and the counter in the next block counts by mistake.

3.3.3 Frequency Divider

The circuit diagram of frequency divider is shown in Fig.3.4. Because we need only one pulse to trigger the SCR switches, we make pulses of long period by the frequency divider and we use one of them. The frequency divider is realized with two 4-stage binary counters 74HC161. We can obtain the pulses of $2 \sim 256$ clock periods ($0.033 \sim 4.3$ second). If the switch is reset after the first pulse, we can get only one pulse. In order to prevent chattering, 0.1 μF capacitor is added in parallel with the reset switch. The length of pulses is set by the switches shown in the lower part of the figure.

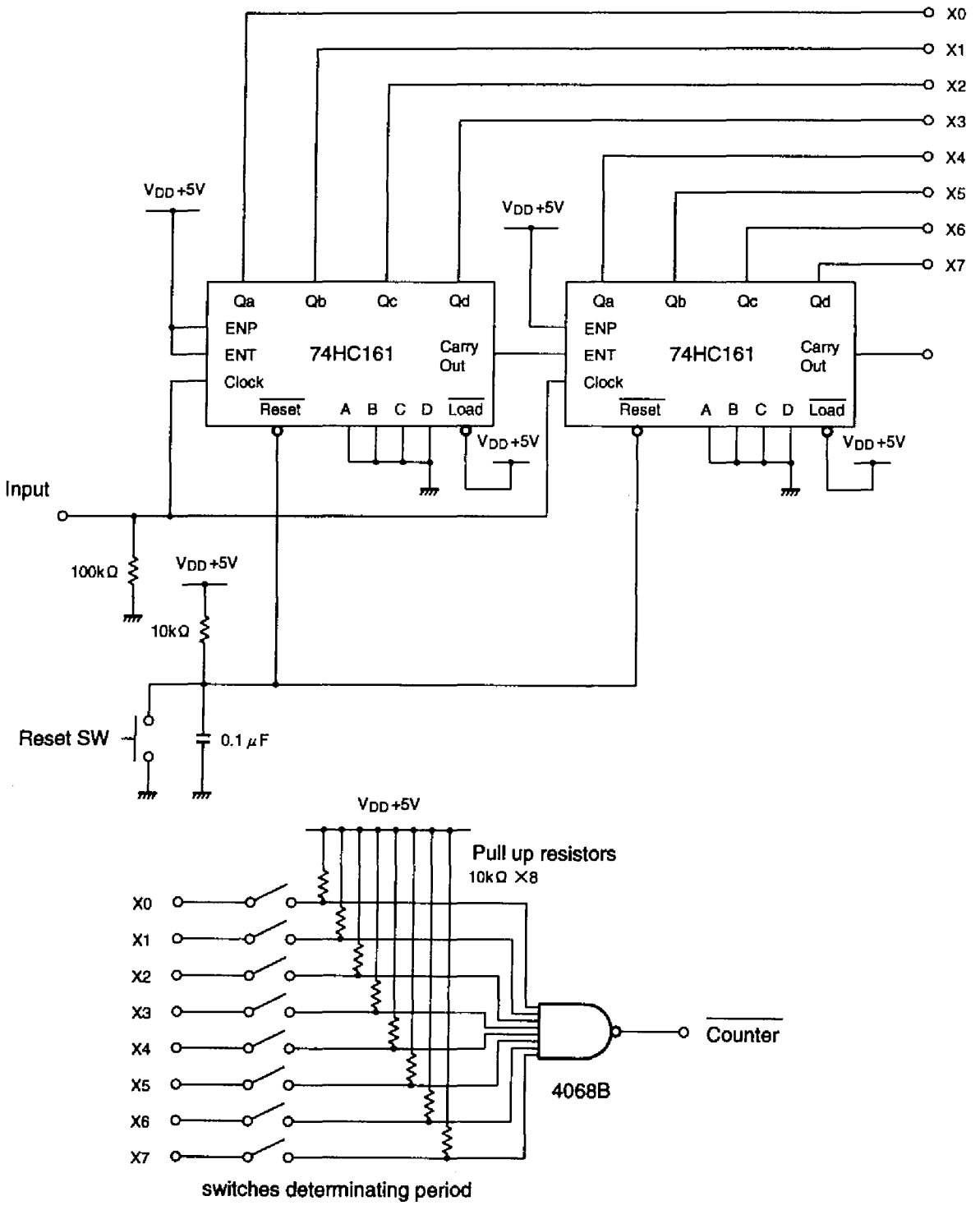

Fig. 3.4: Circuit diagram of frequency divider.

3.3.4 Pulse Delay Circuit

The circuit diagram of pulse delay circuit is shown in Fig.3.5. In this block, the phase of pulses are shifted and the width of pulses are reduced.

In the part of phase shift, the delay time t_d is adjusted by the potentiometer VR_1. By setting the time constant of charge and discharge with VR_1, we can vary the time of crossing the threshold level V_{th} of CMOS. As a result, we can control the delay time of the pulses by adjusting the potentiometer VR_1.

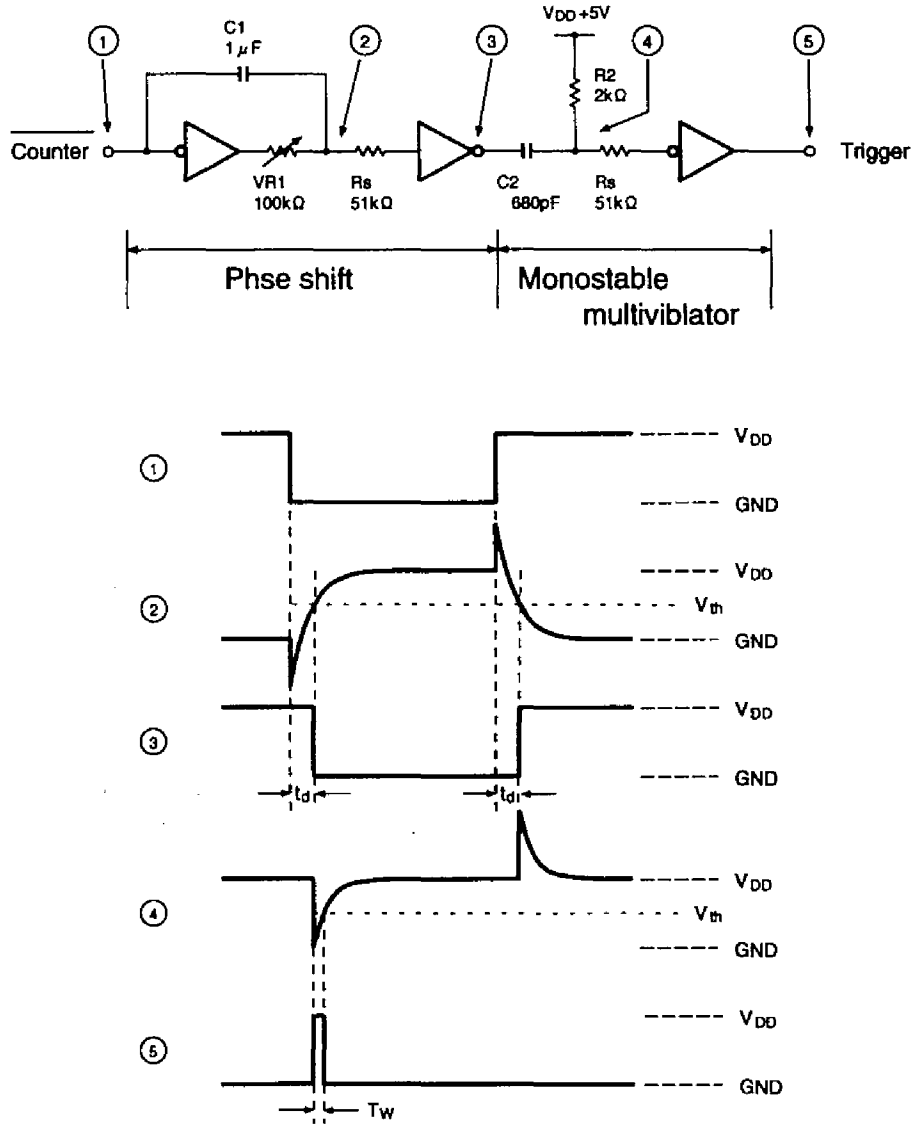

Fig. 3.5: Circuit diagram of pulse delay circuit.

In the part of monostable multiviblator, the width of pulses are determined by the capacitor C_2 and the resistor R_2. That is, by adjusting the time constant of charge and discharge, we can set the time of crossing the threshold level V_{th}. As a result, we can set the width of trigger pulses. The relation of the pulse width T_w and the time constant C_2R_2 is represented below;

$$\left(1 - e^{-\frac{T_w}{C_2R_2}}\right) V_{DD} = \frac{1}{2}V_{DD}. \tag{3.2}$$

In this case, we set the width of pulses $T_w \simeq 1\mu s$.

3.3.5 Driver for SCR

The circuit diagram of SCR driver is shown in Fig.3.6. In this block the pulses are amplified and drive three pulse transformers. The diodes which are connected in parallel with primary windings prevent the transistor from the counter-electromotive force of the pulse transformers. The outputs of pulse transformer trigger the first thyristors and the DC source supply its voltage to the SCR switches.

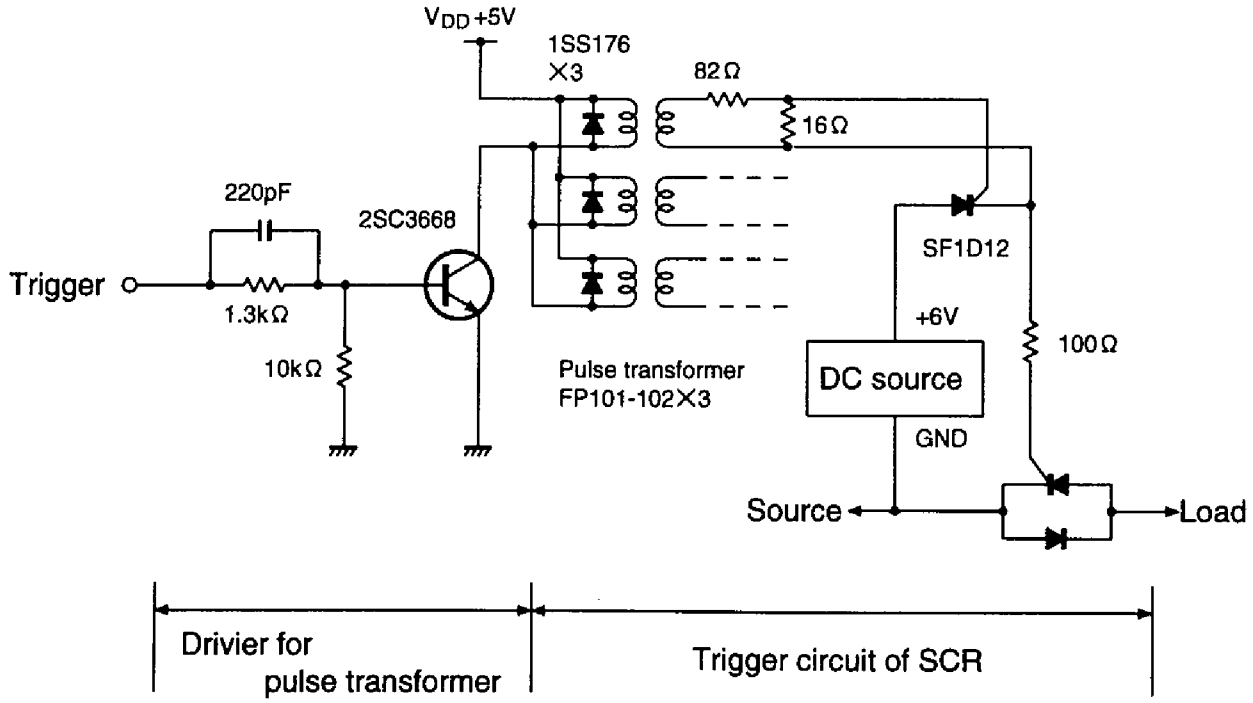

Fig. 3.6: Circuit diagram of SCR driver.

3.3.6 Behavior of the Phase Controller

We confirm the behavior of the phase controller. As a synchronizing signal, we adopt commercial single-phase AC100V which synchronizes to the source of experimental circuit.

The behavior of phase controller is shown in Fig.3.7. The switching phase is set to $\theta = 0°$, 90°, 180°, 270°. The reference for the phase angle θ is the source line-voltage E_a in Fig.3.1 which is the voltage between phase-b and phase-c of voltage source. The line-voltage E'_a represents the voltage of the right-hand side of SCR switches shown in Fig.3.1. Because the capacitor of phase-a is initially charged to 50 V, E'_a show DC 50V before the switch is closed. From the figure, we can confirm the phase controller operates accurately.

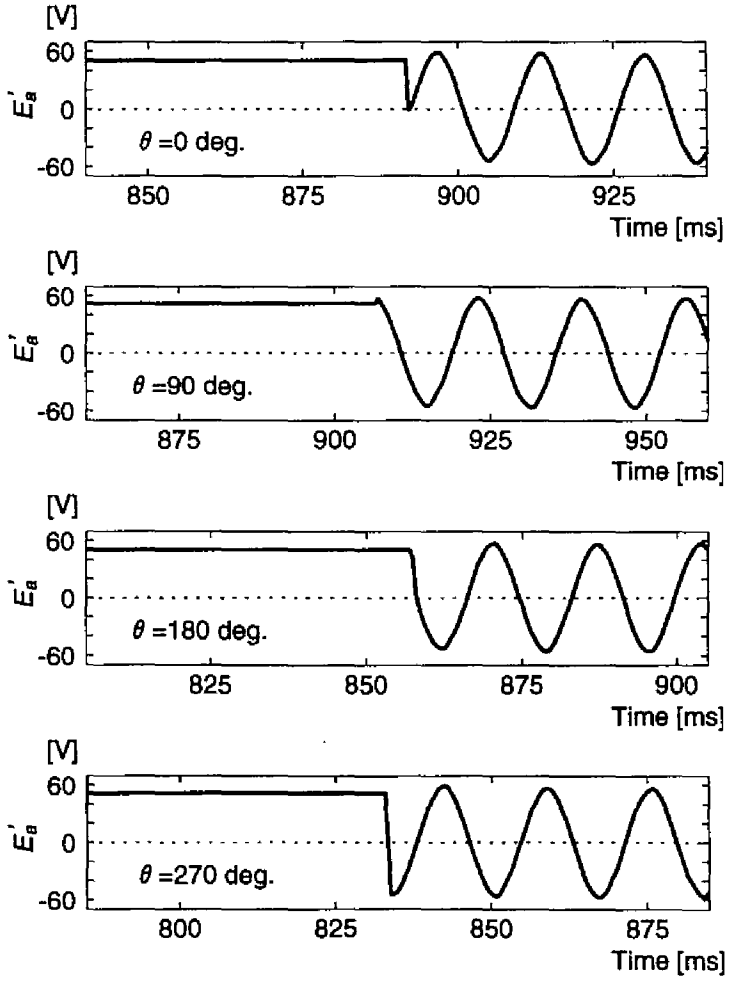

Fig. 3.7: The behavior of phase controller.

3.4 Magnetizing Characteristics

The measuring system of the magnetizing characteristics of nonlinear inductors are illustrated in Fig.3.8. In this figure, the frequency of voltage source is 60Hz. The current i and the flux of nonlinear inductors are obtain from the terminal voltage of r_T and the output of integration, respectively. The result of measurement is shown in Fig.3.9. Because the effects of hysteresis is very small, we can neglect them. The three nonlinear inductors evidently have almost the same magnetizing characteristics.

The direct-current resistance of inductors are 1.1 Ω.

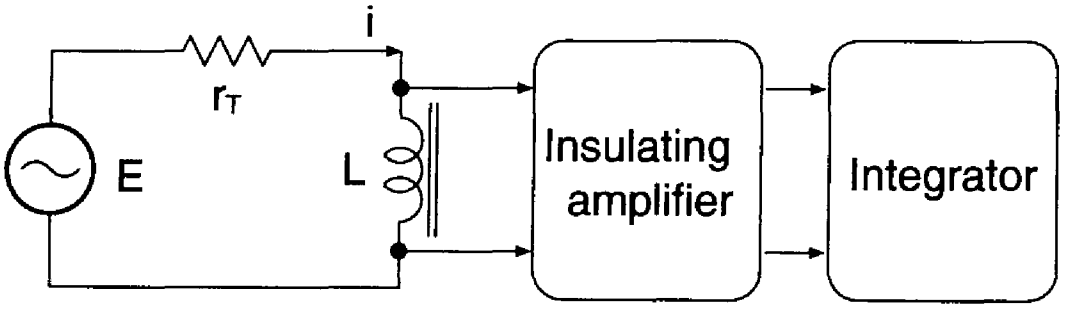

Fig. 3.8: The measuring system of magnetizing characteristics.

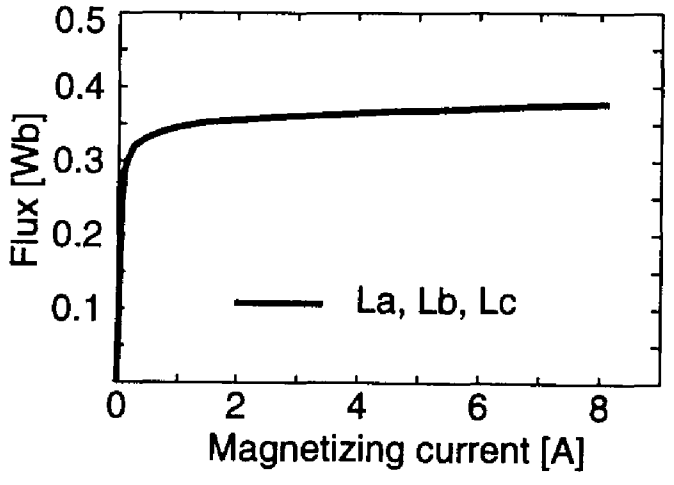

Fig. 3.9: Magnetizing characteristics of nonlinear inductors.

3.5 Experimental Method

3.5.1 System of Measurement

The measuring system of experiment is illustrated in Fig3.10. The measuring system is insulated by seven insulating amplifiers. The output of insulating amplifiers are connected to three oscilloscopes, a digital spectrum analyzer and an AD converter of eight port. We can observe six wave forms by the three oscilloscopes simultaneously. With the digital spectrum analyzer, we can obtain frequency spectra on real time. The output of the digital spectrum analyzer is connected to a recorder. On the other hand, the output of analog-digital converter(A/D converter) is taken in the memory of a computer and we can analyze the wave forms.

For the purpose of obtaining Poincare section, the oscilloscopes and A/D converter can be triggered externally. The trigger signals are generated by synchronizing signal generator and pulse delay circuit. The design of those circuits are similar to those of phase control circuit.

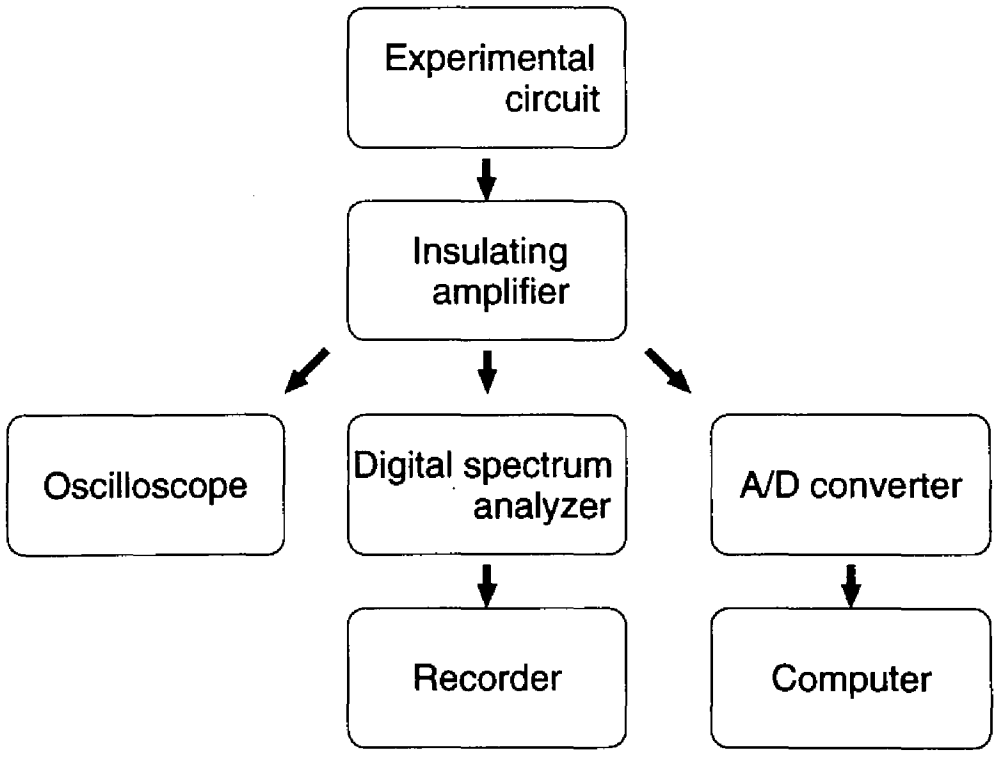

Fig. 3.10: The measuring system of experiment.

3.5.2 Generation of Oscillations

In this section, the fundamental method of generating oscillations is shown. We can choose the amplitude of source line-voltage E_Δ, series resistance R, series capacitance C and delta connected resistance r. Without notice, the resistor is fixed to $r = 3.1\Omega$ where the resistance of inductor 1.1Ω is contained. The processes of generating several oscillations and observe bifurcation phenomena are shown below;

(1) We set the series resistance R, the series capacitance C and the amplitude of source line-voltage E_Δ.

(2) We discharge all capacitors and charge one of them to a given initial voltage.

(3) We close the circuit at a given phase angle θ by triggering the SCR switches simultaneously with phase controller.

(4) We observe generated oscillations by the measuring system. If the generated oscillation is desired, we advance experiment (5). If the desired oscillation is not generated, we try (3) once more.

(5) We observe bifurcation phenomena by increasing or decreasing the parameter E_Δ. The bifurcations are confirmed by the waveforms on the oscilloscopes and the the frequency spectra on the digital spectrum analyzer.

In the step (2), without notice, the capacitor of phase-c is charged. In this method, the initial voltage of capacitors and the initial phase of voltage sources are determined exactly. The initial fluxes are affected by remanent magnetizations so that the reappearance of the generating oscillations are not guaranteed completely. Hence, the step (3) is tried repeatedly until the desired oscillation is obtain.

3.5.3 Region of 1/3-subharmonic Oscillation

Paying attention to 1/3-subharmonic oscillations, several oscillations are generated in the three-phase circuit by the above method. Considering the number of dominant inductors, the 1/3-subharmonic oscillations are classified into three modes. That is,

M_1 mode: Oscillations excited by any one of the three nonlinear inductors. In this mode the current flows dominantly through only one inductor and the three-phase circuit operates as if it were a single-phase circuit.

M_2 mode : Oscillations excited by any two of the three nonlinear inductors. In this mode the current flows dominantly through only two inductors and the three-phase circuit operates as if it were a two-phase circuit.

M_3 mode : Oscillations excited by all the three nonlinear inductors.

The modes M_1 and M_2 are structurally unsymmetric oscillations. The structurally symmetric oscillations belongs to M_3 mode.

Further, varying the capacitances, the region of 1/3-subharmonic oscillations on E_Δ-X_C plane is investigated by the above method. Here, E_Δ is the amplitude of the source line-voltage and X_C is defined by the susceptance of capacitors, that is, $X_C \triangleq 1/\omega C$. In this experiment the initial value of circuit elements, initial charge voltage and switching phase are determined to obtain the largest region of 1/3-subharmonic oscillations of the three modes. The result is shown in Fig.3.11.

In the higher part of the susceptance $X_C > 40\Omega$, because we cannot decrease the capacitance by less than $7.5\mu F$, the region of the generation can not be obtained. When the source voltage E_Δ is about 70V and the susceptance X_C is higher than about 30Ω, we cannot investigate the region of 1/3-subharmonic oscillations because of the harmonic resonances. When the source voltage E_Δ is about $40 \sim 50$V and the susceptance X_C is about 25Ω, the region cannot be obtained accurately because the 1/3-subharmonic oscillations last for some time and fade away.

In the lower part of the source E_Δ, the region of M_1 and M_3 overlap each other. In this region the transition between M_1 and M_3 can be observed. The transition is shown in Fig.3.12. We can observe only the transition from M_3 to M_1 on the lower side of M_3 region. On the other cases, the 1/3-subharmonic oscillations faded away.

The regions of M_2 and M_3 seem not to overlap each other. However, on the boundary between M_2 and M_3 the modes changes each other so that we cannot determine the boundary accurately.

The details of the bifurcations in each regions are described latter.

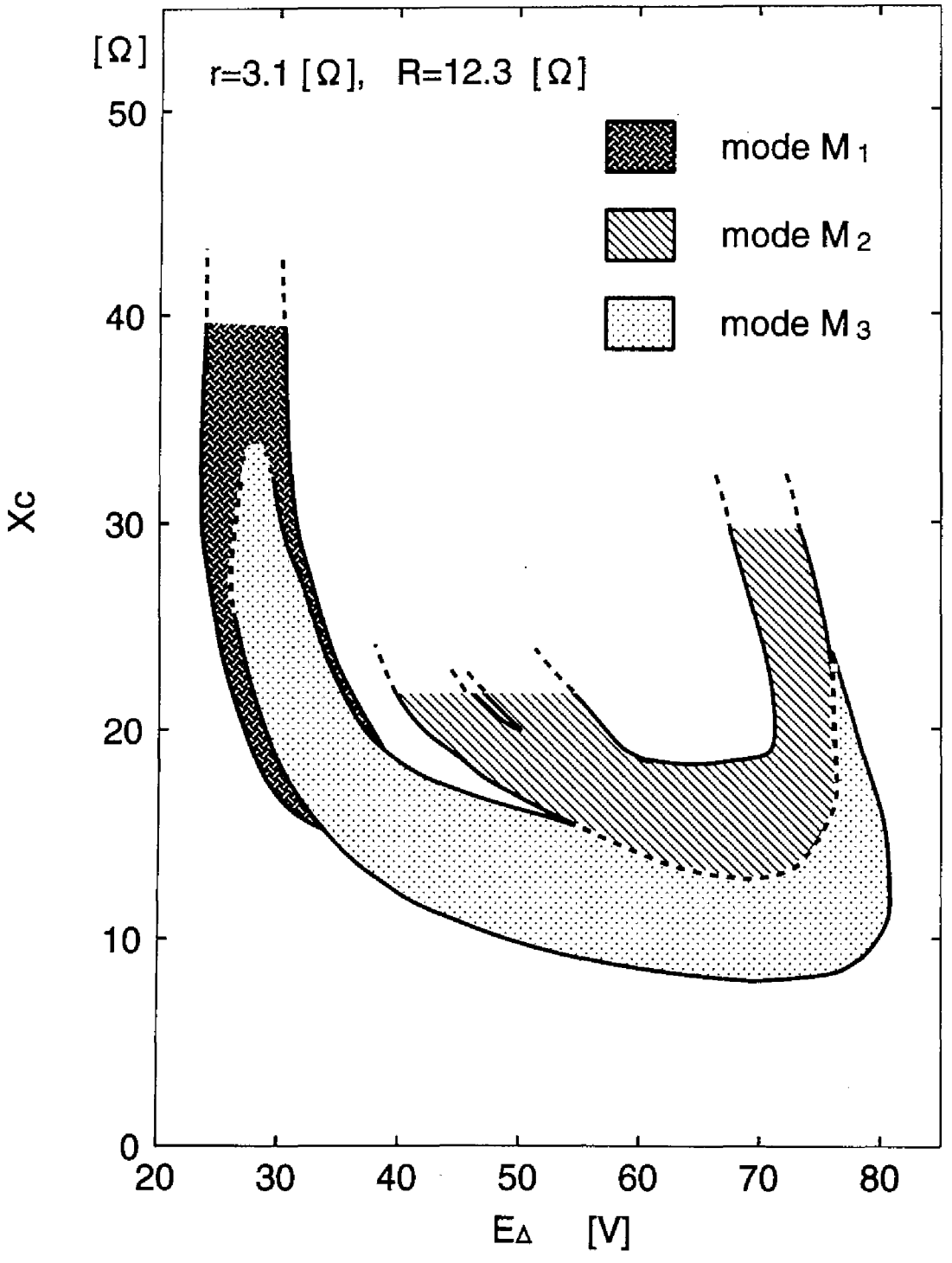

Fig. 3.11: The region of 1/3-subharmonic oscillations (experiment).

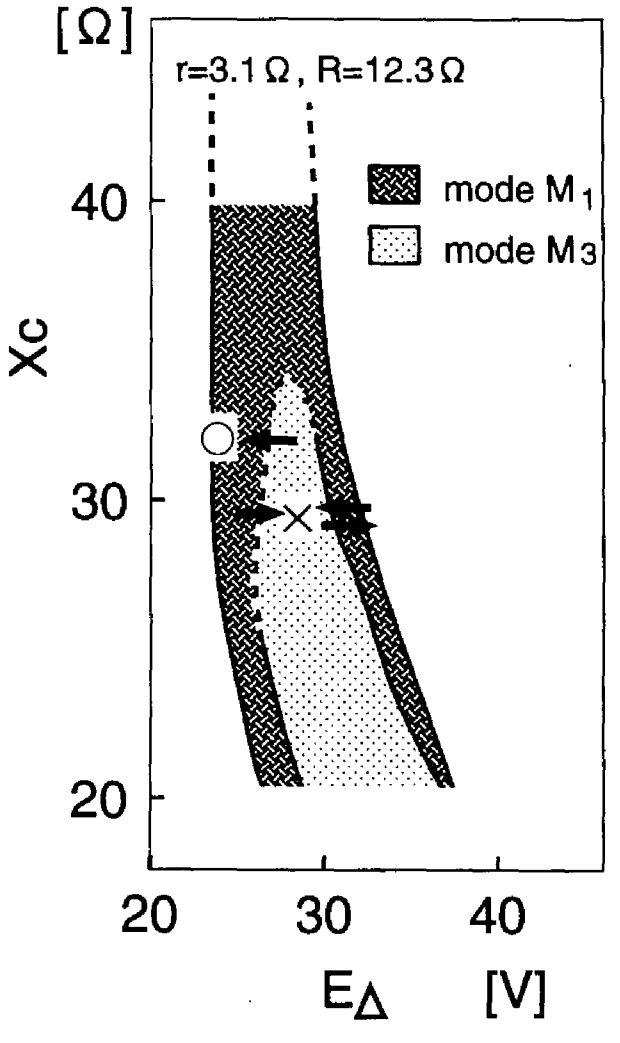

Fig. 3.12: The transition of 1/3-subharmonic oscillations M_1 and M_3 (experiment).

Chapter 4

Single-phase 1/3-Subharmonic Oscillation

4.1 Introduction

In this section the bifurcation phenomena of single-phase 1/3-subharmonic oscillations are investigated [108]. First, the periodic solution curves are analyzed. Next, a single-phase-like circuit is defined and the comparison with the periodic solution curves of 1/3-subharmonic oscillation in the single-phase circuit is made. Further a coupled single-phase circuit is defined and the modes of oscillation are revealed. Furthermore, the bifurcation sets are shown and compared with those of single-phase-like circuit. Finally, the experimental results are shown.

4.2 Periodic Solution Curve in Three-phase Circuit

4.2.1 Setting of Parameter

We set the series resistance $R = 12.3\Omega$ and the delta-connected resistance $r = 3.1\Omega$. As for the magnetizing characteristics, we apply the spline approximation of the real experimental results shown in section 3.4. The scaling factors are determined $\alpha_\phi = 2.86$ and $\alpha_i = 0.76$ so that the point (1,1) may be on the scaled magnetizing characteristics. The susceptance of the capacitors are set to $\eta = 0.27$ ($X_C = 27.2\Omega$).

The period in Eq.(2.33) are set to $T = 6\pi$ and Runge-Kutta method is applied to calculating integrals. The convergence criterion is determined to $\epsilon_G = 10^{-7}$ in Eq.(2.53).

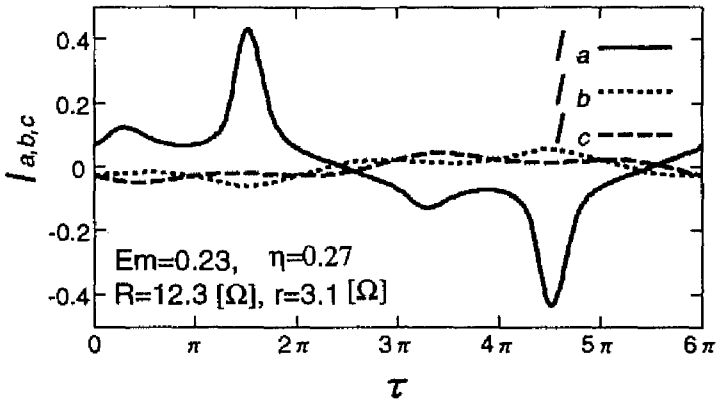

Fig. 4.1: Current waveforms of stable M_1 oscillation (computation).

4.2.2 Periodic Solution Curve

It is not essential which inductor(L_a, L_b, L_c) is active because the three-phase circuit is structurally symmetric. Then, we pay attention to M_1 oscillations in which the inductor L_a is active and the others are not. Applying the Newton homotopy method which is described in section 2.5.1 at the source amplitude $E_m = 0.23$, we can obtain two periodic solutions of M_1 oscillations; one of which is stable and the other is unstable. The inductor current waveforms of the stable oscillation are shown in Fig.4.1. We can confirm that the current of inductor L_a is large and the currents of inductor L_b and L_c are very small.

Next, applying the general homotopy method which is described in section 2.5.4, we obtain the periodic solution curve. The periodic solution curve on E_m-Ψ_a plane is shown in Fig.4.2. In this figure, the real line and the dotted line represent the stable and unstable solution, respectively. The generated bifurcations are saddle-node bifurcations $S_1 \sim S_6$, pitchfork bifurcations P_1 and P_2, and period doubling bifurcations $D_1 \sim D_4$. The periodic solution curve consists of two loops, that is, $S_1 \to P_1 \to S_2 \to P_2 \to S_3 \to S_4 \to S_1$ (loop 1) and $P_1 \to D_1 \to S_5 \to D_3 \to P_2 \to D_4 \to S_6 \to D_2 \to P_1$ (loop 2). The two loops intersects each other on the pitchfork bifurcations P_1 and P_2. In Fig. 4.2, the bifurcation point P_1 and P_2, D_1 and D_3, D_2 and D_4 nearly overlap each other. The stable region is between S_1 and P_1, P_1 and D_1, P_1 and D_2.

The loop 1 has a symmetry with respect to C_2 on Eq.(2.25). That is, the trajectories of the solutions have origin symmetry and the fluxes don't have DC components. On the

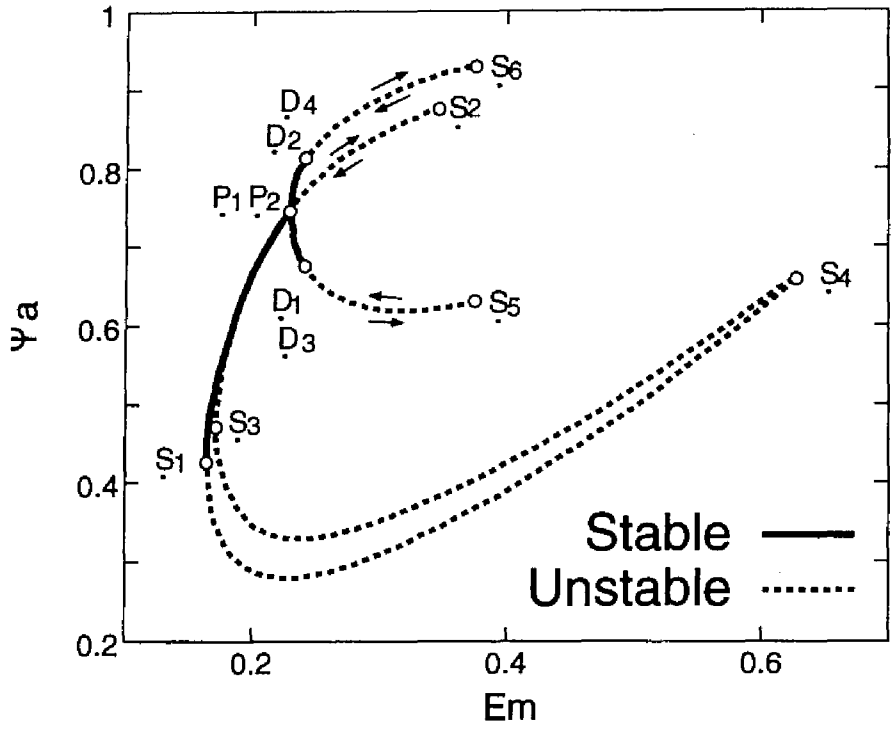

Fig. 4.2: Periodic solution of 1/3-subharmonic M_1 oscillation.

other hand, the loop 2 doesn't have the symmetry. That is, the trajectories of the solutions don't have origin symmetry and the fluxes have DC component. Paying attention to stable solutions, the symmetry with respect to C_2 breaks on the pitchfork bifurcation P_1 and the unsymmetric solutions appear.

On the period doubling bifurcations $D_1 \sim D_4$, the branches of period-6 ($T = 12\pi$) solutions bifurcate from the loop 2. Furthermore, the branches repeat period doubling bifurcations. The branches of period-384 ($T = 768\pi$) solutions can be confirmed.

4.2.3 Variational Waveforms on Bifurcation Points

In order to make clear the effects of bifurcations, we investigate the local center manifold of the bifurcation points. First, we consider the following variational equation:

$$\frac{d}{d\tau}\,\delta\boldsymbol{x}(\tau) \;=\; \frac{\partial \hat{\boldsymbol{f}}(\boldsymbol{x},\tau)}{\partial \boldsymbol{x}}\,\delta\boldsymbol{x}(\tau) \tag{4.1}$$

$$\delta \boldsymbol{x}(0) \;=\; \delta \boldsymbol{x}_0$$

where $\delta \boldsymbol{x}(\tau) \in \boldsymbol{R}^5$. For the purpose of calculating the waveforms on a local center manifold, the initial vector $\delta \boldsymbol{x}_0$ which satisfies $\| \delta \boldsymbol{x}_0 \| = 1$ is determined as follows;

$$\begin{array}{ll} \mathbf{M}\ \delta \boldsymbol{x}_0 = 1 \delta \boldsymbol{x}_0 & \text{for saddle-node and pitchfork bifurcations,} \\ \mathbf{M}\ \delta \boldsymbol{x}_0 = -1 \delta \boldsymbol{x}_0 & \text{for period doubling bifurcations,} \end{array} \tag{4.2}$$

where $\mathbf{M}$ is the monodromy matrix defined by Eq.(2.69). In the case of saddle-node bifurcations and period doubling bifurcations, the vector $\delta \boldsymbol{x}_0$ can be obtained by the vector $\boldsymbol{u}_1$ in Eq.(2.100) and the vector $\boldsymbol{u}$ in Eq.(2.108), respectively. Integrating the variational Eq. (4.1) over the interval $[0, T]$, we obtain the waveforms on a local center manifold

$$\begin{aligned} &(\delta \Psi_a(\tau), \delta \Psi_b(\tau), \delta \Psi_c(\tau), \delta U_a(\tau), \delta U_b(\tau), \delta U_c(\tau)) \\ &\qquad \triangleq (\delta x_1(\tau), \delta x_2(\tau), \delta x_3(\tau), \delta x_4(\tau), \delta x_5(\tau), -\delta x_4(\tau) - \delta x_5(\tau)). \end{aligned} \tag{4.3}$$

Waveforms and the frequency spectra on local center manifolds of bifurcation points $\dot{S}_1$, $\dot{P}_1$, $\dot{S}_2$, and $\dot{D}_1$ are illustrated in Fig.4.3.

As for the bifurcation $\dot{S}_1$, the waveforms of $\delta \boldsymbol{\Psi}$ on the local center manifold are M_1 oscillation, that is, $\delta \Psi_a$ is large and $\delta \Psi_b$ and $\delta \Psi_c$ is small ($\delta \Psi_b$ and $\delta \Psi_c$ almost overlap each other). The frequency spectra of $\delta \Psi_a$ indicates that the waveform is a 1/3-subharmonic oscillation and doesn't have DC component. Thus, on the bifurcation point $\dot{S}_1$, the M_1 oscillation loses its stability by the excitation of M_1 oscillation of order 1/3.

As for the bifurcation $\dot{P}_1$, the waveforms of $\delta \boldsymbol{\Psi}$ on the local center manifold are M_1 oscillation. However the period is $T/2$, that is, the oscillation of order 2/3. It is confirmed by the frequency spectra which contents the components of 2/3 and don't content 1/3. Furthermore, the frequency spectra indicates that the waveform contents DC component. Thus, on the bifurcation point $\dot{P}_1$, the M_1 oscillation loses its stability by the excitation of M_1 oscillation which contents the components of DC and order 2/3. Then, instead of the oscillation, two stable oscillations which contents the components of DC and order 2/3 are generated.

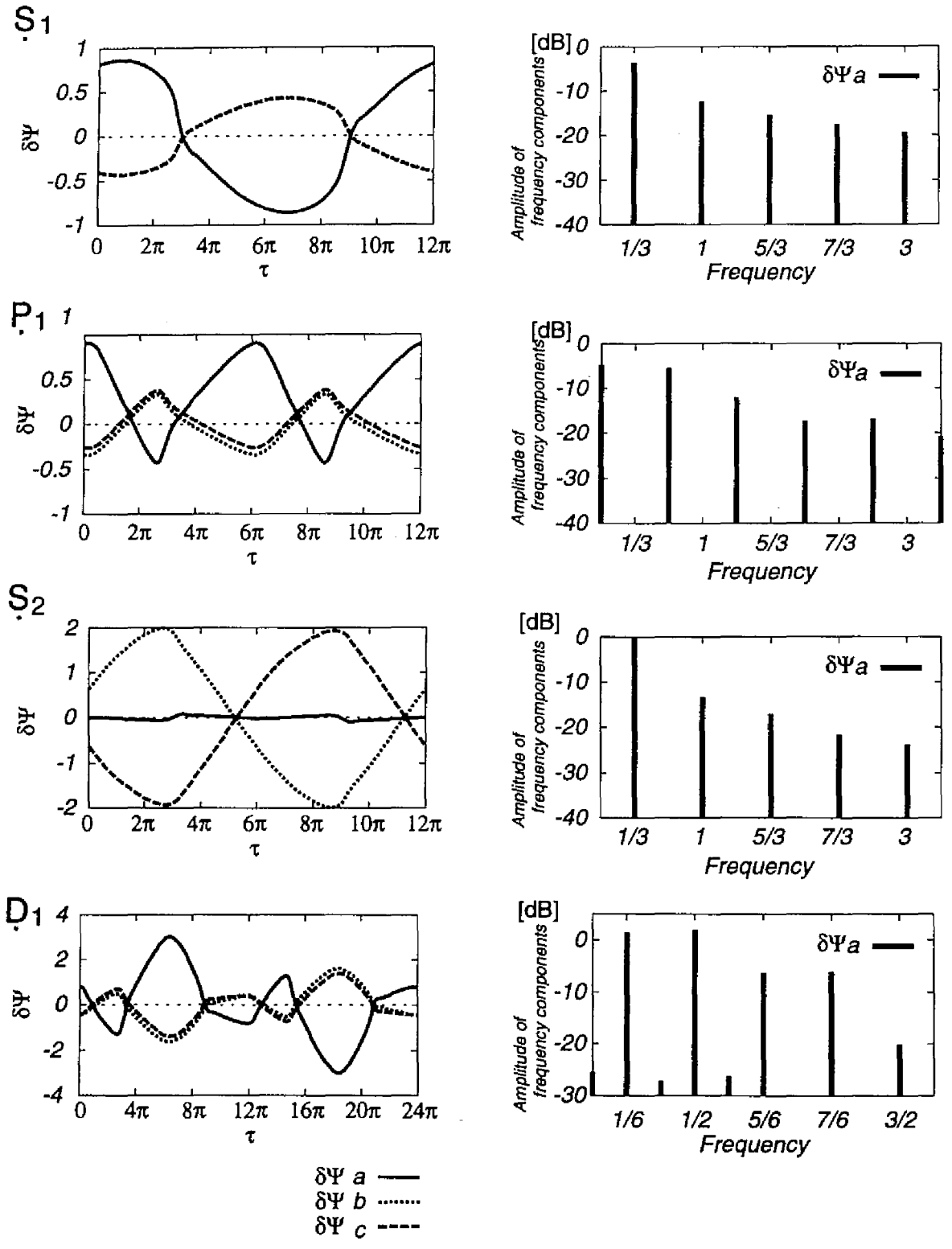

Fig. 4.3: Variational waveforms on center manifold.

As for the bifurcation $\dot{S}_2$, the waveforms of $\delta\Psi$ on the local center manifold are M_2 oscillation, that is, $\delta\Psi_b$ and $\delta\Psi_c$ is large and $\delta\Psi_a$ is small. The frequency spectra of $\delta\Psi_a$ indicates that the waveform is 1/3-subharmonic oscillations and doesn't have DC component. Although the point of $\dot{S}_2$ is the bifurcation in the region of unstable solutions, the degree of unstability σ defined in section 2.6.1 changes by the excitation of M_2 oscillation of order 1/3. The bifurcation $\dot{S}_4$ is similar to this point.

As for the bifurcation $\dot{D}_2$, the waveforms of $\delta\Psi$ on the local center manifold are M_1 oscillation whose period is $2T$, that is, order 1/6 (the scale of $\dot{D}_1$ in the figure is different from others). It is confirmed by the frequency spectra. Thus, on the bifurcation point $\dot{D}_1$, the period-3 M_1 oscillation loses its stability by the excitation of M_1 oscillation which contents the component of order 1/6. Instead of the period-3 oscillation, the stable period-6 oscillation is generated.

4.3 Periodic Solution Curve in Singe-phase-like Circuit

4.3.1 Circuit Equations

As far as the M_1 oscillations are concerned, the current through the phase-a capacitor which is $I_b - I_c$ in the Fig.4.1 is very small. Hence, we consider a single-phase-like circuit shown in Fig.4.4. The single-phase-like circuit is made by opening the phase-a of the three-phase circuit.

The scaled single-phase-like circuit equations are given below;

$$\left.\begin{aligned} \frac{d\Psi_a}{d\tau} &= E_m \sin(\tau) - U + 2\xi(I_c - I_a) - \zeta I_a \\ \frac{d\Psi_c}{d\tau} &= -\frac{1}{2}E_m \sin(\tau) + \frac{1}{2}U + \xi(I_a - I_c) - \zeta I_c \\ \frac{dU}{d\tau} &= 2\eta(I_a - I_c) \end{aligned}\right\} \tag{4.4}$$

where

$$U \triangleq U_b - U_c, \quad I_a = I(\Psi_a), \quad I_c = I(\Psi_c), \quad \Psi_b = \Psi_c.$$

Because the dependency between the inductor currents I_b and I_c, and the dependency between the capacitor voltages of phase-b and phase-c are generated, the single-phase-like

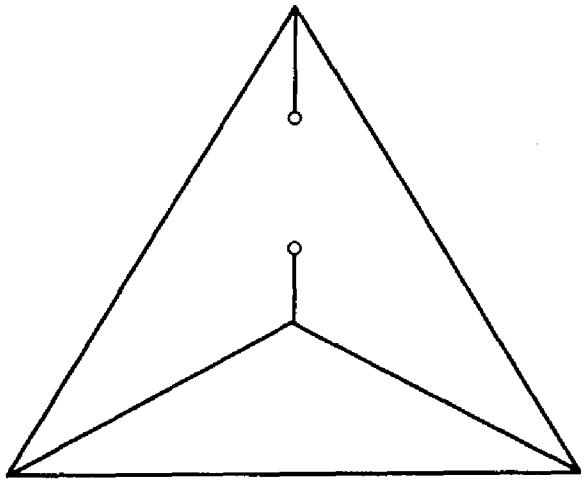

Fig. 4.4: Single-phase-like circuit.

circuit is a three dimensional system.

4.3.2 Periodic Solution Curve

Applying the general homotopy, we obtain the periodic solution curve on E_m-Ψ_a plane which is shown in Fig.4.5. The generated bifurcations are saddle-node bifurcations $\hat{S}_1$ and $\hat{S}_2$, pitchfork bifurcations $\hat{P}_1$ and $\hat{P}_2$, and period doubling bifurcations $\hat{D}_1 \sim \hat{D}_4$. The periodic solution curve consists of two loops, that is, $\hat{S}_1 \rightarrow \hat{P}_1 \rightarrow \hat{P}_2 \rightarrow \hat{S}_2 \rightarrow \hat{S}_1$ (loop $\hat{1}$) and $\hat{P}_1 \rightarrow \hat{D}_1 \rightarrow \hat{D}_3 \rightarrow \hat{P}_2 \rightarrow \hat{D}_4 \rightarrow \hat{D}_2 \rightarrow \hat{P}_1$ (loop $\hat{2}$). The two loops intersect each other on the pitchfork bifurcations $\hat{P}_1$ and $\hat{P}_2$.

The loop $\hat{1}$ has a symmetry with respect to $\mathbf{C}_2$ on Eq.(2.25), that is, the fluxes don't have DC component. On the other hand, the loop $\hat{2}$ doesn't have the symmetry and the fluxes have D.C. components. The stable periodic solutions exists in the neighborhood of $\hat{P}_1$ and $\hat{P}_2$.

Comparing Fig.4.2 with Fig.4.5, we can find a big difference between the periodic solution curve of the three-phase and single-phase-like circuit. The higher part of the amplitude $E_m \simeq 0.68 \sim 0.74$ we can have bifurcation point and stable solutions in the single-phase-like circuit in Fig.4.5. On the other hand there is no such portion of the voltage in the M_1 of three-phase circuit shown in Fig.4.2. In the lower amplitude of $E_m \simeq 0.16 \sim 0.25$ both

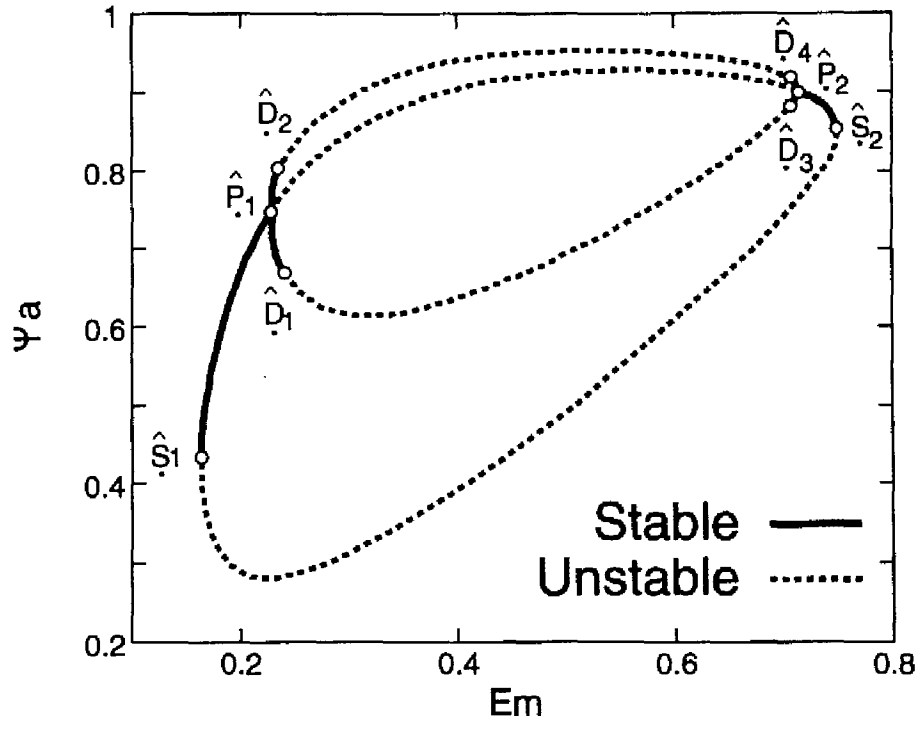

Fig. 4.5: Periodic solution of 1/3-subharmonic oscillations in single-phase-like circuit.

diagrams are fairly in good agreement.

The above difference is caused by the folding back of the solution curve which is generated by the saddle-node bifurcations $\hat{S}_2$, $\hat{S}_5$ and $\hat{S}_6$ of M_1 oscillation. In the next section, we consider the details of the folding back.

4.4 Mode of Oscillation

In this section, we consider the portion where the periodic solution curve of three-phase circuit is different from that of single-phase-like circuit. First, the current waveforms on the bifurcation point $\hat{S}_3$ is illustrated in Fig.4.6. Although this solution is unstable, the mode is like M_2 in which inductors L_a and L_b is active and L_c is not active.

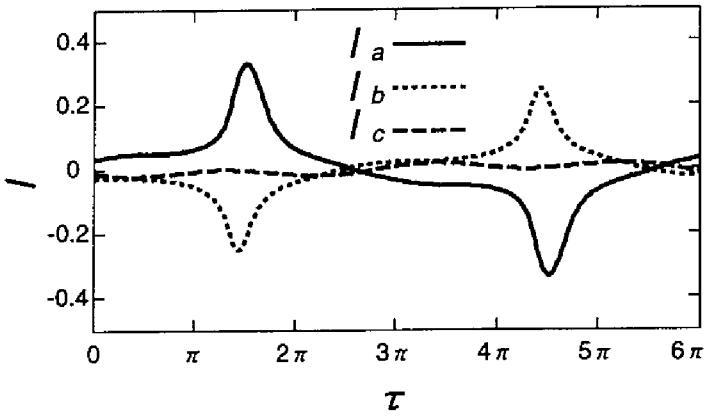

Fig. 4.6: Current waveforms on bifurcation point S_3 (computation).

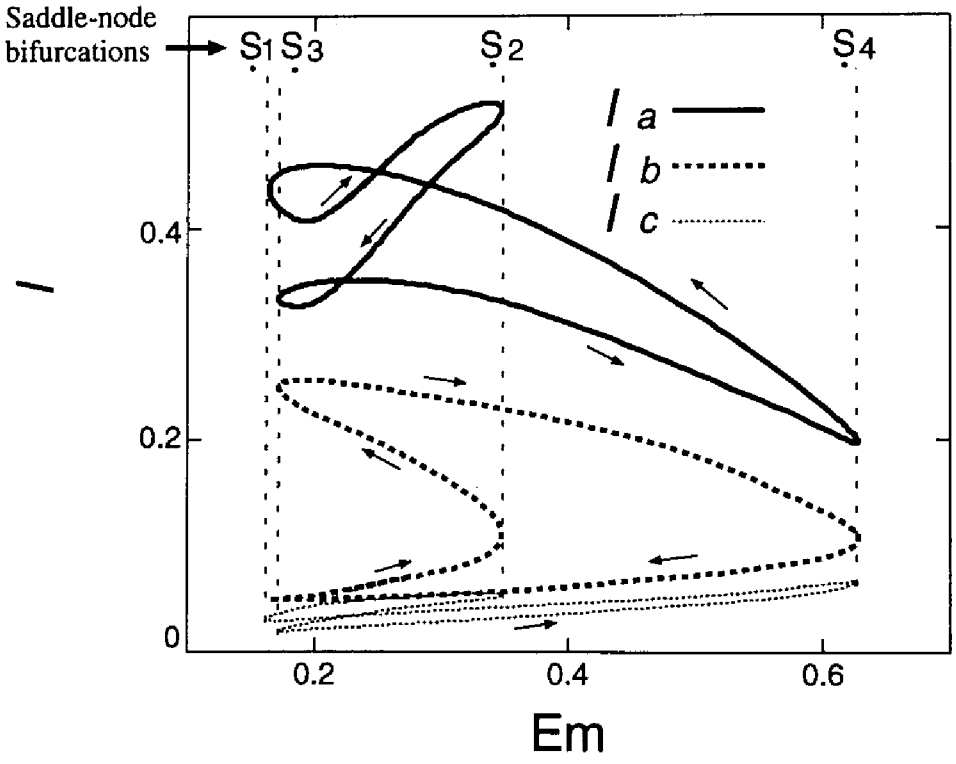

Fig. 4.7: Amplitude characteristics of periodic solution curves of M_1 oscillation.

Then, in order that we make apparent the transition from the mode M_1 to M_2, the amplitude characteristics of the periodic solution curve in the three-phase circuit is shown in

Fig.4.7. The horizontal axis is the source line-voltage E_m and the vertical axis I is the maximum value of inductor currents. If the loop corresponding to the loop 2 in Fig.4.2 is shown, the figure becomes so complicated that only the loop corresponding to the loop 1 is shown. The three loops correspond to the maximum values of inductor currents I_a, I_b and I_c.

On the bifurcation point S_1, the currents through the inductor L_a is large and the other two is very small, that is, the mode M_1. On the other hand, on the bifurcation point S_3, the oscillation is M_2 mode. We can confirm that the mode of oscillations changes on the neighborhood of S_2 and S_4. Paying attention to the maximum values of inductor currents I_b on S_2 and S_4, the current values are about 0.11. The current value corresponds to the flux about 0.30 in the magnetizing characteristics of nonlinear inductor shown in Fig.fig:reizitoksei. It indicates that the saturation of inductor L_b causes the transition from M_1 to M_2 mode and the bifurcation point S_2 and S_4 on which the solution curve folds back is the boundary of the modes.

4.5 Coupled Single-phase Circuit

4.5.1 Coupled Single-phase Circuit Equation

In order to make clear the transition from M_1 to M_2 mode, we consider a coupled single-phase circuit shown in Fig.4.8. That is, by analyzing the coupled single-phase circuit, we try to reveal the effects of coupling of the single-phase oscillation. The coupled single-phase circuit consists of three sigle-phase circuits and connecting resistors $\bar{R}_v$. In a steady state, the coupled single-phase circuit for $\bar{R}_v = 0$ is equivalent to the three-phase circuit shown in Fig.2.1. As increasing the parameter $\bar{R}_v$, the strength of the coupling becomes weak. Eventually, for $\bar{R}_v = \infty$ the circuit is decomposed into three independent single-phase circuits which are two dimensional systems.

We have the following circuit equations with the scaling factors in Eq.(2.4).

$$\frac{d}{d\tau}\begin{bmatrix} \bar{\boldsymbol{\Psi}} \\ \bar{\boldsymbol{U}} \end{bmatrix} = \bar{\boldsymbol{f}}(\bar{\boldsymbol{\Psi}}, \bar{\boldsymbol{U}}, \tau) \tag{4.5}$$

$$\triangleq \begin{bmatrix} \bar{\boldsymbol{E}}(\tau) - \bar{\boldsymbol{U}} - (\bar{\xi} + \bar{\zeta})\bar{\boldsymbol{I}}(\bar{\boldsymbol{\Psi}}) + \frac{\mu}{3}\mathbf{B}(\bar{\xi}\bar{\boldsymbol{I}}(\bar{\boldsymbol{\Psi}}) + \bar{\boldsymbol{U}}) \\ \bar{\eta}\bar{\boldsymbol{I}}(\bar{\boldsymbol{\Psi}}) - \frac{\mu}{3}\frac{\bar{\eta}}{\bar{\xi}}\mathbf{B}(\bar{\xi}\bar{\boldsymbol{I}}(\bar{\boldsymbol{\Psi}}) + \bar{\boldsymbol{U}}) \end{bmatrix} \tag{4.6}$$

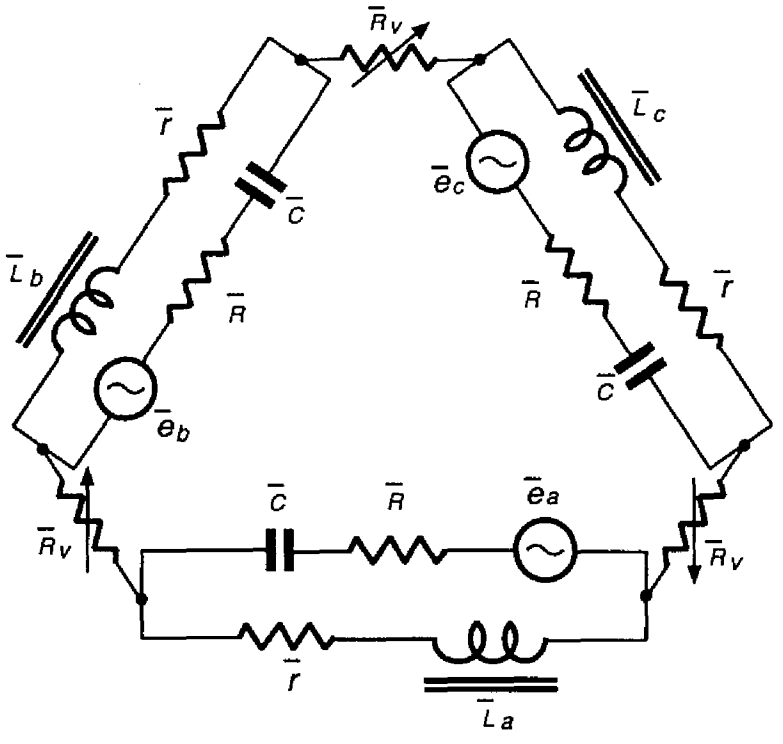

Fig. 4.8: Coupled single-phase circuit.

where,

$$\begin{aligned} \bar{\boldsymbol{\Psi}} &= (\bar{\Psi}_a, \bar{\Psi}_b, \bar{\Psi}_c)' \triangleq \omega \alpha_v \bar{\boldsymbol{\phi}}, \\ \bar{\mathbf{U}} &= (\bar{U}_a, \bar{U}_b, \bar{U}_c)' \triangleq \alpha_v \bar{\boldsymbol{v}}, \end{aligned}$$

and

$$\bar{\xi} = \bar{R}\frac{\alpha_i}{\alpha_v}, \qquad \bar{\zeta} = \bar{r}\frac{\alpha_i}{\alpha_v}, \qquad \bar{\eta} = \frac{1}{\omega \bar{C}}\frac{\alpha_i}{\alpha_v}, \qquad \mu = \frac{1}{1 + \dfrac{\bar{R}_v}{\bar{R}}},$$

$$\mathbf{B} = \begin{pmatrix} 1 & 1 & 1 \\ 1 & 1 & 1 \\ 1 & 1 & 1 \end{pmatrix}.$$

The vectors $\bar{\boldsymbol{\phi}}$ and $\bar{\boldsymbol{v}}$ are the flux-interlinkage and capacitor voltage vectors, respectively. The parameter $\bar{R}_v$ is the resistance of resistor which connects single-phase circuits. The

vector of three-phase voltage source is given by

$$\begin{aligned}\bar{\mathbf{E}}(\tau) &= \alpha_v \bar{e}(\tau) \\ &= \left(E_m \sin(\tau),\ E_m \sin(\tau - \frac{2\pi}{3}),\ E_m \sin(\tau + \frac{2\pi}{3})\right)'.\end{aligned}$$

The vector-valued function $\bar{\boldsymbol{I}}(\bar{\boldsymbol{\Psi}})$ represents the magnetizing characteristics of nonlinear inductors given by

$$\bar{\boldsymbol{I}}(\bar{\boldsymbol{\Psi}}) = (\bar{I}(\bar{\Psi}_a), \bar{I}(\bar{\Psi}_b), \bar{I}(\bar{\Psi}_c))'.$$

Relations between the parameters in the three-phase circuit and those in the coupled single-phase circuit are given by

$$\bar{e} = \mathbf{A}e, \qquad \bar{R} = 3R, \qquad \bar{\tau} = \tau, \qquad \bar{C} = \frac{C}{3}, \qquad \bar{\boldsymbol{I}}(\cdot) = \boldsymbol{I}(\cdot). \tag{4.7}$$

In Eq.(4.6), the parameter $\mu (0 \leq \mu \leq 1)$ represents the coupling coefficient. Setting the parameter $\mu = 1$ ($\bar{R}_v = 0$) and $\bar{U}_a + \bar{U}_b + \bar{U}_c = 0$, we obtain the equation equivalent to the three-phase circuit equation. The relation of the state variables is

$$\left.\begin{aligned}\bar{\boldsymbol{\Psi}} &= \boldsymbol{\Psi} \\ \bar{\boldsymbol{U}} &= \frac{1}{3}\begin{pmatrix} 1 & 4 & -2 \\ -2 & 1 & 4 \\ 4 & -2 & 1 \end{pmatrix}\boldsymbol{U}\end{aligned}\right\}. \tag{4.8}$$

At $\mu = 0$ ($\bar{R}_v \to \infty$), the circuit is decomposed into three independent single-phase circuits. In this article, we call one of them a single-phase circuit.

4.5.2 Transition of Solution Curve

Applying the general homotopy method, we obtain the periodic solution curve on E_m-Ψ_a plane. When the coupling coefficient μ is decreased from 1 to 0, the periodic solution curves is shown in Fig.4.9.

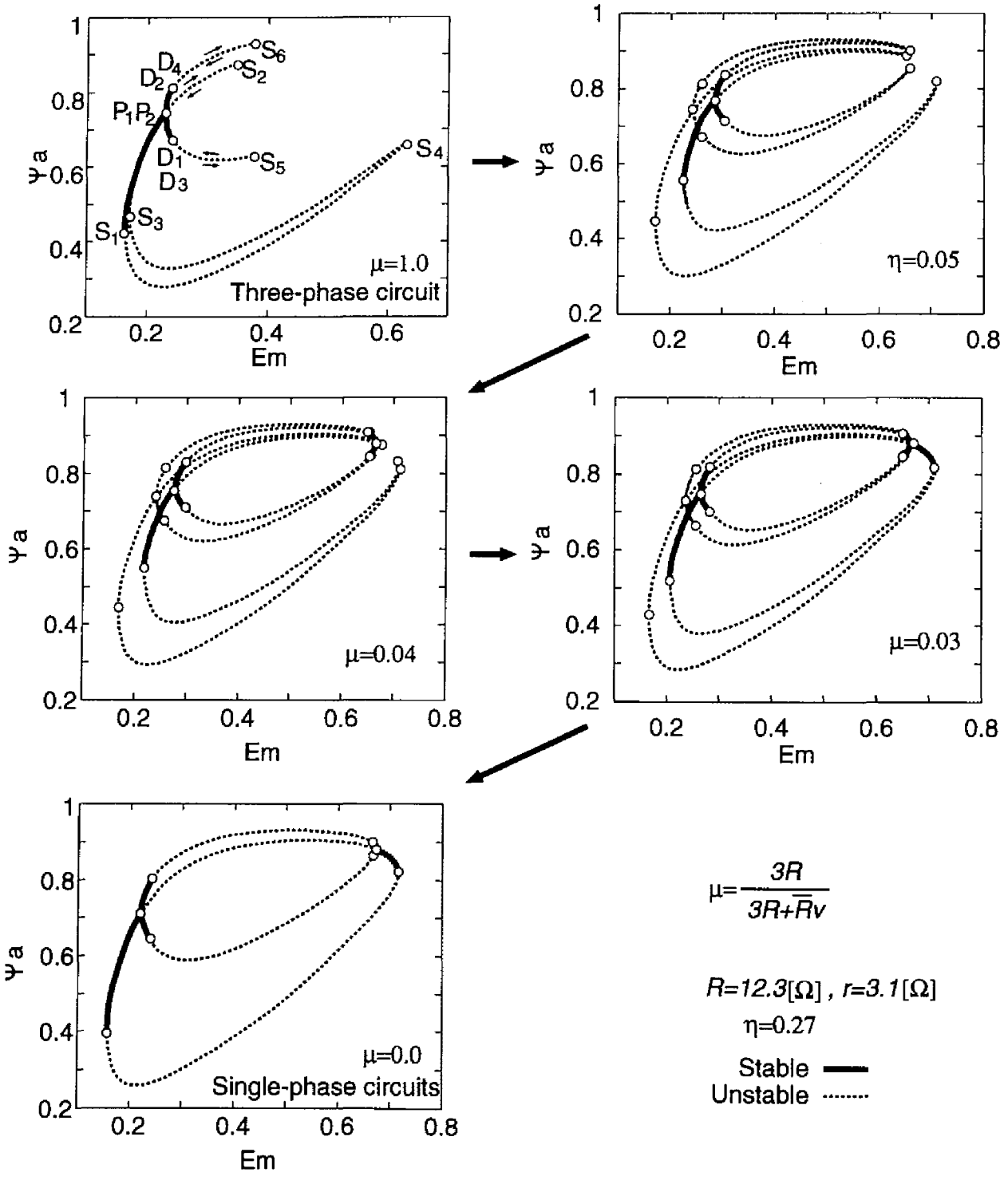

Fig. 4.9: Transition of solution curves from three-phase to single-phase circuit.

At the coupling coefficient $\mu = 1$, the solution curve is equal to that of the three-phase circuit. As decreasing the parameter μ, the folding back points shift to the larger amplitude of E_m ($\mu = 0.05$). Then, pitchfork bifurcations and stable region appear in the higher part of the amplitude E_m ($\mu = 0.04$). Furthermore, the solution curve is divided into two disconnected solution curves one of which contains stable solutions and the other don't contain ($\mu = 0.03$). Eventually, at the coupling coefficient $\mu = 0$ (three independent single-phase circuits), the divided two solution curves overlap each other. One of the solution curves contains the region of stable solutions and is similar to the solution curve in the single-phase-like circuit shown in Fig.4.5. On the other hand, the other solution curve consists of unstable solutions whose degrees of unstability σ are one degree larger than those of the above curve on every point.

At the coupling coefficient $\mu = 0$, the solution curve containing stable solutions corresponds to three single-phase circuits; the solution of one circuit is stable 1/3-subharmonic and the solutions of the other two circuits are fundamental harmonic solutions. In other words, those are M_1 solution in the three sigle-phase circuit and the solution curve is very similar to the solution curve in single-phase-like circuit. On the other hand, the other curve corresponds to three single-phase circuits; the solution of one circuit is stable 1/3-subharmonic, that of another circuit is unstable 1/3-subharmonic and that of the other is fundamental harmonic solution. In other words, those are M_2 solution in the three single-phase circuit. Thus, it becomes apparent that the folded back structure of the solution curve in Fig.4.2 consists of the solution curves of M_1 and M_2 modes in the three single-phase circuits.

4.6 Bifurcation Set

Applying the general homotopy which are described in the section 2.9, we obtain the bifurcation sets. As for the M_1 oscillations in the three-phase circuit, the bifurcation sets on E_m-η plane are shown in Fig.4.10, where the parameter η represents the susceptance of the capacitors and S_i, P_i, D_i ($i = 1, 2, \cdots$) represents the sets of bifurcation points $\dot{S}_i$, $\dot{P}_i$, $\dot{D}_i$, respectively. The bifurcation sets P_1 and P_2 and the bifurcation sets D_1 and D_2 almost overlap mutually, respectively. On the other hand, as for the 1/3-subharmonic oscillations in the single-phase circuit, the bifurcation sets on E_m-η plane are shown in Fig.4.11, where $\hat{S}_i$, $\hat{P}_i$, $\hat{D}_i$ represents the sets of bifurcation points $\dot{\hat{S}}_i$, $\dot{\hat{P}}_i$, $\dot{\hat{D}}_i$, respectively.

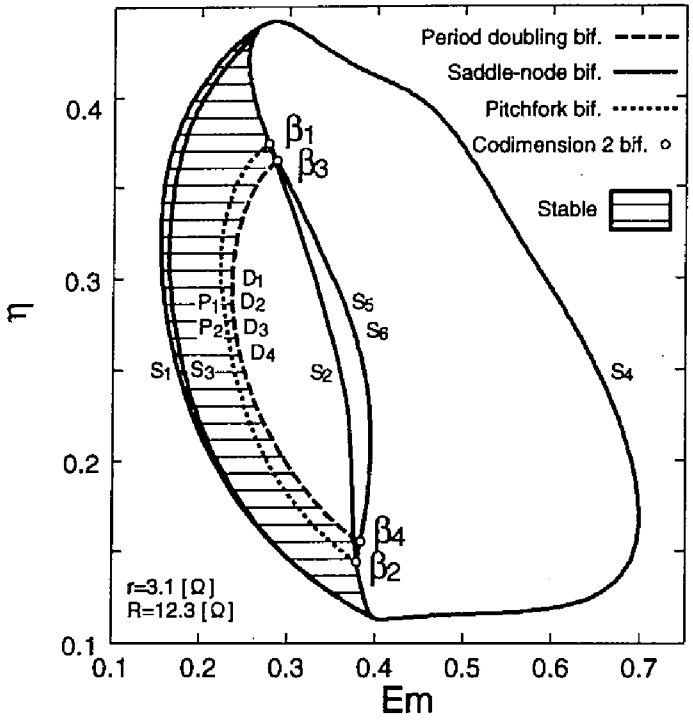

Fig. 4.10: Bifurcation sets of 1/3-subharmonic M_1 oscillations in three-phase circuit.

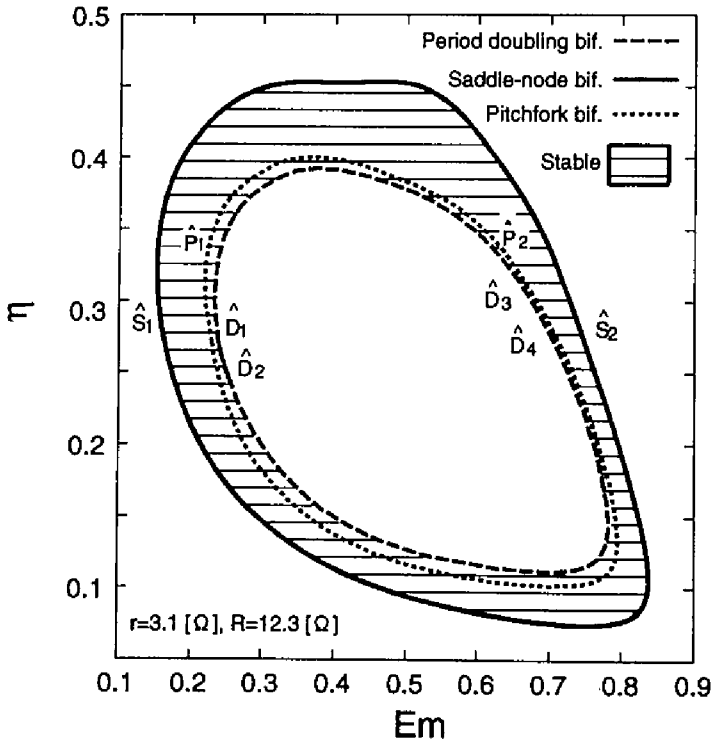

Fig. 4.11: Bifurcation sets of 1/3-subharmonic oscillations in single-phase-like circuit.

In the case of the single-phase-like circuit, the region of stable 1/3-subharmonic oscillations is annular. That is, from outside the structure of the annulus is saddle-node, pitchfork and period doubling bifurcation sets. As a result, there exists stable region in the higher amplitude of the source line-voltage E_m. On the other hand, in the case of the three-phase circuit, the region of the stable M_1 oscillations is restricted in the lower amplitude of E_m. It is caused by the folding back of the periodic solution curve. And the folding back also brings co-dimension two bifurcations $\{\beta_1, \beta_2\} = P_1 \cap S_2 \cap S_5$, $\{\beta_3, \beta_4\} = D_1 \cap S_5$.

4.7 Experimental Results

We choose the same circuit parameters that is denoted in section 4.2.1. That is, the series resistance $R = 12.3\Omega$, the delta-connected resistance $r = 3.1\Omega$ and the susceptance $X_c = 27.2\Omega$ ($C = 97.5\mu F$). When we increase the amplitude of source line-voltage E_Δ, the frequency spectra of active inductor currents of M_1 oscillations are shown in Fig. 4.12. At the lower amplitude of source line-voltage E_Δ, the components 20, 60, 100 Hz which are odd harmonics of order 1/3 can be seen. Increasing E_Δ, we can see the generation of components 40, 80 Hz, that is, even harmonics of order 1/3. Furthermore, at $E_\Delta \simeq 32V$, we can see the generation of 30, 50,$\cdots$ Hz and 25, 35, $\cdots$ Hz. Then after the generation of many frequency components, the M_1 mode comes to a chaotic oscillation. In the chaotic region we can confirm a window of period-3.

The waveforms of inductor currents and capacitor voltages of M_1 by the experiment are shown in Fig.4.13. Fig.4.13(a) shows the M_1 oscillation which contains only the odd harmonics of order 1/3. Here, the topmost figure E_a shows the source line-voltage between phase-b and phase-c which is fundamental harmonic. The v_a, v_b, v_c shows the waveforms of capacitor voltages and I_a, I_b, I_c shows the waveforms of inductor currents. Fig.4.13(b) shows the M_1 oscillations which contains the even harmonics of order 1/3. We can confirm the effects of even harmonics from the waveform of I_a. Fig.4.13(c) shows the chaotic M_1 oscillations. We can confirm the waveforms are not periodic.

Comparing the experimental results with the bifurcation diagram Fig.4.2, the generation of even harmonics of order 1/3 represents the pitchfork bifurcation P_1. The generation of components 30, 50, $\cdots$ Hz represents the period doubling bifurcations D_1 and D_2. Further, the generation of components 25, 35, $\cdots$ Hz and other many components represents the period doubling cascade.

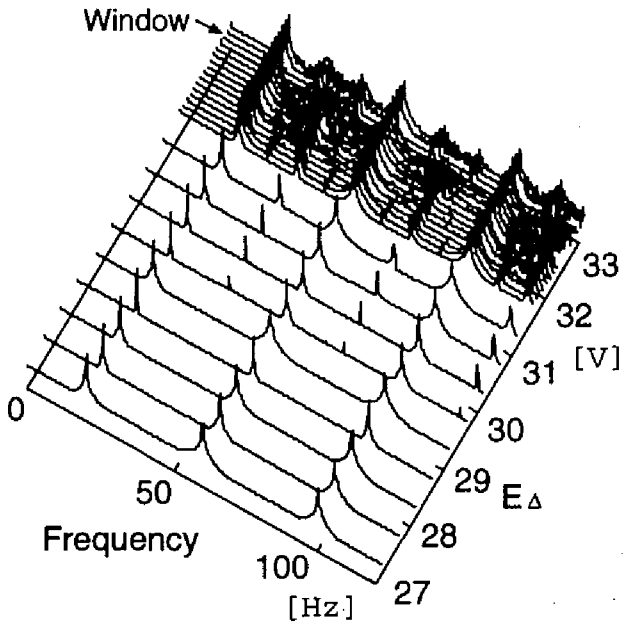

Fig. 4.12: Frequency spectra of active inductor currents.

By varying the source line-voltage E_Δ and the capacitance C, the region of M_1 is obtained by the method shown in section 3.5. In this experiment, the phase angle θ and initial charge of capacitor are chosen every time so that M_1 oscillation may be generated in a wide region. Fig.4.14 shows the bifurcation phenomena of 1/3-subharmonic M_1 oscillation on E_Δ-X_c plane. In the lower part of the susceptance X_c, the region of M_1 oscillation overlaps to that of M_3(Fig.3.11) so that the phase angle θ has to be chosen very delicately. Comparing this figure with the bifurcation diagram Fig.4.10, the generation of the component 40 Hz corresponds to the bifurcation sets P_1 and the generation of the component 30 Hz corresponds to the bifurcation sets D_1 and D_2.

Fig.4.15 shows the bifurcation phenomena of 1/3-subharmonic oscillations in the single-phase-like circuit. In the higher part of source line-voltage E_Δ and susceptance X_c, the 1/3-subharmonic oscillations can not be observed by the harmonic resonance. The structure of bifurcation phenomena is annular and it agrees fairly well with Fig.4.11. Comparing with the three-phase circuit and single-phase-like circuit, in the higher amplitude of E_Δ, there

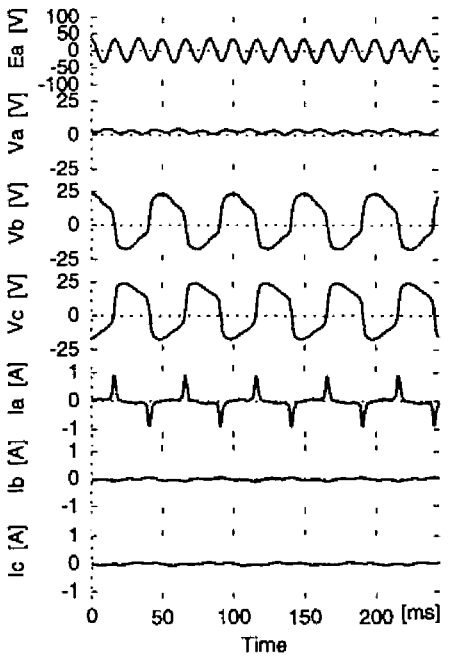

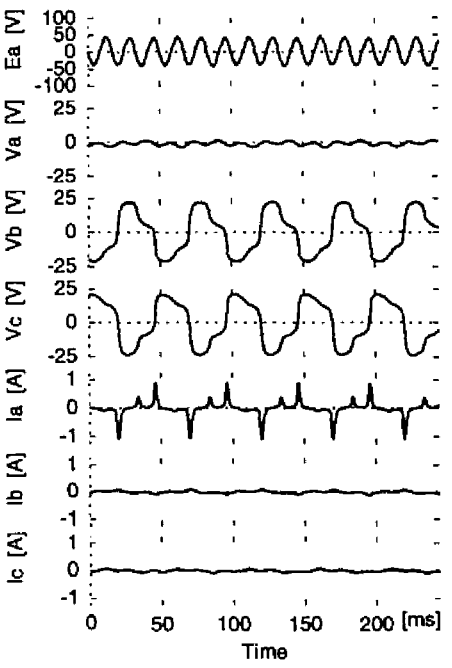

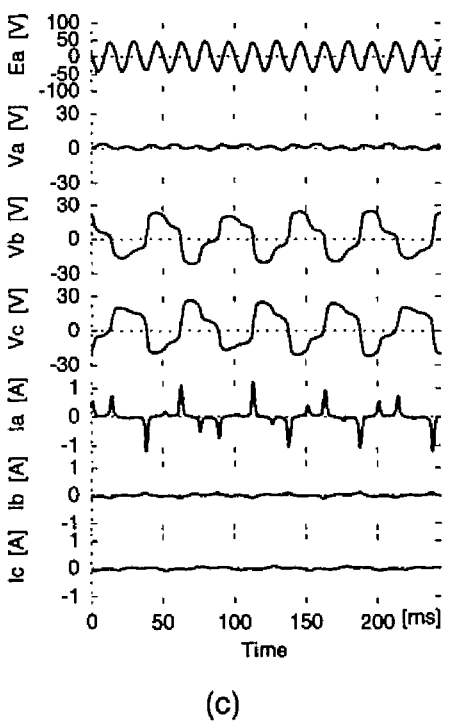

(a) Periodic oscillation (symmetric)
E_Δ=25.0[V], C=97.5[μF],
R=12.3[Ω], r=3.1[Ω]

(b) Periodic oscillation (unsymmetri
E_Δ=30.0[V], C=97.5[μF],
R=12.3[Ω], r=3.1[Ω]

(c) Chaotic oscillation
E_Δ=32.0[V], C=97.5[μF],
R=12.3[Ω], r=3.1[Ω]

Fig. 4.13: Waveforms of M_1 oscillations (experiment).

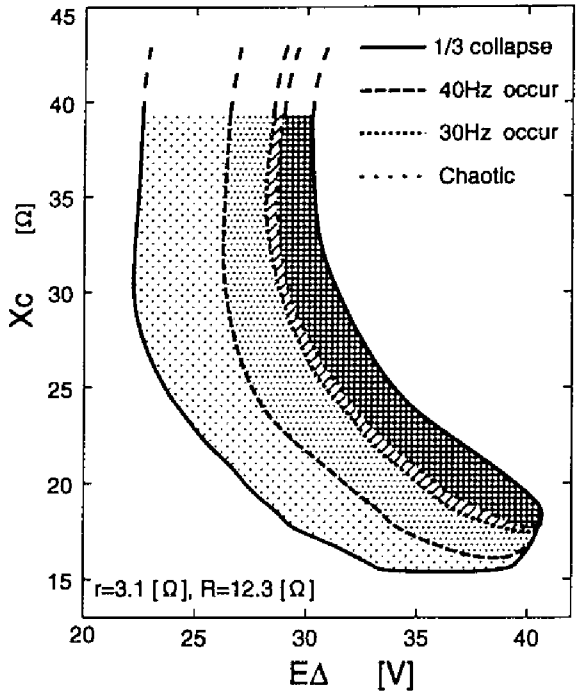

Fig. 4.14: Bifurcation phenomena in three-phase circuit.

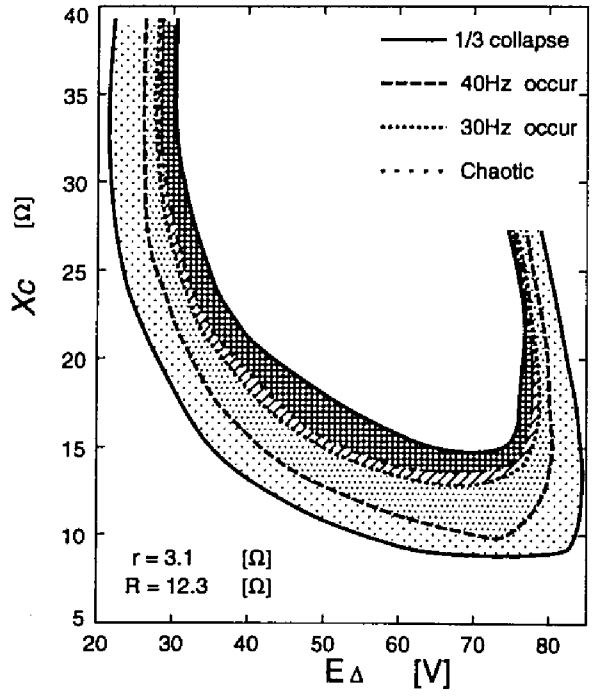

Fig. 4.15: Bifurcation phenomena in single-phase-like circuit.

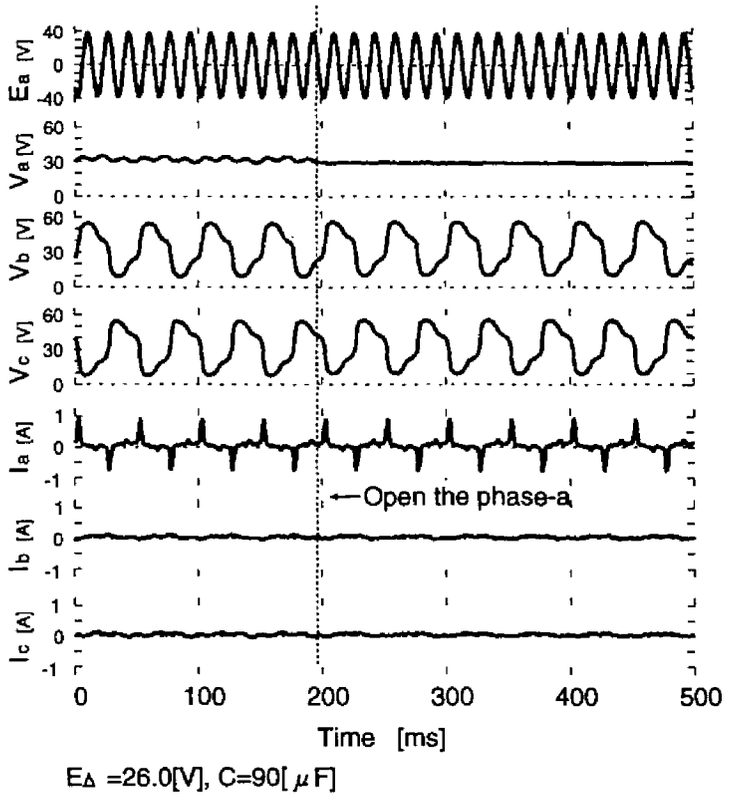

Fig. 4.16: Waveforms of M_1 oscillation when phase-a is cut off.

is a big difference; although M_1 oscillation is not generated in the three-phase circuit, the 1/3-subharmonic oscillation in single-phase-like circuit is generated. On the other hand, the structure of bifurcation phenomena in the lower part of E_Δ is fairly in good agreement.

In order to know if the very weak current of phase-a makes any contribution to the generation of mode M_1, we cut the line of phase-a as shown in Fig.4.16. Then the M_1 oscillation continue and the changes of waveforms are very small. By the experiment we can confirm the similarity of M_1 in the three-phase circuit and 1/3-subharmonic oscillation in the single-phase-like circuit in the lower amplitude of source line-voltage.

As a whole, the experimental results agree fairly well with the analytical one.

4.8 Concluding Remarks

In this section, the bifurcation phenomena of single-phase 1/3-subharmonic oscillations (M_1 mode) in the three-phase circuit is investigated by the homotopy methods and experiments.

For the comparison of the three-phase circuit, the single-phase-like circuit is defined. The results in the single-phase-like circuit reveal that the region of stable 1/3-subharmonic oscillations is annular. From the outside, the structure of the annulus is saddle-node, pitchfork and period doubling bifurcation. Within the period doubling bifurcation set, chaotic attractor appears via period doubling cascade.

Mode M_1 is very similar to 1/3-subharmonic oscillation in single-phase-like circuit with respect to the saddle-node, pitchfork and period doubling bifurcations in the lower amplitude of source voltage. However, the difference between them can be found. The solution curve of M_1 folded back, the stable M_1 doesn't occur in the higher part of source voltage. Moreover, it becomes manifest that the fold brings co-dimension two bifurcations in two-parameter bifurcation diagram.

In order to reveal the relation between M_1 mode and 1/3-subharmonic oscillations in the single-phase circuit, the coupled single-phase circuit is defined. The analyses reveals that the folding back is caused by the coupling of solution curves of stable M_1 oscillations and unstable M_2 oscillations in the three single-phase circuits.

Chapter 5

Two-phase 1/3-Subharmonic Oscillation

5.1 Introduction

In this section, we reveal the bifurcation phenomena of two-phase 1/3-subharmonic oscillations in the three-phase circuit [109]. solution curves and bifurcation sets by homotopy method are analyzed. Next, the comparison with single-phase 1/3-subharmonic oscillation is made. Further the bifurcations in coupled single-phase circuit are analyzed. Finally, experimental results are shown.

5.2 Periodic Solution Curve in Three-phase Circuit

We choose the same circuit parameters that is denoted in section 4.2.1. That is, the series resistance $R = 12.3\Omega$, the delta-connected resistance $r = 3.1\Omega$.

In this section, we pay attention to M_2 oscillations in which the inductors L_a and L_b are active and L_c is not active. By the Newton homotopy method, the periodic solutions of M_2 oscillations are obtained. As for M_2 oscillations which has a symmetry with respect to C_2, the stable region is very small. Hence, we consider unsymmetric oscillations. The inductor current waveforms of the stable oscillation at the source line-voltage $E_m = 0.42$ and the susceptance $\eta = 0.19$ is shown in Fig.5.1. We can confirm that the inductor currents I_a and I_b are large and the inductor current I_c is very small. The waveforms of I_a and I_b are different from each other as regards phase relation and amplitude. The waveform of I_a is similar to that of I_a in M_1 oscillation.

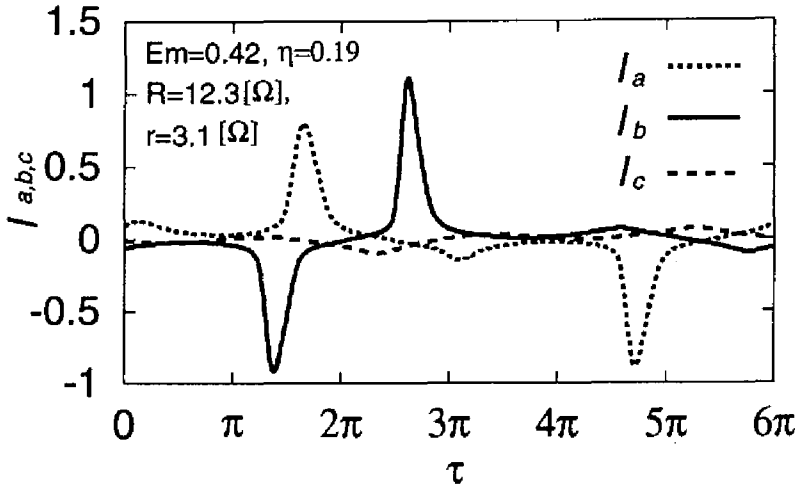

Fig. 5.1: Current waveforms of stable 1/3-subharmonic M_2 oscillation (computation).

Next, applying the general homotopy method, we obtain the periodic solution curve for the susceptance $\eta = 0.125,\ 0.131,\ 0.140,\ 0.145,\ 0.173$. The solution curve on E_m-Ψ_c plane is shown in Fig.5.2. The generated bifurcations are saddle-node bifurcations $S_7 \sim S_{10}$, and Neimark-Sacker bifurcations $N_1 \sim N_4$. A notation, for example, (S, N), shows the portion of the stable solution curve between the bifurcation points denoted in the parenthesis.

For the parameter $\eta = 0.125$, stable and unstable solutions are found accompanied with a couple of saddle-node bifurcations S_7 and S_8. When the parameter η is increased up to 0.131, the stable solution curve (S_7, S_8) splits into two parts (S_7, N_1) and (N_2, S_8) by a couple of Neimark-Sacker bifurcations N_1 and N_2. For the parameter $\eta = 0.140$ the curve (N_2, S_8) of the stable solution curve splits into two parts (N_2, S_9) and (S_{10}, S_8) by a couple of saddle-node bifurcations S_9 and S_{10}. There can be preserved just three portions of stable solution curve. Further, increasing η to 0.145, the curve (S_{10}, S_8) also splits into two parts (S_{10}, N_3) and (N_4, S_8) by a couple of Neimark-Sacker bifurcations N_3 and N_4. Furthermore, for $\eta = 0.173$, we find just two pairs (S_7, N_3) and (N_4, S_8). Thus, the Neimark-Sacker bifurcation occurs on the stable solution curve and splits into two parts.

Next, Fig.5.3 illustrates several bifurcation points of stable M_2 oscillations on E_m-η plane obtained by the general homotopy method. The bifurcations on which stable M_2 oscillation loses its stability, is saddle-node bifurcation $S_7 \sim S_8$, Neimark-Sacker bifurcations $N_1 \sim$

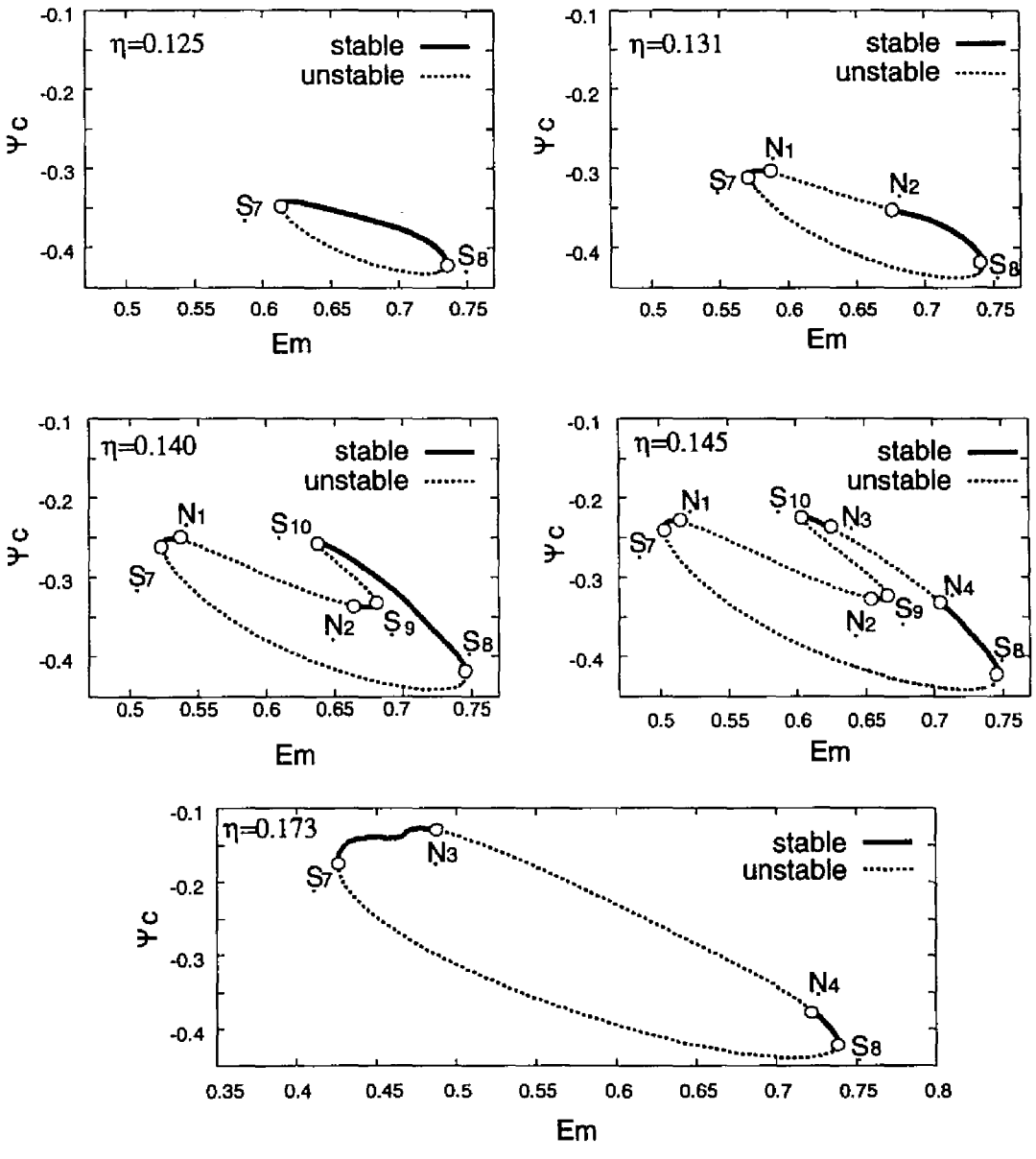

Fig. 5.2: Periodic solution of M_2 oscillation.

N_6, and period doubling bifurcations D_1 and D_2. The regions denoted by A, B and so forth show the region of specified pairs of bifurcation points to be seen when we increase the parameter E_m with η fixed. The orders of bifurcations on the solution curves are also shown in the lower part of the figure. In the region A only a pair of bifurcations S_7-S_8 appears. Increasing the parameter η from the region $A \rightarrow D$, pairs of Neimark-Sacker

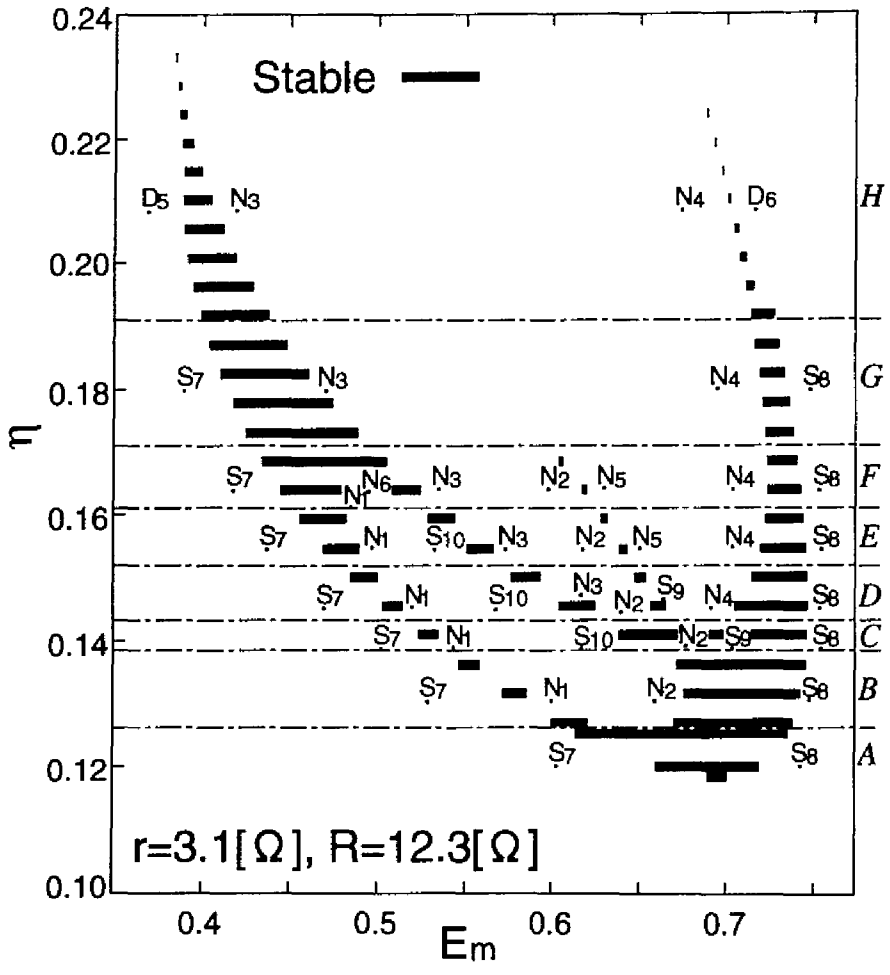

H: $D_5 \rightarrow N_3 \rightarrow N_4 \rightarrow D_6$

G: $S_7 \rightarrow N_3 \rightarrow N_4 \rightarrow S_8$

F: $S_7 \rightarrow N_1 \rightarrow N_2 \rightarrow N_5 \rightarrow N_6 \rightarrow N_3 \rightarrow N_4 \rightarrow S_8$

E: $S_7 \rightarrow N_1 \rightarrow N_2 \rightarrow N_5 \rightarrow S_{10} \rightarrow N_3 \rightarrow N_4 \rightarrow S_8$

D: $S_7 \rightarrow N_1 \rightarrow N_2 \rightarrow S_9 \rightarrow S_{10} \rightarrow N_3 \rightarrow N_4 \rightarrow S_8$

C: $S_7 \rightarrow N_1 \rightarrow N_2 \rightarrow S_9 \rightarrow S_{10} \rightarrow S_8$

B: $S_7 \rightarrow N_1 \rightarrow N_2 \rightarrow S_8$

A: $S_7 \rightarrow S_8$

Fig. 5.3: Bifurcations of stable M_2 oscillations.

bifurcations $\dot{N}_1$-$\dot{N}_2$ and $\dot{N}_3$-$\dot{N}_4$, and saddle-node bifurcations $\dot{S}_9$-$\dot{S}_{10}$ are generated. Further, increasing the η, the stable solutions lose their stability on Neimark-Sacker bifurcations instead of the saddle-node bifurcations in the region $D \to E \to F$. Especially, we can confirm six Neimark-Sacker bifurcations in the region F. Furthermore, the Neimark-Sacker bifurcations disappear in the region G, the saddle-node bifurcation change places with period doubling bifurcations in the region H, and the stable region vanishes by the disappearance of pairs of period doubling and Neimark-Sacker bifurcations.

From the results of the previous chapter, the form of stable region and structure of bifurcations are annular in the case of the 1/3-subharmonic oscillation in the single-phase-like circuit, and folded back annulus in the case of M_1 oscillation in the three-phase circuit. On the other hand, in the case of M_2 oscillation in the three-phase circuit, stable region doesn't exist in higher part of η. Hence, the bifurcation of stable region has U-type structure.

5.3 Bifurcation Set in Three-phase Circuit

5.3.1 Bifurcation Set

Applying the general homotopy method, we obtain the bifurcation sets of mode M_2. The bifurcations sets on E_m-η plane are shown in Fig.5.4, where saddle-node bifurcation sets $S_7 \sim S_{10}$ corresponds to the bifurcation points $\dot{S}_7 \sim \dot{S}_{10}$, Neimark-Sacker bifurcation sets $N_1 \sim N_4$ corresponds to the bifurcation points $\dot{N}_1 \sim \dot{N}_4$, and period doubling bifurcation sets D_5 and D_6 corresponds to bifurcation points $\dot{D}_5$ and $\dot{D}_6$, respectively. In this figure, the $\beta_5 \sim \beta_{10}$ are co-dimension two bifurcations.

The saddle-node bifurcation sets S_7-S_8 and period doubling bifurcation sets D_5-D_6 make loops, respectively. And the co-dimension two bifurcations $\beta_7 = S_7 \cap D_5$ and $\beta_8 = S_8 \cap D_6$ are their intersection points. On the co-dimension two bifurcations β_7, β_8, the eigenvalues Λ of monodromy matrix in section 2.6.1 satisfies $1, -1 \in \Lambda$. The co-dimension two bifurcations $\beta_9 = S_{10} \cap N_6$ and $\beta_{10} = S_9 \cap N_5$ are intersection of Neimark-Sacker and saddle-node bifurcation sets. On those points the eigenvalue set Λ satisfies $1, 1 \in \Lambda$, that is, they are strong 1:1 resonance [27]. The co-dimension two bifurcations $\beta_5 = D_5 \cap N_3$ and $\beta_6 = D_6$ and N_4 are intersection of Neimark-Sacker and period doubling bifurcation sets. On those points the eigenvalue set Λ satisfies $-1, -1 \in \lambda$, that is, they are strong 1:2 resonance.

It becomes manifest that the replacement of bifurcation points and the disappearance

of pairs of period doubling and Neimark-Sacker bifurcations in Fig.5.3 are generated by the co-dimension two bifurcations. In other words, we can say that the U-type bifurcation structure of M_2 oscillations is generated by the co-dimension two bifurcations.

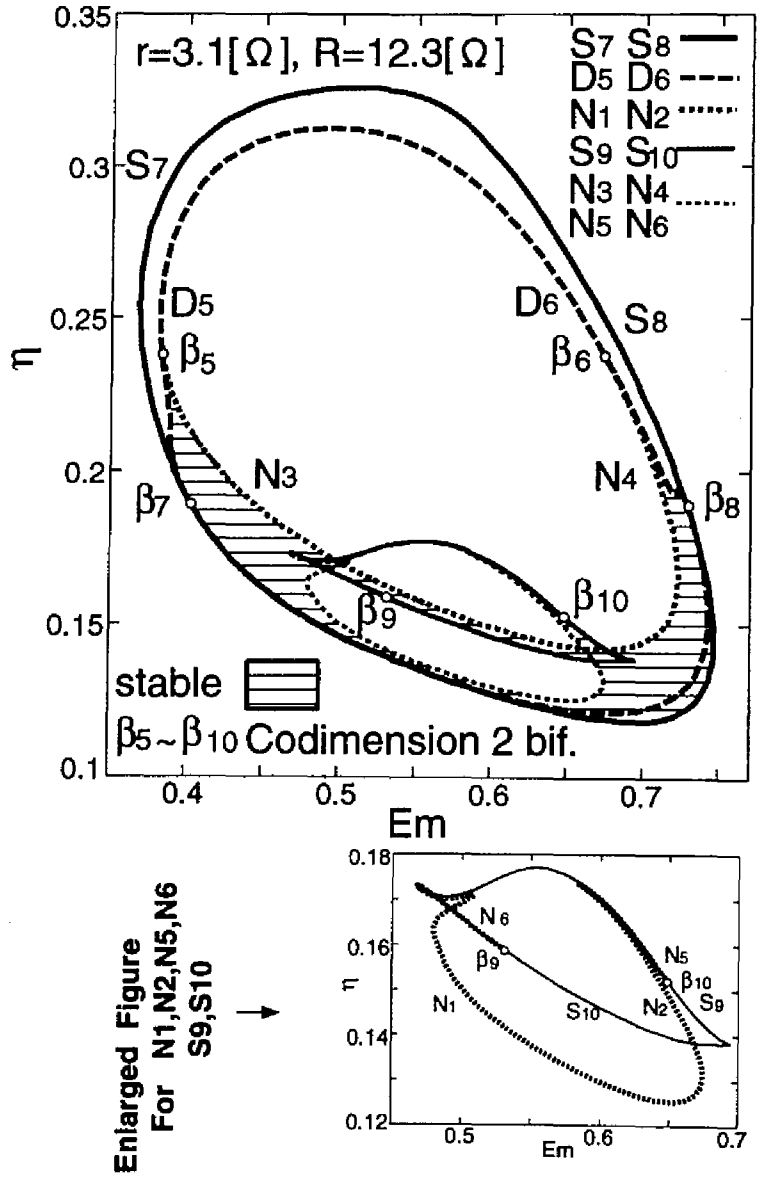

Fig. 5.4: Bifurcation sets of 1/3-subharmonic M_2 oscillations.

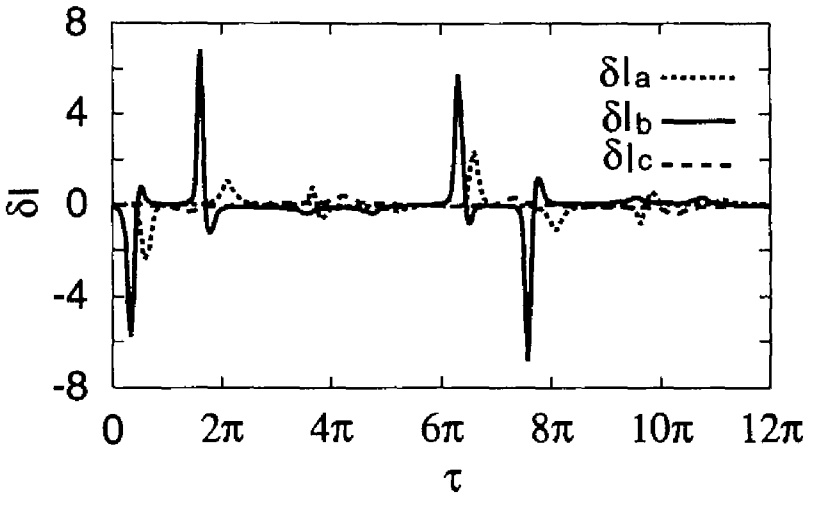

Fig. 5.5: Variational waveforms on center manifold.

5.3.2 Variational Waveforms on Bifurcation Point

The variational waveforms on local center manifold of D_5 ($Em = 0.38, \eta = 0.225$) in the neighborhood of co-dimension two bifurcation β_5 are illustrated in Fig.5.5. The $\delta I_a, \delta I_b, \delta I_c$ are calculated by

$$(\delta I_a, \delta I_b, \delta I_c) \triangleq (\frac{dI_a}{d\Psi_a}\delta\Psi_a, \frac{dI_b}{d\Psi_b}\delta\Psi_b, \frac{dI_c}{d\Psi_c}\delta\Psi_c) \tag{5.1}$$

where $\delta\boldsymbol{\Psi}$ is defined in section 4.2.3. In this figure, the variational current δI_b is larger than others. This peculiarity also can be seen on D_6. That is, the period doubling bifurcations are caused by M_1 oscillation whose δI_b is larger than the others. Thus, the inductor L_b has an effect on the disappearance of the stable region of M_2.

5.4 Comparison with Single-phase 1/3-Subharmonic Oscillation

In order to compare M_2 oscillation with M_1 oscillation, we consider the transition from the single-phase-like to three-phase circuit. That is, we put the variable resistor R_v in the phase-a in the single-phase-like circuit as shown in Fig.5.6 and by decreasing from $R_v = \infty$ to 0, we can transform from the single-phase-like circuit ($R_v = \infty$) to the three-phase circuit ($R_v = 0$).

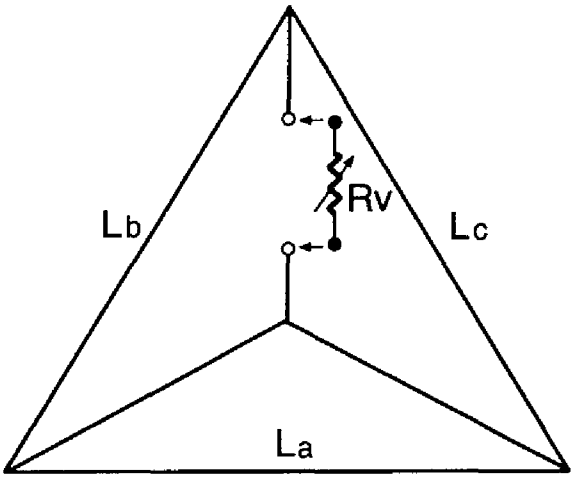

Fig. 5.6: Transition from single-phase-like to three-phase circuit.

The scaled circuit equations are given below;

$$\left.\begin{aligned}
\frac{d\Psi_a}{d\tau} &= E_m \sin(\tau) - U_q - (2\xi+\zeta) I(\Psi_a) + \xi \left\{ I(\frac{\Psi_p+\Psi_q}{2}) + I(\frac{\Psi_p-\Psi_q}{2}) \right\} \\
\frac{d\Psi_p}{d\tau} &= -E_m \sin(\tau) + U_q + 2\xi I(\Psi_a) - (\xi+\zeta) \left\{ I(\frac{\Psi_p+\Psi_q}{2}) + I(\frac{\Psi_p-\Psi_q}{2}) \right\} \\
\frac{dU_a}{d\tau} &= -\eta \left\{ I(\frac{\Psi_p+\Psi_q}{2}) - I(\frac{\Psi_p-\Psi_q}{2}) \right\} \\
\frac{dU_q}{d\tau} &= 2\eta I(\Psi_a) - \eta \left\{ I(\frac{\Psi_p+\Psi_q}{2}) + I(\frac{\Psi_p-\Psi_q}{2}) \right\} \\
\epsilon \frac{d\Psi_q}{d\tau} &= -\xi \left\{ I(\frac{\Psi_p+\Psi_q}{2}) - I(\frac{\Psi_p-\Psi_q}{2}) \right\} \\
&\quad + \epsilon \left[-\sqrt{3} E_m \cos(\tau) + U_a - \zeta \left\{ I(\frac{\Psi_p+\Psi_q}{2}) - I(\frac{\Psi_p-\Psi_q}{2}) \right\} \right]
\end{aligned}\right\} \quad (5.2)$$

where

$$\begin{aligned}
\Psi_p &\triangleq \Psi_b + \Psi_c \\
\Psi_q &\triangleq \Psi_b - \Psi_c \\
U_p &\triangleq U_b + U_c \\
U_q &\triangleq U_b - U_c
\end{aligned} \quad , \qquad \epsilon \triangleq \frac{1}{3 + 2\dfrac{R_v}{R}}.$$

In this equation, setting the parameter ϵ ($0 \leq \epsilon \leq 1/3$) to $\epsilon = 1/3$, the equation represents the three-phase circuit. And setting the parameter $\epsilon = 0$, the equation represents the single-phase-like circuit.

At the susceptance $\eta = 0.19$ the periodic solution curve of Ψ_a on the parameter $\epsilon =$ 0, 0.12, 0.135, 0.143, 0.2, 0.25, and 1/3 is shown in Fig.5.7. The thick and fine line corresponds to the symmetric and unsymmetric solutions with respect to $\mathbf{C}_2$, respectively. The solid line represents stable solutions. The broken line and dotted line represent unstable M_1 solutions in which inductor L_a is active and unstable M_2 solutions in which inductor L_a, L_b are active, respectively. M_2' solutions which are represented by the dash-dotted line is the oscillations in which inductor L_b is especially active. In this figure, only the bifurcations which is described in the following sentences are shown. The prime such as $\dot{\mathrm{D}}_1$ and $\dot{\mathrm{D}}_1'$ shows the mutually symmetric bifurcations with respect to $\mathbf{C}_2$, that is, $\dot{\mathrm{D}}_1'$ corresponds to $\dot{\mathrm{D}}_2$ in Fig.4.2.

Single-phase-like circuit($\epsilon = 0$): The pitchfork bifurcations $\dot{\mathrm{P}}_1$ and $\dot{\mathrm{P}}_3$, and the saddle-node bifurcations $\dot{\mathrm{D}}_1$ and $\dot{\mathrm{D}}_7$ exist. The bifurcations $\dot{\mathrm{P}}_3$ and $\dot{\mathrm{D}}_7$ correspond to the bifurcation $\hat{\dot{\mathrm{P}}}_2$ and $\hat{\dot{\mathrm{D}}}_3$ in Fig.4.5, respectively.

$\epsilon = 0.12$: The solution curve is folded back and M_2 oscillations in which inductors L_a, L_b are active are generated. Additionally, the period doubling bifurcation $\dot{\mathrm{D}}_8$ is generated.

$\epsilon = 0.135$: The solution curve of unsymmetric solution are divided and pitchfork bifurcations $\dot{\mathrm{P}}_2$ and $\dot{\mathrm{P}}_4$, and period doubling bifurcation $\dot{\mathrm{D}}_3$ are generated. The period doubling bifurcation $\dot{\mathrm{D}}_8$ changes to Neimark-Sacker bifurcation $\dot{\mathrm{N}}_3$. Further, the solution curve of M_2' oscillation in which the inductor L_b is especially active appear.

$\epsilon = 0.143$: The solution curve in which M_2' oscillation are included connects to the solution curve of M_2.

$\epsilon = 0.2$: On the solution curve of M_2' pitchfork bifurcations $\dot{\mathrm{P}}_5$ and $\dot{\mathrm{P}}_6$ are generated and unsymmetric solutions in which period doubling bifurcations $\dot{\mathrm{D}}_5$ and $\dot{\mathrm{D}}_6$ can be seen appear. Additionally, the period doubling bifurcation $\dot{\mathrm{D}}_7$ changes to Neimark-Sacker bifurcation $\dot{\mathrm{N}}_4$.

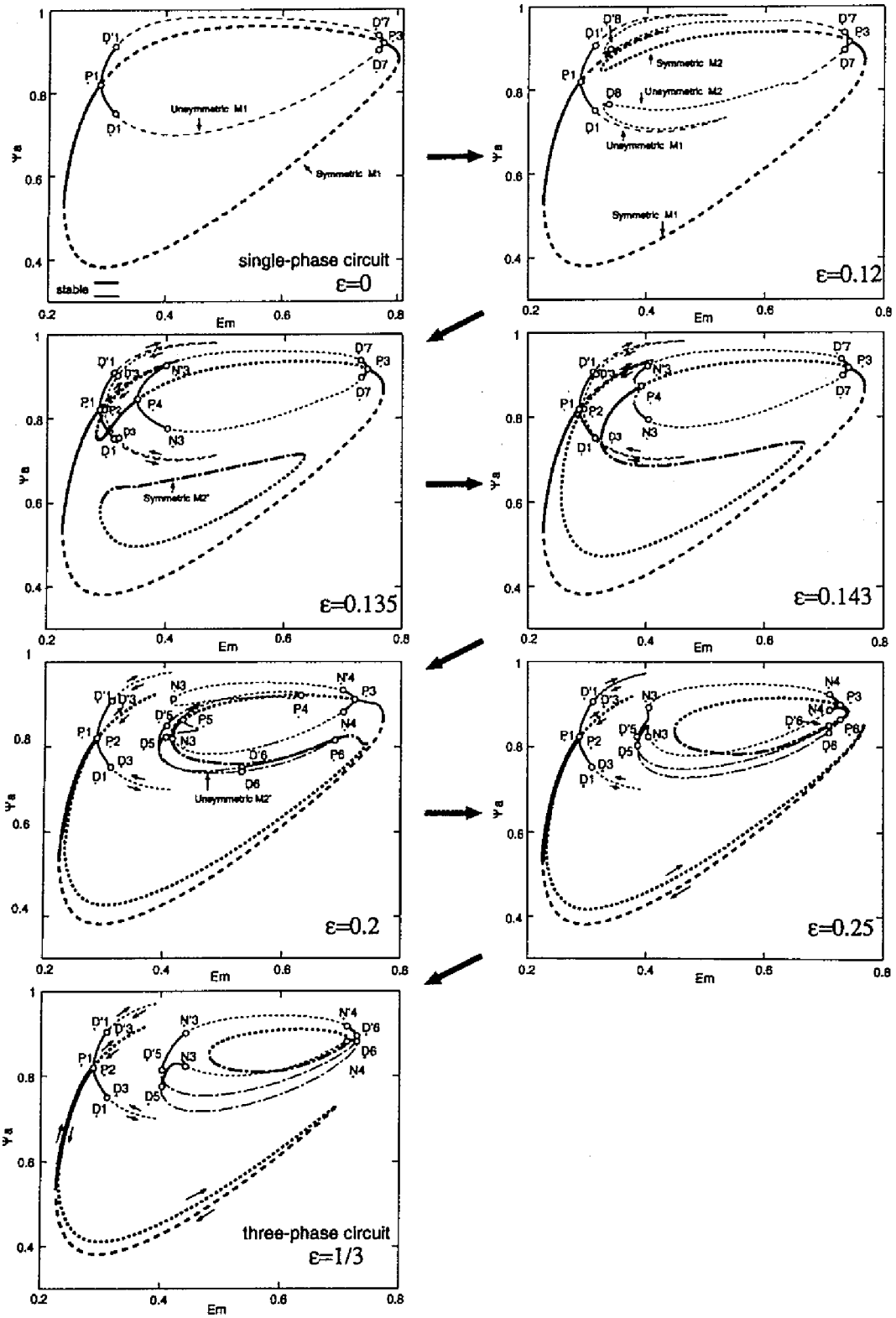

Fig. 5.7: Transition of periodic solutions from single-phase circuit to three-phase circuit.

$\epsilon = 0.25$: The loop of symmetric solutions are divided at $E_m \simeq 0.75$. As a result, the loops which include stable M_2 solution are separated from the loop which includes stable M_1 solutions. Additionally, the solution curves of the unsymmetric M_2 and unsymmetric M_2' connects between $\dot{N}_3$ and $\dot{D}_5$.

Three-phase circuit($\epsilon = 1/3$): The pitchfork bifurcation $\dot{P}_3$ disappears. Simultaneously, two loops of the unsymmetric M_2 solution are separated from the symmetric M_2 solution curve.

Thus, the stable M_1 oscillation is the part which is not affected by the folding back of the solution curve of the 1/3-subharmonic oscillation in the single-phase-like circuit. On the other hand, the stable M_2 oscillation is generated by the connection of the solution curve of M_2' and separation from the solution curve of M_1. That is, the solution curve of M_2 includes both the part which is generated by the activation of inductor L_b on M_1 and the part of M_2' in which the inductor L_b is especially active.

The bifurcation $\dot{D}_5$ and $\dot{D}_6$ which affect the loss of the stable M_2 region are generated in the solution curve of M_2'. Based on the fact and the result of the variational waveform, we can say that the loss of the stability of M_2 are mainly affected by the inductor L_b.

Additionally, Neimark-Sacker bifurcations of M_2 originate in the period doubling bifurcations in single-phase-like circuit ($\dot{D}_8 \rightarrow \dot{N}_3$, $\dot{D}_7 \rightarrow \dot{N}_4$).

5.5 Bifurcations in Coupled Single-phase Circuit

Applying the general homotopy method, we obtain the bifurcation sets in the coupled single-phase circuit. Fig.5.8 illustrates the bifurcation sets on E_m-μ plane at the susceptance $\eta = 0.145$. For this parameter, there exists saddle-node bifurcations $\dot{S}_7 \sim \dot{S}_{10}$, period doubling bifurcations $\dot{D}_5$ and $\dot{D}_6$, and Neimark-Sacker bifurcations $\dot{N}_1 \sim \dot{N}_4$ in the three-phase circuit ($\mu = 1$). On the other hand, the bifurcation diagram in the three single-phase circuits ($\mu = 0$) is similar to that in the single-phase-like circuit shown in Fig.4.5. In the stable solution of the three single-phase circuits, the solutions of two circuits which contain inductor L_a and L_b are stable 1/3-subharmonic solutions and the solution of the other circuit is only fundamental harmonic, that is, M_2 oscillation in the three single-phase circuits.

Thus, it becomes apparent that the M_2 oscillation corresponds to M_2 oscillation in the three single-phase circuits. However, the structure of bifurcations is different between

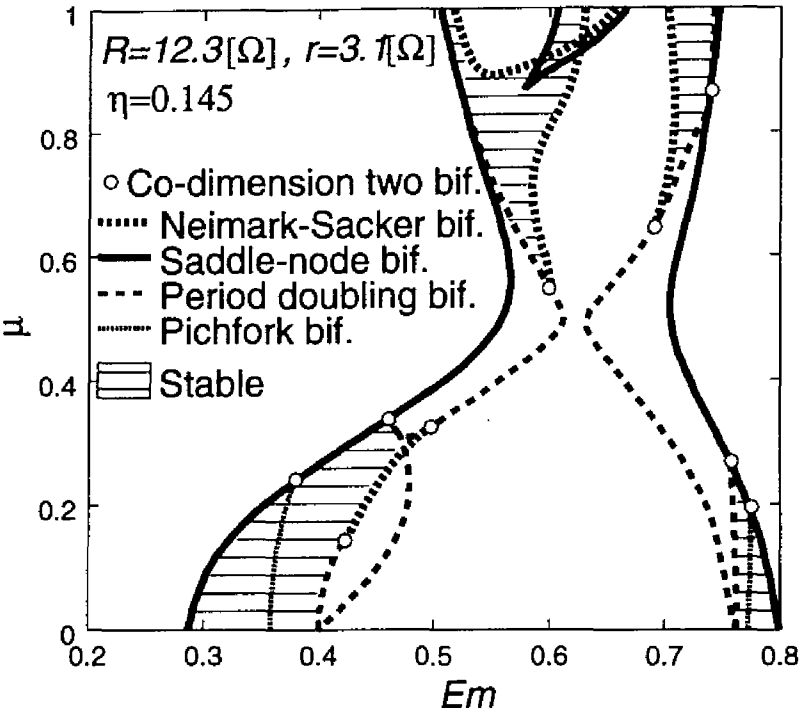

Fig. 5.8: Transition of M_2 oscillation.

the upper and lower side of the coupling coefficient $\mu = 0.5$. Especially, Neimark-Sacker bifurcations are distinctive in the three-phase circuit. N_3 and N_4 are generated by co-dimension two bifurcations of strong 1:2 resonance [27].

5.6 Experimental Results

We fix the series resistance $R = 12.3\Omega$ and the delta-connected resistance $r = 3.1\Omega$ which are chosen in section 5.2. By varying the source line-voltage E_Δ and the capacitance C, the region of M_2 is obtained by the method shown in section 3.5. In this experiment, the phase angle θ and the initial charge of capacitor are chosen so that M_2 oscillation may be generated in a wide region.

Fig. 5.9 shows the bifurcation phenomena of M_2 oscillations on E_Δ-X_c plane. In this figure, the M_2 oscillations are classified into four modes; periodic oscillation, almost periodic oscillation, chaotic oscillation whose attractor doesn't have the origin symmetry and

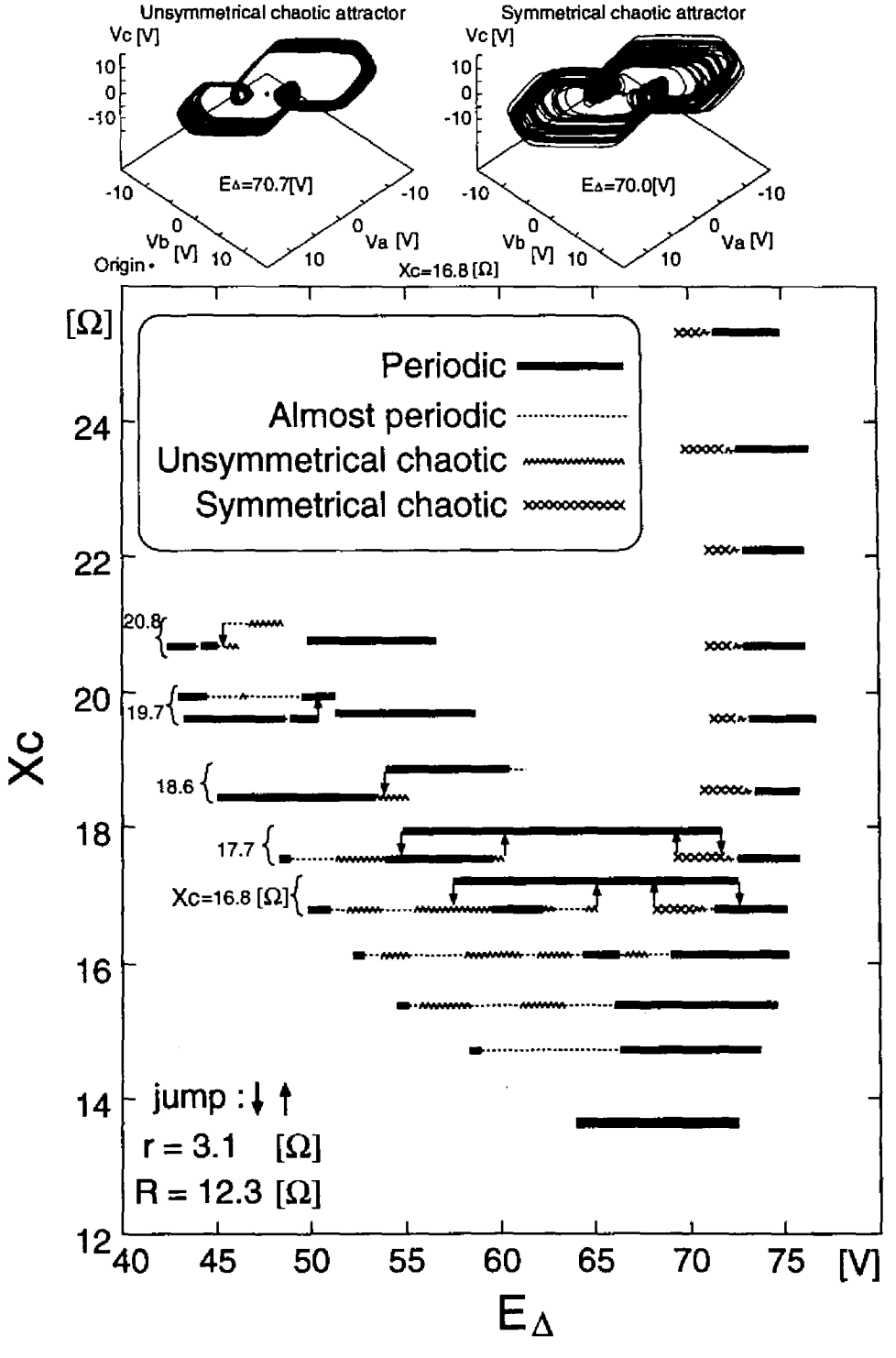

Fig. 5.9: Bifurcation phenomena of 1/3-subharmonic M_2 oscillation.

chaotic oscillation whose attractor has the origin symmetry. The origin symmetry of attractors is equivalent to the symmetry with respect to C_2 symmetry. The example of origin unsymmetric and symmetric attractors are shown in the upper part of the figure. The symmetric attractor is generated by the unification of two unsymmetric attractors. As for almost periodic and periodic oscillations, the trajectory doesn't have origin symmetry in almost every region.

At X_c =16.8, 17.7, 18.6, 19.7, 20.8Ω, jumps occur, then the bifurcation phenomena are shown by the plural lines. That is, the jumps (arrows) in the figure mean that keeping the value $X_c(= 1/\omega C)$ fixed and increasing or decreasing of the line-voltage E_Δ 1/3-subharmonic oscillations bifurcate into another type of 1/3-subharmonic oscillation as indicated arrow heads. The bifurcation structure is so complicated that all bifurcations are not shown in the figure. That is, in the regions of almost periodic oscillations there are small regions of periodic oscillations and in the regions of chaotic oscillations there are small regions of almost periodic and periodic oscillations.

When the X_c is small, M_2 oscillations are periodic ($X_c = 13.6\Omega$). Increasing the parameter X_c, the region of periodic oscillations splits and almost periodic oscillations appear. Next, the region of almost periodic oscillations splits and unsymmetrically chaotic oscillations appear. Further, the region of unsymmetrically chaotic oscillation splits and periodic oscillations, symmetrically chaotic oscillations and jumps appear. Furthermore, unstable region of M_2 oscillations appears between the higher and lower part of the source line-voltage E_Δ. In the region, after it lasts for scores of seconds, M_2 oscillation fades away in a short time. In the lower part of the source line-voltage E_Δ, more complicated bifurcations are generated and in the region where X_c is larger than 20.8Ω stable 1/3-subharmonic oscillations don't exist. On the other hand, in the higher part of the source line-voltage E_Δ, periodic, almost periodic, unsymmetrically chaotic, and symmetrically chaotic oscillations are generated by decreasing E_Δ. The transition of frequency spectrum at $X_c = 19.7\Omega$ is shown in Fig.5.10. At $E_\Delta = 74.0$V M_2 oscillation is periodic and we can confirm even harmonics of order 1/3. At $E_\Delta = 73.0$V several frequency components are generated and the M_2 oscillation becomes almost periodic. At $E_\Delta = 72.7$V many frequency components are generated and M_2 oscillations becomes unsymmetrically chaotic. At $E_\Delta = 72.0$V the frequency components of even harmonics of order 1/3 becomes small and M_2 oscillations becomes symmetrically chaotic.

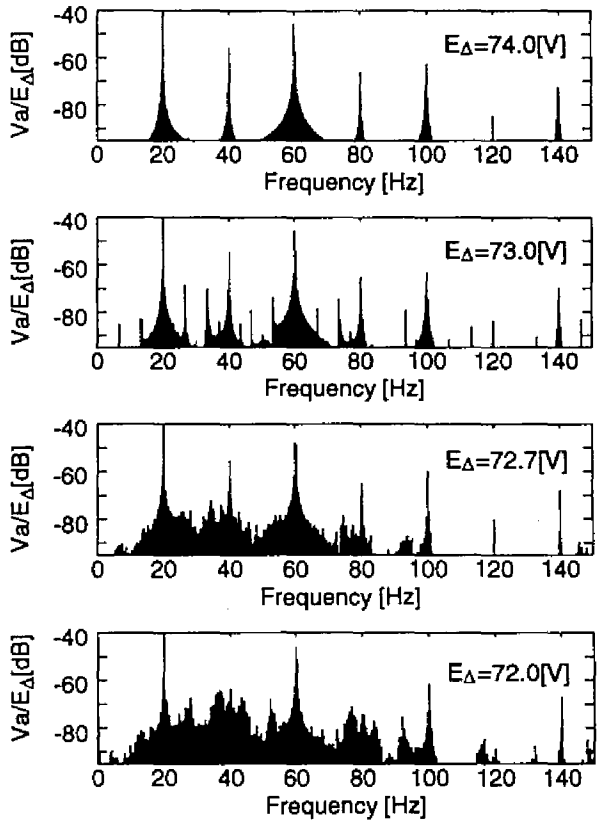

Fig. 5.10: Frequency spectra of capacitor voltage in 1/3-subharmonic M_2 oscillation.

The great difference between Fig.5.9 and Fig.5.4 can be seen in the inside of U-type structure. In Fig.5.9 we can find the stable periodic 1/3-subharmonic oscillation as illustrated by the bold line inside. This difference is possibly due to the small unbalance of the circuit parameters in the real experimental circuit and to neglecting the hysteretic characteristic of the iron cores in the analysis.

The waveforms of inductor currents and capacitor voltages of M_2 by experiments are shown in Fig.5.11. Fig.5.11(a) shows the periodic M_2 oscillation. We can confirm the effects of even harmonics by the waveforms of inductor currents. Fig.5.11(b) shows the almost periodic M_2 oscillation. Fig5.11(c) shows the symmetrically chaotic M_2 oscillation. In this figure the time scale is different from (a) and (b). From the waveforms of capacitor voltages, the oscillation changes two unsymmetric attractors every about 300 [ms].

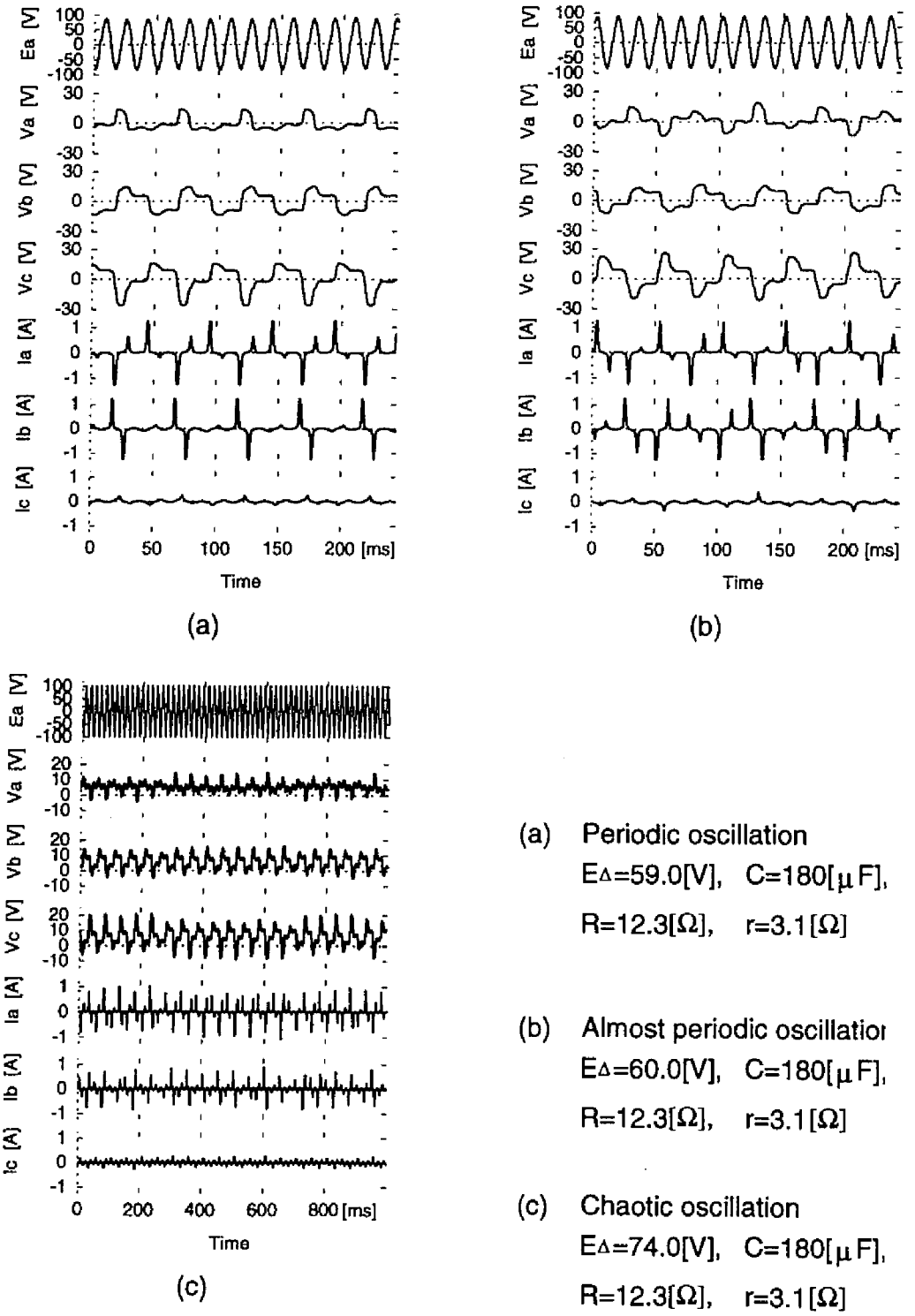

Fig. 5.11: Waveforms of 1/3-subharmonic M_2 oscillations (experiment).

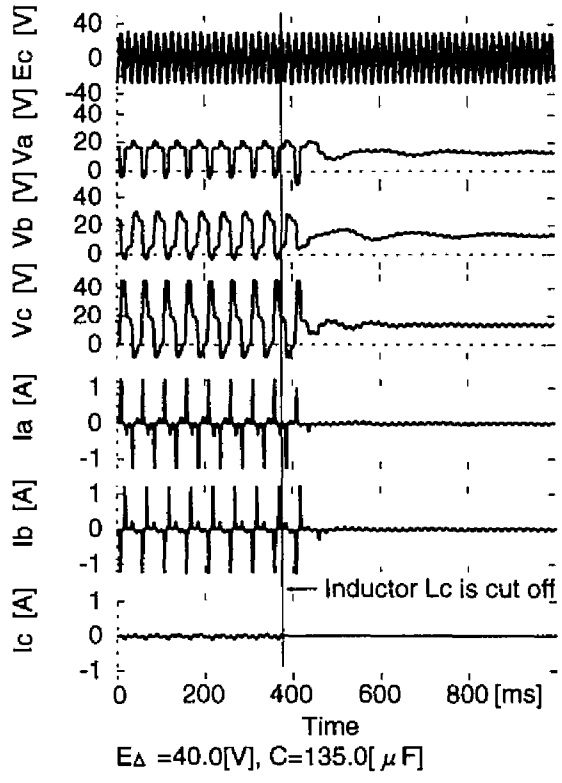

Fig. 5.12: Waveforms of M_2 oscillation when inductor L_c is cut off (experiment).

In mode M_2, one of the three nonlinear inductors is weakly active, that is, the current through the inductor is very small. The inductor, however, contributes much to the generation of mode M_2. This fact is confirmed by the real experiment. While M_2 oscillation continues, the inductor L_c is cut off. Then mode M_2 is faded away and no 1/3-subharmonic oscillation is observed as shown in Fig.5.12. This experimental fact on mode M_2 is quite different from mode M_1 which has already been investigated in section 4.7.

5.7 Concluding Remarks

In this chapter, the bifurcation phenomena of two-phase 1/3-subharmonic oscillations (M_2 mode) in the three-phase circuit are revealed by the homotopy methods and experiments.

The bifurcation phenomena in the region of M_2 is periodic, almost periodic, chaotic oscillation and jumps from outside. Additionally, in the higher region of X_C, M_2 oscillation

becomes unstable. Hence, the bifurcation phenomena of M_2 oscillation is U-type structure. This structure is caused by Neimark-Sacker bifurcation and co-dimension two bifurcation which are generated by the participation of two active inductors.

Further, by the transition from the single-phase-like circuit to the three-phase circuit, the relation between single-phase and two-phase 1/3-subharmonic oscillations becomes manifest. Additionally, the relevancy of bifurcation phenomena in between three-phase and single-phase circuit is revealed by the analysis of the coupled single-phase circuit.

Chapter 6

Symmetric 1/3-Subharmonic Oscillation

6.1 Introduction

In this section, we investigate the symmetric mode of 1/3-subharmonic oscillations in the three-phase circuit. The "symmetric mode" denotes that this mode include symmetric oscillation with respect to C_3. Symmetric modes of 1/3-subharmonic oscillations are classified into two sorts; the oscillations with and without beat. First, we reveal theoretically the generation of symmetrical 1/3-subharmonic oscillations without beat is impossible [114]. Next, the bifurcation of 1/3-subharmonic oscillation with beat is investigated. Then, the relation between the frequency and symmetry is revealed [113]. Further, analysis by means of Lyapnov exponent is made. Finally, the experimental results are shown.

6.2 Pure 1/3-Subharmonic Oscillation

We consider the scaled circuit equation (2.6). First, we define a pure $1/n$-subharmonic solution of Eq.(2.6) which represents a symmetrical periodic $1/n$-subharmonic oscillation without beat in the three-phase circuit.

Definition : Let $[\boldsymbol{\Psi}(\tau), \boldsymbol{U}(\tau)]'$ be a $1/n$-subharmonic solution of Eq.(2.6) with period-n. We call it a ***pure solution***, if the following condition is satisfied:

Condition:

$$\begin{bmatrix} \boldsymbol{\Psi}(\tau) \\ \boldsymbol{U}(\tau) \end{bmatrix} = \mathbf{C}_3 \begin{bmatrix} \boldsymbol{\Psi}(\tau + \frac{2n}{3}\pi) \\ \boldsymbol{U}(\tau + \frac{2n}{3}\pi) \end{bmatrix} \tag{6.1}$$

$$or \qquad \begin{bmatrix} \boldsymbol{\Psi}(\tau) \\ \boldsymbol{U}(\tau) \end{bmatrix} = \mathbf{C}_3^2 \begin{bmatrix} \boldsymbol{\Psi}(\tau + \frac{4n}{3}\pi) \\ \boldsymbol{U}(\tau + \frac{4n}{3}\pi) \end{bmatrix} \tag{6.2}$$

As a necessary condition, we try to show that the right-hand side of either Eq.(6.1) or Eq.(6.2) is also the solution of Eq.(2.6).

Assume that $n = 3k + 1$ $(k = 0, 1, 2, \ldots)$, then

$$\frac{d}{d\tau}\mathbf{C}_3 \begin{bmatrix} \boldsymbol{\Psi}(\tau + \frac{2n}{3}\pi) \\ \boldsymbol{U}(\tau + \frac{2n}{3}\pi) \end{bmatrix} - \boldsymbol{f}\left(\hat{\mathbf{C}}_3\boldsymbol{\Psi}(\tau + \frac{2n}{3}\pi), \hat{\mathbf{C}}_3\boldsymbol{U}(\tau + \frac{2n}{3}\pi), \tau\right)$$

$$= \mathbf{C}_3\frac{d}{d\tau} \begin{bmatrix} \boldsymbol{\Psi}(\tau+\frac{2}{3}\pi+2k\pi) \\ \boldsymbol{U}(\tau+\frac{2}{3}\pi+2k\pi) \end{bmatrix} - \mathbf{C}_3\boldsymbol{f}\left(\boldsymbol{\Psi}(\tau+\frac{2}{3}\pi+2k\pi), \boldsymbol{U}(\tau+\frac{2}{3}\pi+2k\pi), \tau+\frac{2}{3}\pi\right)$$

$$= \mathbf{C}_3\left[\frac{d}{d\tau} \begin{bmatrix} \boldsymbol{\Psi}(\tau+\frac{2}{3}\pi+2k\pi) \\ \boldsymbol{U}(\tau+\frac{2}{3}\pi+2k\pi) \end{bmatrix} - \boldsymbol{f}\left(\boldsymbol{\Psi}(\tau+\frac{2}{3}\pi+2k\pi), \boldsymbol{U}(\tau+\frac{2}{3}\pi+2k\pi), \tau+\frac{2}{3}\pi+2k\pi\right)\right]$$

$$= \mathbf{o}. \tag{6.3}$$

Assume that $n = 3k + 2$ $(k = 0, 1, 2, \ldots)$, then

$$\frac{d}{d\tau}\mathbf{C}_3^2 \begin{bmatrix} \boldsymbol{\Psi}(\tau + \frac{4n}{3}\pi) \\ \boldsymbol{U}(\tau + \frac{4n}{3}\pi) \end{bmatrix} - \boldsymbol{f}\left(\hat{\mathbf{C}}_3^2\boldsymbol{\Psi}(\tau + \frac{4n}{3}\pi), \hat{\mathbf{C}}_3^2\boldsymbol{U}(\tau + \frac{4n}{3}\pi), \tau\right)$$

$$= \mathbf{C}_3^2\frac{d}{d\tau} \begin{bmatrix} \boldsymbol{\Psi}(\tau+\frac{4}{3}\pi+2k\pi) \\ \boldsymbol{U}(\tau+\frac{4}{3}\pi+2k\pi) \end{bmatrix} - \mathbf{C}_3^2\boldsymbol{f}\left(\boldsymbol{\Psi}(\tau+\frac{4}{3}\pi+2k\pi), \boldsymbol{U}(\tau+\frac{4}{3}\pi+2k\pi), \tau+\frac{4}{3}\pi\right)$$

$$= \mathbf{C}_3^2\left[\frac{d}{d\tau} \begin{bmatrix} \boldsymbol{\Psi}(\tau+\frac{4}{3}\pi+2k\pi) \\ \boldsymbol{U}(\tau+\frac{4}{3}\pi+2k\pi) \end{bmatrix} - \boldsymbol{f}\left(\boldsymbol{\Psi}(\tau+\frac{4}{3}\pi+2k\pi), \boldsymbol{U}(\tau+\frac{4}{3}\pi+2k\pi), \tau+\frac{4}{3}\pi+2k\pi\right)\right]$$

$$= \mathbf{o}. \tag{6.4}$$

Thus, if $n = 3k + 1$ and $n = 3k + 2$ then the necessary condition is satisfied. On the other hand, assume that $n = 3k$ $(k = 1, 2, \ldots)$, then the right-hand side of Eq.(6.1) is

$$\begin{aligned}
&\frac{d}{d\tau}\mathbf{C}_3 \begin{bmatrix} \boldsymbol{\Psi}(\tau + \frac{2n}{3}\pi) \\ \boldsymbol{U}(\tau + \frac{2n}{3}\pi) \end{bmatrix} - \boldsymbol{f}\left(\widehat{\mathbf{C}}_3\boldsymbol{\Psi}(\tau + \frac{2n}{3}\pi), \widehat{\mathbf{C}}_3\boldsymbol{U}(\tau + \frac{2n}{3}\pi), \tau\right) \\
&= \mathbf{C}_3\frac{d}{d\tau}\begin{bmatrix} \boldsymbol{\Psi}(\tau + 2k\pi) \\ \boldsymbol{U}(\tau + 2k\pi) \end{bmatrix} - \mathbf{C}_3\boldsymbol{f}\left(\boldsymbol{\Psi}(\tau + 2k\pi), \boldsymbol{U}(\tau + 2k\pi), \tau + \frac{2}{3}\pi\right) \\
&= \mathbf{C}_3\left[\frac{d}{d\tau}\begin{bmatrix}\boldsymbol{\Psi}(\tau + 2k\pi)\\ \boldsymbol{U}(\tau + 2k\pi)\end{bmatrix} - \boldsymbol{f}\left(\boldsymbol{\Psi}(\tau + 2k\pi), \boldsymbol{U}(\tau + 2k\pi), \tau + \frac{2}{3}\pi + 2k\pi\right)\right] \\
&= \mathbf{C}_3\left[\boldsymbol{f}\left(\boldsymbol{\Psi}(\tau + 2k\pi), \boldsymbol{U}(\tau + 2k\pi), \tau + 2k\pi\right)\right. \\
&\qquad\qquad \left. - \boldsymbol{f}\left(\boldsymbol{\Psi}(\tau + 2k\pi), \boldsymbol{U}(\tau + 2k\pi), \tau + \frac{2}{3}\pi + 2k\pi\right)\right] \\
&= \mathbf{C}_3\begin{bmatrix} \boldsymbol{E}(\tau) - \boldsymbol{E}(\tau + \frac{2}{3}\pi) \\ \mathbf{o} \end{bmatrix}
\end{aligned} \tag{6.5}$$

and the right-hand side of Eq.(6.2) is

$$\begin{aligned}
&\frac{d}{d\tau}\mathbf{C}_3^2 \begin{bmatrix} \boldsymbol{\Psi}(\tau + \frac{4n}{3}\pi) \\ \boldsymbol{U}(\tau + \frac{4n}{3}\pi) \end{bmatrix} - \boldsymbol{f}\left(\widehat{\mathbf{C}}_3^2\boldsymbol{\Psi}(\tau + \frac{4n}{3}\pi), \widehat{\mathbf{C}}_3^2\boldsymbol{U}(\tau + \frac{4n}{3}\pi), \tau\right) \\
&= \mathbf{C}_3^2\frac{d}{d\tau}\begin{bmatrix} \boldsymbol{\Psi}(\tau + 4k\pi) \\ \boldsymbol{U}(\tau + 4k\pi) \end{bmatrix} - \mathbf{C}_3^2\boldsymbol{f}\left(\boldsymbol{\Psi}(\tau + 4k\pi), \boldsymbol{U}(\tau + 4k\pi), \tau + \frac{4}{3}\pi\right) \\
&= \mathbf{C}_3^2\left[\frac{d}{d\tau}\begin{bmatrix}\boldsymbol{\Psi}(\tau + 4k\pi)\\ \boldsymbol{U}(\tau + 4k\pi)\end{bmatrix} - \boldsymbol{f}\left(\boldsymbol{\Psi}(\tau + 4k\pi), \boldsymbol{U}(\tau + 4k\pi), \tau + \frac{4}{3}\pi + 4k\pi\right)\right]. \\
&= \mathbf{C}_3^2\left[\boldsymbol{f}\left(\boldsymbol{\Psi}(\tau + 4k\pi), \boldsymbol{U}(\tau + 4k\pi), \tau + 4k\pi\right)\right. \\
&\qquad\qquad \left. - \boldsymbol{f}\left(\boldsymbol{\Psi}(\tau + 4k\pi), \boldsymbol{U}(\tau + 4k\pi), \tau + \frac{4}{3}\pi + 4k\pi\right)\right] \\
&= \mathbf{C}_3^2\begin{bmatrix} \boldsymbol{E}(\tau) - \boldsymbol{E}(\tau + \frac{4}{3}\pi) \\ \mathbf{o} \end{bmatrix}.
\end{aligned} \tag{6.6}$$

Thus, the right-hand sides of Eq.(6.5) and Eq.(6.6) are not identically equal to $\mathbf{o}$. That is,

the right-hand sides of Eq.(6.1) and Eq.(6.2)

$$C_3 \begin{bmatrix} \boldsymbol{\Psi}(\tau + 2k\pi) \\ \boldsymbol{U}(\tau + 2k\pi) \end{bmatrix}, \qquad C_3^2 \begin{bmatrix} \boldsymbol{\Psi}(\tau + 4k\pi) \\ \boldsymbol{U}(\tau + 4k\pi) \end{bmatrix} \tag{6.7}$$

are not the solution of Eq.(2.6). As a result, a pure $1/3k$-subharmonic oscillation ($k = 1, 2, \ldots$) can not be generated in the three-phase circuit. Especially, as for the 1/3-subharmonic oscillation, it becomes apparent that pure M_3 oscillation is impossible.

6.3 1/3-Subharmonic Oscillation with Beat

6.3.1 Periodic Solution Curve

In this section, we consider M_3 oscillations accompanied with beat. We choose the same circuit parameter that is denoted in section 4.2.1. That is, the series resistance $R = 12.3\Omega$ and the delta-connected resistance $r = 3.1\Omega$.

By the Newton homotopy method, the periodic solution of M_3 oscillations are obtained. Fig.6.1 shows the waveforms of inductor currents of the stable period-13 oscillation at the source amplitude $E_m = 0.40$ and the susceptance $\eta = 0.118$. The period-13 oscillation denotes that the period of oscillation is 13 times as long as the period of the voltage source. In the case of period-13 oscillation we integrate over the interval $[0, 26\pi]$ in Eq. (2.33).

From the figure, we can confirm the main frequency of the oscillation is about order 1/3. The oscillation has the symmetry with respect to C_3.

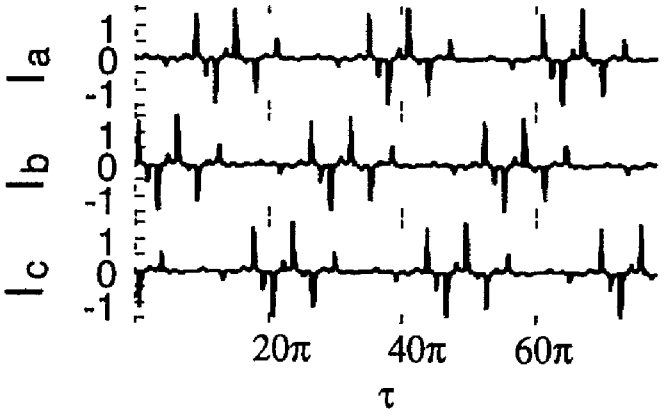

Fig. 6.1: Current waveforms of stable 1/3-subharmonic M_3 oscillation with beat.

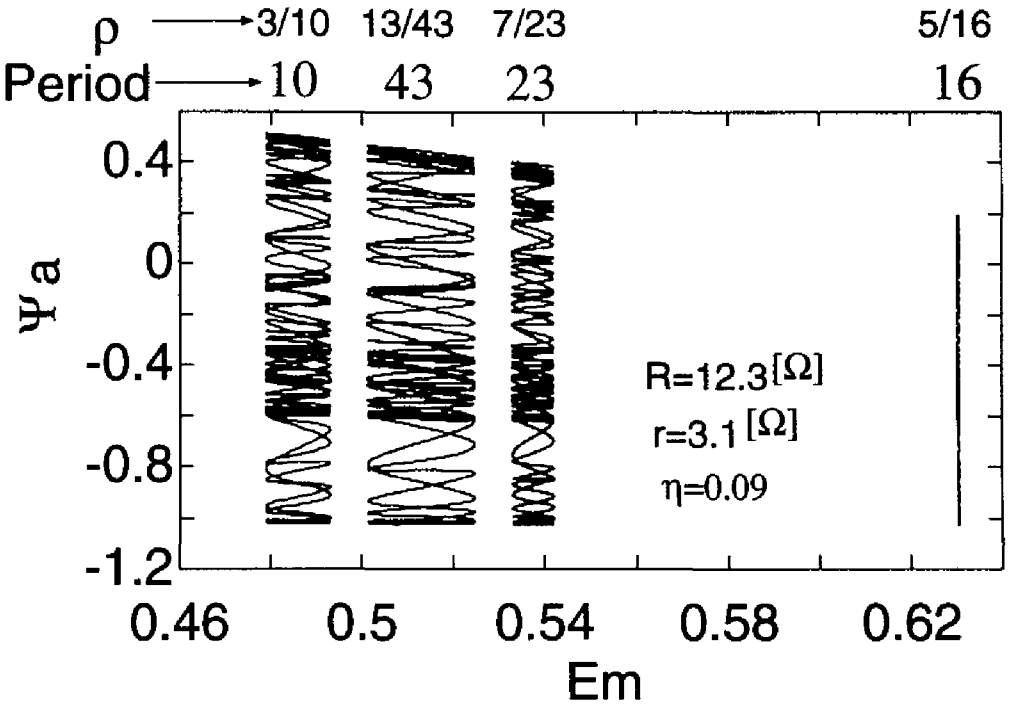

Fig. 6.2: Periodic solution curve of 1/3-subharmonic M_3 oscillations.

Next, applying the general homotopy, we can obtain the periodic solution curves for the susceptance $\eta = 0.09$. The solution curves on E_m-Ψ_a plane is shown in Fig.6.2. In this figure, the solution curves of period 10, 43, 23, 16 are shown. The rotation number ρ is defined below [34]:

$$\rho \triangleq \frac{f_1}{f_2} \tag{6.8}$$

where f_1 is the main frequency of the periodic oscillation and f_2 is the frequency of the voltage sources. As E_m decreased, the rotation number decreases and observed ρ agrees with the subset of the Farey series [34]. Although saddle-node, period doubling, Neimark-Sacker bifurcations are generated on the solution curves, they are not shown in the figure.

The characteristic feature in this figure is the number of equivalent solutions on a solution curve. Here we call solutions equivalent if they can be related by Eqs.(2.15) and (2.24). The number of equivalent solutions contained in the solution curves of period-10 is 60 which can be rewritten as $6n$ where n denotes the period-n. Then, from the results in section 2.3,

the solution of period-10 doesn't have symmetry with respect to C_3 and C_2. On the other hand, in the case of period-43, the number of equivalent solutions is 43 which indicates that the period-43 solutions have symmetry with respect to C_3 and C_2. In the same way, because the numbers of period-23 and period 16 are 69 and 96, the period-23 solutions have symmetry with respect to C_2 and the period-16 solutions doesn't have both symmetries.

Consequently, as for the solution curves in the figure, the number of solutions which are not equivalent is two; the one is stable and the other is unstable. The two sorts of solutions are connected by saddle-node bifurcations in turn. It indicates that the trajectories are on a torus and the periodic oscillations occur by mode lockings [35].

6.3.2 Relation between Frequency and Symmetry

When the solutions are period-q, the rotation number can be represented $\rho = p/q$ where p is a positive integer. Because 1/3-subharmonic oscillations accompanied with beat are 1:3 internal resonance [10], the frequency component $\rho' = (q - 2p)/q$ is also large. Hence the frequency of the beat is represented as $(\rho' - \rho)/2 = (q - 3p)/2q$.

Now, we consider the symmetric period-q 1/3-subharmonic solution with beat with respect to C_3. Assume that the frequency components of $3k/q$ $(k = 1, 2, \ldots)$ of the symmetric 1/3-subharmonic solution with respect to C_3 exists, the phases of the frequency components of the capacitor voltages U_a, U_b and U_c agree each other. Here, $U_a + U_b + U_c = constant$ is satisfied by Eq.(2.30). As a result, the frequency components of $3k/q$ can not be contained in the symmetric 1/3-subharmonic solution with beat. Then as for the symmetry C_3, the following conditions have to be satisfied:

$$\begin{cases} p \neq 3k & k = 1, 2, \cdots \\ q - 2p \neq 3l & l = 1, 2, \cdots. \end{cases} \tag{6.9}$$

The conditions can be rewritten as

$$q - p = 3k \quad k = 1, 2, \cdots. \tag{6.10}$$

Eq.(6.10) is the necessary condition of the symmetric 1/3-subharmonic oscillation accompanied with beat with respect to C_3.

Next, we consider the symmetric period-q 1/3-subharmonic solution with beat with respect to C_2. In the same way, the frequency components of $2k/q$ $(k = 1, 2, \ldots)$ can not be

contained in the symmetric 1/3-subharmonic solution with beat. Then as for the symmetry $\mathbf{C}_2$, the following conditions have to be satisfied:

$$\begin{cases} p \neq 2k & k = 1, 2, \cdots \\ q - 2p \neq 2l & l = 1, 2, \cdots. \end{cases} \tag{6.11}$$

The conditions can be rewritten as

$$q - p = 2k \quad k = 1, 2, \cdots. \tag{6.12}$$

Eq.(6.12) is the necessary condition of the symmetric 1/3-subharmonic oscillation accompanied with beat with respect to $\mathbf{C}_2$.

6.4 Lyapnov Exponent

As the three-phase circuit is a five dimensional system, it has five Lyapnov exponents $\lambda_1 \geq \cdots \geq \lambda_5$ [36, 37]. Fig.6.3 shows the largest and second largest Lyapnov exponents λ_1 and λ_2 of the M_3 oscillation. When the susceptance of the capacitors η is small, a stable period-13 oscillation exists. Increasing η, the oscillation becomes almost periodic by Neimark-Sacker bifurcation at $\eta \simeq 0.115$. Further, at $\eta \simeq 0.12$ the oscillation becomes chaotic. In the region of chaotic oscillations, there exist small regions of periodic and almost periodic oscillations. Furthermore, at $\eta = 0.143$ the oscillation becomes hyperchaotic [34]. In the region of chaotic oscillations, there exist small regions of periodic, almost periodic and chaotic oscillations. The generation of the hyperchaos is special feature in M_3 mode.

6.5 Experimental Results

We fix the series resistance $R = 12.3\Omega$ which is chosen in section 6.3.1. The region of M_3 exists on the outside of M_2 in Fig.3.11. When the capacitances are fixed to $C = 195\mu\mathrm{F}(X_c = 13.6\Omega)$ and the source line-voltage E_Δ is increased, the spectra of capacitor voltage v_a is shown in Fig.6.4. The horizontal axis represents the frequency and the vertical axis represents the amplitude of frequency components of the ratio v_a/E_Δ.

At $E_\Delta = 38.1\mathrm{V}$, the main frequency is 18 Hz which corresponds to the rotation number $\rho = 3/10$. It is a period-10 oscillation and the waveforms of the capacitor voltages and inductor currents are shown in Fig.6.5(a). This oscillation is accompanied with beat and don't have symmetries with respect to $\mathbf{C}_3$ and $\mathbf{C}_2$.

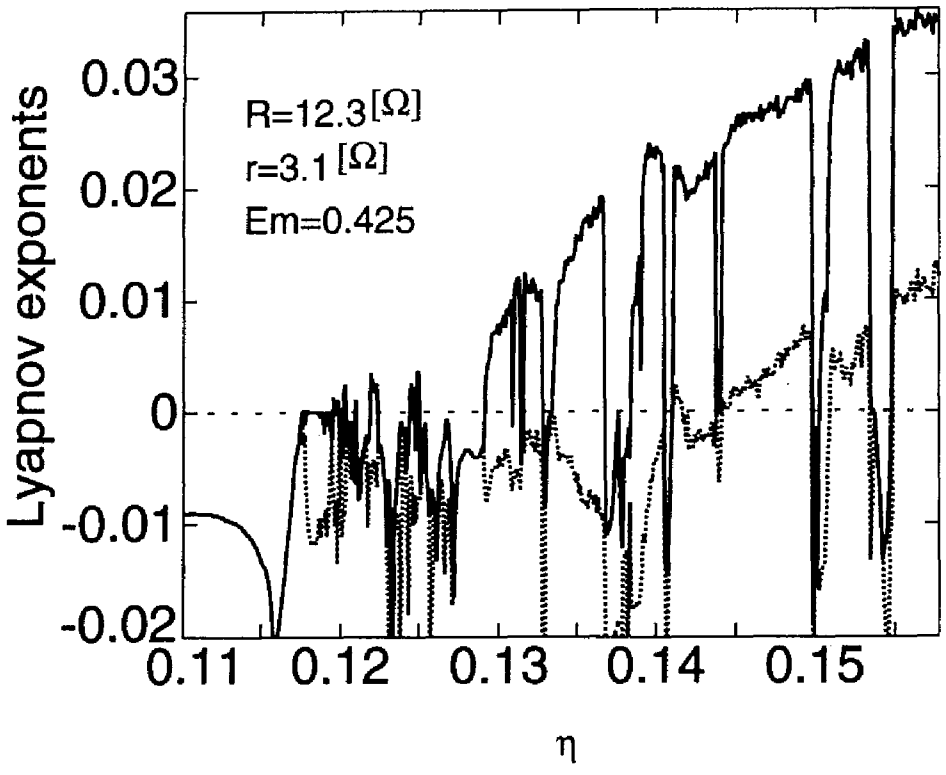

Fig. 6.3: Lyapnov exponents of M_3 oscillation.

Increasing the source line-voltage E_Δ, chaotic oscillations appear (E_Δ = 39.5V) and next period-23 oscillation whose main frequency is 18.26Hz appears (E_Δ = 43.3V). Further increasing E_Δ, the period of beat becomes long gradually and periodic and nonperiodic oscillations appear alternatively. The period-10, 23, 13, 29, 16, 35, 19 oscillations corresponding to the rotation numbers ρ = 3/10 (18Hz), 7/23 (18.26Hz), 4/13 (18.46Hz), 9/29 (18.62Hz), 5/16 (18.75Hz), 11/35 (18.86Hz), 6/19 (18.95Hz) are observed one after another.

When E_Δ is larger than 57.5V, the oscillation becomes chaotic (E_Δ =59.0V) and the component of 40Hz becomes large (E_Δ =62.0, 65.2 V). The waveforms at E_Δ = 62.0V is shown in Fig.6.5(b). The envelope of waveforms is distinctive. The period of beat becomes further long and the M_2 mode occurs consequently. This oscillation has the components of 20, 40 and 60 Hz, and the rotation number ρ is 1/3.

Further increasing E_Δ, M_2 oscillation changes into M_3 oscillation (E_Δ = 69.0V) and the

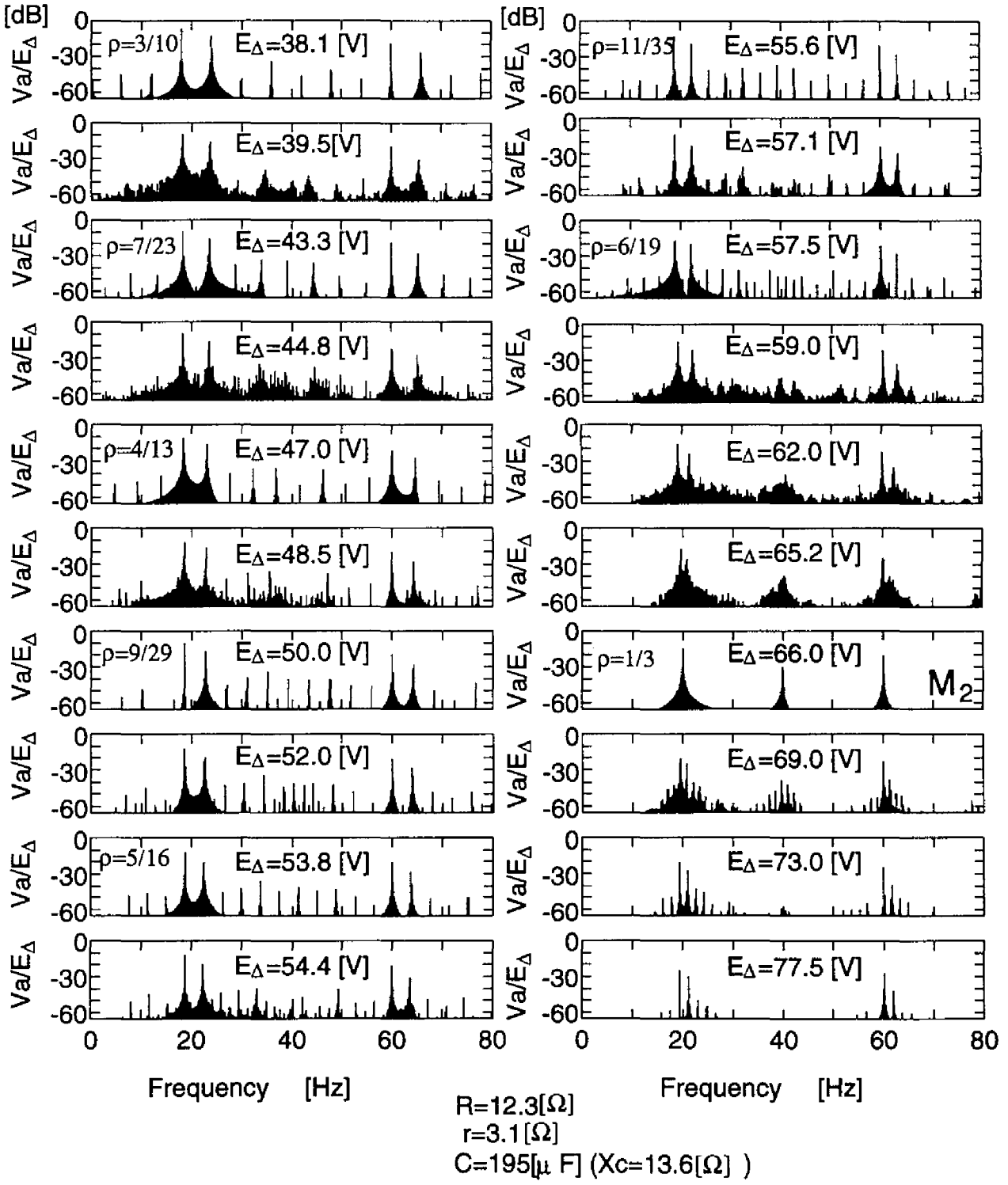

Fig. 6.4: Capacitor voltage spectra of 1/3-subharmonic M_3 oscillations.

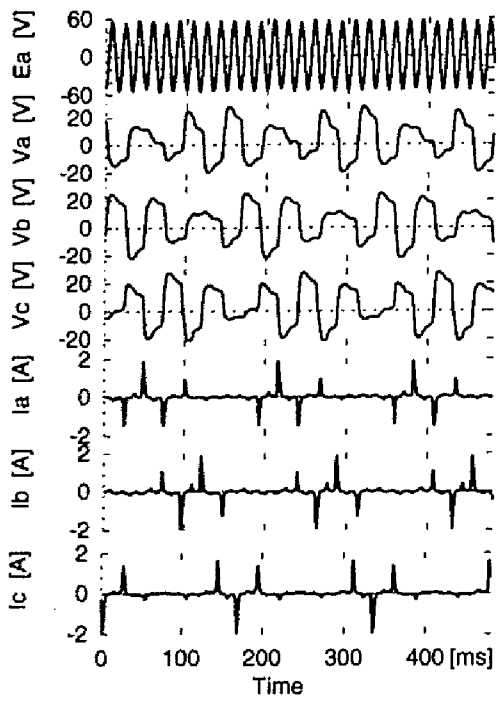

(a)

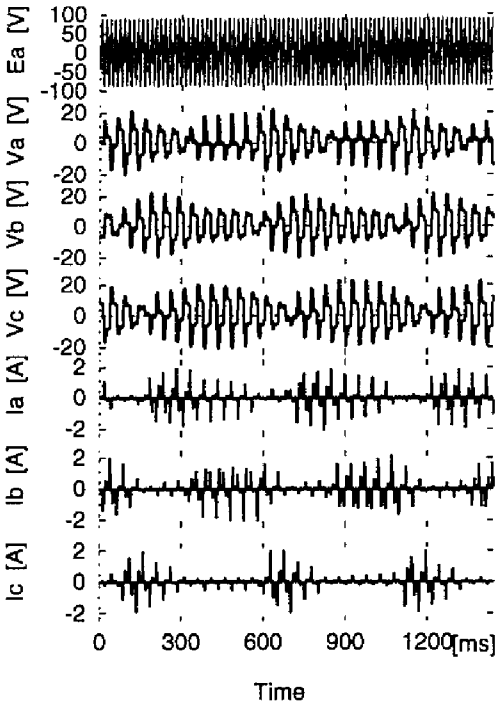

(b)

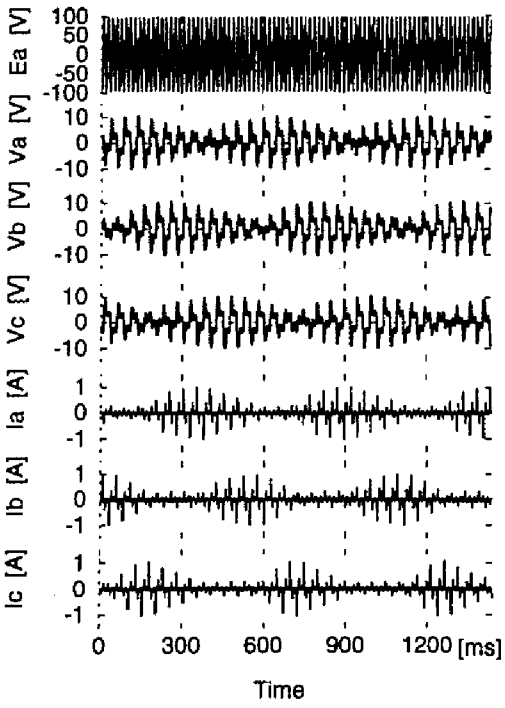

(c)

(a) Periodic mode M_3
E_Δ=38.1[V],C=195[μF],
R=12.3[Ω],r=3.1[Ω]

(b) Chaotic mode M_3
E_Δ=62.0[V], C=195[μF],
R=12.3[Ω],r=3.1[Ω]

(c) Almost periodic mode M_3
E_Δ= 77.5[V], C=195[μF],
R=12.3[Ω],r=3.1[Ω]

Fig. 6.5: Waveforms of 1/3-subharmonic M_3 oscillations (experiment).

component of 40Hz becomes small (E_Δ =73.0, 77.5V). The period of beat becomes short again. The waveforms at E_Δ = 77.5V is shown in Fig.6.5(c). The oscillation seems to be almost periodic.

Thus, the bifurcation of M_3 oscillation is mode locking and unlocking. Increasing the source line-voltage, the period of beat becomes long and M_2 oscillation are generated. In these points, the experimental results agree fairly with the analytical results.

6.6 Concluding Remarks

In this section, first we consider the generation of pure modes from the viewpoint of symmetry of the circuit equation and reveal that a pure 1/3-subharmonic oscillation cannot be generated in the three-phase circuit. As a result, M_3 mode has to be accompanied with beat. Considering the above result, a pure 1/3-subharmonic oscillation reported in [10] seems to be a nearly 1/3-subharmonic oscillation whose main frequency is of order 2/5 which could not discriminate strictly from order 1/3 at the time.

Next, we consider M_3 oscillation accompanied with beat. By the analysis of homotopy method, the special feature of M_3 oscillation is that the periodic solution curve consists of many equivalent solutions. It becomes apparent that they are caused by the mode locking and unlocking. Further, the relation between frequency and symmetry are revealed.

By the analysis on the view point of Lyapnov exponent, it becomes manifest that there exists hyperchaotic M_3 oscillation. The oscillation is special feature of M_3 oscillation.

By experiments, M_3 oscillations are confirmed and the mode locking and unlocking bifurcation phenomena are observed. Additionally, the generation of periodic, almost periodic, chaotic oscillations are also confirmed.

Chapter 7

Harmonic Oscillation

7.1 Introduction

In this section, we reveal the bifurcation phenomena of harmonic oscillations whose main frequency component is equal to that of the voltage source [116]. The harmonic oscillations are classified into three modes. Several distinctive phenomena different from 1/3-subharmonic oscillations are generated. The differences of the phenomena in between the three-phase and single-phase circuit are revealed by periodic solution curve and bifurcation sets. In order to clarify the transition from three-phase to single-phase circuit, the bifurcation phenomena of coupled-single-phase circuit are investigated. The analytical results are compared with the experimental ones. Additionally, as for the relation between the phase angle and the generated modes, several experimental results are shown.

7.2 Three Modes in Three-phase Circuit

Considering the number of dominant inductors, harmonic oscillations are classified into three modes. That is,

M_3 mode : Oscillations excited by all the three nonlinear inductors. This oscillation has the symmetry with respect to C_3.

M_1 mode : Oscillations excited by any one of the three nonlinear inductors.

M_3' mode : Oscillation excited by all the three nonlinear inductors. This oscillation doesn't have the symmetry with respect to C_3.

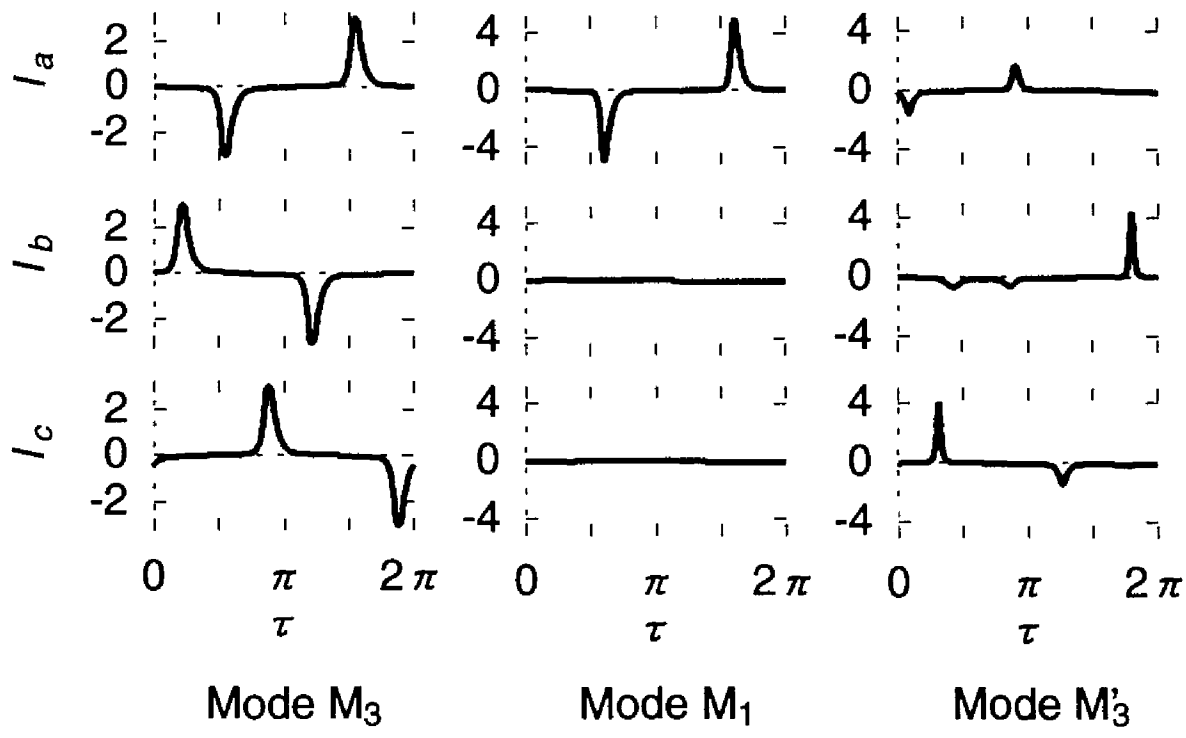

Fig. 7.1: Inductor current waveforms of harmonic oscillations (computation).

Applying the Newton homotopy method, we can obtain the inductor current waveforms of the three modes shown in Fig.7.1. Unsymmetric modes have different amplitudes in each inductor currents.

7.3 Analytical Results of Symmetric Oscillation

7.3.1 Bifurcation Phenomena of Mode M_3

We set the series resistance $R = 2.5\Omega$ and the delta-connected resistance $r = 3.1\Omega$. In the case of M_3 the following relation based on Eq.(2.25) is satisfied;

$$\begin{bmatrix} \boldsymbol{\Psi}(0) \\ \boldsymbol{U}(0) \end{bmatrix} = \mathrm{C}_3 \begin{bmatrix} \boldsymbol{\Psi}(\frac{2}{3}\pi) \\ \boldsymbol{U}(\frac{2}{3}\pi) \end{bmatrix}. \tag{7.1}$$

In stead of the boundary condition (2.33), we can adopt the condition (7.1). Then the interval of the integration can be reduced to $[0, 2\pi/3]$.

Applying the general homotopy method, we investigate bifurcation phenomena. Fig.7.2 shows the typical amplitude characteristics of mode M_3 for several values of the parameter η. Here, the vertical axis I is the maximum value of inductor currents. In this figure, we can find saddle-node bifurcations $S_1 \sim S_4$, pitchfork bifurcations P_1 and P_2, Neimark-Sacker bifurcations $N_1 \sim N_6$, and period doubling bifurcation D_1.

For the parameter $\eta = 0.45$, the bifurcation points S_1 and S_2 mean the jumps caused by the resonance of harmonic oscillation. This has been called the ferroresonance [1]. On the pitchfork bifurcation points P_1 and P_2, the emanating branch ($P_1 \to N_3 \to N_4 \to P_2$) implies the oscillations containing DC component in the fluxes. That is, the symmetry with respect to C_2 breaks on the pitchfork bifurcation P_1 and P_2. On the point of Neimark-Sacker bifurcations N_3 and N_4, the periodic oscillations lose their stability and almost periodic oscillations occur.

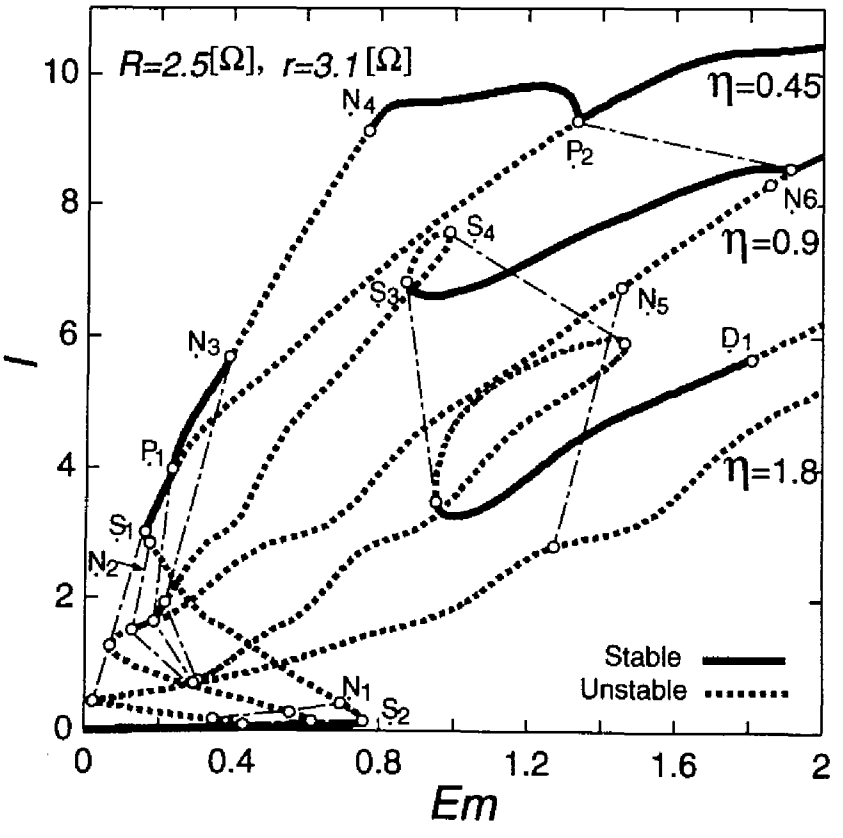

Fig. 7.2: Amplitude characteristics of harmonic M_3 oscillation.

For the parameter $\eta = 0.9$, the jumping point, on which the periodic oscillation loses its stability, changes from S_1 to N_2. Additionally, the bifurcation N_4 disappears accompanied by the generation of S_3 and S_4. For the parameter $\eta = 1.8$, we can find D_2, and it is distinctive that the stable region between N_2 and N_3 is very small.

7.3.2 Bifurcation Sets of Mode M_3

Applying the general homotopy method, we obtain the bifurcation sets. The bifurcation sets of mode M_3 on E_m-η plane is shown in Fig.7.3 where S_i, P_i, N_i and D_i $(i = 1, 2, \ldots)$ represent the sets of bifurcation points S_i, P_i, N_i and D_i, respectively. We can find co-dimension two bifurcations $\beta_1 = N_1 \cap S_1$, $\beta_2 = N_2 \cap S_1$, $\beta_3 = N_4 \cap S_3 \cap S_4$, $\beta_4 = N_6 \cap N_7 \cap P_2$, $\beta_5 = N_7 \cap D_2$. The bifurcation points β_3 and β_5 are strong 1:1 and 1:2 resonance, respectively. On β_4, the bifurcation set N_6 intersects P_2, resulting in the generation of N_7.

For the comparison of Fig.7.3, the bifurcation sets of harmonic oscillations in the single-phase circuit is shown in Fig.7.4. The parameter is set to $\bar{R} = 3R = 7.5\Omega$ and $\bar{r} = r = 3.1\Omega$. In the single-phase circuit, we can find saddle-node bifurcations $\hat{S}_1$ and $\hat{S}_2$, pitchfork bifurcations $\hat{P}_1$ and $\hat{P}_2$, and period doubling bifurcations $\hat{D}_1$ and $\hat{D}_2$. The single-phase circuit is two dimensional system and the magnetizing characteristics is monotonically increasing, hence with aid of Liouville's formula a co-dimension two bifurcation and Neimark-Sacker bifurcation are proved not to occur.

In comparison with the single-phase circuit, it becomes apparent that the special feature of the three-phase circuit is the generation of Neimark-Sacker bifurcations. The sets of the Neimark-Sacker bifurcation connect the saddle-node, pitchfork and period doubling bifurcation sets with co-dimension two bifurcations as is easily seen in Fig.7.3. Additionally, the loss of stability in resonant region is also distinctive.

7.3.3 Transition from Three-phase to Single-phase Circuit

For the purpose of revealing the relation between the single-phase circuit and the three-phase circuit, we analyze the coupled single-phase circuit described in section 4.5. The bifurcation sets on the parameter $\bar{\eta} = 3\eta = 5.4$ is shown in Fig.7.5. The upper figure is for $0 \leq \mu \leq 1$ and the lower is an enlarged diagram of the upper for $0 \leq \mu \leq 0.1$. In this figure, bifurcations on $\mu = 1$ correspond to the bifurcation points in the three-phase circuit

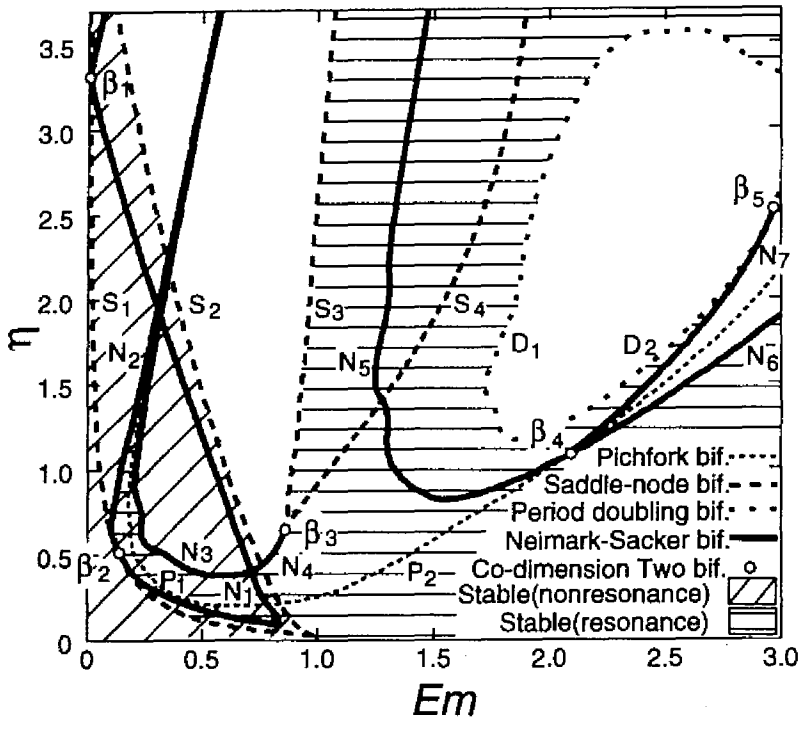

Fig. 7.3: Bifurcation sets of harmonic M_3 oscillation.

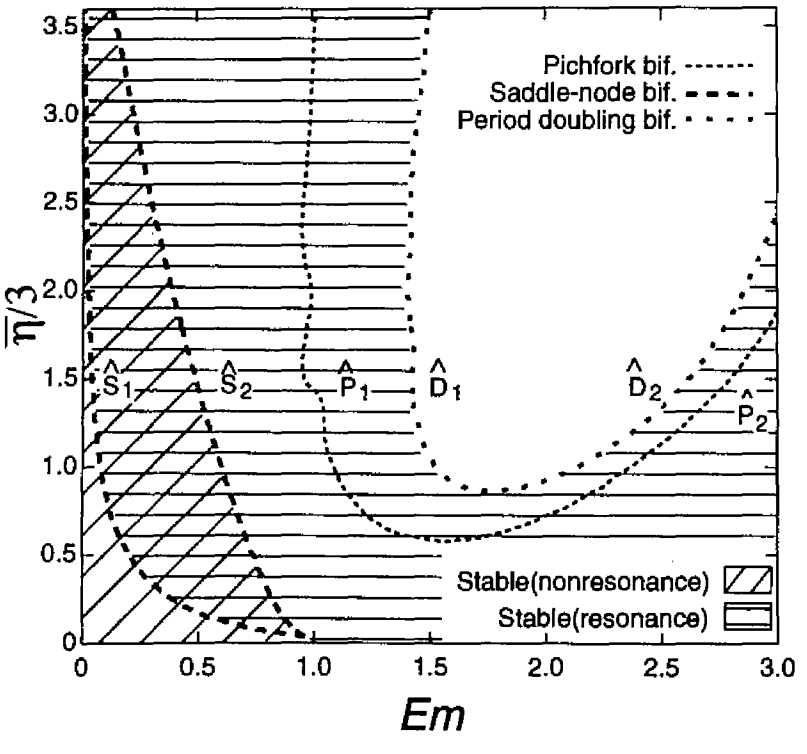

Fig. 7.4: Bifurcation sets of harmonic oscillation in single-phase circuit.

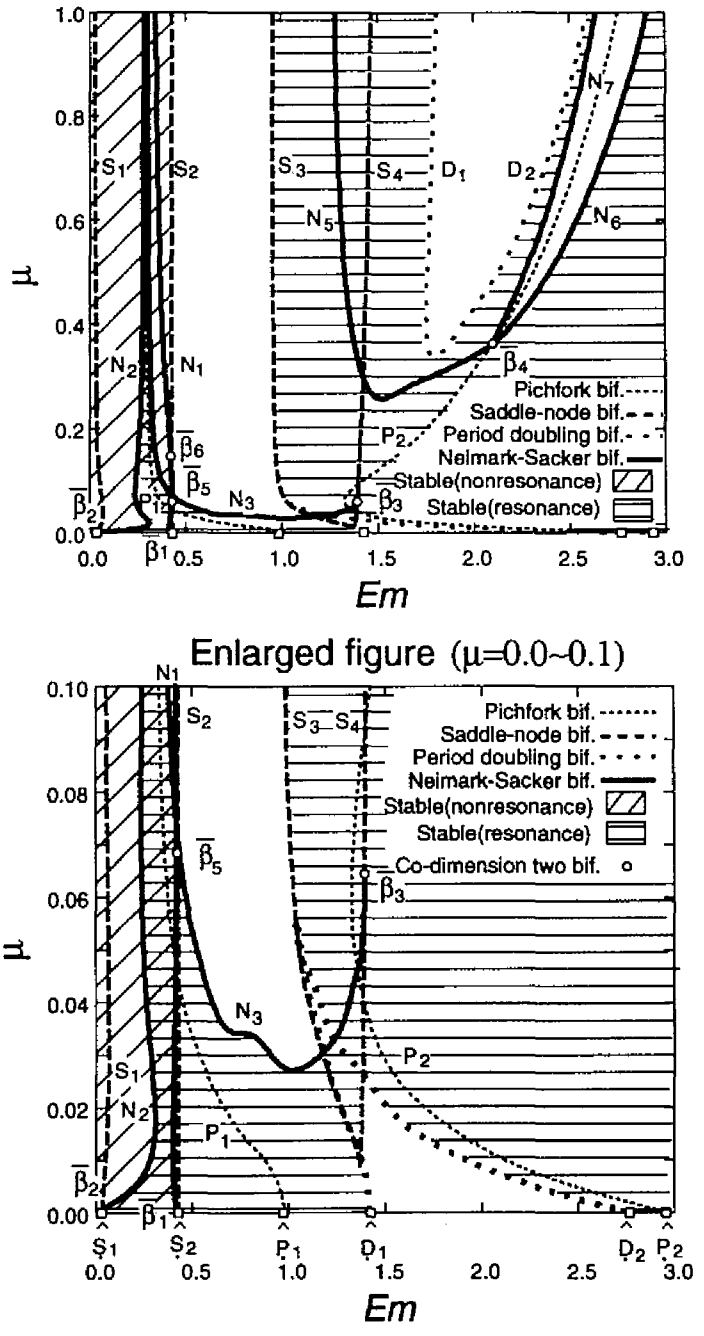

Fig. 7.5: Bifurcation sets of harmonic M_3 oscillation in coupled single-phase circuit.

and those on $\mu = 0$ correspond to the bifurcation points in the single-phase circuit.

It becomes apparent that $\dot{S}_1$, $\dot{S}_2$, $\dot{P}_1$ and $\dot{P}_2$ in the three-phase circuit are connected directly with $\hat{S}_1$, $\hat{S}_2$, $\hat{P}_1$ and $\hat{P}_2$ in the single-phase circuit, respectively. Additionally, the

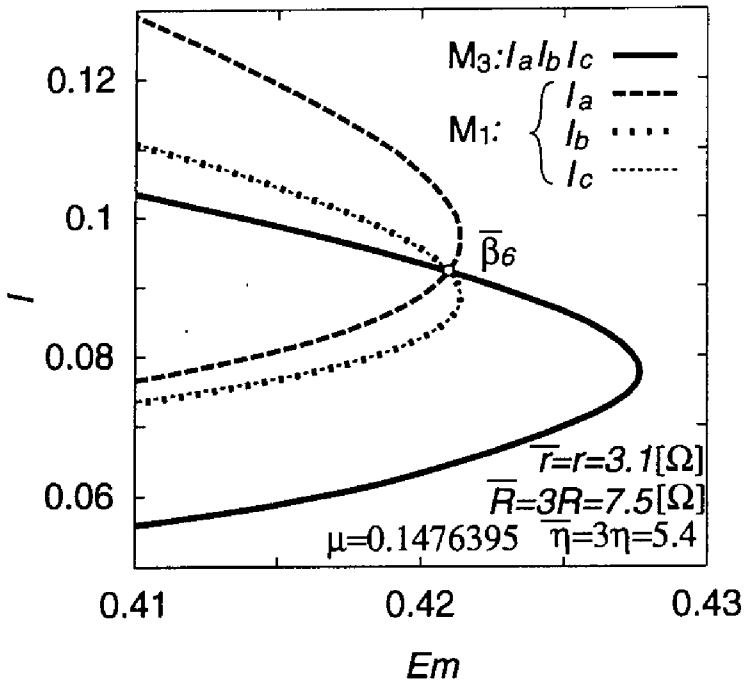

Fig. 7.6: Symmetry breaking bifurcation.

bifurcation sets N_1 and N_2 emanate from S_2 and S_1 on co-dimension two bifurcations $\bar{\beta}_1$ and $\bar{\beta}_2$ with strong 1:1 resonances, respectively. And by the co-dimension two bifurcations $\bar{\beta}_2$ and $\bar{\beta}_3$, the unstable regions in resonance are generated. As for other bifurcations, the transitions which occur when μ decreases are similar to those which occur when η decreases.

On the co-dimension two bifurcation $\bar{\beta}_6(\mu = 0.1476395)$, the monodromy matrix has eigenvalues $\exp(\pm 2\pi/3)$, that is, the point is strong 1:3 resonance. The amplitude characteristics in the neighborhood of the bifurcation $\bar{\beta}_6$ is shown in Fig.7.6. Here, in order to obtain the unsymmetric solutions with respect to C_3, the general homotopy is adopted to the boundary condition Eq.(2.33) in the integral interval $[0, 2\pi]$ instead of Eq.(7.1). In the figure, the M_3 solution is represented by solid lines which overlap each other because of the symmetry with respect to C_3. On the other hand, the branches emanating from the bifurcation $\bar{\beta}_6$ don't have the symmetry. These branches represent a part of M_1 solution curve. That is, M_1 branch is generated from the M_3 branch on the co-dimension two bifurcation $\bar{\beta}_6$. Thus, we can confirm the break of the symmetry on the Neimark-Sacker bifurcation of strong 1:3 resonance.

7.4 Analytical Results of Single-phase Oscillation

7.4.1 Bifurcation Phenomena of Mode M_1

Because M_1 solution don't have the symmetry with respect to C_3, we adopt the boundary condition Eq.(2.33) of the integral interval $[0, 2\pi]$.

The typical amplitude characteristics of mode M_1 for the parameter $\eta = 0.9$ are shown in Fig.7.7. Since the maximum values of inductor currents are different each other, three loops of amplitude characteristics are shown. In this figure, we can find saddle-node bifurcations $S_5 \sim S_8$ and Neimark-Sacker bifurcation N_8. In the higher amplitude of E_m, M_1 oscillation loses its stability on the Neimark-Sacker bifurcation N_8, and jumps to M_3 oscillation without the generation of almost periodic oscillation. We can find that the loops are folded back on S_6 and S_8 where an inductor begins to excite. This phenomenon is also observed in the case of the single-phase 1/3-subharmonic oscillation in the three-phase circuit described in chapter 4.

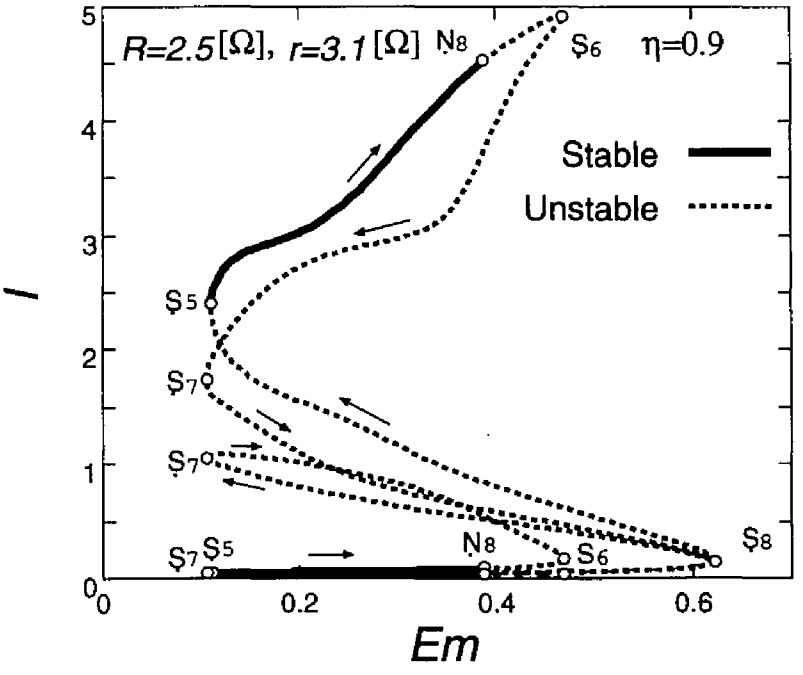

Fig. 7.7: Amplitude characteristics of harmonic M_1 oscillation.

7.4.2 Bifurcation Sets of Mode M_1

Fig.7.8 shows the bifurcation sets of mode M_1 on E_m-η plane. We can find co-dimension two bifurcations $\{\beta_6, \beta_7\}$=$N_8 \cap S_6$. The stable region is restricted in the lower amplitude of E_m by N_8. Additionally, it is distinctive that the bifurcation sets of S_7 and S_8 are fairly in good agreement with S_1 and S_2 in Fig.7.3, respectively.

7.4.3 Transition from Three-phase to Single-phase Circuit

Fixing the parameter $\eta = 0.9(\bar{\eta} = 2.7)$, we trace the bifurcations from $\mu = 1$ to $\mu = 0$ in the coupled single-phase circuit. The bifurcation sets are shown in Fig.7.9. It becomes apparent that S_5, S_6, S_7 and S_8 can be traced to $\mu = 0$ where S_5 and S_6 intersect S_7 and S_8 on $\hat{S}_1$ and $\hat{S}_2$ in the single-phase circuit, respectively. The bifurcation set N_8 emanates from S_6 on co-dimension two bifurcation $\bar{\beta}_7$ with strong 1:1 resonance. Fig.7.10 shows the amplitude characteristics at $\mu = 0$. This indicates that mode M_1 corresponds to three single-phase circuits one of which is resonant and the others are not resonant. This explains

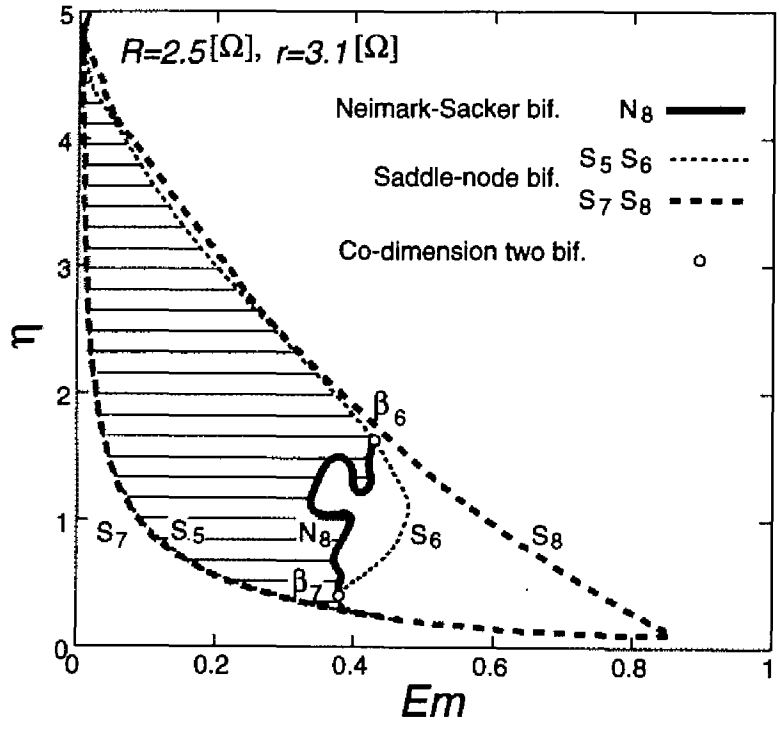

Fig. 7.8: Bifurcation sets of mode M_1.

the reason why the region of M_1 in Fig.7.8 overlaps to the regions enclosed by $\hat{S}_1$-$\hat{S}_2$ in Fig.7.4 and by S_1-S_2 in Fig.7.3. In other words, the mode M_1 can be generated in the region where two stable solutions exist.

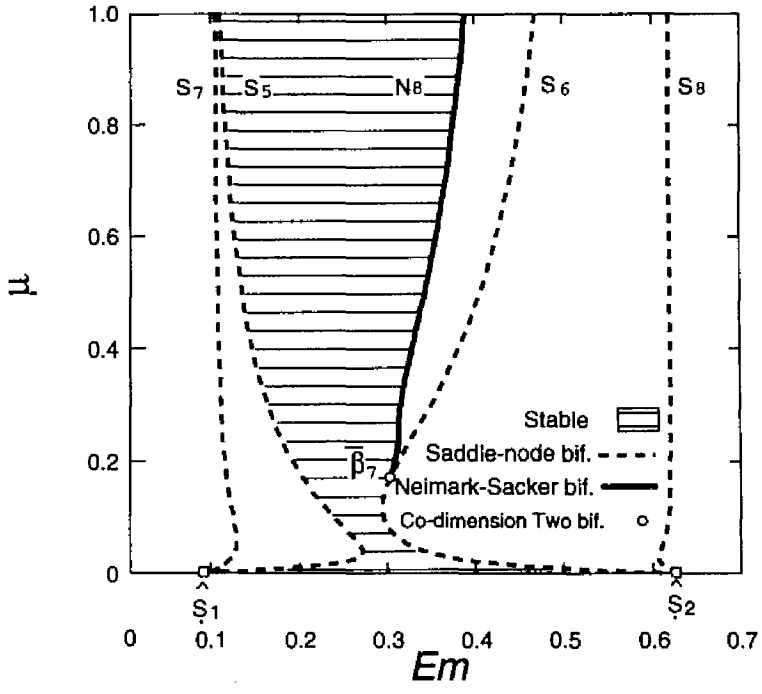

Fig. 7.9: Bifurcation sets of harmonic M_1 oscillation in coupled single-phase circuit.

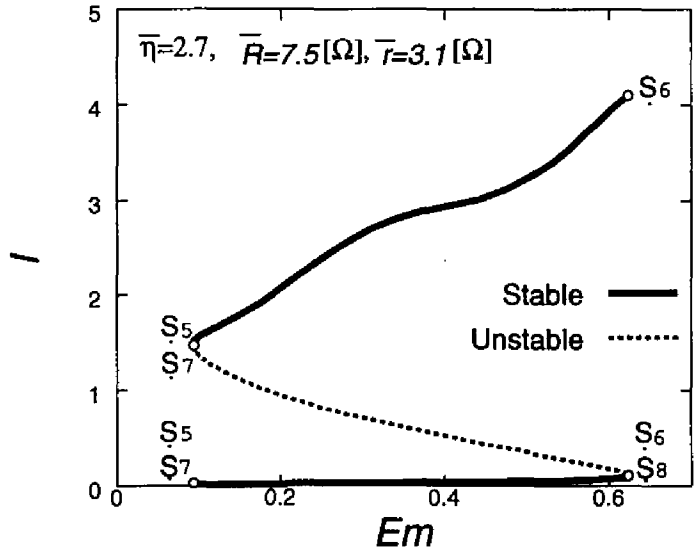

Fig. 7.10: Amplitude characteristics of harmonic M_1 oscillation in single-phase circuit.

7.5 Analytical Results of Unsymmetric Oscillation

7.5.1 Bifurcation Phenomena of Mode M_3'

The typical amplitude characteristics of mode M_3' for the parameter $\eta = 2.4$ and $R = 1.0\Omega$ is shown in Fig.7.11. As for mode M_3', since the maximum values of inductor currents are different each other, one of the three curves of amplitude characteristics are shown. In this figure, we can find saddle-node bifurcations $S_9 \sim S_{13}$, Neimark-Sacker bifurcations $N_9 \sim N_{11}$, and period doubling bifurcation D_3. In the higher part of the amplitude, the loop $S_{11} \rightarrow N_9 \rightarrow S_{12} \rightarrow N_{11} \rightarrow N_{10} \rightarrow S_{13} \rightarrow \cdots \rightarrow D_3 \rightarrow S_{11}$ is closed. On the Neimark-Sacker bifurcation N_9, the periodic oscillation loses its stability and almost periodic oscillation is generated.

7.5.2 Bifurcation Sets of Mode M_3'

Fig. 7.12 shows the bifurcation sets of mode M_3' on E_m-η plane. If all the bifurcations are shown, the figure becomes so complicated that only the bifurcations where the oscillations lose their stability are shown. We can find co-dimension two bifurcations $\beta_8 \sim \beta_{15}$. On N_9, N_{11}, N_{12} and N_{14}, we can see the generation of almost periodic M_3' oscillations.

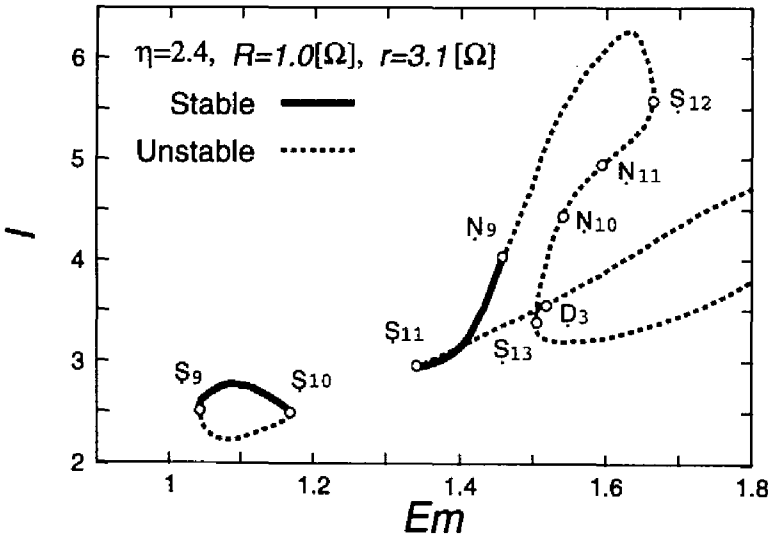

Fig. 7.11: Amplitude characteristics of harmonic M_3' oscillation.

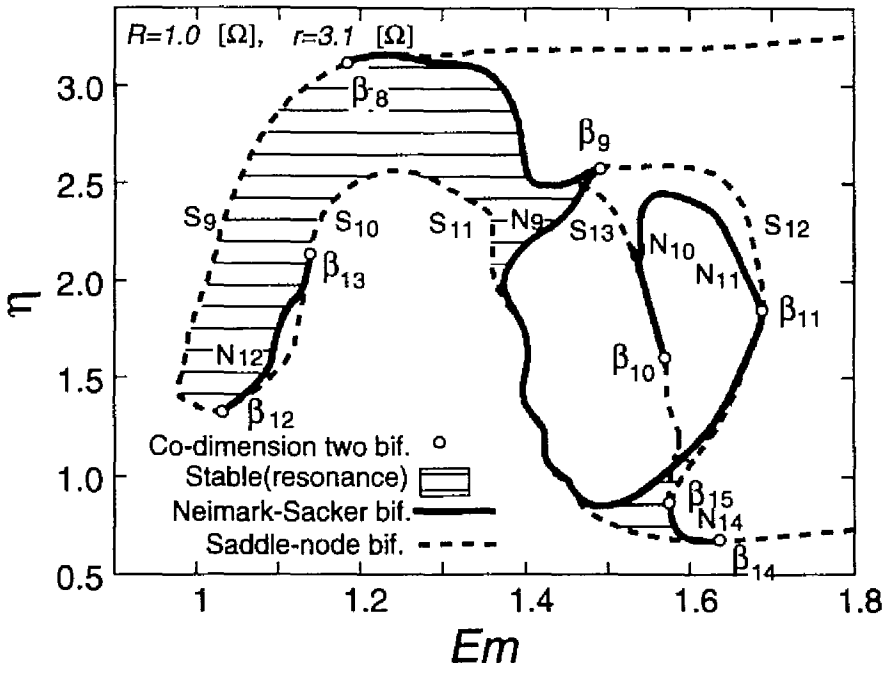

Fig. 7.12: Bifurcation sets of harmonic M_3' oscillation.

In the coupled single-phase circuit, as the coupling parameter μ is decreased, mode M_3' disappears. This indicates that there exists no corresponding oscillation to M_3' in the single-phase circuit.

7.6 Experimental Results

We fix the series resistance $R = 2.5\Omega$ and the delta-connected resistance $r = 3.1\Omega$ which is chosen in section 7.3.1 and make experiment for the parameter X_c =42.2, 88.4, 176.8, 353.7 Ω in the three-phase circuit and for the parameter X_c =29.4, 58.9, 117.9, 235.8Ω in the single-phase circuit. Fig.7.13 and Fig.7.14 show the bifurcation phenomena on E_Δ-X_c plane in the three-phase circuit and the single-phase circuit, respectively. Jumps (arrows) in the figure mean that keeping the value X_c fixed and increasing or decreasing of line-voltage E_Δ the oscillations bifurcate into another type of oscillations as indicated arrow head.

In Fig.7.13, mode M_3 is classified below:

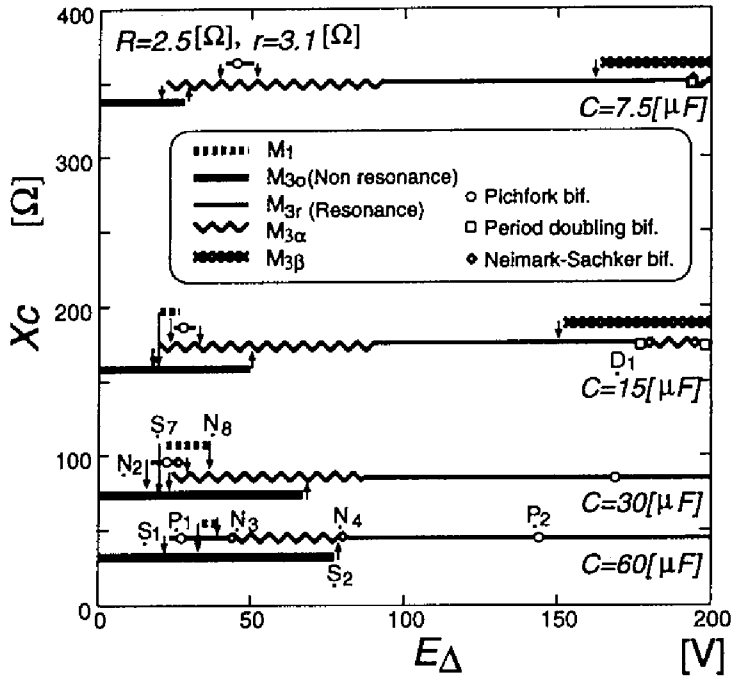

Fig. 7.13: Bifurcation phenomena in three-phase circuit (experiment).

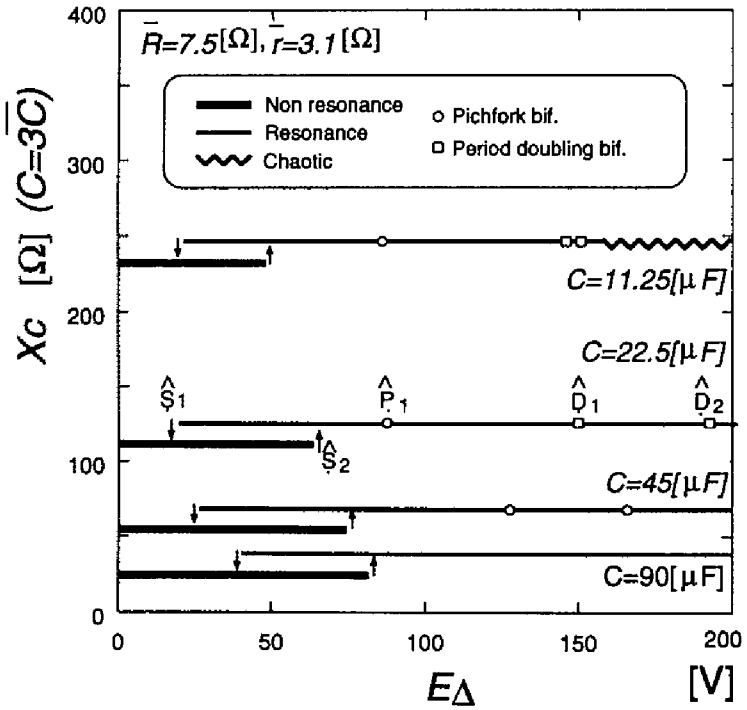

Fig. 7.14: Bifurcation phenomena in single-phase circuit (experiment).

M_{3o}: Nonresonant periodic M_3 oscillations.

M_{3r}: Resonant periodic M_3 oscillations.

$M_{3\alpha}$: M_3 oscillations accompanied with beat. The phase of beat is equivalent in phase-a,b,c (Fig.7.15).

$M_{3\beta}$: M_3 oscillations accompanied with beat. The phase of beat is shifted in phase-a,b,c (Fig.7.15).

At the parameter $X_c = 42.2\Omega$, we can confirm the bifurcations $\dot{S}_1$, $\dot{S}_2$, $\dot{P}_1$, $\dot{N}_3$, $\dot{N}_4$, and $\dot{P}_2$ of mode M_3 which correspond to the analytical results for $\eta = 0.45$ in Fig.7.2. We can also find the generation of mode M_1. By increasing the parameter X_c, the region of nonperiodic oscillation is enlarged (X_c=88.4Ω). At $X_c = 176.8$, the period doubling bifurcation $\dot{D}_1$ can be observed. After the period doubling bifurcation $\dot{D}_1$ Neimark-Sacker bifurcation occurs and almost periodic $M_{3\alpha}$ oscillations are generated. Additionally, the $M_{3\beta}$ oscillations which have the region of almost periodic and chaotic oscillation can be observed. The experimental results in the three-phase circuit agree fairly with analytical ones.

In Fig.7.14 the jumps accompanied by the harmonic resonance which corresponds to the saddle-node bifurcation $\hat{\dot{S}}_1$ and $\hat{\dot{S}}_2$, pitchfork bifurcation $\hat{\dot{P}}_1$, and the period doubling bifurcations $\hat{\dot{D}}_1$ and $\hat{\dot{D}}_2$ are confirmed. The results agree fairly with the analytical ones shown in Fig.7.4. At $C = 11.25[\mu F]$, after the period doubling bifurcation $\hat{\dot{D}}_1$, chaotic oscillation via period doubling cascade is observed.

The experimental waveforms of inductor currents and capacitor voltage of nonperiodic oscillations in the three-phase circuit are shown in Fig.7.15. Fig.7.15(a) shows almost periodic oscillation of mode $M_{3\alpha}$ which are generated by the Neimark-Sacker bifurcation $\dot{N}_3$. In this figure, the beat of phase-a,b,c is same. Fig.7.15(b) shows chaotic oscillation of mode $M_3\alpha$ which bifurcates from the almost periodic $M_{3\alpha}$. In the figure, we can observe the inductor currents circulate in the delta-connection changing the direction every about 125 [ms]. This oscillation is special feature of the three-phase circuit on the point of the circulation in the delta-connection. Fig.7.15(c) shows the almost periodic oscillation of mode $M_{3\beta}$ which appears in the larger part of the source line-voltage E_Δ.

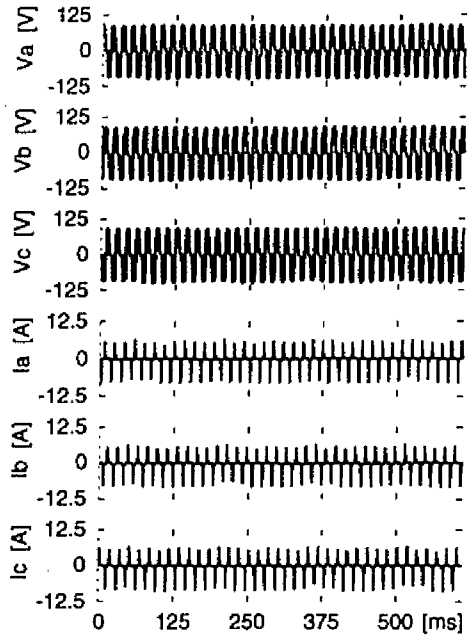

(a)

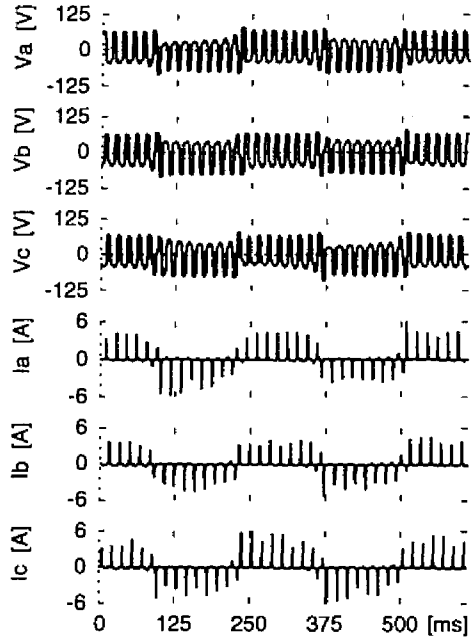

(b)

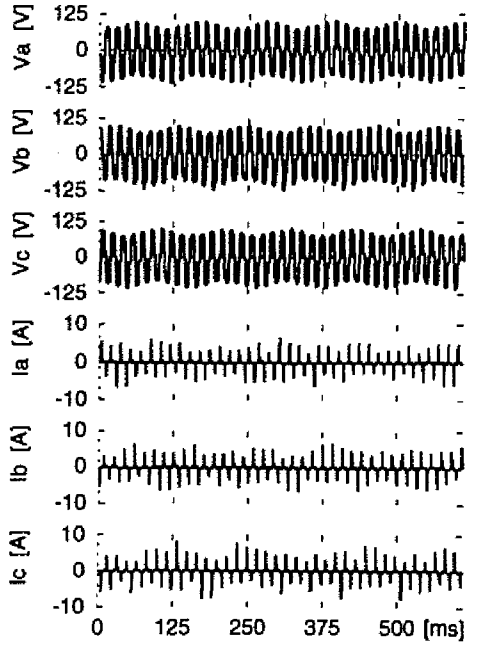

(c)

(a) Mode $M_{3\alpha}$ (Almost periodic
E_Δ=49.0[V], C=60.0[μF],
R=2.5 [Ω], r=3.1[Ω]

(b) Mode $M_{3\alpha}$ (Chaotic)
E_Δ=25.0[V], C=30.0[μF],
R=2.5 [Ω], r=3.1[Ω]

(c) Mode $M_{3\beta}$
E_Δ=164.0[V], C=15.0[μF],
R=2.5 [Ω], r=3.1[Ω]

Fig. 7.15: Waveforms of harmonic M_3 oscillations (experiment).

7.7 Phase Control

7.7.1 Experimental Method

In this section, the effects of the phase angle at which the source voltages are applied to the three-phase circuit are investigated by experiment. We set the same parameter that is chosen in the experiment of the previous section, that is, the series resistance $R = 2.5\Omega$ and the delta-connected resistance $r = 3.1\Omega$. Additionally, we choose the parameter $X_c = 42.2\Omega$ and source line-voltage $E_\Delta = 36.5$V. At the parameter, three sorts of oscillations are generated, that is, M_{3o}, M_{3r} and M_1 modes (Fig.7.13).

The initial charged capacitor voltage v_c is set to 75V. Then, we close the circuit on several phase angles θ by the phase controller and observe the transient phenomena.

7.7.2 Transient Waveform

The relation between the phase angle θ and generated oscillations are shown in table 7.1.

Table 7.1: Relation between θ and oscillations.

θ	generated oscillation			
0°	M_{3+}			
60°	M_{3+}			
120°	M_{3+}			
180°	M_{3+}	M_{3-}		
210°	M_{3o}	M_{3-}	M_{1a}	
240°	M_{3-}	M_{3+}	M_{1c}	M_{3o}
270°	M_{3o}			
300°	M_{1b}	M_{3+}	M_{3-}	M_{3o}

The mode M_{3r} is classified into M_{3+} and M_{3-} because two mutually symmetric oscillations with respect to C_2 exist. As for mode M_1, the suffix a,b or c represents an active inductor L_a, L_b or L_c, respectively. Although the phase angle θ is fixed, several oscillations are generated at θ =180°, 210°, 240° and 300°. That is caused by remanent magnetizations. However, the modes on the most left side in table 7.1 are the most frequently generated.

The transient waveform is shown in Fig.7.16. At θ = 0°, 60°, 120°, the transient state is very short and the first peak of the current I_b appears at about phase angle 210° of E_a

regardless of the closed phase angle θ. At θ =180°, mode M_{3+} and M_{3-} are generated. In the case of M_{3+} we can confirm the chaotic $M_{3\alpha}$ oscillation shown in Fig.7.15(b) in the transient state. At θ =210°, the mode M_{3o}, M_{3-} and M_{1a} are generated. In the case of M_{3o}, we can confirm the 1/2-subharmonic M_1 oscillation in the transient state. In the case of M_{1a}, the transient state is very short. At θ =240°, four sorts of oscillations are generated. As for M_{1c} , the transient state is very short. At θ =270°, only M_{3o} can be generated. At θ = 300°, four sorts of oscillations are generated. As for M_{1b}, the transient state is very short.

Thus, the phase angle θ affects the generating oscillations. Mode M_{3+} of θ = 0°, 60°, 120° and M_1 have very short transient states. M_{3+} is frequently generated but M_1 is not frequently. Other oscillations often have transient states which are similar to the chaotic $M_{3\alpha}$ oscillation shown in Fig.7.15(b).

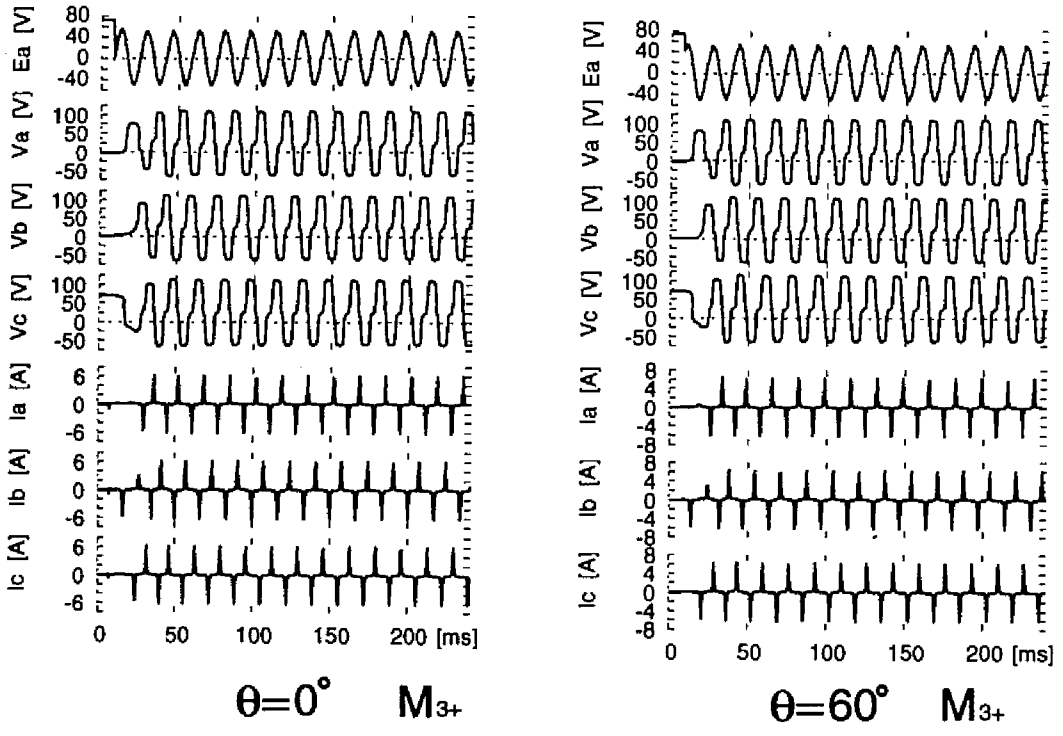

Fig. 7.16: Transient waveforms.

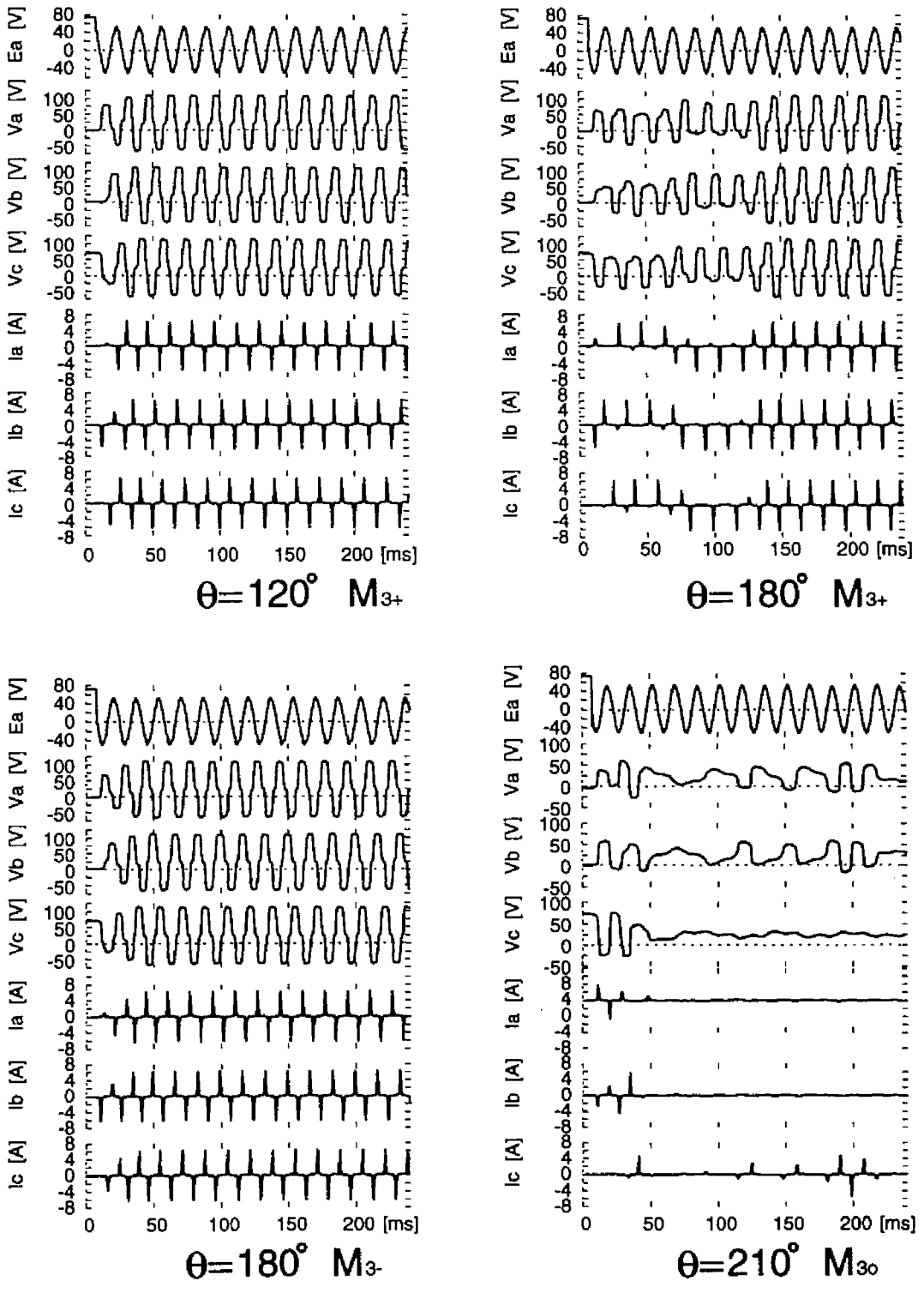

Fig. 7.16: Transient waveforms.

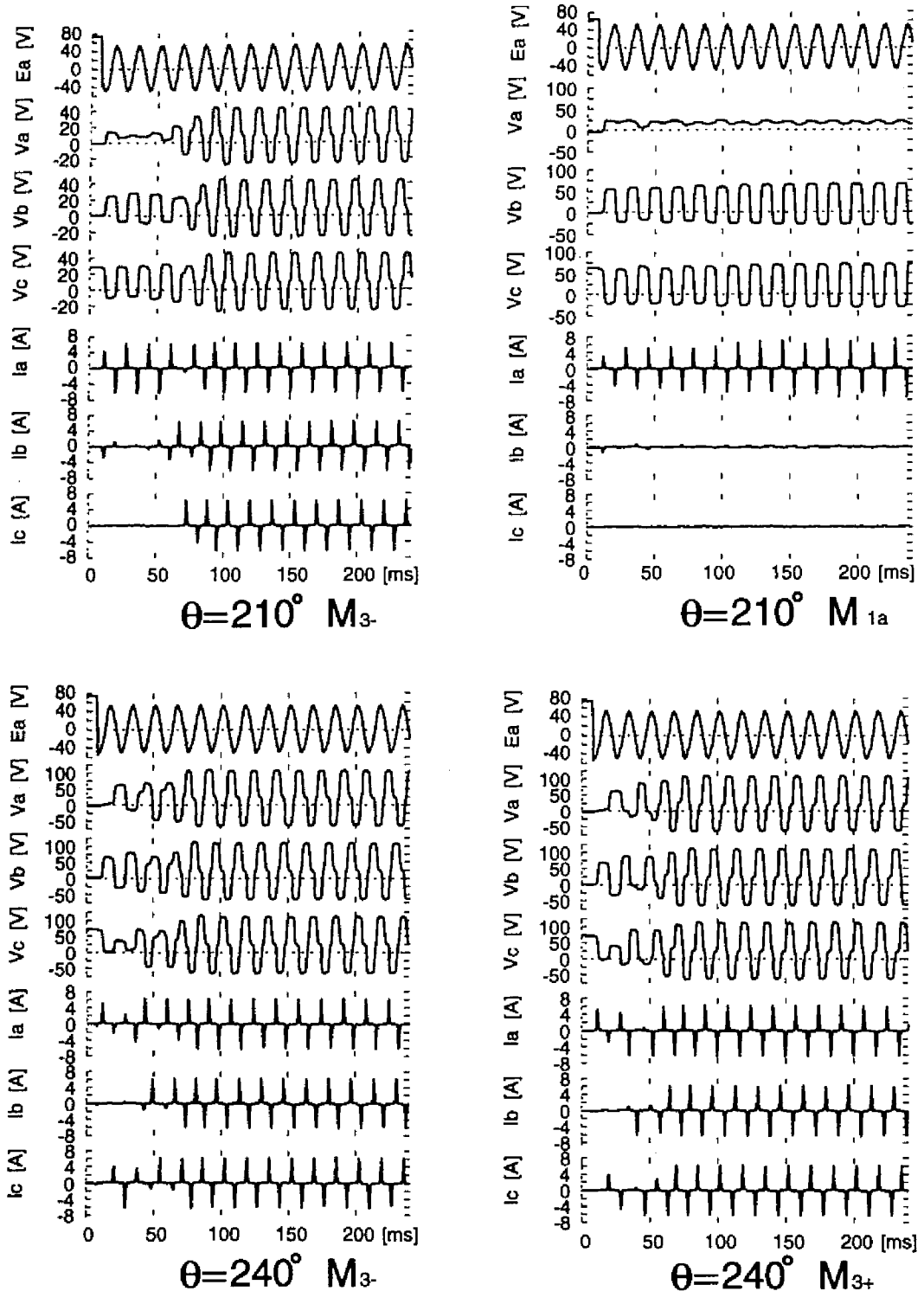

Fig. 7.16: Transient waveforms.

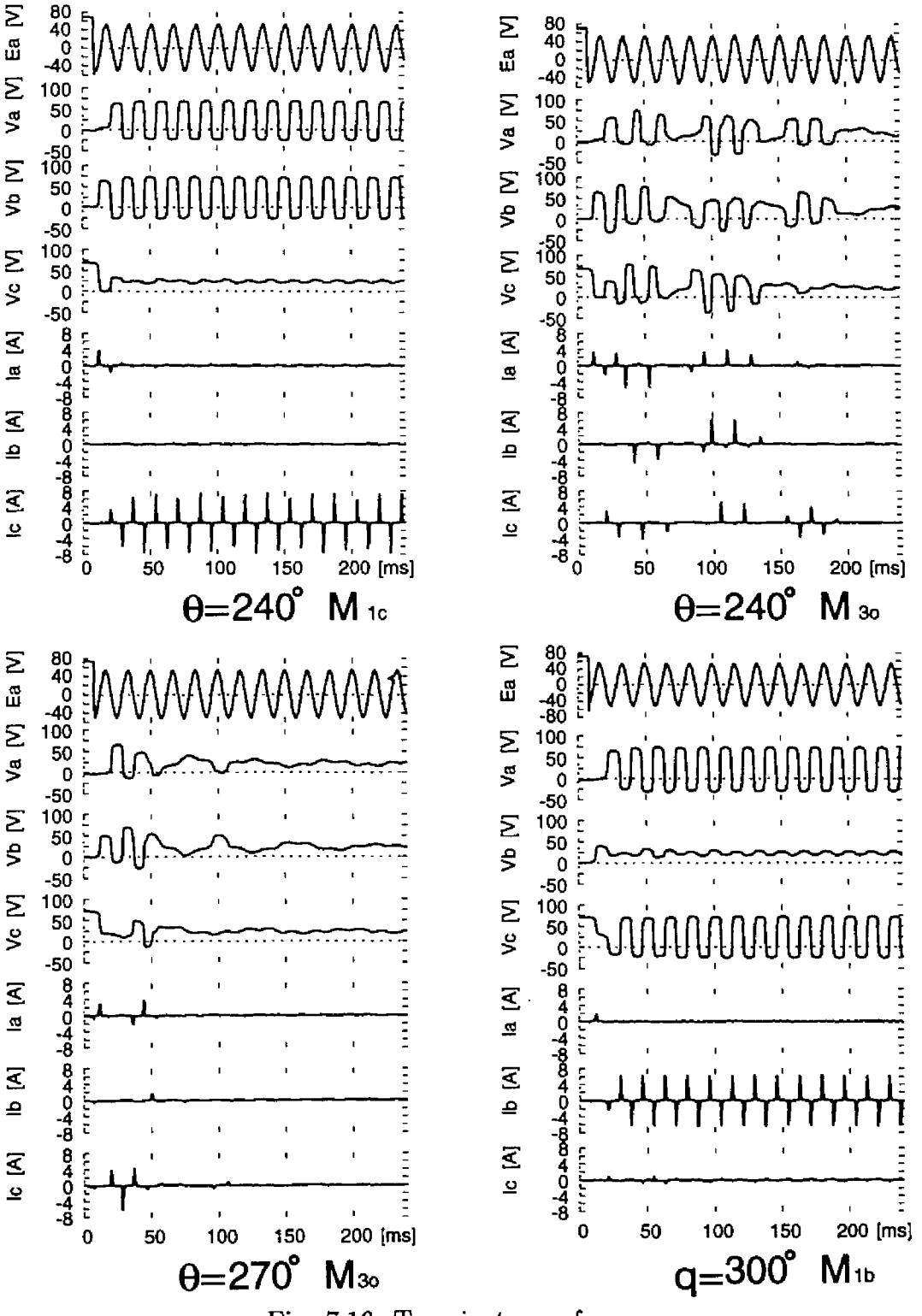

Fig. 7.16: Transient waveforms.

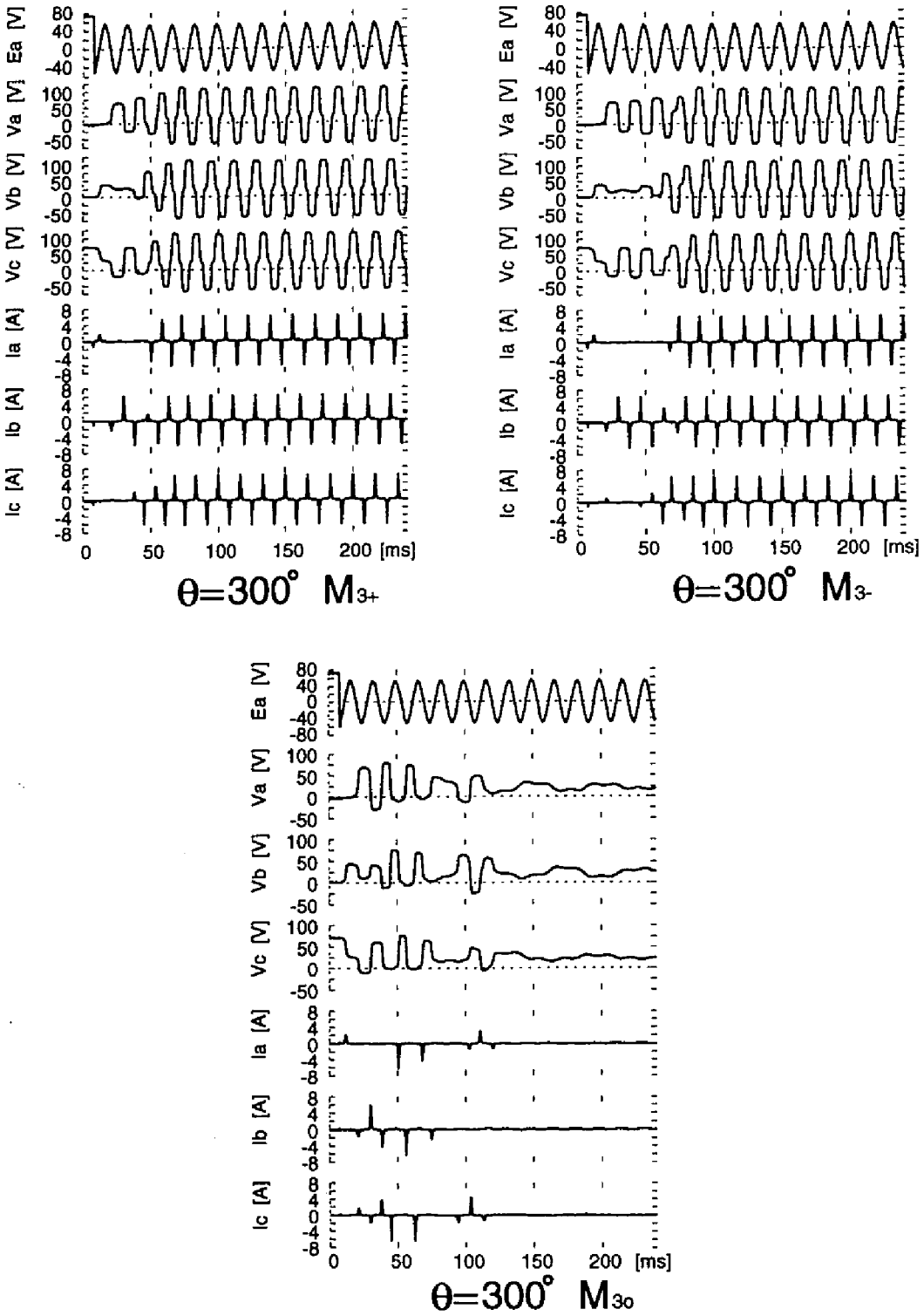

Fig. 7.16: Transient waveforms.

7.7.3 Transient Trajectory

In order to clarify the effect of the phase angle θ, we consider the $0\alpha\beta$ transformation. That is, the components of capacitor voltage v_a, v_b, v_c can be represented by 0-, α-, β-components.

$$\begin{bmatrix} v_0 \\ v_\alpha \\ v_\beta \end{bmatrix} = \begin{pmatrix} \frac{1}{3} & \frac{1}{3} & \frac{1}{3} \\ \frac{2}{3} & -\frac{1}{3} & -\frac{1}{3} \\ 0 & \frac{1}{\sqrt{3}} & \frac{-1}{\sqrt{3}} \end{pmatrix} \begin{bmatrix} v_a \\ v_b \\ v_c \end{bmatrix}, \quad \begin{bmatrix} v_a \\ v_b \\ v_c \end{bmatrix} = \begin{pmatrix} 1 & 1 & 0 \\ 1 & -\frac{1}{2} & \frac{\sqrt{3}}{2} \\ 1 & -\frac{1}{2} & -\frac{\sqrt{3}}{2} \end{pmatrix} \begin{bmatrix} v_0 \\ v_\alpha \\ v_\beta \end{bmatrix} \tag{7.2}$$

Fig.7.17 shows the transient trajectories on v_α-v_β plane. In the figures, the three arrows represents the directions of v_a, v_b, v_c. The initial point of the trajectory is in the direction of v_c because only the phase-c capacitor is charged.

At $\theta = 0°$, $60°$, $120°$ the initial direction of the trajectory is orthogonal to the arrow-b, that is, the electric charge are discharged through the inductor L_b. In the case of M_{3+} at θ =180°, the initial direction of the trajectory becomes a little inner and the transient trajectory is attracted to two triangle-like orbit which represents the chaotic $M_{3\alpha}$ oscillation.

At $\theta = 210°$ the initial direction of the trajectory is opposite to the arrow-c, that is, the electric charge is discharged through inductors L_a and L_b simultaneously. The steady state trajectory of M_{1c} is orthogonal to the arrow-a. In the case of M_{1c} the trajectory proceed to stead state smoothly. In the case of M_{3-} the transient trajectory is attracted to M_{1c} orbit.

At $\theta = 240°$, $270°$, $300°$ the initial direction of the trajectory is orthogonal to the arrow-a, that is, the electric charge are discharged through the inductor L_a. The first current is large at θ =240° and small at θ =300°. Then, the next current is I_a, I_c at 240° and I_b, I_c at θ =300°. In the case of M_{3-} and M_{3+} at θ =240°, the initial direction of the trajectory is opposite to the steady state orbit. Then, the transient trajectory is attracted to the orbit of the chaotic $M_{3\alpha}$ oscillation once. In the case of M_{1c} at $\theta = 240°$ and M_{1b} at $\theta = 300°$, the trajectory proceeds to steady state smoothly.

Thus, the $0\alpha\beta$ transformation make clear that the steady state is affected by the initial direction of the trajectory. At θ=0° $\sim$ 120° the trajectories can proceed to M_{3+} smoothly. In other cases, however, the trajectory cannot proceed to M_{3+} smoothly. Then other steady states appear. In the case of M_1, the proceeding is rapid. As for the other oscillations, the trajectories tend to be attracted transiently to the chaotic $M_{3\alpha}$ orbit once.

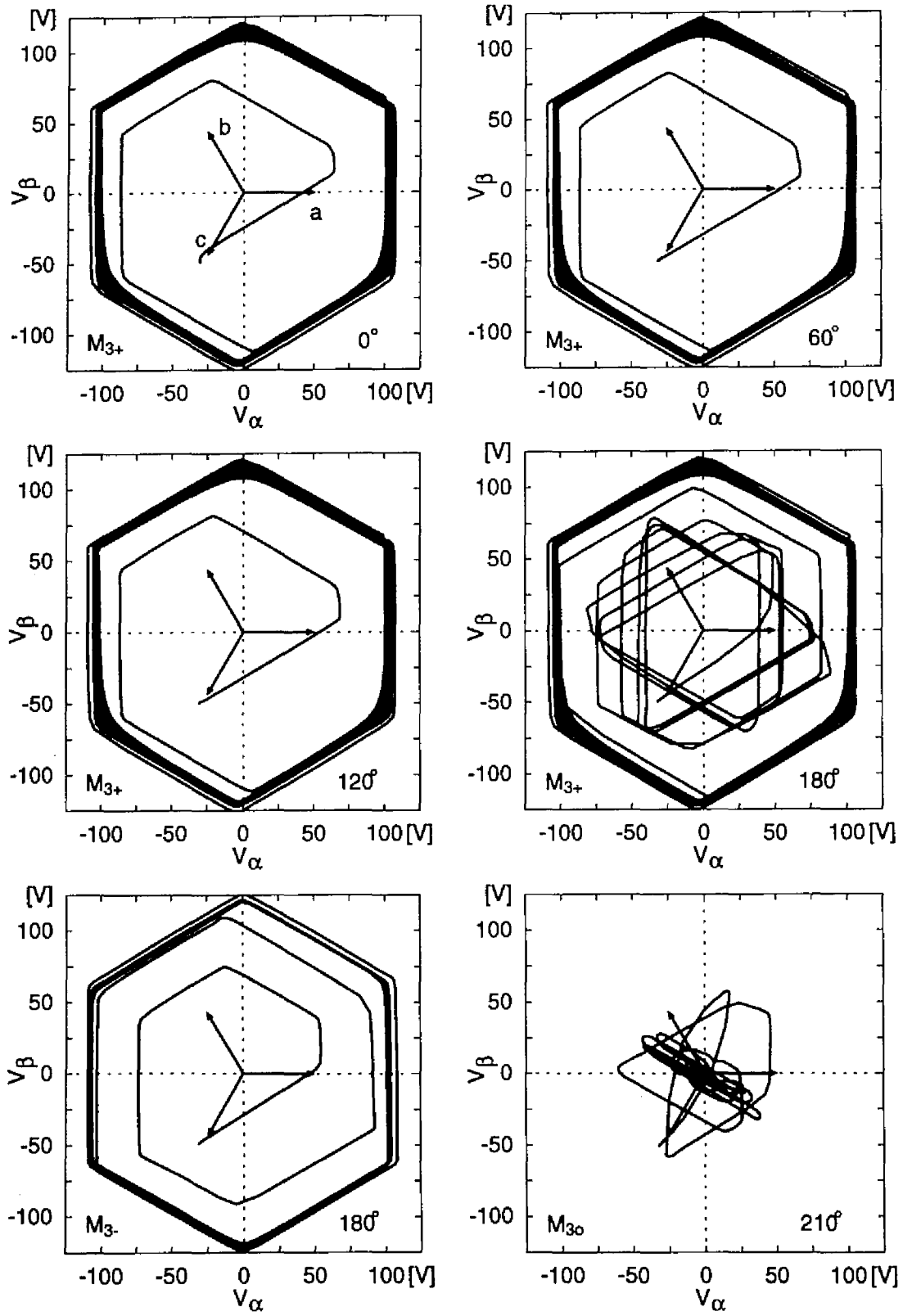

Fig. 7.17: Transient trajectory (The degree means the phase angle θ).

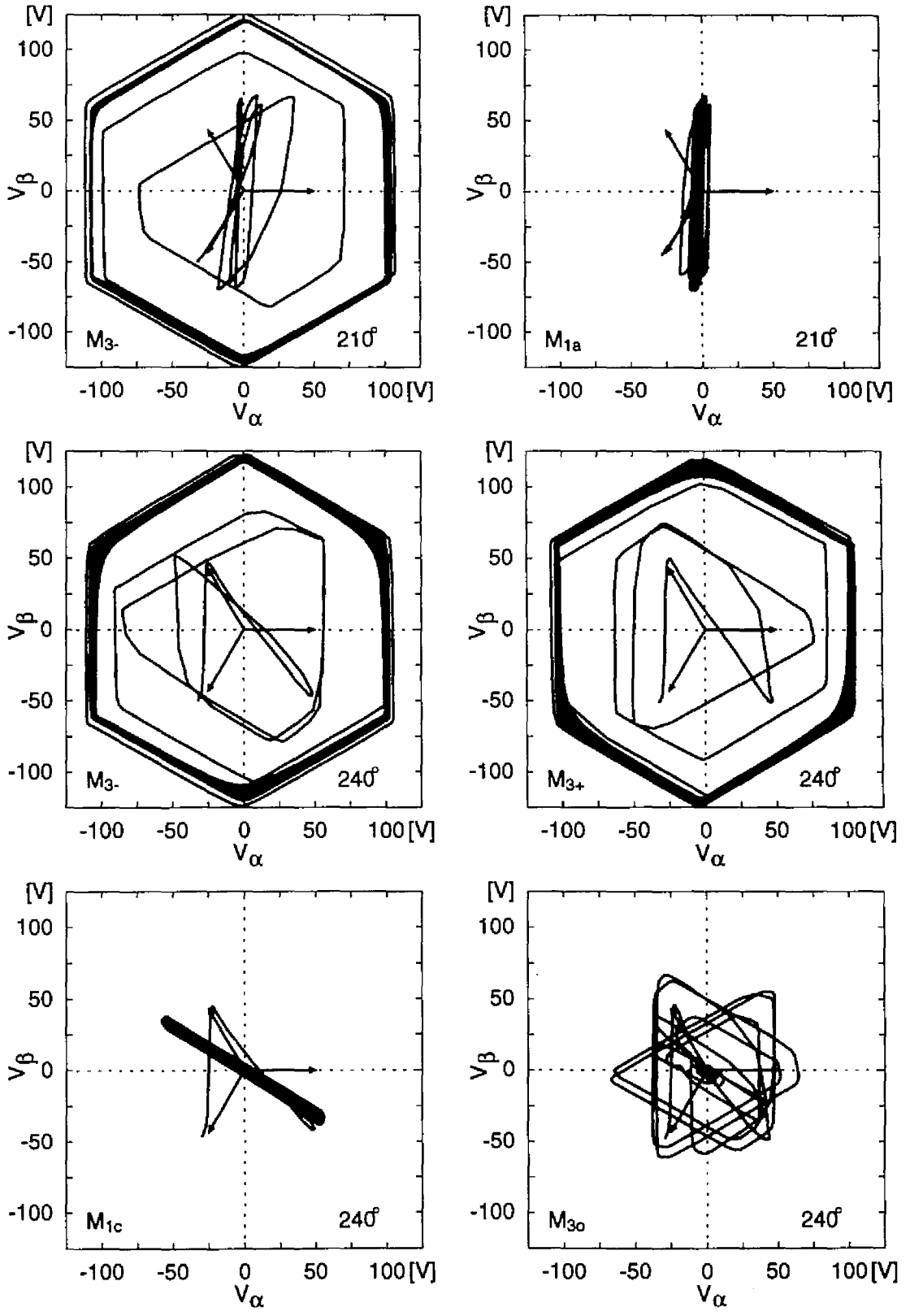

Fig. 7.17: Transient trajectory.

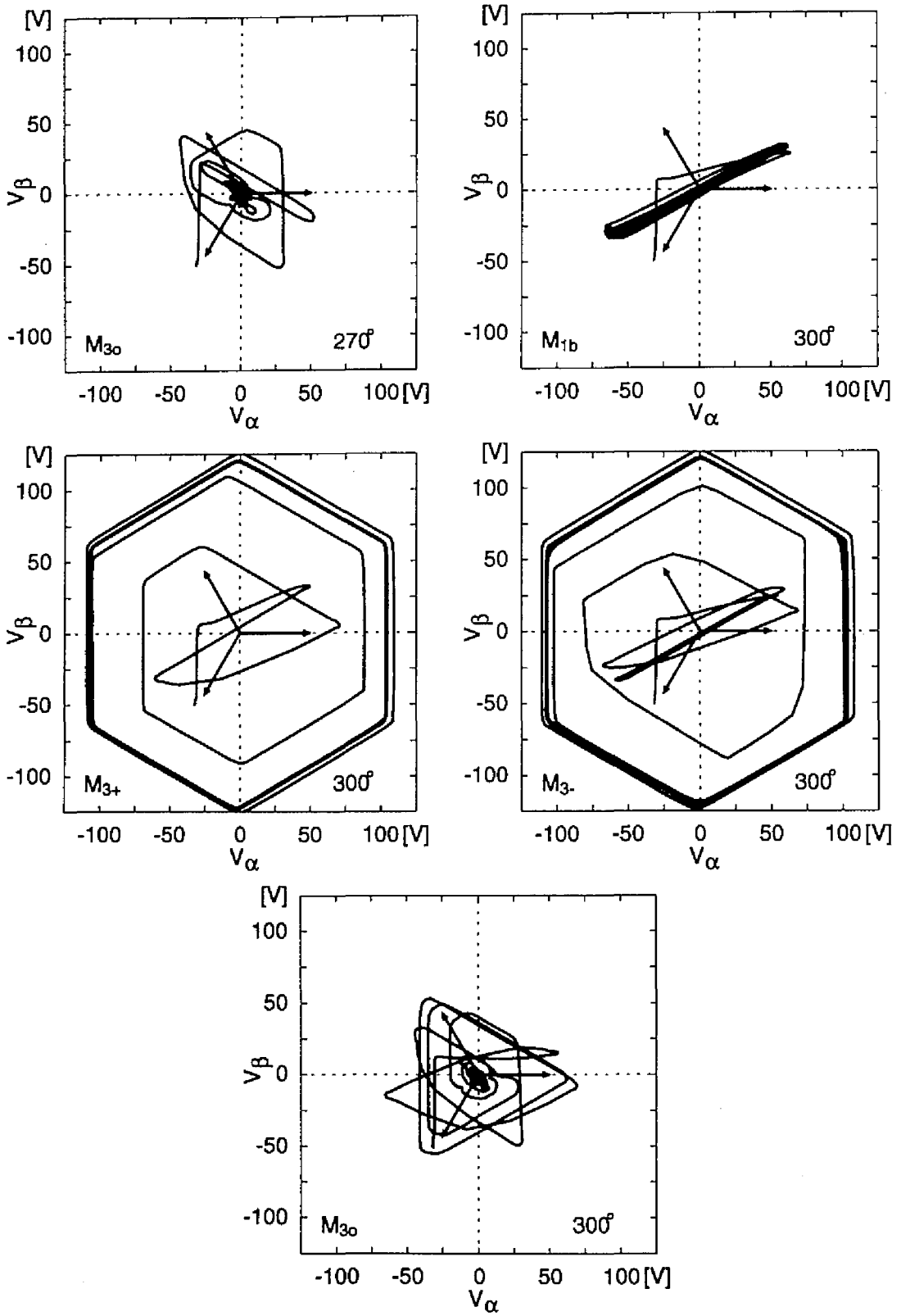

Fig. 7.17: Transient trajectory.

7.8 Concluding Remarks

In this section, several bifurcations of three modes of harmonic oscillations are revealed by the homotopy method and real experiment.

In the single-phase circuit, there exist a pair of saddle-node bifurcations which means the harmonic resonance, pitchfork bifurcations, and period doubling bifurcations. Needless to say, these bifurcations can be found in the three-phase circuit. In addition, Neimark-Sacker and co-dimension two bifurcations exist. These two characterize the bifurcations of the three-phase circuit. Additionally, there exist distinctive chaotic oscillations of mode $M_{3\alpha}$ in the unstable regions which are generated by above bifurcations.

Additionally, analyzing the bifurcations of the coupled single-phase circuit, the relations as well as differences between the three-phase circuit and single-phase circuit are revealed. The mode M_1 corresponds to the three single-phase circuits one of which is resonant and the others are not resonant. On the other hand, the mode M_3' is special feature of the three-phase circuit.

Furthermore, the transient states of several oscillations are investigated by the experiment with phase controller. The relation between the phase angle and generated mode becomes manifest.

Chapter 8

1/2-Subharmonic Oscillation

8.1 Introduction

In this section, we reveal the bifurcation phenomena of 1/2-subharmonic oscillations in the three-phase circuit. The 1/2-subharmonic oscillations are classified into three modes. The periodic solution curves and bifurcation sets of each modes are investigated. Further, in order to clarify the difference of the phenomena in the three-phase, single-phase-like and single-phase circuit, the periodic solution curves and bifurcation sets of the 1/2-subharmonic oscillations in single-phase-like and single-phase circuit are also investigated. Additionally, experimental results are shown.

8.2 Three Modes in Three-Phase Circuit

We set the series resistance $R = 2.5\Omega$ and the delta-connected resistance $r = 3.1\Omega$. Applying the Newton homotopy method with the period $T = 4\pi$, we obtain several 1/2-subharmonic oscillations. Considering the number of dominant inductors, periodic 1/2-subharmonic oscillations are classified into three modes. That is,

M_1 mode : Oscillations excited by any one of the three nonlinear inductors.

M_3 mode : Pure oscillations excited by all the three nonlinear inductors.

M_3' mode : Pure oscillation excited by all the three nonlinear inductors. The amplitude of inductor currents is small.

The waveforms of capacitor voltages and inductor currents of the three modes are shown in Fig.8.1. In this figure, the waveforms over the interval $[0, 4T]$ are shown. We can confirm the amplitude of inductor currents in mode M_3' is small.

The above oscillations don't have the symmetry with respect to $\mathbf{C}_2$ which is defined by Eq.(2.25). The fact can be shown below.

Let $[\boldsymbol{\Psi}(\tau), \boldsymbol{U}(\tau)]'$ be a period-n solution of Eq.(2.6). Assume that $n = 2k+1$ ($k = 0, 1, \ldots$), then the right-hand side of the Eq.(2.25) satisfies

$$\begin{aligned}
&\frac{d}{d\tau}\mathbf{C}_2 \begin{bmatrix} \boldsymbol{\Psi}(\tau + n\pi) \\ \boldsymbol{U}(\tau + n\pi) \end{bmatrix} - \boldsymbol{f}\left(\widehat{\mathbf{C}}_2\boldsymbol{\Psi}(\tau + n\pi), \widehat{\mathbf{C}}_2\boldsymbol{U}(\tau + n\pi), \tau\right) \\
&= \mathbf{C}_2\frac{d}{d\tau} \begin{bmatrix} \boldsymbol{\Psi}(\tau + (2k+1)\pi) \\ \boldsymbol{U}(\tau + (2k+1)\pi) \end{bmatrix} - \mathbf{C}_2\boldsymbol{f}\left(\boldsymbol{\Psi}(\tau + (2k+1)\pi), \boldsymbol{U}(\tau + (2k+1)\pi), \tau + \pi\right) \\
&= \mathbf{C}_2\left[\frac{d}{d\tau}\begin{bmatrix}\boldsymbol{\Psi}(\tau + (2k+1)\pi)\\ \boldsymbol{U}(\tau + (2k+1)\pi)\end{bmatrix} - \boldsymbol{f}\left(\boldsymbol{\Psi}(\tau + (2k+1)\pi), \boldsymbol{U}(\tau + (2k+1)\pi), \tau + (2k+1)\pi\right)\right] \\
&= \mathbf{o}. \qquad (8.1)
\end{aligned}$$

Thus, the right-hand side of Eq.(2.25) satisfies Eq.(2.6).

On the other hand, assume that $n = 2k$ ($k = 1, 2, \ldots$), then the right-hand side of the Eq.(2.25) satisfies

$$\begin{aligned}
&\frac{d}{d\tau}\mathbf{C}_2 \begin{bmatrix} \boldsymbol{\Psi}(\tau + 2k\pi) \\ \boldsymbol{U}(\tau + 2k\pi) \end{bmatrix} - \boldsymbol{f}\left(\widehat{\mathbf{C}}_2\boldsymbol{\Psi}(\tau + 2k\pi), \widehat{\mathbf{C}}_2\boldsymbol{U}(\tau + 2k\pi), \tau\right) \\
&= \mathbf{C}_2\frac{d}{d\tau} \begin{bmatrix} \boldsymbol{\Psi}(\tau + 2k\pi) \\ \boldsymbol{U}(\tau + 2k\pi) \end{bmatrix} - \mathbf{C}_2\boldsymbol{f}\left(\boldsymbol{\Psi}(\tau + 2k\pi), \boldsymbol{U}(\tau + 2k\pi), \tau + \pi\right) \\
&= \mathbf{C}_2\left[\frac{d}{d\tau}\begin{bmatrix}\boldsymbol{\Psi}(\tau + 2k\pi)\\ \boldsymbol{U}(\tau + 2k\pi)\end{bmatrix} - \boldsymbol{f}\left(\boldsymbol{\Psi}(\tau + 2k\pi), \boldsymbol{U}(\tau + 2k\pi), \tau + \pi + 2k\pi\right)\right] \\
&= \mathbf{C}_2\left[\boldsymbol{f}\left(\boldsymbol{\Psi}(\tau + 2k\pi), \boldsymbol{U}(\tau + 2k\pi), \tau + 2k\pi\right)\right. \\
&\qquad\qquad \left. - \boldsymbol{f}\left(\boldsymbol{\Psi}(\tau + 2k\pi), \boldsymbol{U}(\tau + 2k\pi), \tau + \pi + 2k\pi\right)\right] \\
&= \mathbf{C}_2 \begin{bmatrix} \boldsymbol{E}(\tau) - \boldsymbol{E}(\tau + \pi) \\ \mathbf{o} \end{bmatrix}. \qquad (8.2)
\end{aligned}$$

Thus, the right-hand side of Eq.(8.2) is not identically equal to $\mathbf{o}$. That is, the right-hand side of the Eq.(2.25) cannot be the solution of Eq.(2.6). As a result, period-$2k$ oscillation

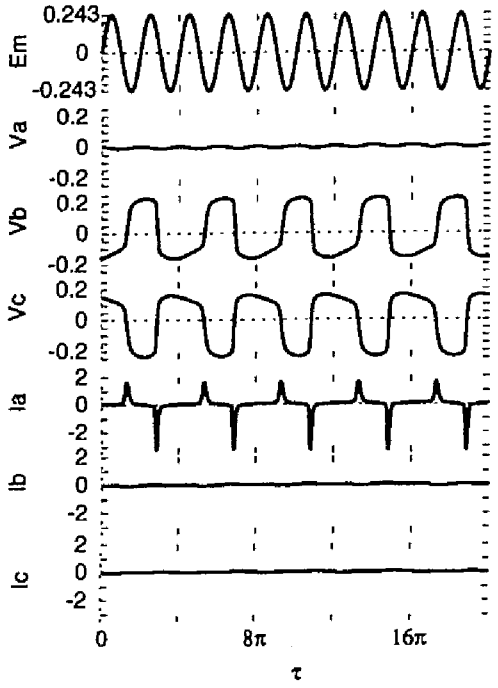

(a)

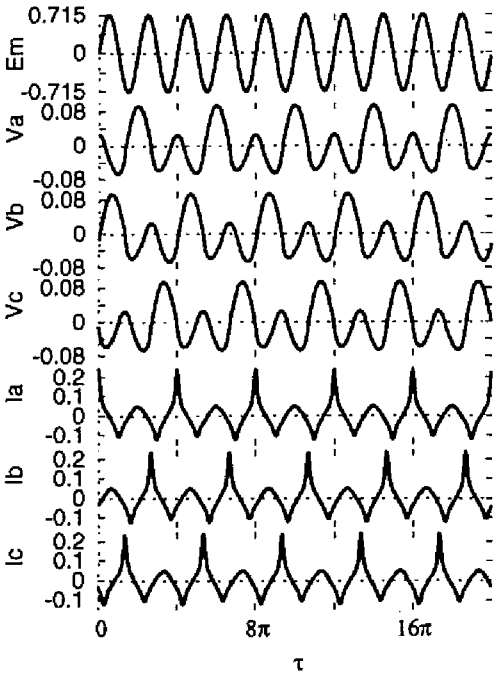

(b)

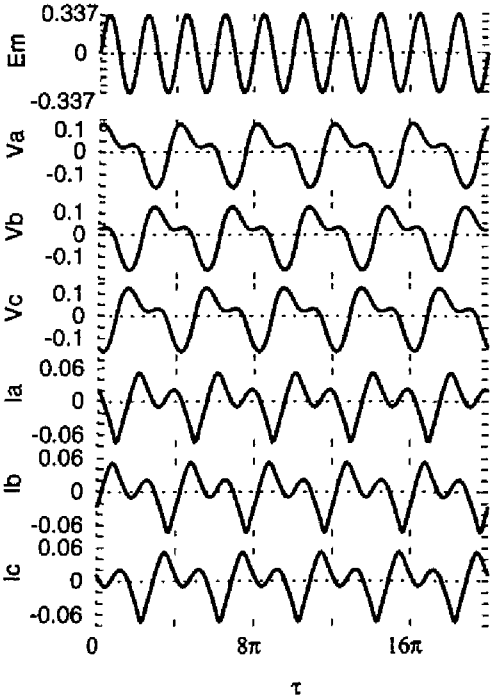

(c)

(a) Mode M_1
Em=0.243, η=0.22,
R=2.5[Ω], r=2.0[Ω]

(b) Mode M_3
Em=0.715, η=0.4,
R=1.0[Ω], r=0.8[Ω]

(c) Mode M_3'
Em=0.337, η=1.06,
R=2.5[Ω], r=2.0[Ω]

Fig. 8.1: Waveforms of periodic 1/2-subharmonic oscillations of the three modes.

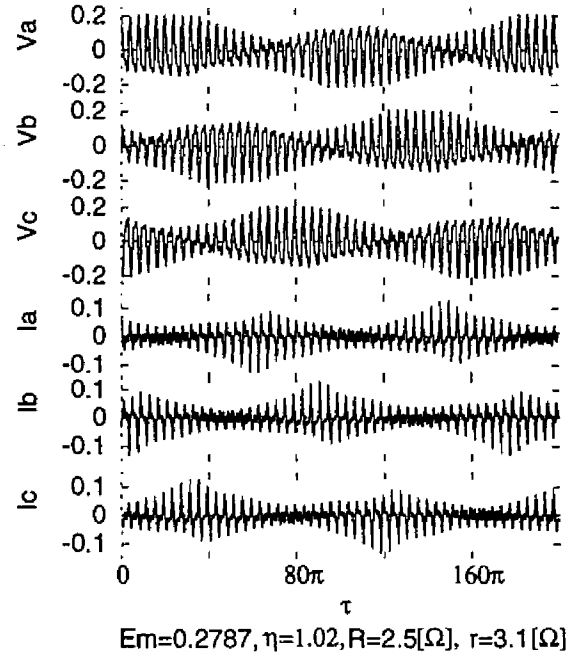

Fig. 8.2: Waveforms of an almost periodic 1/2-subharmonic oscillation with beat.

$(k = 1, 2, \ldots)$ can not have the symmetry with respect to $\mathbf{C}_2$. Especially, as for the 1/2-subharmonic oscillation, it becomes apparent that 1/2-subharmonic oscillation of period-2 doesn't have symmetry with respect to $\mathbf{C}_2$.

Except for the periodic oscillations, almost periodic oscillations accompanied with beat are generated. Fig.8.2 shows the waveforms by computation. The oscillation is generated near the M_3' region.

8.3 Single-phase Oscillation

8.3.1 Periodic Solution Curve

In this section, we pay attention to M_1 oscillation in which the inductor L_a is active and the other two are not. Applying the general homotopy method, we investigate the bifurcation phenomena of mode M_1. Fig.8.3 shows the periodic solution curve on E_m-Ψ_a plane at $\eta = 0.22$. The generated bifurcations are saddle-node bifurcations $\mathrm{S}_1 \sim \mathrm{S}_4$, period doubling bifurcations $\mathrm{D}_1 \sim \mathrm{D}_6$, and Neimark-Sacker bifurcation N_1. The solution curve

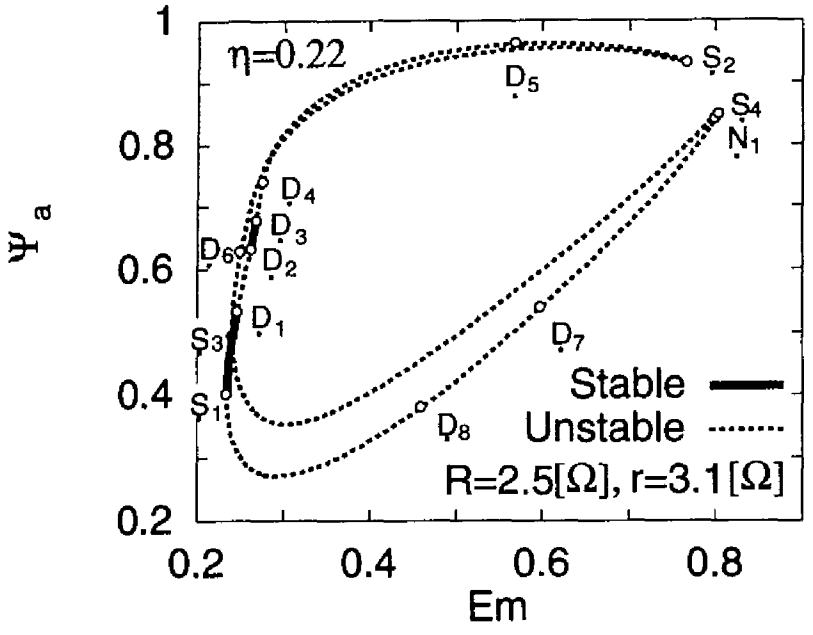

Fig. 8.3: Periodic solution curve of 1/2-subharmonic M_1 oscillation in three-phase circuit.

is folded back on the bifurcation S_2 and S_4. The stable region is in the lower part of the amplitude E_m and splits into two parts, that is, between S_1 and D_1 and between D_2 and D_3. The pitchfork bifurcations which are observed in the solution curve of the single-phase 1/3-subharmonic oscillation are not generated because the 1/2-subharmonic oscillation doesn't have the symmetry with respect to $\mathbf{C}_2$.

For the comparison of Fig.8.3, the solution curve in the single-phase-like circuit is shown in Fig.8.4. In the single-phase-like circuit, saddle-node bifurcations $\hat{S}_1$ and $\hat{S}_2$, and period doubling bifurcations $\hat{D}_1 \sim \hat{D}_4$ are generated. The stable region is in the lower and higher part of the amplitude E_m. That is, between $\hat{S}_1$ and $\hat{D}_1$ and between $\hat{D}_2$ and $\hat{D}_3$ in the lower part and between $\hat{D}_4$ and $\hat{S}_2$ in the higher part.

Comparing Fig.8.3 and Fig.8.4, we can find that the folding back of solution curve in the three-phase circuit is distinctive. As a result, the folding back in the three-phase circuit make the stable region in the higher part of E_m in the single-phase-like circuit disappear. On the other hand, in the lower part of E_m ($S_1 \rightarrow D_3$ and $\hat{S}_1 \rightarrow \hat{D}_3$) both diagrams are fairly in good agreement.

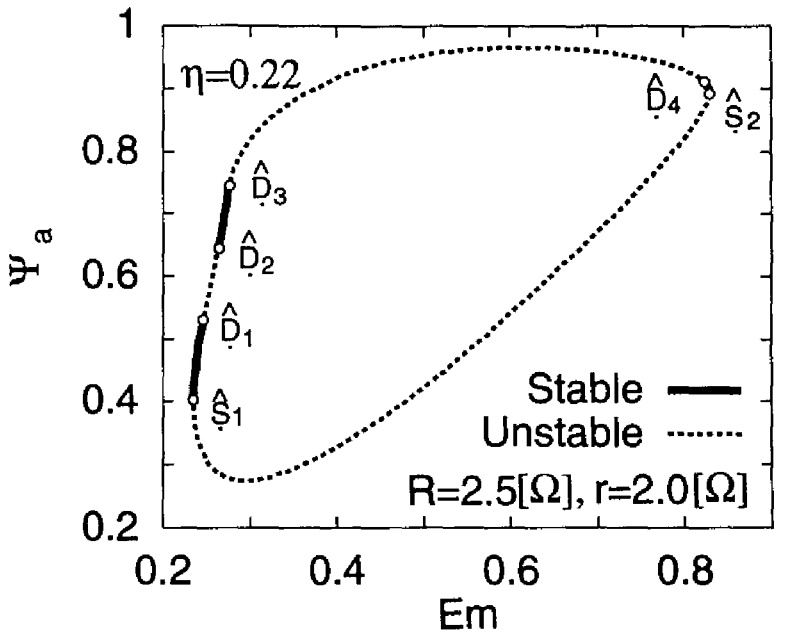

Fig. 8.4: Periodic solution curve of 1/2-subharmonic oscillation in single-phase-like circuit.

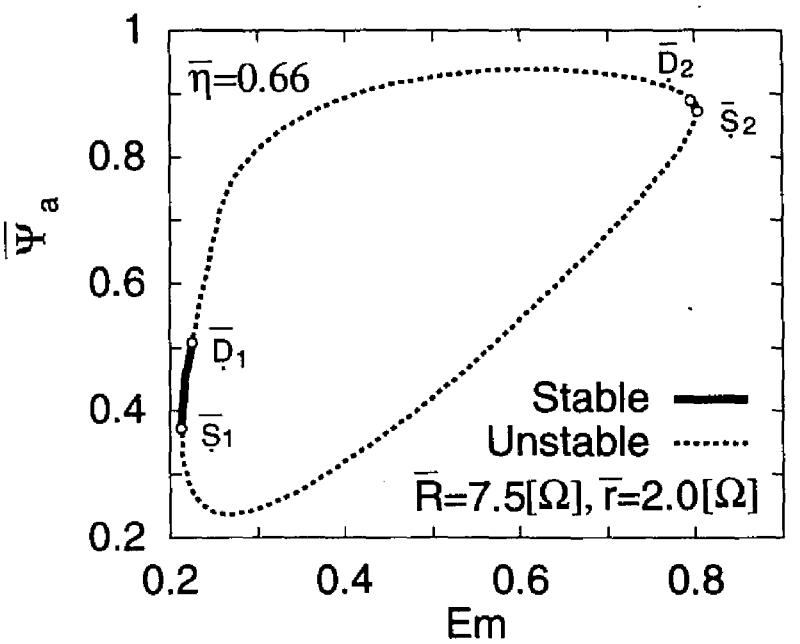

Fig. 8.5: Periodic solution curve of 1/2-subharmonic oscillation in single-phase circuit.

Next, we compare with the periodic solution curve in the single-phase circuit which is shown in Fig.8.5. In the single-phase circuit, saddle-node bifurcations $\bar{S}_1$ and $\bar{S}_2$, and period doubling bifurcations $\bar{D}_1$ and $\bar{D}_2$ are generated. The stable part is in the lower and

higher part of the amplitude E_m. That is, between $\bar{S}_1$ and $\bar{D}_1$ in the lower part and between $\bar{D}_2$ and $\bar{S}_2$ in the higher part.

Comparing Fig.8.4 and Fig.8.5, in the higher part of E_m both diagrams are fairly in good agreement. However, as far as the structure of the stable part in the lower part of E_m is concerned, both diagrams are different each other. Thus, in the lower part of E_m the solution curve in the single-phase-like circuit is more similar to that in the three-phase circuit than that in the single-phase circuit.

8.3.2 Bifurcation Set

Applying the general homotopy method, we obtain the bifurcation sets. The bifurcation sets of mode M_1 on E_m-η plane is shown in Fig.8.6. In this figure, only the bifurcations on which stable solutions lose their stability are shown. In the higher part of η the stable region lose its stability by saddle-node bifurcation set on the outer boundary and period doubling bifurcation set on the inner boundary. In the lower part of both E_m and η, the structure of bifurcation sets are so complicated that the enlarged figure is also shown in Fig.8.6. There exist several period doubling bifurcation sets and Neimark-Sacker bifurcation sets connects them. In the part where E_m is higher and η is lower, there is not stable region because of the folding back of the solution curve.

For the comparison of Fig.8.6, the bifurcation sets of 1/2-subharmonic oscillations in the single-phase-like and single-phase circuit are shown in Fig.8.7 and Fig.8.8, respectively. As for the single-phase circuit, the stable region is annular. As for the single-phase-like circuit, the stable region is also annular as a whole. However, there is salience in the part $E_m \simeq 0.3, \eta \simeq 0.2$. This special feature make differences in the solution curves of the single-phase-like and single-phase circuit. This region corresponds to the region of complicated structure in the three-phase circuit.

In comparison with the single-phase-like and single-phase circuit, the special feature of the three-phase circuit is that there is not stable region in the higher part of E_m in the lower part of η. This feature is caused by the folding back of the solution curve and is also observed on the single-phase 1/3-subharmonic oscillation in the three-phase circuit. Additionally, the connections between Neimark-Sacker and period doubling bifurcation sets are distinctive in the three-phase circuit.

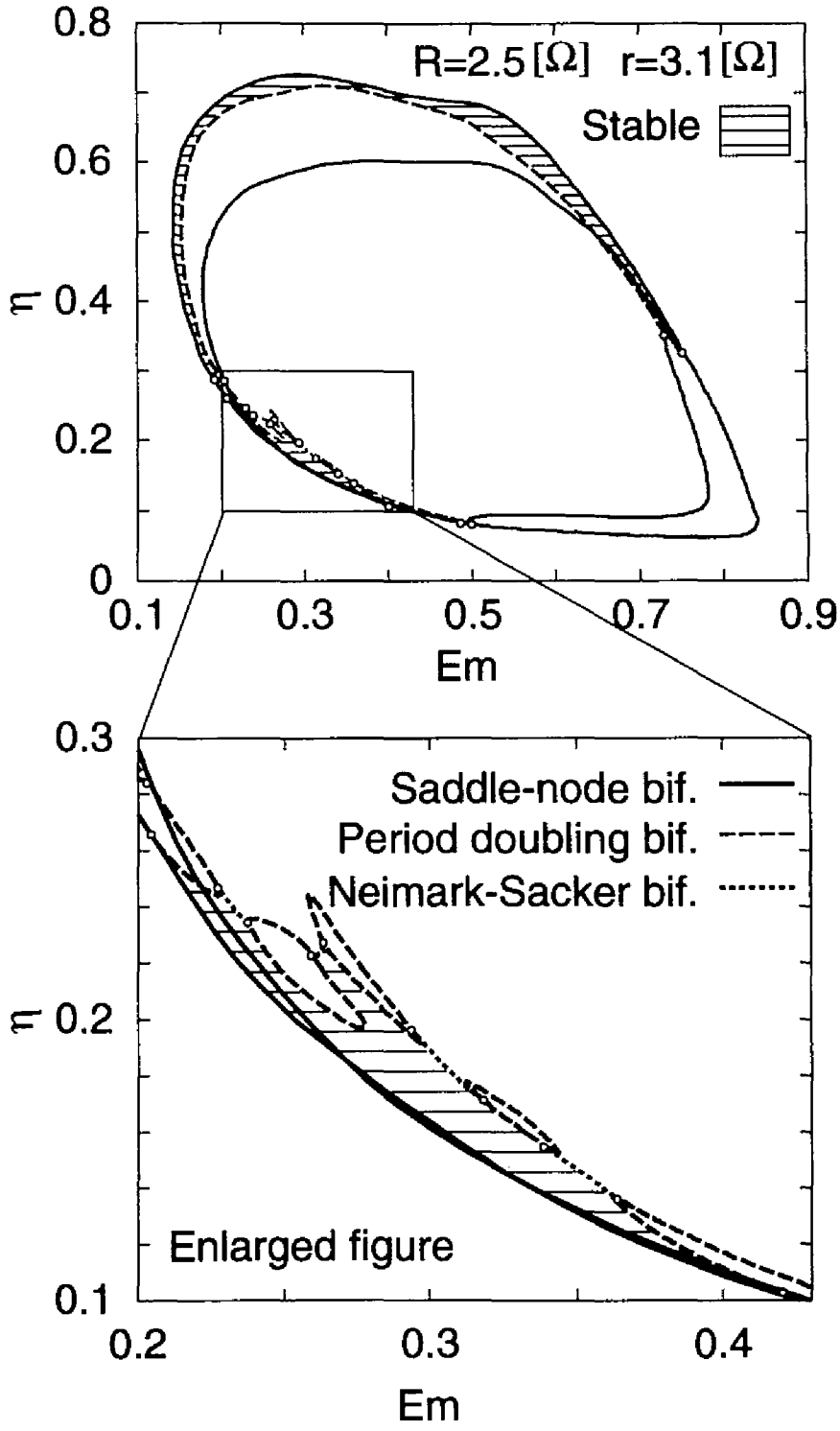

Fig. 8.6: bifurcation sets of 1/2-subharmonic M_1 oscillation.

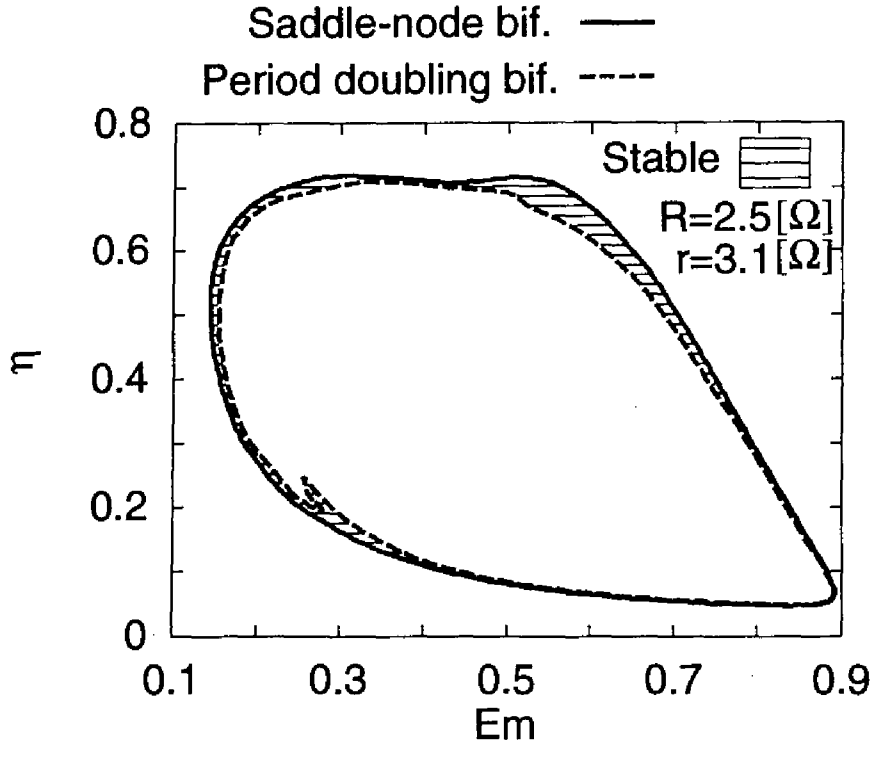

Fig. 8.7: Bifurcation sets of 1/2-subharmonic oscillation in single-phase-like circuit.

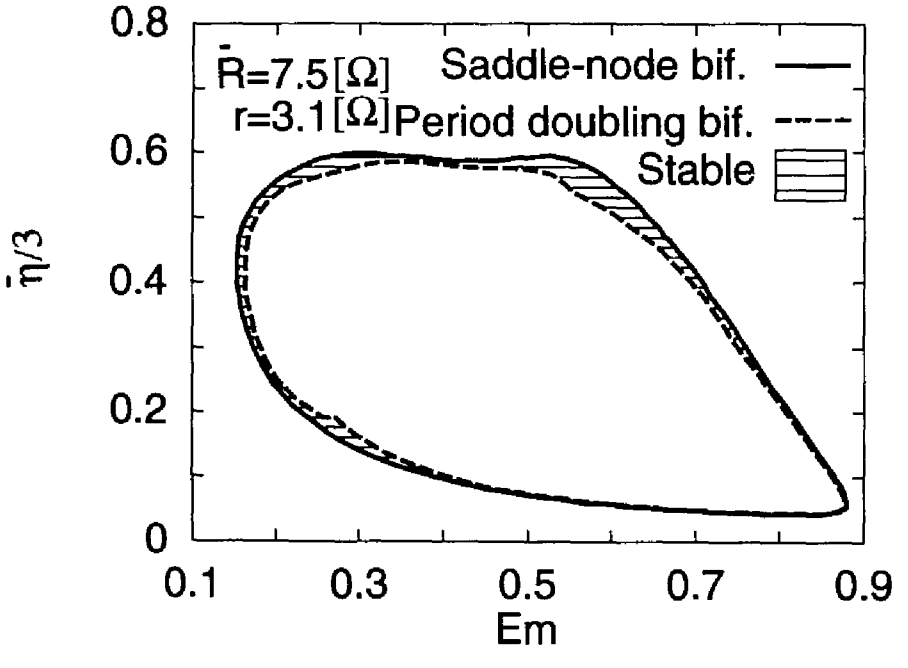

Fig. 8.8: Bifurcation sets of 1/2-subharmonic oscillation in single-phase circuit.

8.3.3 Experimental Results

We fix the series resistance $R = 2.5\Omega$ and the delta-connected resistance $r = 3.1\Omega$ which are chosen in section 8.2. By increasing or decreasing the source line-voltage E_Δ and the capacitance C, the region of single-phase 1/2-subharmonic oscillation is obtained by the method shown in section 3.5. In this experiment, the phase angle at which the source voltage are applied and the initial charge of capacitor are chosen every time so that the oscillation may be generated in a wide region.

Fig.8.9 shows the bifurcation phenomena of 1/2-subharmonic and 1/3-subharmonic oscillations on E_Δ-X_c plane. The 1/2-subharmonic oscillation is generated in the region of larger amplitude of E_Δ than 1/3-subharmonic oscillation and the region is restricted in the lower part of E_Δ.

Fig.8.10 shows the bifurcation phenomena of 1/2-subharmonic oscillations in the single-phase-like circuit. In the higher part of the source line-voltage E_Δ, the 1/2-subharmonic oscillations can not be observed by the harmonic resonance.

Comparing the single-phase-like circuit with the three-phase circuit, the relation between the regions of order 1/2 and 1/3 is similar. However, the 1/2-subharmonic oscillation in the higher part of source line-voltage is distinctive in the single-phase-like circuit.

Thus, the experimental results agree fairly with the analytical ones.

8.4 Symmetric Oscillation

8.4.1 Analytical Results of Mode M_3

We set the series resistance $R = 1.0\Omega$ and the delta-connected resistance $r = 0.8\Omega$. The typical amplitude characteristics of mode M_3 for the parameter $\eta = 0.9$ are shown in Fig.8.11. Here, the vertical axis I is the maximum value of inductor currents. In this figure, we can find saddle-node bifurcations S_5 and S_6 and Neimark-Sacker bifurcations N_2 and N_3. The stable region is restricted in the higher amplitude of E_m and the oscillation loses its stability by the Neimark-Sacker bifurcation N_2.

The bifurcation sets of mode M_3 on E_m-η plane is shown in Fig. 8.12. In this figure, only the bifurcations on which stable solutions lose their stability are shown. The large stable region is confirmed in the higher amplitude of E_m. Additionally, a small stable region is confirmed in the part $E_m \simeq 0.3, \eta \simeq 0.05$ which is enlarged in the figure. Also

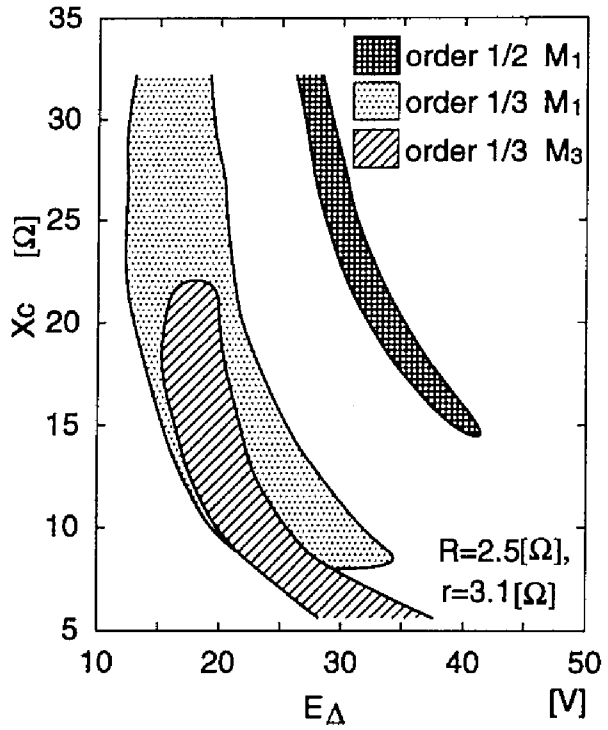

Fig. 8.9: Bifurcation phenomena of 1/2-subharmonic M_1 oscillations (experiment).

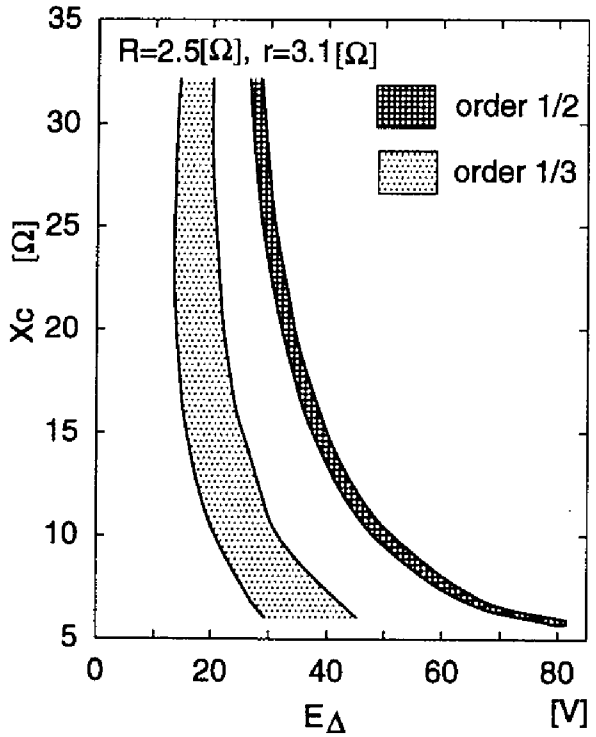

Fig. 8.10: Bifurcation phenomena of 1/2-subharmonic oscillations in single-phase-like circuit (experiment).

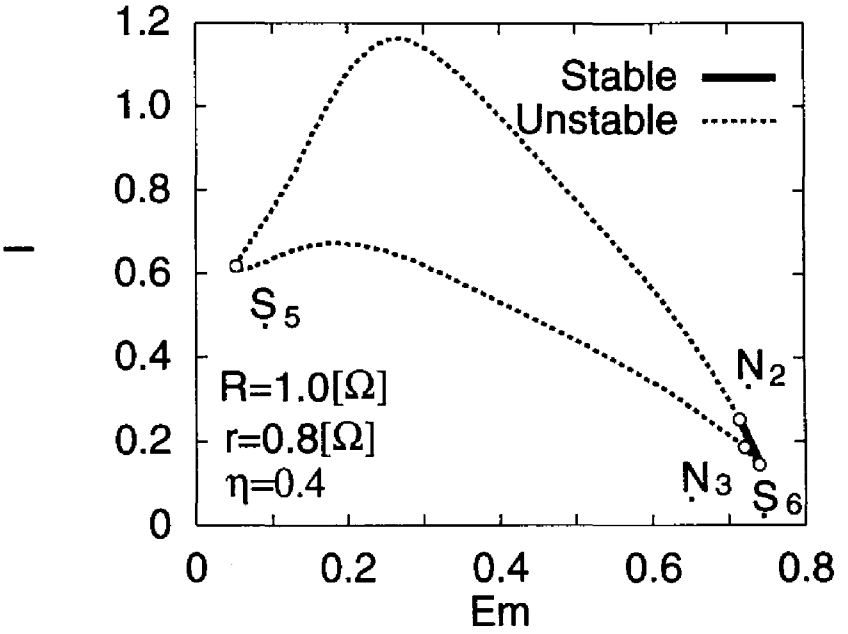

Fig. 8.11: Amplitude characteristics of 1/2-subharmonic M_3 oscillation.

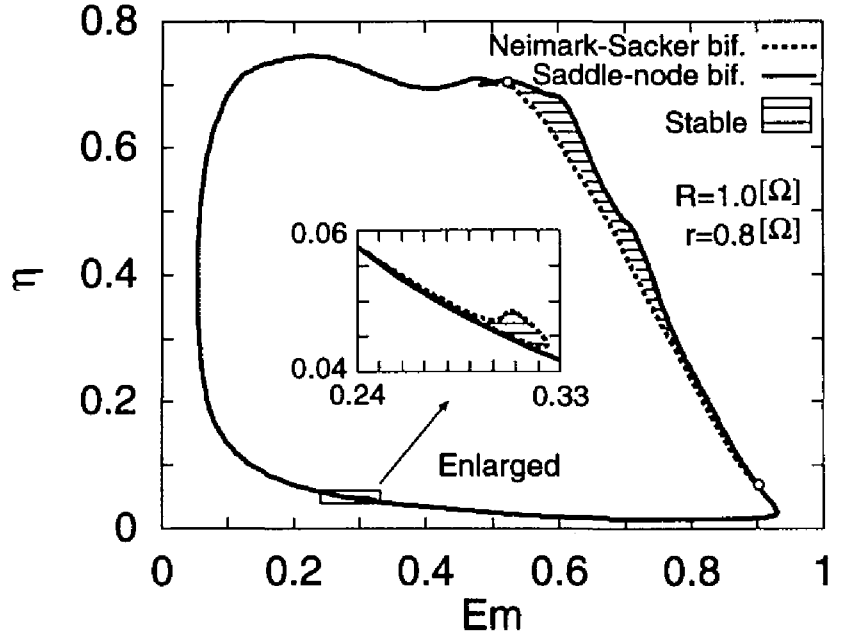

Fig. 8.12: Bifurcation sets of 1/2-subharmonic M_3 oscillation.

in this region, the solution lose its stability by Neimark-Sacker bifurcation. Thus, the loss of stability by Neimark-Sacker bifurcation is special feature. Additionally, it is distinctive that there is not large stable region in the lower part of the amplitude E_m.

8.4.2 Analytical Results of M_3'

We set the series resistance $R = 1.0\Omega$ and the delta-connected resistance $r = 0.8\Omega$. The typical amplitude characteristics of mode M_3' for the parameter $\eta = 1.06$ are shown in Fig.8.13. In this figure, we can find only saddle-node bifurcations S_7 and S_8.

The bifurcation sets of mode M_3' on E_m-η plane is shown in Fig.8.14. There is only saddle-node bifurcation sets. For the comparison of Fig.8.14, the bifurcation sets of 1/2-subharmonic oscillations in the single-phase circuit are shown in Fig.8.15. This oscillation is observed in the higher part of η than the oscillations shown in Fig.8.8. In this figure, only saddle-node bifurcation sets are generated. The region form is also similar to that in the three-phase circuit. Thus, as for the mode M_3' the structure of bifurcations in the three-phase and single-phase circuit agrees fairly.

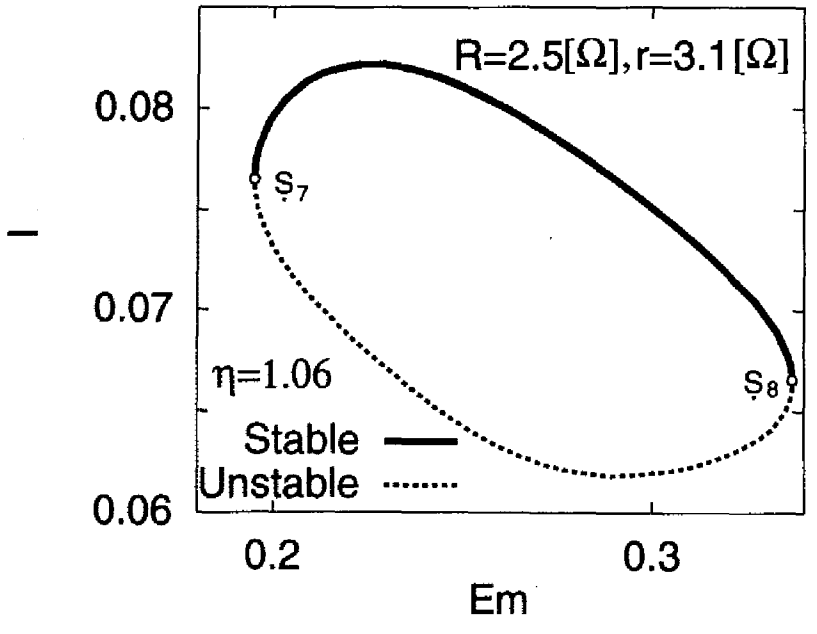

Fig. 8.13: Amplitude characteristics of 1/2-subharmonic M_3' oscillation.

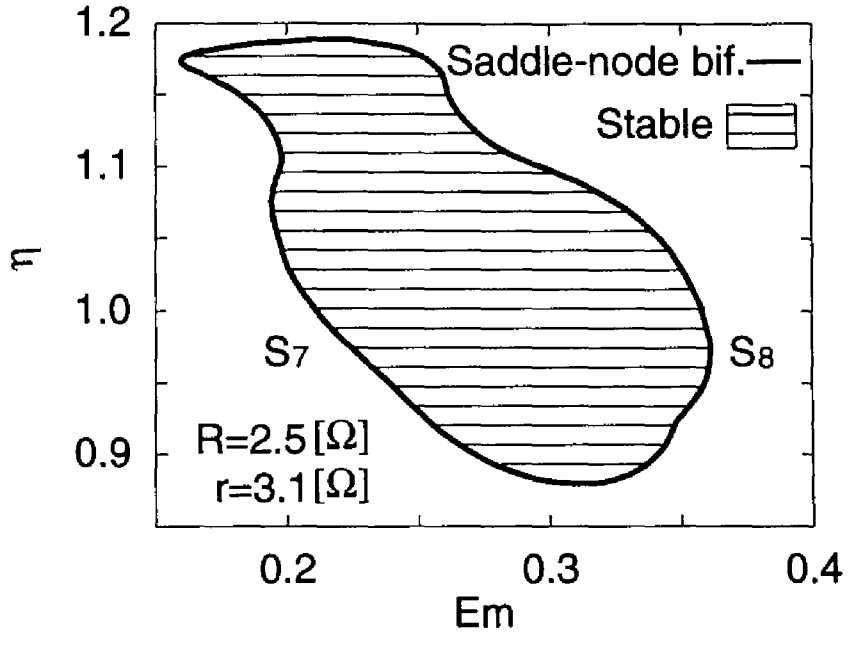

Fig. 8.14: Bifurcation sets of 1/2-subharmonic M_3' oscillation.

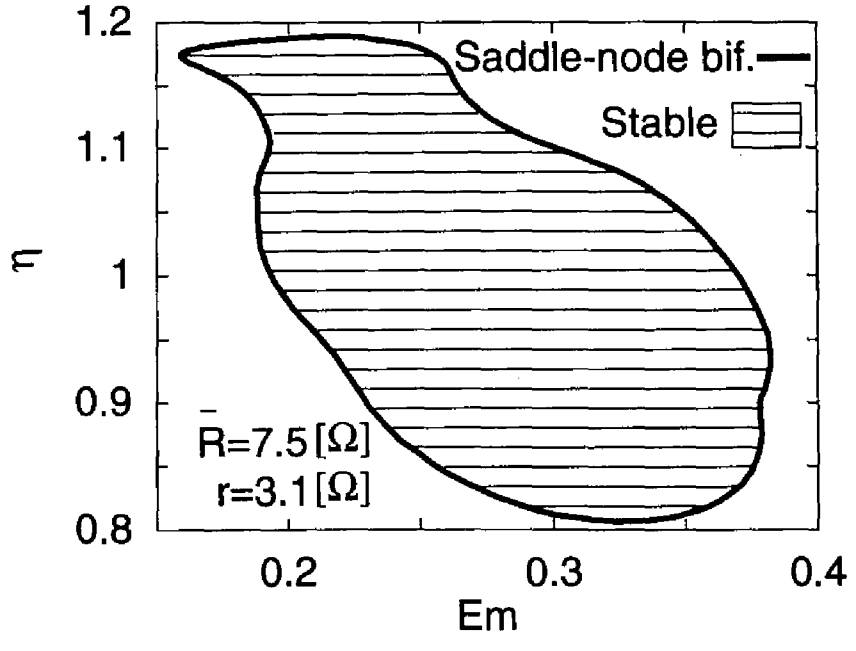

Fig. 8.15: Bifurcation sets of 1/2-subharmonic oscillation in single-phase circuit.

8.5 Concluding Remarks

In this section, several bifurcations of three modes of 1/2-subharmonic oscillations are revealed by the homotopy method and real experiment.

For the comparison of the single-phase oscillation in the three-phase circuit, the single-phase-like and single-phase circuit are investigated. The structure of stable regions of these two circuits are annular, that is, the outer boundary is saddle-node bifurcation and the inner boundary is period doubling bifurcation. On the other hand, in the three-phase circuit, because of the folding back of the solution curve, there is not stable region on the higher part of E_m. Another special feature is the connections between Neimark-Sacker and period doubling bifurcation sets. This structure can not be found in the single-phase-like and single-phase circuit.

As for M_3 oscillation, it is distinctive that the large stable region is restricted in the higher part of the amplitude E_m and the solution loses its stability by Neimark-Sacker bifurcation.

As for M_3' oscillation, the solution curve and bifurcation sets are very simple. Additionally, there exist oscillations in the single-phase circuit which corresponds to M_3' oscillations. As far as mode M_3' is concerned, the solution curve and bifurcation sets in the three-phase circuit and the single-phase circuit are almost same.

Chapter 9

Conclusions

In this thesis, the bifurcation phenomena in the three-phase circuit is investigated by the homotopy methods and experiments. The special features of the three-phase circuit are revealed by comparing with the single-phase circuit and the single-phase-like circuit. Further, in order to reveal the effects of the nonlinear couplings, the coupled single-phase circuit is also investigated.

In chapter 4, the bifurcation phenomena of single-phase 1/3-subharmonic oscillations are investigated. It becomes manifest that the three-phase circuit is distinctive in the point of the folding back of the periodic solution curve. As a result, the stable region of the single-phase 1/3-subharmonic oscillation in the three-phase circuit is restricted in the lower amplitude of the source voltage although the structure of the single-phase-like circuit is annular. Further, it is shown that the folding back is caused by the participation of the secondary inductor.

In chapter 5, the bifurcation phenomena of two-phase 1/3-subharmonic oscillations are investigated. It becomes apparent that the participation of two active inductors causes Neimark-Sacker bifurcations and co-dimension two bifurcations. As a result, the bifurcation phenomena of two-phase 1/3-subharmonic oscillation is U-type structure. Additionally, the relation between single-phase and two-phase 1/3-subharmonic oscillation are revealed by the coupled single-phase circuit and single-phase-like circuit.

In chapter 6, the bifurcation phenomena of symmetric 1/3-subharmonic oscillations are investigated. It is revealed that a pure 1/3-subharmonic oscillation cannot be generated in the three-phase circuit. As for the oscillation accompanied with beat, the solution curve which include many equivalent solutions is distinctive. The beat causes the mode locking

and unlocking. Additionally, the relation between frequency and symmetry is revealed. Further, the hyperchaotic oscillation is confirmed.

In chapter 7, the bifurcation phenomena of harmonic oscillations are investigated. There exist three modes of periodic oscillations. It becomes manifest that Neimark-Sacker bifurcation and co-dimension two bifurcation are distinctive in the three-phase circuit. As a result, the periodic oscillations lose their stability and distinctive chaotic oscillations which are caused by the delta-connection of nonlinear inductor are generated. Additionally, the relations as well as differences between the three-phase circuit and single-phase circuit are revealed by the coupled single-phase circuit. Further, the transient states of several oscillations are investigated by the experiment with phase controller and the relation between the closed phase angle and generated mode becomes clear.

In chapter 8, the bifurcation phenomena of 1/2-subharmonic oscillations are investigated. There exist three modes of periodic oscillations. As for the single-phase 1/2-subharmonic oscillation, the structure of folding back which is also observed in the single-phase 1/3-subharmonic oscillation are shown. Additionally, it becomes evident that the connections of Neimark-Sacker and period doubling bifurcation sets are distinctive in the three-phase circuit. As for the symmetric 1/2-subharmonic oscillation with large inductor currents, it is shown that the participation of three active inductors causes Neimark-Sacker bifurcation and the stable region is restricted in the higher amplitude of voltage sources. On the other hand, the symmetric 1/2-subharmonic oscillations with small inductor currents are similar to the 1/2-subharmonic oscillations in the single-phase circuit.

As a whole, the experimental results agree fairly with the analytical ones.

Thus, several distinctive feature in the three-phase circuit is revealed. The feature is caused by the nonlinear coupling and the symmetry of the three-phase circuit.

Acknowledgments

I wish to express my sincere gratitude to Professor Kohshi Okumura at Kyoto University for his continuous guidance and encouragement in all aspects of this study.

I also benefited very much from valuable discussions with Dr. Satoshi Ichikawa at Kyoto University.

The work on the experimental device was greatly guided and supported by Mr. Tsutomu Yamada at Hitachi Research Laboratory when he was a graduate student at Kyoto University.

Thanks are also given the members of Okumura Laboratory (Department of Electrical Engineering, Kyoto University) for their comments and technical supports.

Bibliography

[1] C. Hayashi: "Non-linear Oscillations in Physical Systems", McGraw Hill, New York (1964).

[2] Y. Ueda, N. Akamatsu, C. Hayashi : "Computer simulation of nonlinear ordinary differential equations and non-periodic oscillations", Trans. IECEJ, **56-A**, pp. 218–225 (1973).

[3] M. Goto: "Undamped electric oscillation and electric instability of a transmission system", IEEJ, **51**, pp. 759–771 (1931).

[4] I. A. Wright: "Three-phase subharmonic oscillation in symmetrical power systems", IEEE Trans, **PAS-90**, 3, pp. 1295–1304 (1971).

[5] C. Kieny: "Application of the bifurcation theory in studying and understanding the global behavior of a ferroresonant electric power circuit", IEEE Trans., **PD-6**, 2, pp. 866–872 (1991).

[6] J. R. Marti and A. C. Soudack: "Ferroresonance in power systems: Fundamental solutions", Proc. IEE-C, **138**, 4, pp. 321–329 (1991).

[7] B. A. Mork and D. L. Stuehm: "Application of nonlinear dynamics and chaos to ferroresonance in distribution systems", IEEE Trans., **PD-9**, 2, pp. 1009–1017 (1994).

[8] A. E. A. Araujo: "Ferroresonance in power systems: chaotic behavior", Proc. IEE-C, **140**, 2, pp. 237–240 (1993).

[9] K. Okumura and A. Kishima: "Nonlinear oscillations in three-phase circuit", IEEJ, **96B**, 12, pp. 599–606 (1976).

[10] K. Okumura and A. Kishima: "Subharmonic oscillations in three-phase circuit", IEEJ, **97B**, 4, pp. 199–206 (1977).

[11] K. Okumura and A. Kishima: "Subharmonic oscillations in three-phase circuit", Int. J. of Nonlinear Mechanics, **20**, No.5/6, pp. 427–438 (1985).

[12] K. Okumura, S. Fukuda, A. Kishima : "Analysis of frequency entrainment in three-phase circuits", IEEJ, **107B**, 3, pp. 115–122 (1987).

[13] K. Okumura, S. Nakamura, A. Kishima: "Experimental and analytical investigation on 1/3-subharmonic oscillations in three-phase circuit", IEEJ, **107B**, 1, pp. 1–8 (1987).

[14] K. Okumura and N. Miyamoto: "Subharmonic entrainment of frequency in nonlinear three-phase circuits with symmetry", IEEE Proc. ISCAS, **4**, pp. 2624–2627 (1993).

[15] K. Okumura and T. Yamada: "Unsymmetrical subharmonic oscillations in symmetrical nonlinear three-phase circuit", Proc. 3rd International Specialist Workshop on NDES, pp. 71–74 (1995).

[16] Y. Katsuta and H. Kawakami: "Bifurcations of equilibriums and periodic solutions in nonlinear autonomous system with symmetry", IEICEJ Trans. Fundamentals, **75A**, 6, pp. 1035–1044 (1992).

[17] Y. Katsuta and H. Kawakami: "Bifurcations of periodic solutions in nonlinear nonautonomous system with symmetry", IEICEJ Trans. Fundamentals, **76A**, 12, pp. 1753–1760 (1993).

[18] M. Golubitsuky, I. Stewart, D. G. Schaeffer : "Singularities and Groups in Bifurcation Theory Vol. II", Springer-Verlag, New York (1988).

[19] D. H. Sattinger: "Topics in Stability and Bifurcation Theory, Lecture Notes in Mathematics 762", Springer-Verlag, New York (1979).

[20] T. J. Aprille and T. N. Trick: "Steady-state analysis of nonlinear circuits with periodic inputs", IEEE Proc., **60**, No. 1, pp. pp. 108–116 (1972).

[21] C. B. Garcia and W. I. Zangwill: "Pathway to Solutions, Fixed Points, and Equilibria", Prentice-Hall London (1981).

[22] Wiggins, S : "Introduction to Applied Nonlinear Dynamical Systems and Chaos", Springer-Verlag, New York (1990).

[23] S. N. Chow and J. K. Hale: "Methods of Bifurcation Theory", Springer-Verlag, New York (1982).

[24] G. Ioss and D. Joseph: "Elementary Stability and Bifurcation Theory", Springer-Verlag, New York (1980).

[25] H. B. Keller: "Lectures on Numerical Method in Bifurcation Problems", Springer-Verlag Heidelberg (1987).

[26] Y. A. Kuznetsov: "Elements of Applied Bifurcation Theory", Springer-Verlag New York (1995).

[27] V. I. Arnold: "Geometrical Methods in the Theory of Ordinary Differential Equations", Springer-Verlag New York (1983).

[28] H. Kawakami: "Bifurcation of periodic responses in forced dynamic nonlinear circuits: computation of bifurcation values of the system parameters", IEEE Trans., **CAS-31**, 3, pp. 248–260 (1984).

[29] G. Moore and A. Spence: "The calculation of turning points of nonlinear equations", SIAM J. Numer. Ana., **17**, 4, pp. 567–576 (1980).

[30] G. Moore: "The numerical treatment of non-trivial bifurcation points", Numer. Funct. Anal. Optim., **2**, pp. 441–472 (1980).

[31] Guckenheimer and Holmes: "Nonlinear Oscillations, Dynamical Systems, and Bifurcations of Vector Fields", Springer-Verlag, New York (1983).

[32] R. Seydel: "Practical Bifurcation and Stability Analysys", Springer-Verlag, New York (1994).

[33] T. Yoshinaga and H. Kawakami: "Codimension two bifurcation in nonlinear circuits with periodically forcing term", IEICE Trans. Fundamentals, **72A**, 11, pp. 1821–1828 (1989).

[34] R. C. Hilborn: "Chaos and Nonlinear Dynamics", Oxford University Press (1994).

[35] J. M. T. Thompson, H. B. Stewart, Y.Ueda : "Safe, explosive, and dangerous bifurcations in dissipative dynamical systems", Phys. Rev., **E 49**, pp. 1019–1027 (1994).

[36] I. Shimada and T. Nagashima: "A numerical approach to ergodic problem of dissipative dynamics systems", Progr. Theor. Phys., **61**, 6, pp. 1605–1616 (1979).

[37] T. S. Parker and L. O. Chua: "Practical numerical algorithms for chaotic systems", Springer-Verlag, New York (1989).

References by the Author

[101] T. Hisakado and K. Okumura:" On Modes and Bifurcations of 1/3-Subharmonic Oscillations in Nonlinear Three- Phase Circuit with Symmetry," Record of The 1994 Kansai-Section Joint Convention of Institutes of Electrical Engineering, Japan, G1-26, 1994.

[102] T. Hisakado and K. Okumura:" On Unsymmetrical Phenomena of 1/3-Subharmonic Oscillations in Symmetrical Three-Phase Circuit," Proc. IEICE General Conference, SA-2-6, 1995.

[103] T. Hisakado, T. Yamada and K. Okumura:"On Single-Phase 1/3-Subharmonic Oscillations in Three-Phase Circuit", Technical Report of IEICE, NLP95-3, pp.17-24, 1995.

[104] T. Hisakado, T. Yamada and K. Okumura:"On Two-Phase 1/3-Subharmonic Oscillations in Three-Phase Circuit", Technical Report of IEICE, NLP95-70, pp.47-54, 1995.

[105] K. Okumura and T. Hisakado, "On the Bifurcations of Subharmonic Oscillations in Nonlinear Three-Phase Circuit," Proc. ISCAS, 3, pp.44-47, 1996.

[106] K. Okumura and T. Hisakado, "Several Bifurcations of Subharmonic Oscillations in Nonlinear Three-Phase Circuit," Proc. 4th International Specialist Workshop on NDES, pp.369-374, Seville 1996.

[107] T. Hisakado and K. Okumura:" On Bifurcation of Fundamental Harmonic Oscillations," Proc. IEICE General Conference, SA-2-5, pp437-438, 1996.

[108] T. Hisakado, T. Yamada and K. Okumura:" Single-Phase 1/3-Subharmonic Oscillations in Three-Phase Circuit," IEICE Trans. Fundamentals, **J79-A**, No. 9, pp.1553-1561, 1996.

[109] T. Hisakado and K. Okumura:" Two-Phase 1/3-Subharmonic Oscillations in Three-Phase Circuit," IEICE Trans. Fundamentals, **J80-A**, No. 2, pp.355-362, 1997.

[110] T. Hisakado and K. Okumura:" Bifurcations of Harmonic Oscillations in Three-Phase Circuit", Technical Report of IEICE, NLP96-5, pp.157-164, 1996.

[111] T. Hisakado and K. Okumura: "Analytical and Experimental Approach to Bifurcation Phenomena of Subharmonic Oscillations," Proc, NOLTA'96, pp. 129-132, 1996.

[112] T. Hisakado and K. Okumura:" On Relation between single-phase and two-phase 1/3-subharmonic Oscillations in Symmetrical Three-Phase Circuit," Record of The 1995 Kansai-Section Joint Convention of Institutes of Electrical Engineering, Japan, G1-9, 1995.

[113] T. Hisakado and K. Okumura:" The Generation of Symmetry on Subharmonic Oscillations in Three-phase Circuit," Record of The 1996 Kansai-Section Joint Convention of Institutes of Electrical Engineering, Japan, G1-8, 1996.

[114] T. Hisakado and K. Okumura:" The Generation of Symmetrical Subharmonic Oscillations in Three-phase Circuit," Proc. IEICE General Conference, A-2-27, p.84 , 1997.

[115] T. Hisakado and K. Okumura:" Relevancy of Bifurcation Phenomena of 1/3-Subharmonic Oscillation in between Three-phase and Single-phase Circuit," Proc. IEEJ General Conference, 5, 1997.

[116] T. Hisakado and K. Okumura:" Bifurcation Phenomena of Harmonic Oscillations in Three-phase circuit," IEICE Trans. Fundamentals, **E80-A**, No. 6, pp. 1127-1134, 1997.

Appendix A

Generation of Pitchfork Bifurcation

Pitchfork bifurcation arises from special properties which make $\tilde{H}_{01}$ and $\tilde{H}_{20}$ vanish. This can occur in the three-phase circuit by the symmetry with respect to $\mathbf{C}_2$ [24]. To clarify the generation of pitchfork bifurcation, we define the determining equation of the periodic solution by multiple shooting method [26]. Using the mapping $\mathbf{T}_{1/2} : \boldsymbol{R}^{10} \rightarrow \boldsymbol{R}^{10}$, we express the boundary condition instead of Eq.(2.33);

$$\begin{bmatrix} \boldsymbol{x}_0^1 \\ \boldsymbol{x}_0^2 \end{bmatrix} = \mathbf{T}_{1/2}(\boldsymbol{x}_0^1, \boldsymbol{x}_0^2) \tag{A.1}$$

where

$$\boldsymbol{x}_0^1 = \boldsymbol{x}^1(0) \in \boldsymbol{R}^5 \tag{A.2}$$

$$\boldsymbol{x}_0^2 = \boldsymbol{x}^2(0) \in \boldsymbol{R}^5 \tag{A.3}$$

$$\mathbf{T}_{1/2}(\boldsymbol{x}_0^1, \boldsymbol{x}_0^2) = \int_0^{T/2} \begin{bmatrix} \hat{\boldsymbol{f}}(\boldsymbol{x}^1, s) \\ \hat{\boldsymbol{f}}(\boldsymbol{x}^2, s + T/2) \end{bmatrix} ds + \begin{bmatrix} \boldsymbol{x}^1(0) \\ \boldsymbol{x}^2(0) \end{bmatrix}. \tag{A.4}$$

$$\tag{A.5}$$

Then, we define a nonlinear equation

$$\mathbf{F}_{1/2}(\boldsymbol{x}_0) \triangleq \mathbf{S}\boldsymbol{x}_0 - \mathbf{T}_{1/2}(\boldsymbol{x}_0) = \mathbf{o} \tag{A.6}$$

where

$$\boldsymbol{x}_0 = \begin{bmatrix} \boldsymbol{x}_0^1 \\ \boldsymbol{x}_0^2 \end{bmatrix} \in \boldsymbol{R}^{10}, \qquad \mathbf{T}_{1/2}(\boldsymbol{x}_0) = \mathbf{T}_{1/2}(\boldsymbol{x}_0^1, \boldsymbol{x}_0^2) \tag{A.7}$$

$$\mathbf{S} = \begin{pmatrix} \mathbf{o} & \hat{\mathbf{S}} \\ \hat{\mathbf{S}} & \mathbf{o} \end{pmatrix} \in \boldsymbol{R}^{10} \times \boldsymbol{R}^{10}, \tag{A.8}$$

$$\hat{\mathbf{S}} = diag(-1, -1, -1, -1, -1) \in \boldsymbol{R}^5 \times \boldsymbol{R}^5. \tag{A.9}$$

Here, $\mathbf{S}^2 = \mathbf{1}$ is satisfied. Assume that $T = (2k+1)2\pi$ $(k = 0, 1, \ldots)$, then the following relation is satisfied from the symmetry with respect to $\mathbf{C}_2$,

$$\mathbf{F}_{1/2}(\mathbf{S}\boldsymbol{x}_0) = \mathbf{S}^2\boldsymbol{x}_0 - \int_0^{T/2} \begin{bmatrix} \hat{\boldsymbol{f}}(\hat{\mathbf{S}}\boldsymbol{x}^2, s) \\ \hat{\boldsymbol{f}}(\hat{\mathbf{S}}\boldsymbol{x}^1, s+T/2) \end{bmatrix} ds + \mathbf{S}\boldsymbol{x}_0 \tag{A.10}$$

$$= \mathbf{S}^2\boldsymbol{x}_0 - \int_0^{T/2} \begin{bmatrix} \hat{\mathbf{S}}\hat{\boldsymbol{f}}(\boldsymbol{x}^2, s+T/2) \\ \hat{\mathbf{S}}\hat{\boldsymbol{f}}(\boldsymbol{x}^1, s) \end{bmatrix} ds + \mathbf{S}\boldsymbol{x}_0 \tag{A.11}$$

$$= \mathbf{S}\mathbf{F}_{1/2}(\boldsymbol{x}_0) \tag{A.12}$$

If a solution has symmetry with respect to $\mathbf{C}_2$, then the relation

$$\mathbf{S}\boldsymbol{x}_0 = \boldsymbol{x}_0 \tag{A.13}$$

is satisfied. Now, we define another general homotopy function $\mathbf{H} : \boldsymbol{R}^{11} \to \boldsymbol{R}^{11}$

$$\mathbf{H}(\boldsymbol{x}_0, \mu) \triangleq \mathbf{F}_{1/2}(\boldsymbol{x}_0 \mid \mu) \tag{A.14}$$

and $\mathbf{H}$ satisfies

$$\mathbf{H}(\mathbf{S}\boldsymbol{x}_0, \mu) = \mathbf{S}\mathbf{H}(\boldsymbol{x}_0, \mu). \tag{A.15}$$

Differentiating Eq.(A.15) yields

$$\frac{\partial \mathbf{H}}{\partial \boldsymbol{x}_0}(\mathbf{S}\boldsymbol{x}_0, \mu)\mathbf{S} = \mathbf{S}\frac{\partial \mathbf{H}}{\partial \boldsymbol{x}_0}(\boldsymbol{x}_0, \mu). \tag{A.16}$$

When Eq.(A.13) is satisfied, the eigenvector $\boldsymbol{u}_1 \in \boldsymbol{R}^{10}$ belonging to the simple eigenvalue zero of $\dfrac{\partial \mathbf{H}}{\partial \boldsymbol{x}_0}$ on a singular point $(\boldsymbol{x}_0^*, \mu^*)$ satisfies

$$\mathbf{S}\boldsymbol{u}_1 = \pm\boldsymbol{u}_1. \tag{A.17}$$

Here, we can derive $\tilde{H}(x, \nu)$ in the same way as shown in Eq.(2.71) $\sim$ (2.85). When $\mathbf{S}\boldsymbol{u}_1 = -\boldsymbol{u}_1$ holds, the following equations are satisfied;

$$\tilde{H}_{01} = \left\langle \boldsymbol{v}_1, \frac{\partial \mathbf{H}}{\partial \mu} \right\rangle = \left\langle \boldsymbol{v}_1, \mathbf{S}\frac{\partial \mathbf{H}}{\partial \mu} \right\rangle$$

$$= \left\langle \mathbf{S}'\boldsymbol{v}_1, \frac{\partial \mathbf{H}}{\partial \mu} \right\rangle = -\left\langle \boldsymbol{v}_1, \frac{\partial \mathbf{H}}{\partial \mu} \right\rangle,$$

and

$$\tilde{H}_{20} = \left\langle \boldsymbol{v}_1, \frac{\partial^2 \mathbf{H}}{\partial \boldsymbol{x}_0^2}(\boldsymbol{u}_1, \boldsymbol{u}_1) \right\rangle = \left\langle \boldsymbol{v}_1, \frac{\partial^2 \mathbf{H}}{\partial \boldsymbol{x}_0^2}(\mathbf{S}\boldsymbol{u}_1, \mathbf{S}\boldsymbol{u}_1) \right\rangle$$
$$= \left\langle \mathbf{S}'\boldsymbol{v}_1, \frac{\partial^2 \mathbf{H}}{\partial \boldsymbol{x}_0^2}(\boldsymbol{u}_1, \boldsymbol{u}_1) \right\rangle = -\left\langle \boldsymbol{v}_1, \frac{\partial^2 \mathbf{H}}{\partial \boldsymbol{x}_0^2}(\boldsymbol{u}_1, \boldsymbol{u}_1) \right\rangle.$$

Hence, $\tilde{H}_{01}$ and $\tilde{H}_{02}$ vanish and pitchfork bifurcation occurs.

Appendix B

Chaotic Harmonic Oscillation

The chaotic $M_{3\alpha}$ oscillation is also generated in computation. The waveforms at $E_m = 0.275$, $\eta = 1.0$, $R = 1.0\Omega$ and $r = 3.1\Omega$ are shown in Fig.B.1. In this figure, the fluxinterlinkage Ψ_0 is defined below;

$$\Psi_0 \triangleq \Psi_a + \Psi_b + \Psi_c. \tag{B.1}$$

The waveforms of inductor currents show that the currents change the direction every about 20π and in a term the currents circulate in the delta-connection. On the other hand, the waveform of zero-sequence flux Ψ_0 is distinctive, that is, in a term the waveform is nearly monotone increasing or decreasing. The Ψ_0 satisfies the following equation;

$$\frac{d}{d\tau}\Psi_0 = -rI_0, \qquad where \quad I_0 \triangleq I_a + I_b + I_c. \tag{B.2}$$

Then, Ψ_0 increases or decreases monotonically while the currents circulate in a direction. As a result, the circulating currents cannot continue for a long span in a direction except for $r = 0$. On the other hand, Ψ_0 at $r = 0$ is a constant and the circulating currents can last. Now, assume that the oscillations are approximated by the oscillations at $r = 0$ in a short span, then we analyze periodic harmonic oscillations at $r = 0$.

We fix the delta-connected resistances $r = 0\Omega$, series resistance $R = 2.5\Omega$, and $\eta = 1.0$. The typical amplitude characteristics of harmonic oscillations at $\Psi_0 = 0$, 0.1, 0.35 are shown in Fig.B.2. In this figure, only the bifurcations on which stable solutions lose their stability are shown.

At $\Psi_0 = 0$, there are saddle-node bifurcations $S_1 \sim S_3$ and pitchfork bifurcations P_1 and P_2. The saddle-node bifurcations S_1 and S_2 represents harmonic resonances and the pitchfork bifurcation represents the generation of oscillations which have DC components

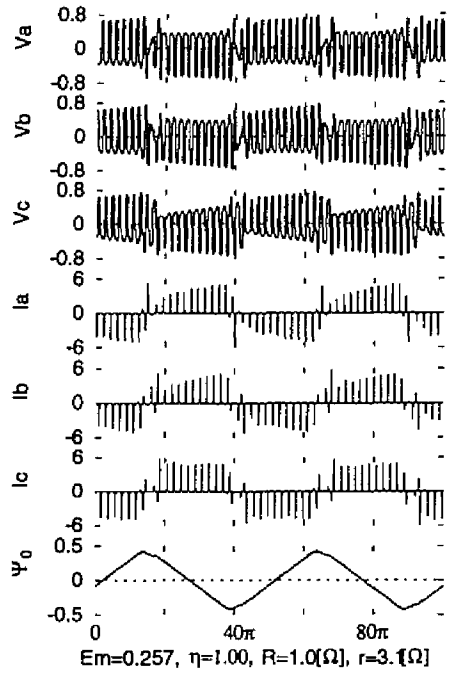

Fig. B.1: Waveforms of chaotic $M_{3\alpha}$ oscillation.

in the inductor currents. The stable solutions are classified into three sorts, that is, the nonresonant oscillations which don't have DC components in the inductor currents, the resonant oscillations which don't have DC components in the inductor currents and the resonant oscillations which have DC components in the inductor currents.

At $\Psi_0 = 0.1$, the existence of Ψ_0 causes the disappearance of pitchfork bifurcations. That is, the pitchfork bifurcations P_1 and P_2 disappear, and in the places saddle-node bifurcations S_6 and S_5 appear. The stable solution with DC components in the inductor currents at $\Psi_0 = 0$ changes to two sorts of solution at $\Psi_0 = 0.1$; the one is the oscillation whose Ψ_0 and $\bar{I}_0$ are same sign and the other is opposite, where $\bar{I}_0$ represent the DC component of I_0.

At $\Psi_0 = 0.35$, the region of the oscillation whose Ψ_0 and $\bar{I}_0$ are opposite sign becomes small and disappears when the Ψ_0 is further increased.

Next, fixing the source line-voltage $E_m = 0.257$, we obtain the DC components $\bar{I}_0$ against the fluxinterlinkage Ψ_0 of the periodic solutions at r=0Ω, $R = 1.0\Omega$ and $\eta = 1.0$ shown in Fig.B.3. In this figure, the solutions in the first and third quadrant represent the same sign

solutions and the solutions in the second and forth quadrant represent the opposite sign solutions. The stable solutions at $\bar{I}_0 \simeq \pm 0.13$ represents the resonant oscillations which have DC components in the inductor currents and the stable solutions in the neighborhood of the origin correspond to the resonant oscillations which don't have DC components in the inductor currents at $\Psi_0 = 0$. The former stable opposite sign solutions disappear by saddle-node bifurcations at $|\Psi_0| \simeq 0.36$.

From the results, we can guess the oscillation at $r = 2.5\Omega$. That is, when $\bar{I}_0 < 0$ and $\Psi_0 < 0$ are satisfied, Ψ_0 increases monotonically, and when Ψ_0 exceeds 0.36, the oscillation disappears and change to the oscillation $\bar{I}_0 > 0$, $\Psi_0 > 0$ as shown by the arrows ① and ② in Fig.B.3. Then Ψ_0 decreases monotonically, and when Ψ_0 exceeds -0.36, the oscillation

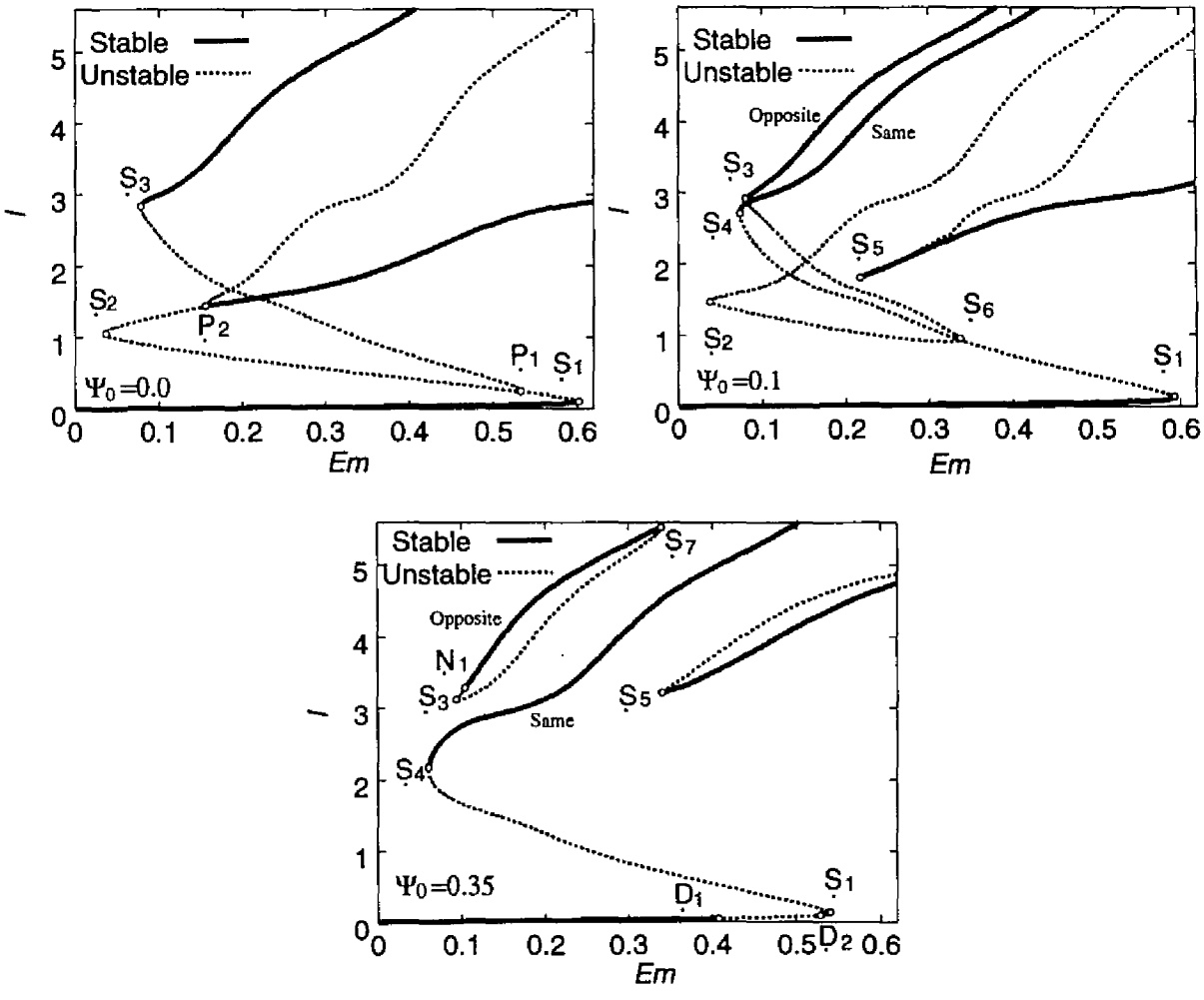

Fig. B.2: Amplitude characteristics at $r = 0\Omega$, $R = 1.0\Omega$, $\eta = 1.0$.

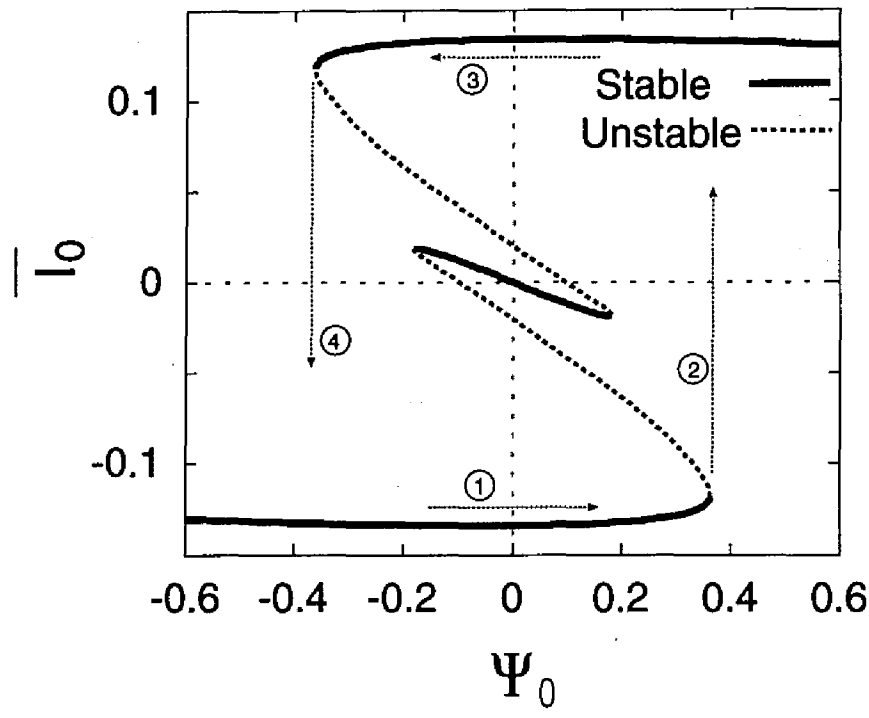

Fig. B.3: The DC component of $\bar{I}_0$ against the fluxinterlinkage Ψ_0 at r =0Ω.

disappears and changes to the oscillation $\bar{I}_0 < 0$, $\Psi_0 < 0$ as shown by the arrows ③ and ④. Thus, the oscillation continues as alternately changing the direction of inductor currents.

The fact indicates that the oscillation is based on the two solutions which are generated by the disappearance of the pitchfork bifurcation P_1.